GOLD BASED NANOMATERIALS:
BIOMOLECULE DETECTION, DRUG RELEASE AND
CATALYTIC APPLICATIONS

Ph. D. THESIS

by

SHAHBAZ AHMAD LONE

DEPARTMENT OF CHEMISTRY
INDIAN INSTITUTE OF TECHNOLOGY ROORKEE
ROORKEE-247667 (INDIA)
APRIL, 2019

GOLD BASED NANOMATERIALS:
BIOMOLECULE DETECTION, DRUG RELEASE AND CATALYTIC APPLICATIONS

A THESIS

*Submitted in partial fulfilment of the
requirements for the award of the degree*

of

DOCTOR OF PHILOSPHY

in

CHEMISTRY

by

SHAHBAZ AHMAD LONE

**DEPARTMENT OF CHEMISTRY
INDIAN INSTITUTE OF TECHNOLOGY ROORKEE
ROORKEE-247667 (INDIA)
APRIL, 2019**

INDIAN INSTITUTE OF TECHNOLOGY ROORKEE
ROORKEE

CANDIDATE'S DECLARATION

I hereby certify that the work being presented in the current thesis entitled "**GOLD BASED NANOMATERIALS: BIOMOLECULE DETECTION, DRUG RELEASE AND CATALYTIC APPLICATIONS** " in partial fulfilment of the requirement for the award of the Degree of Doctor of Philosophy and submitted in the Department of Chemistry of the Indian Institute of Technology Roorkee, is an authentic record of my own work during the period from December, 2014 to April, 2019 under the supervision of Dr. Kalyan K. Sadhu, Assistant Professor, Department of Chemistry, Indian Institute of Technology Roorkee, Roorkee.

The matter presented in this thesis has not been submitted by me for award of any other degree of this or any other Institution.

Signature of the Candidate

This is to certify that the above statement made by student is correct to the best of my knowledge.

Signature of Supervisor

The Ph.D Viva-Voce Examination of **Mr. Shahbaz Ahmad Lone**, Research Scholar, has been held on **13-08-2019.**

Chairperson, SRC   **Signature of External Examiner**

This is to certify that the student has made all the corrections in the thesis.

Signature of Supervisor   **Head of the Department**

**Dated:**____13-8-2019____

Dedicated with love
to
My Parents
and
Grand parents

ABSTRACT

The thesis entitled, "**Gold based nanomaterials: biomolecule detection, drug release and catalytic applications**" has been divided into four chapters.

Chapter 1 presents a general introduction for the gold nanoparticles (AuNP) and their properties. The origin of color in the AuNP solution due to surface plasmon resonance (SPR) and its utility in the detection of biomolecules were discussed. The unique properties displayed by gold nanomaterials are determined by their morphologies. Various methods to control the morphologies of the nanoparticles includes the use of different shapes of seed and different capping agents like DNA, amino acids and proteins for controlling the shape of gold nanoarchitectures. Materials containing two or more different nanoscale functionalities are attractive candidates for advanced nanomaterials. Bimetallic gold-iron nanomaterials being magnetic in nature possess hybrid properties were discussed for their uses in the magnetic resonance imaging, drug delivery process and in the catalytic process of organic or inorganic reactions.
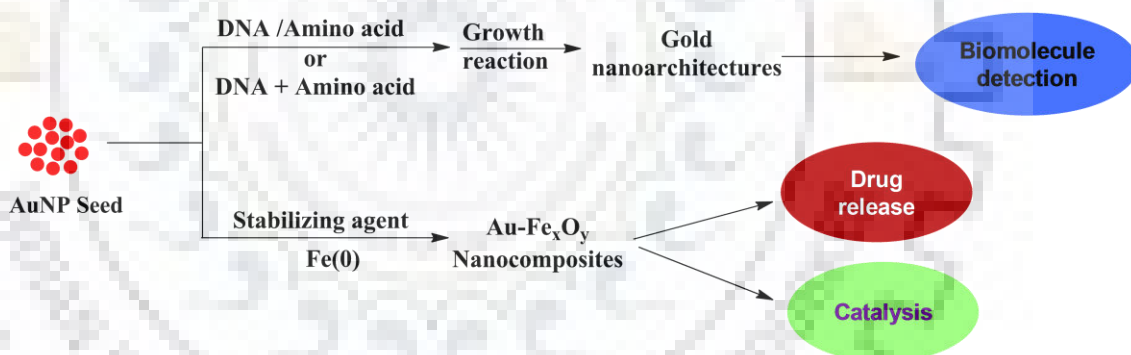
Scheme A. Gold based nanomaterials for biomolecule detection, drug release and catalytic application.

The last part of this chapter discusses the scope of the present work. Different gold nanoarchitectures can be formed by growth controlled reactions using seed mediated methods. The growth reactions in presence of DNAs or natural amino acids and their combination can be utilized for the development of different gold nanoarchitectures, which might be suitable for the detection of biomolecule such as targeted DNA or targeted peptide sequence. Facile methods for the synthesis of gold based nanocomposites can be developed for different catalytic and drug release applications.

Chapter 2 describes the formation of the gold based architectures after the growth reactions from the separate treatment of amine modified DNAs and natural amino acids. This chapter has been divided into two sections.

Section A describes the role of reducing agent for formation of nanoflowers and nanospheres with single strand amine modified DNA

Gold nanoseeds (AuNP seed) were synthesized by the citrate reduction method. Growth mediated formation of gold nanoflowers from AuNP seed was studied in the presence of 600 nM DNA and reducing agents hydroxylamine and hydroquinone.**PMR**(H_2N-C_6-5'-ACATCAGT-3') resulted in nanoflower formation only with hydroxylamine, **PML** (H_2N-C_6-5'-GATAAGCT-3') or no DNA, resulted in nanospheres with both reducing agents. The growth reactions by variation of seed concentration (0.15 nM to 0.45 nM) were examined with both reducing agents. With hydroxylamine nanoflowers were formed for PMR only at high seed amount. In the case of hydroquinone reduction, nanoflowers were formed only at low seed concentration. Control experiments with **MMR** (H_2N-C_6-5'-TCTTCTGT-3'), **MML** (H_2N-C_6-5'-GTTTTGCT-3') and other thymine modified DNAs did not show any nanoflower formation. The role of 5'-ACA and amine terminal for the development of nanoflowers was confirmed with other mutated sequences, both end modified and non modified PMR. The requirement of 8-mer sequences for the gold nanoflowers formation was monitored by decreasing length of PMR. The nanoflowers and nanosphere obtained from **PMR** and **PML** were used for detection of DNA sequence of miR-21with hydroquinone.

Section B describes the selective formation of coral shaped nanomaterials with methionine (Met). AuNP were incubated with all natural amino acids (9 mM) followed by addition of hydroxylamine and gold salt. Arg, His, Ser, Phe, Met, Trp developed blue colored and others developed red colored solutions or got precipitated. Transmission electron microscopy (TEM) confirmed formation of coral shaped nanostructures with Met and aggregated or non-aggregated with other amino acid. Controlled reactions with other molecules and inorganic salts containing sulfur resulted in aggregated or non aggregated nanoparticles. On decreasing amino acid concentration to 50 μM aggregation was observed only for His and Met and coral formation from Met was inhibited. Seed variation methodology with three representative amino acids Arg, His and Met at 50 μM were performed within the range 0.03 nM to 0.45 nM. In the case of Arg, the intensity of absorption increased with increasing seed amount and other two amino acids showed blue shift in the absorption peak with increasing seed amount. Decreasing trend of particle size with increasing seed amount was observed from TEM images. In the case of Met, network structure was observed at low seed amount.

Chapter 3 describes the growth reaction of AuNP after the combined treatment of amine modified DNAs and selected amino acids. This chapter has been divided into two sections.

Section A describes the role of amine modified DNA for detection of single Arg over Lys substitution in peptide. In order to develop a tool for the detection of Arg, the earlier growth reactions with all natural amino acids were further explored in presence of **PMR**. The nanoseeds were incubated with 600 nM **PMR** prior to addition of 9 mM amino acid. Arg resulted in the formation of nanoflowers whereas aggregated or non-aggregated spherical nanoparticles were observed for other amino acids. This confirmed the selectivity of Arg among the amino acids for the nanoflowers formation which is due to strong hydrogen bonding between Arg and DNA. For further improvement in the selective detection process of Arg, the amino acid concentration was lowered to 50 µM, interestingly, at this concentration, Arg selectively formed nanoflowers, Met and His did not form aggregation. The selective detection of Arg to form gold nanoflowers was further applied for detection of Arg in a peptide sequence Ac-(AAAAR)$_3$A-NH$_2$ (RRR) and Ac-(AAAA)$_3$K$_2$RA-NH$_2$ (KKR) containing single arginine. This was compared with Lys substituted peptides Ac-(AAAAK)$_3$A-NH$_2$ (KKK)

Section B describes the time dependent growth reactions of AuNPs with **PMR** and MMR in presence of amino acids containing polar side chains Ser, Thr, Asn and Gln. Gold nanoseeds were incubated with these amino acids for 30 minutes followed by the addition of hydroxylamine and gold salt. Nanoparticles synthesized with Ser changed red color to blue immediately while others resulted in red color and developed blue color gradually with time. The growth reactions were again performed in presence of 600 nM **PMR** and **MMR** before addition of amino acids. **PMR** selectively inhibited aggregation for Ser based reaction whereas both **PMR** and **MMR** inhibited the aggregation for Thr, Asn and Gln based reactions, confirmed from TEM images and DLS measurements. The sensitivity of the DNA for interactions with Thr, Asn and Gln was performed by lowering the concentration of DNA for aggregate formation observed after 12 h by appearance of dual peaks in the absorption spectra. The sensitivity was rationalized as a combined effect of specific van der Waals interaction, hydrogen bonding and water mediated bonds between DNA and these amino acids.

Chapter 4 describes the seed mediated approach for the formation of gold-iron oxide nanocomposites for doxorubicin release and catalysts for oxygen evolution reaction. This chapter has been divided into two sections.

Section A describes the benign and straight forward one-pot syntheses for Au-Fe$_x$O$_y$(**1−9**) using sodium citrate as a stabilizing agent and iron powder as a reducing agent and metal source. The Au:Fe ratios in the nanocomposites were modulated by changing the seed concentration, amount of stabilizing agent and reducing agent. The exchange bias (EB), which arises from the interaction between antiferromagnetic hematite (Fe$_2$O$_3$) and ferromagnetic magnetite (Fe$_3$O$_4$) present within the nanocomposites, was found to increase progressively from **7**→**6**→**9** at 5K. EB of **5** was coincidental with **7** at 5K, while it showed anomalous behavior at high temperature due to presence of unblocked Fe$_3$O$_4$, γ-Fe$_2$O$_3$ and α-Fe$_2$O$_3$ in nanocomposite**5**. The coercivity at 5K increased progressively from samples **5**→**7**→**6**→**9**.These citrate stabilized Au-Fe$_x$O$_y$ nanocomposites were utilized for catalytic applications of organic nitroarene reduction process and host-guest chemistry with doxorubicin drug.

Section B describes the syntheses of tryptophan stabilized Au-Fe$_x$O$_y$ nanocomposites as electro catalysts for oxygen evolution reaction (OER). Among all natural amino acids, only the solution containing tryptophan developed a violet color, indicating the formation of gold nanomaterials. Nanocomposites **(10–25)** were synthesized by varying the seed concentration and Fe amount. The representative nanocomposite**10**, **15**, **21** and **25** were used as electro catalysts in OER reaction. The polarization curves demonstrated the better OER activity of the catalysts compared to the mixture of seeds and commercially available Fe$_2$O$_3$ and Fe$_3$O$_4$. Chronoamperometry test was carried out for the nanocomposites to check the stability at their corresponding over potentials for 5 h indicating a long-term viability of these materials. Slight loss in the iron content was observed after the post electrochemical behavior indicating materials are sufficiently stable.

The thesis ends with an overall conclusion and provides scopes for further research in this area.

ACKNOWLEDGEMENTS

"Be aware of your worth; use all of your power to achieve it"

Dr. Iqbal

TABLE OF CONTENTS

Title	Page No.

Chapter 3   Growth reaction of gold nanoparticles after the combined treatment of amine modified DNAs and selected amino acids

Chapter 4   Gold iron oxide nanocomposites for doxorubicin release and catalysts for oxygen evolution reactions

List of Schemes

List of Figures

Chapter 2

Chapter 3

Chapter 4

List of Tables

Chapter 4

List of Abbreviations

AuNP	Gold nanoparticle
SPR	Surface Plasmon Resonance
p-βCD	Pyridinium–β–cyclodextrin chloride
CTAB	Cetyltrimethylammonium bromide
TOAB	Tetraoctylammonium bromide
PVP	Poly(N-vinylpyrrolidone)
PEG	Polyethyleneglycol
PEI	Polyethyleneimine
Arg	Arginine
Ala	Alanine
Asn	Aspargine
Cys	Cysteine
His	Histidine
Lys	Lysine
Glu	Glutamic acid
Asp	Aspartic acid
Ser	Serine
Thr	Threonine
Glu	Glutamine
Val	Valine
Leu	Leucine
Ile	Isoleucine
Tyr	Tyrosine
Met	Methionine
Trp	Tryptophan
Phe	Phenylalanine
Pro	Proline
Gly	Glycine
Sec	Selenocysteine
DNA	Deoxyribonucleic acid
ssDNA	Single strand deoxyribonucleic acid
dsDNA	Double strand deoxyribonucleic acid
RNA	Ribonucleic acid

miRNA	micro Ribonucleic acid
PCR	Polymerase chain reaction
RCA	Rolling cycle ampilification
HCR	Hybridization chain reaction
acac	Acetylacetonato
OA	Oleic acid
OAm	Oleylamine
TEOS	Tetraethylorthosilicate
PVA	Polyvinyl alcohol
pNIPAAm	Poly (N-isopropylacrylamide)
LCST	Lower critical solution temperature
FC	Field cooling
ZFC	Zero field cooling
EB	Exchange bias
MRI	Magnetic resonance imaging
HA	Hydroxylamine
HQ	Hydroquinone
TEM	Transmission electron microscopy
FE–SEM	Field emission scanning electron microscope
DLS	Dynamic light scattering
HSA	Human serum albumin
GSH	Glutathione reduced
GSSG	Glutathione oxidised
AApusc	Amino acids containing polar uncharged side chain
PDI	Polydispersity index
IR	Infra red
XPS	X-ray photoelectron spectroscopy
SQUID	Superconducting quantum interference device
PXRD	Powder X-ray diffraction
OER	Oxygen evolution reaction
No DNA	No DNA
PMR	H_2NC_6-5′-ACATCAGT-3′
PML	H_2NC_6-5′-GATAAGCT-3′

MMR	H_2NC_6-5′-TCTTCTGT-3′
MML	H_2NC_6-5′-GTTTTGCT-3′
PMR'	5′-ACATCAGT-3′-C_7NH_2
No mod	5′-ACATCAGT-3′
Both Mod	H_2NC_6-5′-ACATCAGT-3′-C_7NH_2
PMA	H_2NC_6-5′-AAATCAGT- 3′
PMT	H_2NC_6-5′-ATATCAGT- 3′
PMG	H_2NC_6-5′-AGATCAGT- 3′
PM3	H_2NC_6-5′-ACA-3′
PM4	H_2NC_6-5′-ACAT-3′
PM5	H_2NC_6-5′-ACATC-3′
PM6	H_2NC_6-5′-ACATCA-3′
PM7	H_2NC_6-5′-ACATCAG-3′
PMRTI	H_2NC_6-5′-TCATCAGT-3′
PMRT2	H_2NC_6-5′-TTATCAGT-3′
PMRT3	H_2NC_6-5′-ACTTCAGT-3′
PMRT4	H_2NC_6-5′-ATTTCAGT-3′
PMT5	H_2NC_6-5′-ACATCTGT-3′
PMA2	H_2NC_6-5′-ACAAAGCT-3′
MML'	H_2NC_6-5′-ACATTGCT-3′

Chapter 1
General Introduction

1.1 NANOPARTICLES: CONCEPT

Nanoscience and nanotechnology are recent innovative developments of science and engineering that are developing at a very fast pace. They are driven by the desire to formulate materials with novel and improved properties that are likely to impact virtually all areas of physical and chemical sciences, biological sciences, health sciences, and other interdisciplinary fields of science and engineering. Particles with sizes in the range of $1-100$ nm are called nanoparticles. Nanoparticles are atoms or molecules bonded together (these particles usually contain 10^6 atoms or fewer) and are intermediate in size between individual atoms and aggregates large enough to be called bulk material.[1] These particles may be dispersed in gaseous, liquid, or solid media or may be covered by shells or deposited on other substrate material. Generally all possible components, covering shells, embedding medium may be a metal, semiconductor or a dielectric leaving open all possible combinations. The nanoparticles are larger than individual atoms and molecules but are smaller than the bulk solid, materials in the nanometer size regime. Nanoparticles show properties that are intermediate between a macroscopic solid and an atomic or molecular system. Three major factors that are responsible for these differences are high surface to volume ratio, quantum size effect, and electrodynamic interactions.

Interest in metallic nanoparticles has increased because they can artificially be tailored to novel materials with extraordinary properties. The materials properties of the nanoparticles are very attractive and cover a diverse range depending on the number of the surface atoms. In the small sized nanoparticles there are two different size effects: intrinsic size effect and extrinsic size effect. Intrinsic size effect is related to the changes in volume and surface of the material properties. Electronic and structural properties like ionization potentials, binding energies, chemical reactivity, crystallographic structure, melting temperatures and optical properties depends on the particle size and geometry. With increase in the size of the particle the energy levels continue to split and finally merge into the quasi-continuous band structure for the bulk solid. For small sized particles the optical properties are size dependent and for large particles the electrodynamic theory can be applied using bulk optical constants and this is known as extrinsic size effects. Colloidal solutions of the noble metals like, copper, silver, and gold, show distinctive colors that have received considerable attention from researchers. The interesting colors observed in colloidal gold solutions have led to broad study of their optical properties, an effort to compare their behavior under diverse micro environmental conditions.[2-7]

1.2 GOLD NANOPARTICLES: COLOR

Metal nanoparticles particularly gold, attracted substantial attention because of many interesting properties and potential technological applications.[8-11] The optical properties of isolated gold nanoparticles have been extensively studied.[12,13] When gold is divided into smaller particles, the radius to the wavelength ratio becomes important, and when the size of particle is smaller than the wavelength, the Rayleigh approximation (i.e. no retardation) holds and the mathematics becomes simple.[14] Mie in 1908 shown that Plasmon excitation is present when the radius is large compared with the wavelength of light and in that case, the retardation effect should be included to get the correct results. Noble metal nanoparticles display a characteristic strong absorption band in the visible region and this is a small particle effect, since the band is absent in the individual atom or in the bulk.[12-14]

Spherical gold nanoparticles (AuNPs) exhibit a range of colors (e.g., brown, orange, red and purple) in aqueous solution as the core size increases from 1 to 100 nm, and generally show a size relative absorption peak from 500 to 550 nm.[15,16] The physical origin of the light absorbed by the metal nanoparticles is the coherent oscillation of the conduction band stimulated by the incident light. When the oscillations of the surface electrons matches with the frequency of the incident light, resonance can be achieved as a result strong electromagnetic fields will form on the surfaces of nanoparticles (Figure 1.1) along with the appearance of a distinctive absorption peak in the visible frequency range called Surface Plasmon Resonance (SPR).[17] However, this band is absent in both small nanoparticles (d < 2 nm) and the bulk material. The intense red color of gold nanoparticles is the manifestation of SPR.
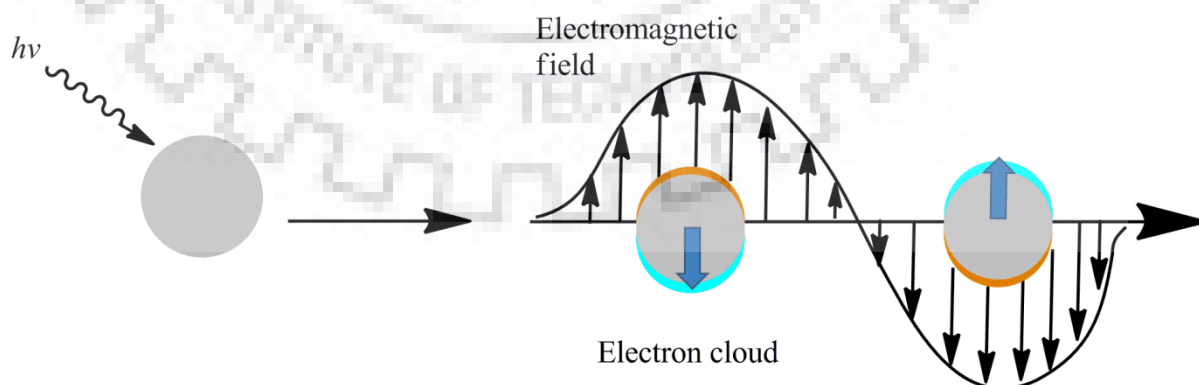
Figure 1.1 Schematic illustration of Surface Plasmon, the electric field induces polarization of the free electrons on the surface of the metal sphere.

The electromagnetic wave polarizing the surface charges in interface of nanoparticle surfaces and external medium like air or water. These oscillations are very sensitive to the events taking place at the nanoparticle-medium interfaces and can be lead to shift of absorption band accompanying with color changes of the nanoparticle solutions. SPR can be influenced by the nanoparticle size, shape, surface coating and local environment.[18-20] Gold nanoparticles are the most commonly used candidates for fabricating SPR sensing strategies because their Plasmon absorption bands generally lie in the visible region. The remarkable red shift of SPR often causes a distinctive color change of the AuNP solutions from red to blue or purple, which can be seen by the naked eye. The distinct physical and chemical properties possessed by gold nanoparticles (AuNPs) like unique optoelectronic properties, high stability, ease of synthesis and excellent biocompatibility make them excellent materials for the fabrication of novel chemical and biological sensors (Figure 1.2).[21,22] The interaction between the recognition element and the analyte can change physicochemical properties of AuNPs like SPR, conductivity, redox behavior etc., that in turn can produce a detectable response signal. AuNPs offer a suitable platform for multifunctionalization with a wide range of organic or biological ligands for the selective binding and detection of small molecules and biological targets.[9,23] The analytes of the AuNP-based assays mainly include small organic molecules,[24-27] proteins, [25-27] and nucleic acids.[26-30]
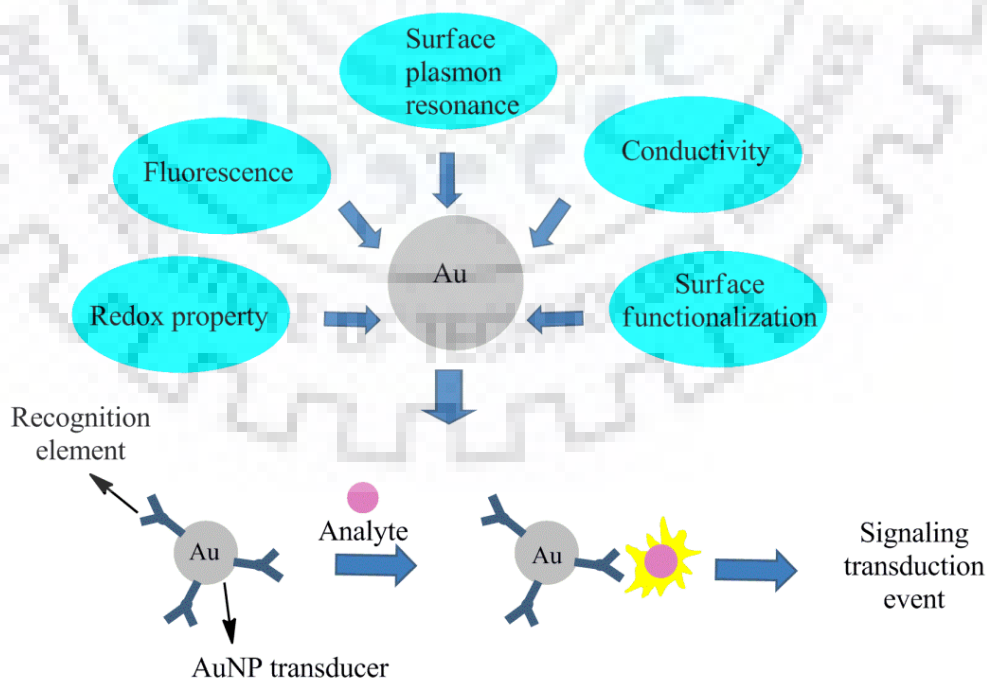
Figure 1.2 Physical properties of AuNPs and schematic illustration of AuNP-based detection system.

1.3 SYNTHESIS AND SURFACE FUNCTIONALIZATION

Faraday in 1857 reported the formation of deep-red solutions of colloidal gold by reduction of an aqueous solution of chloroaurate ($AuCl_4^-$) using phosphorus in CS_2 (a two-phase system).[31] Various methods for AuNPs preparation have been developed for synthesis of AuNPs from last two decades, focusing on control over their size, shape, solubility, stability, and functionality.[32-34] It is worth noting that the term colloid and cluster are frequently used interchangeably; the former generally refers to particles having diameters more than 10 nm, while the latter commonly refers to smaller particles. Few synthetic methods and their modifications are discussed in the following sub headings.

1. 3.1 Citrate and Related Particle Preparation Methods

Among the conventional methods that have been used for the syntheses of gold nanoparticles is the citrate reduction method. In 1951 Turkevich *et al.* developed a synthetic method for preparing AuNPs by treating hydrogen tetrachloroaurate ($HAuCl_4$) with citric acid in boiling water, where citrate acts as both reducing and stabilizing agent and provides gold nanoparticles of 20 nm diameter (Figure 1.3).[35]
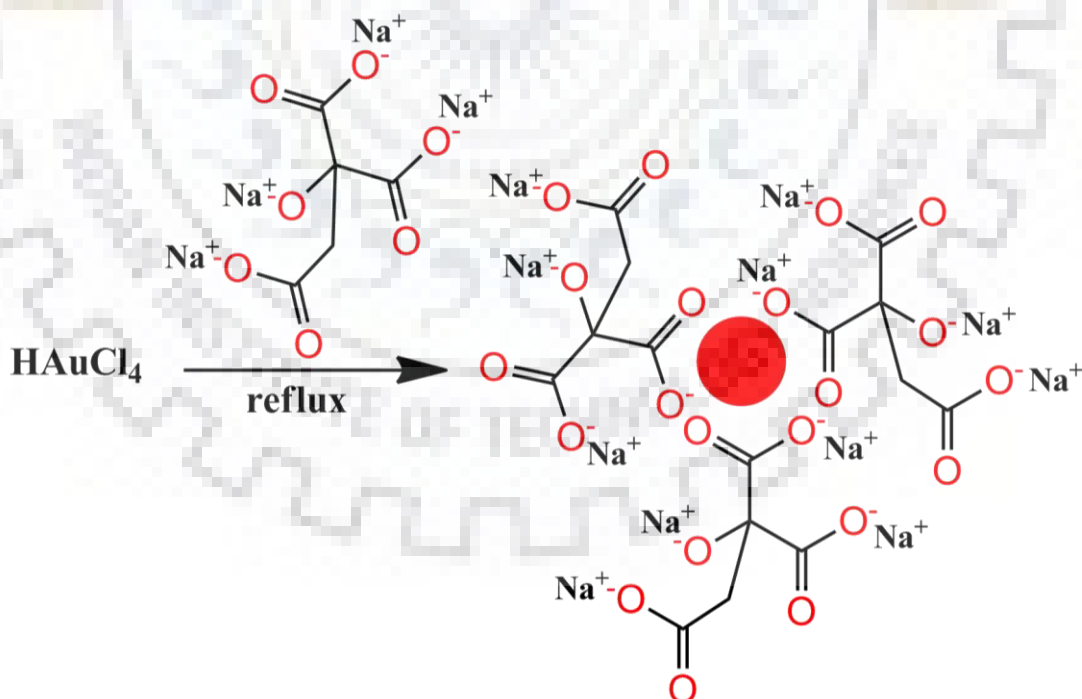
Figure 1.3 Citrate-stabilized AuNPs prepared by refluxing $HAuCl_4$ (aq.) solution where citrate acts as both stabilizing ligand and reducing agent.

Frens further modified this method by varying the gold−to−citrate ratio for control of particle size.[36] This protocol has been widely employed to prepare dilute solutions of moderately stable spherical AuNPs with diameters of 10 to 20 nm, though larger AuNPs (e.g., 100 nm) can also be prepared.[11] As large nanoparticles are synthesized it is difficult to obtain monodispersity by this method. Chow and Zukoski provided the kinetics of the Turkevich process.[37] Sodium 3-mercaptopropionate stabilized AuNPs was prepared by simultaneous addition of citrate salt and an amphiphile surfactant; the size was controlled by varying the stabilizer/gold ratio.[38] The classic Turkevitch−Frens synthesis with citrate stabilizer is practically convenient, produces nanoparticles with high stability and is used as a precursor for AuNPs based systems.

1.3.2 Other methods of reduction

Other common reducing agents include sodium borohydride[39] and amine molecules.[40] The addition of stabilizing agent is often required with these reducing agents. Luong *et al*. synthesized 5−6 nm gold nanoparticles by reduction of sodium borohydride in presence of mono−6−deoxy−6−pyridinium−β−cyclodextrin chloride (p-βCD).[41] Resulting gold nanoparticles were capable of oxidizing the reduced p-βCD, leading to the formation of the p-β CD−gold complex via hydrogen bonding and ionic interaction. Jhonsone *et al*. used the dual reductants like tannic acid and sodium borohydride, ascorbic acid and sodium borohydride for gold nanoparticle syntheses.[42] Astruck *et al*. used sodium borohydride as reductant and stabilizer for the syntheses of gold nanoparticles.[43]

1.3.3 Seed mediated methods for enlargement of Colloidal Au Nanoparticles

Natan *et al*. described a method for the enlargement of colloidal gold nanoparticles called "Seeding" approach.[44] It is based on the colloidal gold surface catalyzed reduction of Au^{3+} by NH_2OH to obtain nanoparticles of upto 100 nm in diameter (Scheme 1.1).
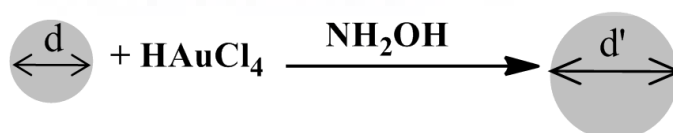
Scheme 1.1 Hydroxylamine seeding of colloidal Au nanoparticles

The approach grows existing nanoparticles into bigger ones determined by the initial particle diameter and Au^{3+} added. The resulting particles exhibit improved monodispersity because of

improved size distributions related to citrate reduction method. The work was further improved by Murphy[45] and Liz-Marzan[46] for synthesis of monodisperse AuNPs of upto ~180 nm in diameter with ascorbic acid as a reducing agent and cetyltrimethylammonium bromide (CTAB) as surfactant. However CTAB strongly binds to the surface and restricted possibility of further functionalization. Seed-mediated synthetic strategies, using different reducing agents and adjusting reaction conditions were reported from last ten to twelve years. Use of 2-mercaptosuccinic acid[47], hydroquinone[48] and ascorbic acid[49] as reducing agent in aqueous solution were developed. The method allows better control of nanoparticle size and results in improved size distribution and nanoparticles formed are extremely stable. Puntes developed seed mediated enlargement of citrate stabilized AuNPs upto 200 nm size. The growth was controlled by adjusting the reaction conditions: temperature, gold precursor to seed particle concentration, and pH.[50] The method provides highly monodisperse nanoparticles. Coreduction of gold and silver salts by seed growth approach resulted in the formation of monodispersed gold-silver alloy nanoparticles with controlled size and composition.[51] Core shell Au/FePt nanoparticles were also synthesized by seed-mediated method using gold nanoparticles as seeds under inert conditions.[52] Seed-mediated method were also used to control the shape and size of the nanoparticles.[50] Nanoparticle of size ranging between 3.5 nm to 10 nm were achieved by combining use of two reducing agents tannic acid and sodium citrate.[53] Au nanorings were also prepared by seed-mediated approach through site selective growth of Au on the periphery of Pd ultrathin nanosheets.[54] Seed-mediated methods have been used to ultraprecisely control the size and shape of gold nanocubes through anisotropic growth.[55] Seed mediated methods provide greater control over the nanoparticle size and provides a platform for the creation of more versatile nanomaterials.[56] Seed mediated methods improved results regarding the traditional Frens method as it produces highly monodisperse particles, increases concentration and allows better control over size and shape.

1.3.4 The Brust−Schiffrin Method for Thiol-protected AuNPs

Initial attempt of stabilizing AuNPs with alkane thiols [57] was achieved by Brust and Schiffrin in 1994. They reported a two-phase synthetic strategy (the Brust–Schiffrin method), utilizing strong thiol-gold interactions to protect AuNPs with thiol ligands (Figure1.4). The method is based on the phase transfer reaction where $AuCl_4^-$ is transferred from aqueous phase to toluene using the surfactant tetraoctylammonium bromide (TOAB) and reduced by sodium borohydride ($NaBH_4$) in presence of dodecanethiol. The addition of $NaBH_4$, a quick change in color from orange to deep brown takes place in organic phase.[58] The gold nanoparticles of diameter 1.5-

5 nm are generated in toluene. These thiol-protected AuNPs possess better stability because of the strong thiol-gold interaction and can be easily handled, characterized, and functionalized. The bromide ion was found to play a significant role (a preferable precursor) in the Brust-Schiffrin synthesis of thiol protected gold nanoparticles.[59]

Figure 1.4 Brust-Schiffrin methods for two-phase synthesis of AuNPs by reduction of gold salts in presence of external thiol ligands.

1.3.5 Place Exchange Method to form Mixed Monolayer AuNPs

The substitution of thiol ligands by different thiols called place exchange was reported by Murray *et al.*[60,61] This method introduces chemical functionality onto the AuNPs in a divergent fashion where initially anchored thiol ligands are exchanged in by free thiol ligands (Figure 1.5 A). The reaction time and the feed ratio of the functional ligands control the loading efficiency onto AuNPs surface. Introduction of two or more ligands provides mixed protective layer for synergetic applications.[62] A wide range of functional groups can be utilized in the synthesis of AuNPs by the use of functionalized thiols to place exchange with phosphine stabilized nanoparticles (Figure1. 5B). [63,64]

1.3.6 Physical Methods for Particle Modification

Physical methods allow further modification of the structure and hence properties of AuNPs**.** Methods like digestive ripening,[65-68] conventional ripening,[69] UV and laser radiations[70,72] have considerably reduced average particle size and polydispersity and triggered formation of 2D and 3D super lattices. Ultrasonic fields can also provide control in the reduction rate of $AuCl_4^-$ and can be used to control the size of the core.[73]

1.3.7 Polymer–Stabilized AuNPs

Commonly used polymers for stabilization include polydopamine,[74-76] poly(Nvinylpyrrolidone) (PVP),[77] polyethyleneglycol (PEG),[78] polyethyleneimine (PEI),[79] and polystyrene.[80,81]

A)

B)

R_1= Br, CN, Ph, OH COOH, COOCH$_3$

R_2 = -(CH$_2$)$_n$CH$_3$ (n= 2, 5, 7, 11, 15, 17)
-p-Ph-OH, -p-Ph-Ph, -p-Ph-CH$_3$
-(CH$_2$)$_3$Si(OCH$_3$)$_3$
-(CH$_2$)$_n$COOH (n= 1, 2, 6, 11)
-(CH$_2$CH$_2$O)$_n$CH$_2$CH$_2$OH (n= 1, 2)
-(CH$_2$)$_2$PO(OH)$_2$
-(CH$_2$)$_2$NMe$_3$Cl
-(CH$_2$)$_2$SO$_3$Na

Figure 1.5(A) General schemes for place exchange reaction for alkane thiol protected AuNPs using functionalized thiols, (B) examples of particles that can be rapidly generated.

1.3.8 Other Capping Ligands

Apart from the thiol ligands a variety of other ligands have been used to stabilize and functionalize the gold nanoparticles. These include disulfides,[82] multivalent thiols,[83] olyamine,[84,85] thioethers,[86] porphyrins,[87] and hydroquinone.[88]

1.4 BIO MOLECULE STABILIZED GOLD NANOPARTICLES

Development of synthetic protocols for monolayer protected water dispersible gold nanoparticles of potential interest for biological applications are biofunctionalized nanoparticles. The syntheses are simpler than the Brust–Schiffrin method and more easily adaptable to large scales, provided the relevant criteria of size control, stability, and functionalization. Biomolecules can be conjugated directly to the surface of gold nanoparticles or surface-bound stabilizing ligands or coatings, either directly or using small cross-linking molecules and other intermediaties.[89] Biological molecules containing acidic or basic group like amino acids and nucleic acid are efficient in gold nanoparticle stabilization because of electrostatic interaction between the gold nanoparticles and the bio molecules, provides one of the easiest ways to functionalize goldnanoparticles.[90]

1.4.1 Amino acid stabilized gold nanoparticles

Amino acids are the organic compounds containing amine (-NH$_2$) and carboxyl (-COOH) functional groups, along with a side chain (R group) which is specific to each amino acid.[91] Amino acids having both amine and carboxyl group attached to the first carbon atom called alpha carbon have particular importance. They are known as α-amino acids or more commonly amino acids. These consist of twenty two proteinogenic amino acids which are the building blocks of the proteins. In the form of proteins amino acids resided the second largest component of human muscles after water. All 22 amino acids are L–stereoisomers although few D–isomers occur in bacteria. Twenty of the proteinogenic amino acids are directly encoded by the triplet codon and are known as standard amino acids. The other two selenocystein (in prokaryates) and pyrrolysine (in archae) are non-standard amino acids encoded by variant codons. Amino acids in solution at neutral pH exist as dipolar ions also called zwitterions in which amino group is protonated (-NH$_3^+$) and carboxylic group is deprotonated (-COO$^-$). The amino acids vary in size, shape, charge, hydrogen-bonding capacity, hydrophobic character, and chemical reactivity. They can be classified into four groups according to their side chain and charge carried at physiological pH (7.4). The side chain makes the amino acid charged, hydrophobic or hydrophilic in nature.[92]

1.4.1.1 Amino acids with electrically charged side chain

These include positively charged side chains arginine (Arg), histidine, (His), lysine (Lys) and negatively charged side chain glutamic acid (Glu) and aspartic acid (Asp) (Figure 1.6 and 1.7).

Asp and Glu contains extra carboxylic group and are acidic in nature. Arg, His and Lys are basic in nature. Lys has been also grouped into essential amino acids.
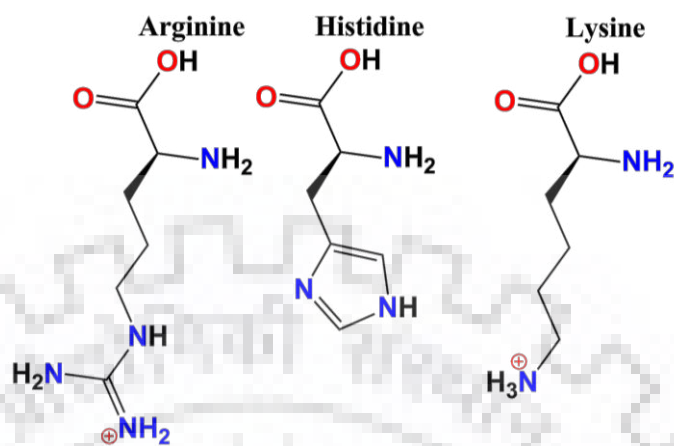
Figure 1.6 Structure of amino acids with positive charged side chain.
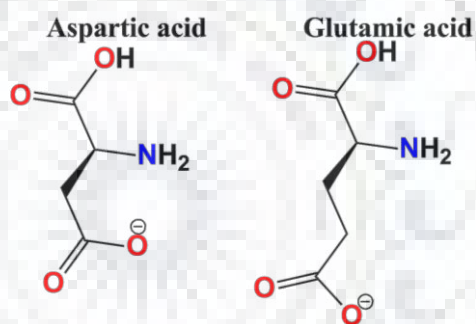
Figure 1.7 Structure of amino acids with electrically charged side chain.

1.4.1.2 Amino acids with polar uncharged side chain

These include serine (Ser), threonine (Thr), aspargine (Asn) and glutamine (Gln) (Figure 1.8). Among them Thr is an essential amino acid
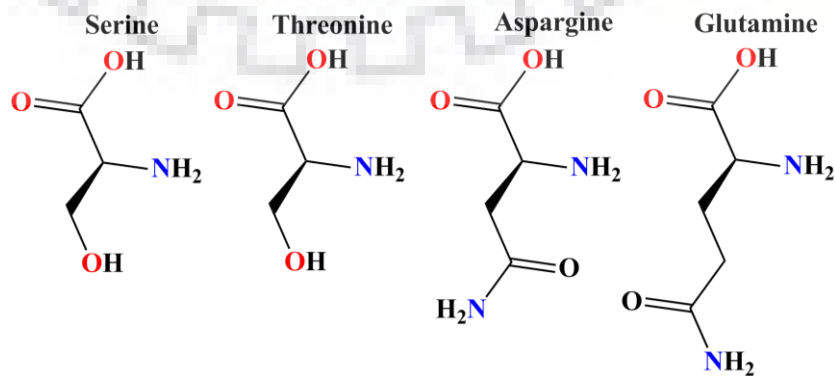
Figure 1.8 Structure of amino acids with polar uncharged side chain.

1.4.1.3 Amino acids with hydrophobic side chain

These include alanine (Ala), valine (Val), leucine (Leu), isoleucine (Ile), tyrosine (Tyr), methionine (Met), tryptophan (Trp) and phenyalanine (Phe) (Figure 1.9). Tyr, Phe, and Trp contain aromatic side chain where as others contain aliphatic side chain. Among them Val, Leu, Ile, Met, Phe, and Trp, are the essential amino acids.
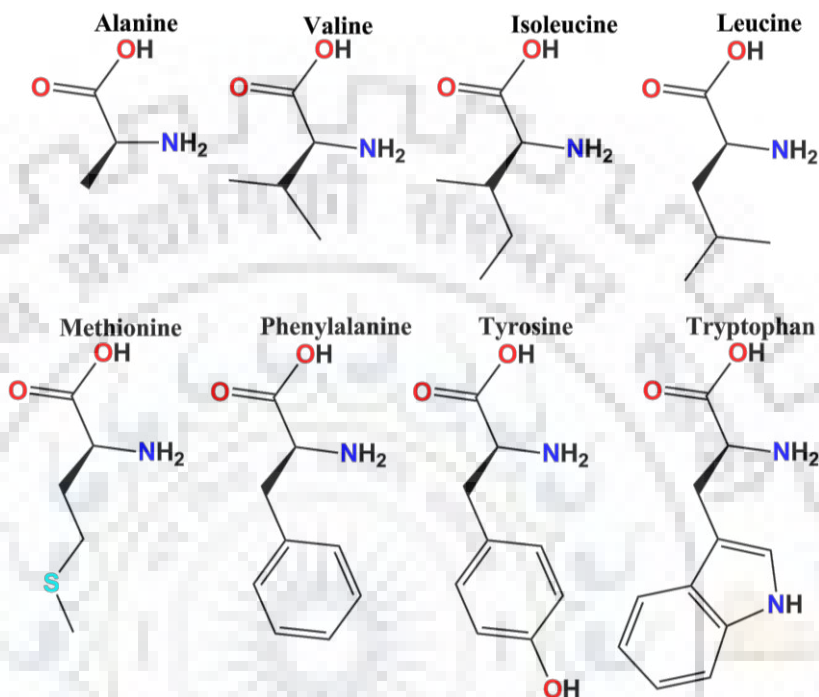
Figure 1.9 Structure of amino acids with hydrophobic side chain

1.4.1.4 Other amino acids

These include cysteine (Cys), selenocystine (Sec), proline (Pro) and glycine (Gly) (Figure 1.10).
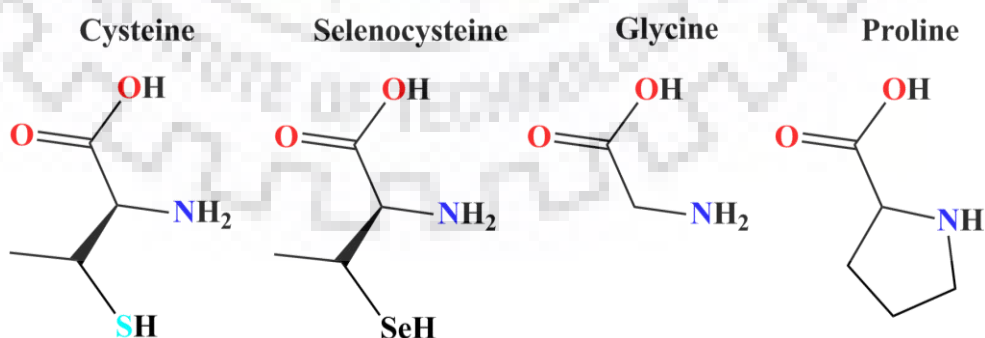
Figure 1.10 Structure of amino acids cysteine, selenocysteine, glycine and proline.

Spherical gold nanoparticles have been synthesized by the reduction of chloroauricacid with sodium borohydride and stabilized by amino acid tyrosine, lysine and glycine.[93-95]

Gold nanoplates have been synthesized with aspartic acid.[96] Maekawa *et al.* have used all the twenty amino acids for the synthesis of gold nanoparticles and prepared a series of different colored solutions.[97] Tryptophan has been used both a stabilizing and reducing agent for gold nanoparticle syntheses and used in imaging human neuronal cells.[98] Proteins have also been used for the stabilizing agent for gold nanoparticles and naoclusters.[99-101]

1.4.2 DNA functionalization of gold

DNA, abbreviation as deoxyribonucleic acid is a polymer composed of monomeric units called nucleotides. The nucleotides are composed of nitrogenous bases, sugar molecule and a phosphate group. The sugar is deoxyribose sugar and the nitrogenous bases are of two types purines and pyrimidines. Purines include adenine (A) and guanine (G) which are fused five and six membered heterocyclic rings while pyrimidines are six membered include cytosine (C) and thymine (T) (Figure 1.11A). The DNA molecule consists of two long polynucleotide chains which are held together by means of hydrogen bonding and run antiparallel to each other. Each of the chain is known as strand. Two types of bases form different number of hydrogen bonds AT forms two hydrogen bonds where GC forms three hydrogen bonds (Figure 1.11B).
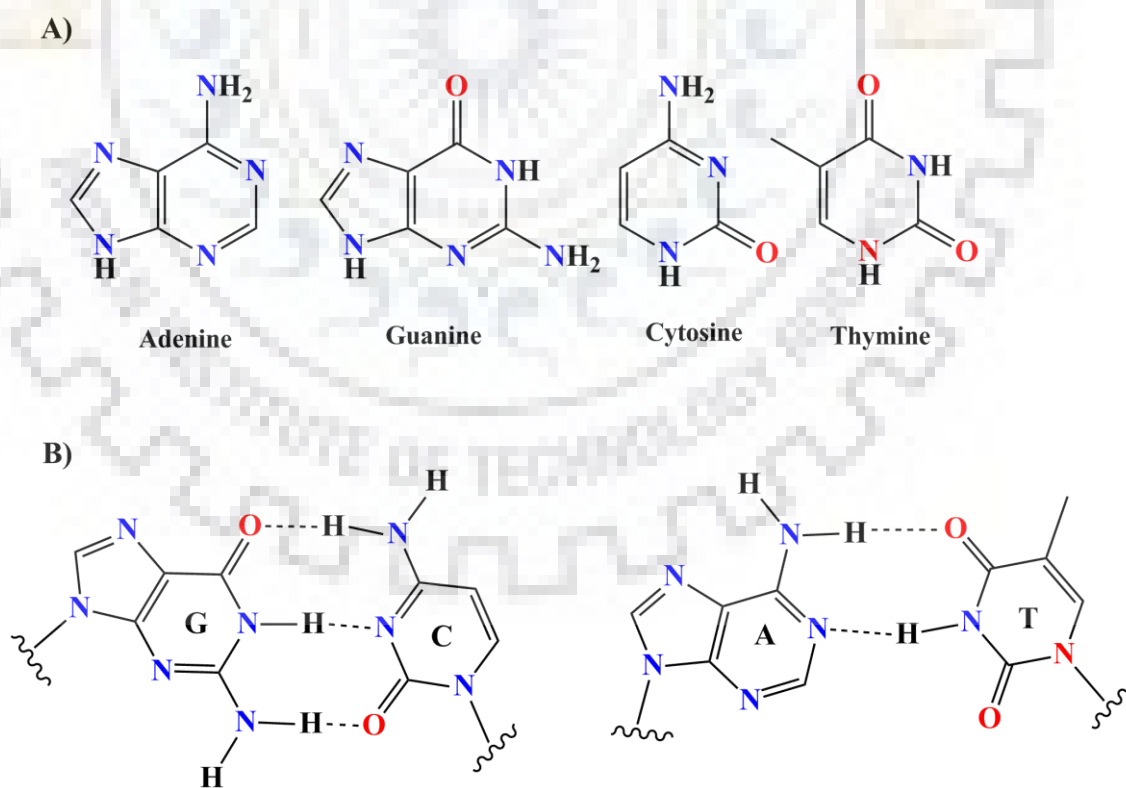
Figure 1.11 (A) Structures of nucleobases of DNA. **(B)** Hydrogen boning between nucleobases GC base pair with three hydrogen bonds.and AT base pair with two hydrogen bonds.

The structure of a four-nucleotide DNA with a sequence of 5'-ATCG-3'is shown in (Figure 1.12).[102]Single stranded DNA oligonucleotides are most frequently used for functionalization of gold nanoparticles. The thiolate DNA adsorbs to the gold nanoparticles through sulphur atoms as well as non-specific adsorption through bases as mentioned above. Because of this the hybridisation efficiency of as such DNA is very poor.[102] To make the DNA to adopt upright conformation different methods have been developed.
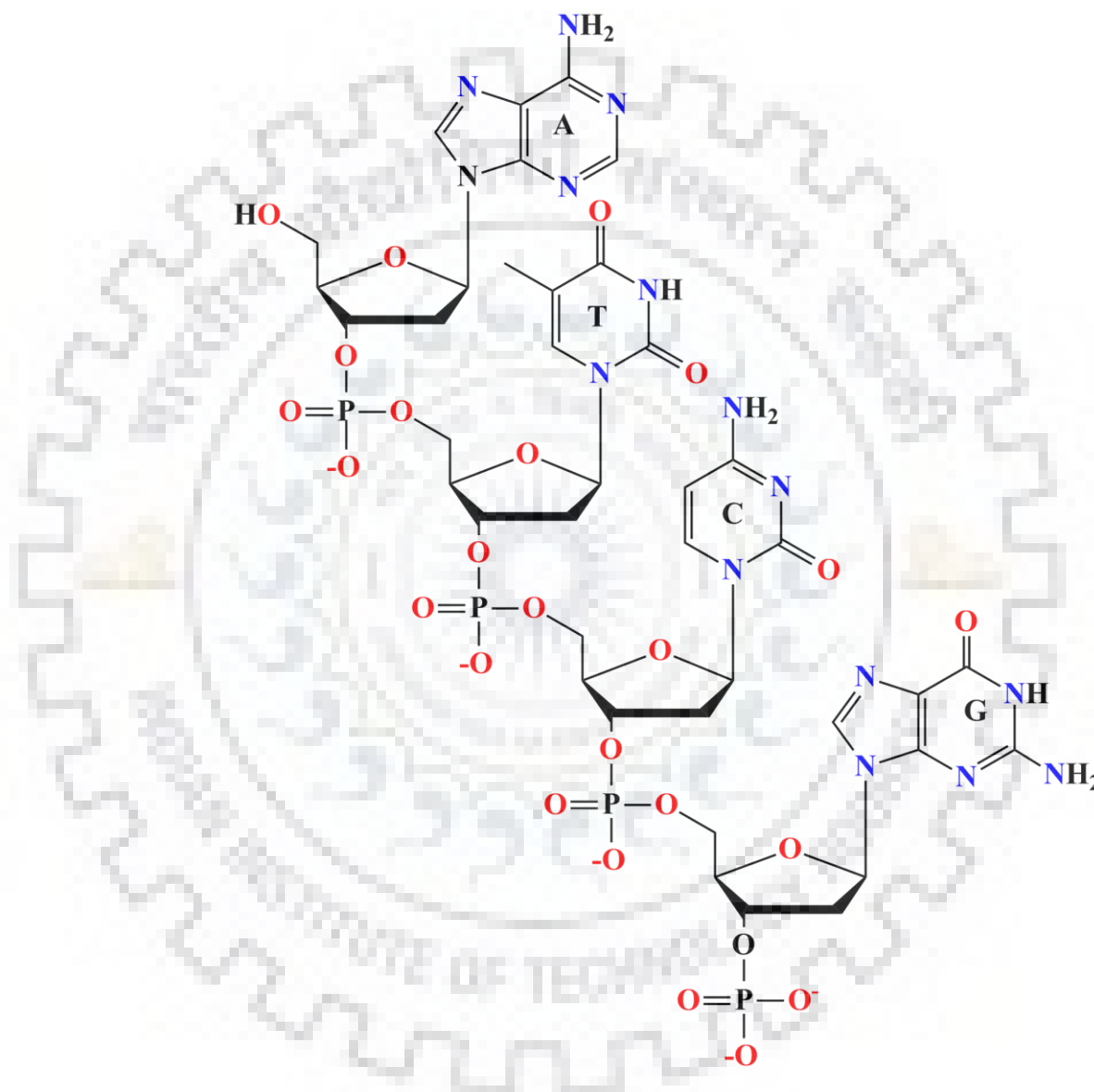
Figure 1.12 Structures of 4–mer DNA.

.

1.4.3 The salt–aging method

Due to colloidal stability problem 1 M salt cannot be directly added to screen charge repulsion for DNA attachment. To tackle this problem salt aging method was developed by Mirkin and

coworkers.[103,104] The thiolated DNA is mixed with AuNPs in the ratio of 300:1. After incubation NaCl solution is added slowly drop wise with shaking to reach final concentration of 50 mM. The sample is further incubated for one or more hours and more salt is added in increments to reach final concentrationof 300 mM and the sample is again incubated for overnight (Figure 1.13).
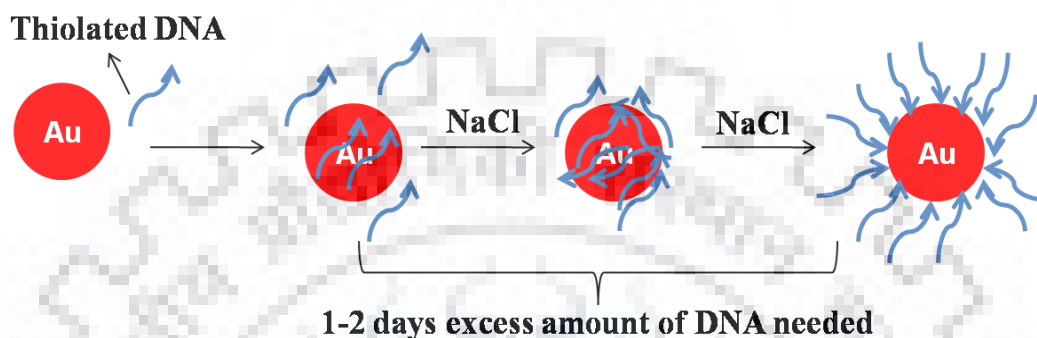
Figure 1.13 The salt-aging process for the DNA attachment to citrate stabilized gold nanoparticles.

1.4.4 Surfactant−assisted DNA functionalization

The direct salt-aging method works well with the smaller nanoparticles not with large gold nanoparticles because they are prone to aggregation. To address this issue Mirkin and co-workers used surfactants and AuNPs up to 250 nm could be consistently functionalized. Surfactant molecules, such as sodium dodecyl sulfate (SDS), tween 20, and carbowax were used. In a typical procedure DTT treated gold nanoparticles were treated with 0.01% SDS in a phosphate buffer followed by the usual salt aging process.[105]

1.4.5 The low pH assisted method

Liu *et al.* developed an improved method that takes only few minutes for attaching DNA to the gold nanoparticles.[106] In this method 13 nm AuNPs are incubated with thiolated DNA for a brief period. The final aliquot of 10 mM sodium citrate buffer is added quickly. Three minutes after incubation the sample is centrifuged to remove the nonattached DNA and the pH is adjusted back to 7. The role of the acid is to overcome the kinetic barrier for DNA attachment. The basis of this method is the protonation of DNA bases adenine and cytosine at pH 3. This method works well with poly−A spacer DNA even nonthiolated, as they form rigid poly−A duplex directly bind to AuNP surface.[107]

1.4.6 Modified DNA

Replacing the conventional thiol modified DNA with other spacers involves the use of modified DNA. Gilland and coworkers used a cationic polyspermine terminated DNA (ZNA) to functionalize gold nanoparticles of large size (40 and 80 nm).[108] Lou and coworkers used PEG−modified DNA to afford high loading of different size gold nanoparticles.[109] Aleksandra *et al.* have studied the amine modified ssDNA to the adsorption of gold nanoparticles.[110] Liu and coworkers used phosphorothioate (PS)-modified poly-A DNA for high conjugation by removing thiol. The same group recently used bromine as a robust backfiller for controlling of DNA conformation. The bromide displaces the adsorbed DNA and forces it to adopt upright conformation.They have also shown alingment of DNA on gold nanoparticles by freeze directed stretching.[111-113]

1.5 PHYSICAL PROPERTIES

1.5.1 Size-Dependent Electronic properties

AuNPs have quantum size effect that leads to discrete electron transition energy levels. For example, hexanethiol functionalized AuNPs shows 15 redox states at room temperature[114] signifying that AuNPs can have molecule-like redox properties.[115] The quantized capacitance charging behavior of AuNPs can be tuned by external ligands, magnetic fields and electrolyte ions, thus becoming potential candidates in applications for electronic devices and electrochemical labels.[116,117] In addition to redox activity AuNPs feature SPR which is known to be influenced by size, solvent, ligand, interparticle distance, and temperature. Murray and coworkers observed shift in the spectral with change in the refractive index of the solvent.[118] SPR is also prone by electron dephasing, only electron-electron interactions are involved in the process rather than electron-phonon coupling.[119] However, experimental data from femto second light scattering confirmed the occurrence of both processes in the individual AuNPs.[120] SPR frequency also depends on the proximity of the nanoparticles, aggregation of nanoparticles results in the red shift of SPR peak and broadening in surface plasmon band changing the color of solution from red to blue[121] making AuNPs attractive candidates for colorimetric sensors.

1.5.2 Optoelectronic Properties

The AuNPs size dispersity changes from batch to batch and makes difficult to obtain an accurate estimation of its concentration. Theortical calculations for extinction coefficient of

AuNPs were calculated by El−Sayed *et al*. and for 40 nm molar extinction coefficient (ε) is 7.66×10^9 M^{-1} cm^{-1} at 528 nm considerably higher than the common organic dyes rhodamine-6G (ε = 1.16×10^5 M^{-1} cm^{-1} at 530 nm) and malachite green (ε = 1.49×10^5 M^{-1} cm^{-1} at 617 nm).[122] Later the size, concentration and the extinction coefficients of AuNPs were determined both theortically and experimentally.[123]

1.5.3 Fluorescence Quenching

Fluoresence quenching is observed when fluorophores are attached to the gold nanoparticle surface. When the emission spectrum overlaps with plasmon band of gold nanoparticle surface quenching occurs.[124] Photo induced electron transfer is another process that quenches the fluorophere and can be modulated by charging or discharging of gold core.[125]

1.6 COLORIMETRIC SENSING

AuNPs aggregation of suitable sizes (d > 3.5 nm) instigate interparticle surface plasmon coupling, resulting in a visible color change from red to blue at nanomolar concentrations.The color change provides the practical platform for sensing of the target analyte that directly or indirectly triggers the aggregation of AuNPs and makes AuNP as a sensory element for broad spectrum of innovative approaches for the detection of biomolecules (nucleic acids and proteins), small molecules and metal ions in a rapid and efficient manner.[3e] Uptake and cytotoxicity of the gold nanospheres in human cells were also studied.[126,127]

1.6.1 Detection of nucleic acid

DNA detection methods have attracted extensive researcher's efforts because of broad applications for virus detection, transgenic detection, and early diagnosis of diseases.[128-131] Conventional techniques for the detection of oligonucleotide are based on the fluorescence and radioactive detection methods (e.g., PCR, RT−PCR, Northern blot, Southern blot, and high density microarrays).[132] Nucleic acid template reactions have also been used for the detection of nucleic acids. Many nucleic acid encoded chemistries have been developed and improved and a set of bioorthogonal reactions are available including template native ligation, Staudinger reaction, tetraazine mediated transfer reactions and carbon-carbon bond formation.[133] Ruthenium catalyzed photo reduction reactions were also used for the detection of miRNA.[134,135] Seitz and coworkers used quantumdots PNA conjugates for target catalyzed RNA detection.[136]

AuNP due to their low cost, simplicity and practicality have been used for colorimetric detection of oligonucleotide targets.[137,138] For colorimetric detection of DNA there are two major methods of detection one involves the inter crosslinking of gold nanoparticles in presence of the target and the second is non−crosslinking detection depends on difference in binding properties of single strand DNA (ssDNA) and double strand DNA (dsDNA) towards gold nanoparticles.[137-139] ssDNA is flexible, can partially uncoil and easily adsorbed on the AuNP. This provides additional stability to gold nanoparticles and prevents salt induced aggregation.[137-139] Advantage of the second strategy lies in the removal of covalent functionalization of particles required in the three-component sandwich assay format (inter cross linking). DNA mediated gold assembly was first demonstrated by Mirkin by fabricating the gold nanoparticles with the thiolated DNA.[104,140] In this approach two single strand modified AuNP probes complementary bind with the target strand leading to aggregation of nanoparticles (Figure 1.14).
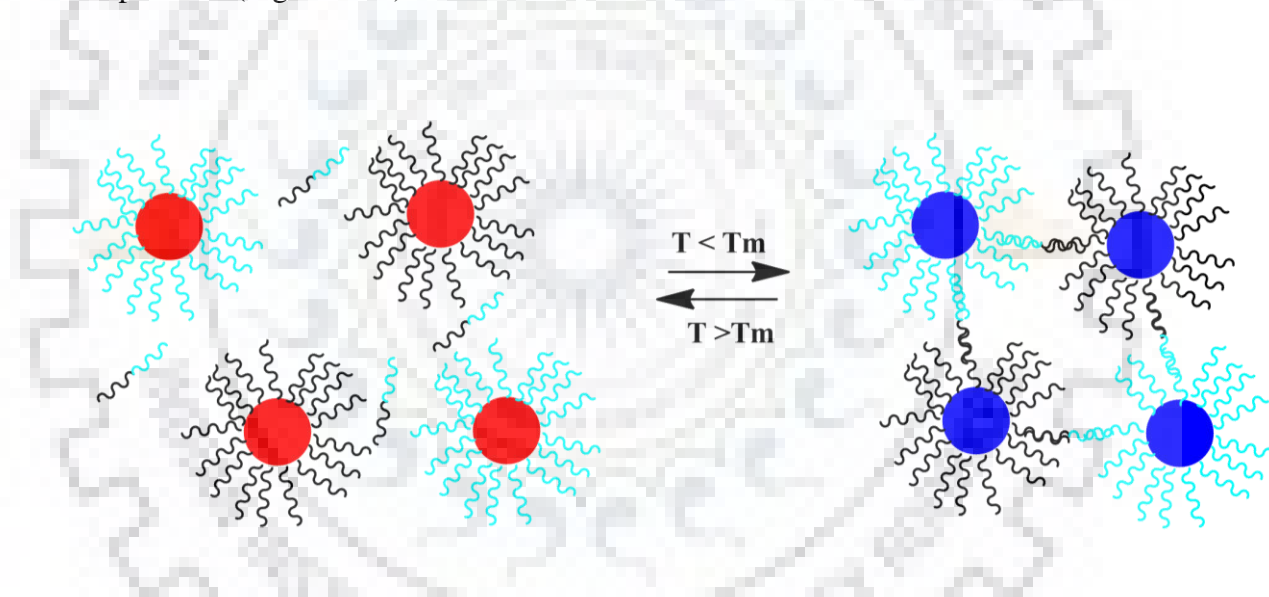
Figure 1.14 Aggregation of oligonucleotide AuNPs in presence of complementary target DNA leading to change in color of solution from red to blue.

Rothberg *et al.* shown that citrate-stabilized AuNPs can discriminate ssDNA and double-stranded DNA (dsDNA) at the level of 100 fmol through simple electrostatic interact-tions.[141] Liu and coworkers used combination of rolling cycle amplification (RCA) and nicking endonuclease-assisted nanoparticle amplification (NEANA) for detection of DNA.[142] They used padlock oligonucleotide probe for RCA reactions that has sequence identical to the linker probe and two complementary segments present at the opposite end of the molecule.The nicking endonuclease and the linker probe are added to initiate the NEANA

process for the detection. Davis and coworkers achieved the rapid colorimetric detection of target DNA by disassembly of the gold nanoparticles aggregate functionalized with DNA. They used toehold mediated strand displacement and temperature control over a wide range including room temperature to obtain colorimetric detection of 10 pmol DNA from the disassembly of the gold nanoparticles.[143] Ma and co-workers reported colorimetric DNA detection based on hairpin approach. Two hairpins species modified on Au nanoparticle surface and in the presence of target the hairpins open and the get assembled on the target molecule resulting in aggregation of nanoparticles.[144] He and coworkers reported colorimetric DNA detection from hybridization chain reaction (HCR) and gold nanoparticles. Hairpin DNA with single strands were designed and attached to the AuNP which stabilizes them from salt induced aggregation. The target DNA hybridises with the hairpin DNA and forms the double stranded DNA through HCR. As a result the dsDNA provides less stabilization and undergo salt induced aggreg- ation.[145] Li and coworkers used DNA based SPR biosensor for miRNA detection based on gold nanoparticles and DNA supersandwitch. The DNA linked gold nanoparticles hybridises with the capture DNA on the gold film to amplify SPR signal and also initiates the subsequent amplifications. This causes the electronic coupling between the gold nanoparticles and the Au film leading to shift of resonance angle.[146]

MicroRNAs (miRNAs) are single-stranded noncoding RNAs with a typical short length of 21−23 nucleotide found in plants, animals and some viruses. They play important role in different biological processes like posttranscriptional regulation of protein expression either by inhibition of mRNA translation or repression of mRNAS, cellular processes such as cell differentiation and cell cycle progression and apoptosis.[147,148] They can be described as "multivalent," with one miRNA capable of targeting multiple genes, thus can regulate the expression of several proteins. In tumour cells they function as oncogenes. Nanoflares (Au nanoparticles modified with oligonucleotide associated with fluorophores) were used for the detection of miRNA. These have high cellular uptake, do not require transfecting agents and are enzymatic stable.[149,150] Jiang and coworkers developed electrostatic assembled nucleic acid nanostructure of gold nanoparticles that enables HCR for mRNA detection.[151] Haam and coworkers used satellite like gold nanoparticles for the detection of miRNA.[152] They prepare satellite gold nanoparticles and functionalized them with the molecular beacons at pH 3. The gold nanoparticles possess high loading efficiency of molecular beacons than the conventional gold nanoparticle based molecular beacons and have high cellular uptake. Rad and coworkers used positively charged gold nanoparticles for the detection of miRNA−155.

The prepared positively charged polyethylenimine (PEI) capped AuNP which were used to trap the negatively charged miRNA (P-AuNPs/miR-155 complex). The thiolate hairpin is covalently attached to citrate capped gold nanoparticles forming C–AuNPs/probe. By mixing P-AuNPs/miR–155 complex and C-AuNPs/probe DNA /RNA duplex is formed and aggregation occurs.[153]

1.6.2 Detection of proteins

Protein biomarkers are the targets for most medical diagnostics.[154,155] The concentration of these proteins can also provide information about the stage of disease. Convenient, fast and cheap methods for protein detection are of great interest and gold nanoparticles in this context are gaining importance because of remarkable optical properties.[4,25] Chen and co-workers detected α–fetoprotein from the aggregation of AuNPs using rolling cycle amplification reactions. A DNA primer was binded to AuNPs and was isothermally extended to generate single-stranded DNA (ssDNA). Various concentration of the α–fetoprotein (AFP) antigen was added and subsequent padlock DNA was added and RCA was carried out. The AuNP containing surplus padlock DNA gets aggregated in the supernatant. The detectionof limit was 33.45 pg mL^{-1}.[156] Wang *et al.* developed the competition binding assay to measure the binding affinity of glyconanoparticles AuNPs conjugated with underivatized mono–, oligo– and polysaccharides with model protein (lectin Con A).[157] Carbohydrate functionalized AuNPs are used for the detection of carbohydrate binding proteins.[158-161] Gibson and coworkers used polymer stabilized glycosylated AuNPs for screening of carbohydrate–lectin interactions.[160] They also used gold nanoparticle aggregation as a probe for detection of antifreeze (Glyco) protein.[161] Shin and coworkers used glycan conjugated nanoparticles for probing cell surface carbohydrate binding proteins.[162] Okada and coworkers developed multivalent carbohydrate probes on AuNPs, capable of removing non-specific proteins and has high affinity of selective detection of carbohydrate binding proteins.[163] Aptamer binding gold nanoparticles were used for the detection of Thrombin.[164] Dong *et al.* have reported the aptamer–based colorimetric protein sensing method using unmodified AuNP probes.[165] In their sensor design the AuNPs were first stabilized with thrombin-binding aptamers. Interaction of thrombin folds the aptamers into a G-quadruplex/duplex structure due to the aptamer protein recognition. Folding of aptamer induces rigid structure which leads to AuNPs aggregation and a detection limit of 0.83 nM was obtained.

Dithiol functionalized peptides generate AuNPs assemblies used for the colorimetric detection of proteases. The proteases can disperse the gold nanoparticles assembly or can cause aggregation of nanoparticles functionalized with the thiol moieties. Presence of thermolysin (enzyme that peptide bonds) hydrolyses the peptide NP–conjugate leading to AuNP dispersion and color change from blue to red (Figure1.15).[166-168]
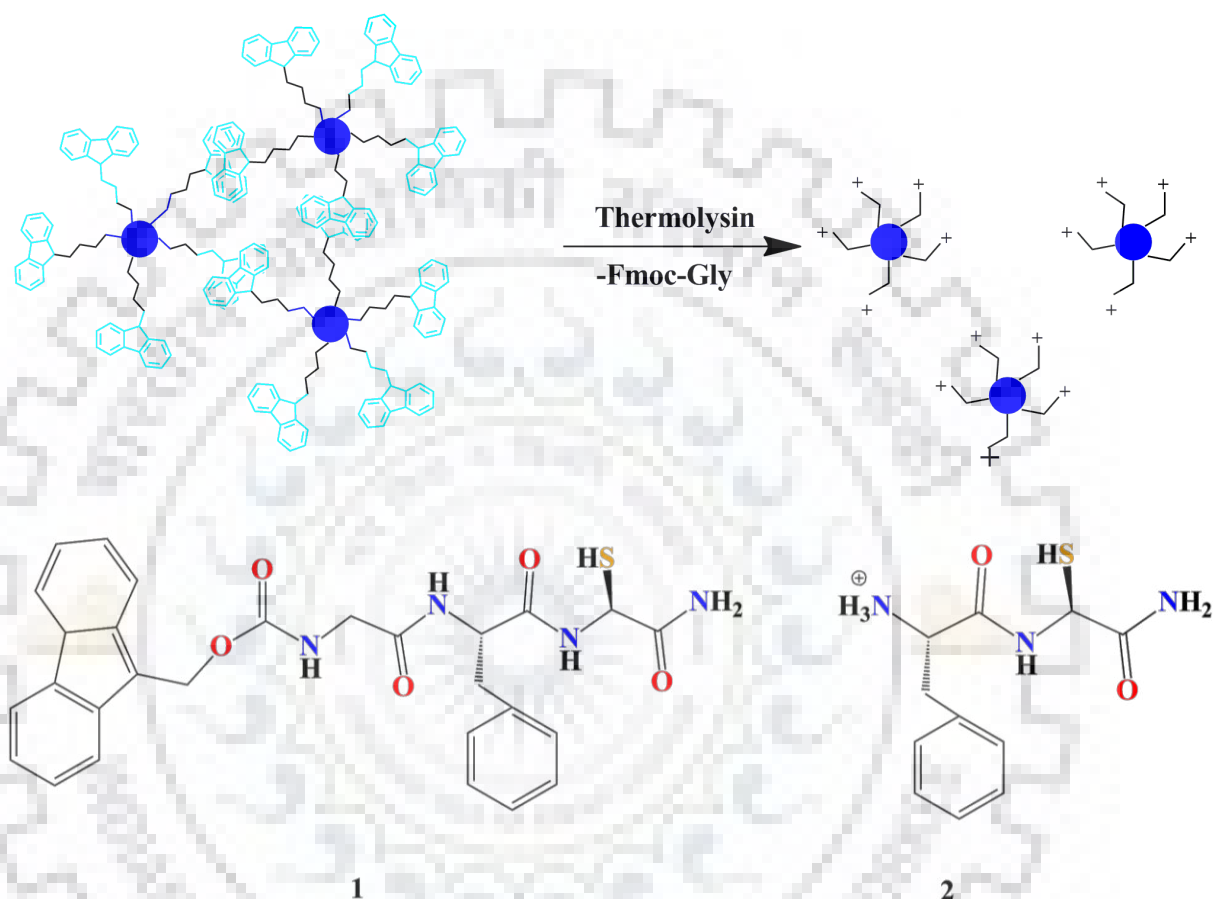
Figure 1.15 Schematic representations of the protease-triggered NP dispersion approach; following addition of thermolysin and generation of 2.

Mirkin *et al.* developed a real-time colorimetric screening process for endonuclease activity using DNA-mediated AuNPs assemblies. Aggregates of the AuNPs interconnected by DNA duplexes were prepared. Cleavage of the duplexes by deoxyribonuclease I (DNase I) breaks the nanoparticle assembly producing colour change from blue to red. The color change was used to moniter the activity of enzyme (Figure 1.16).[169] Liang and coworkers developed sensitive and selective method based on specificity of DNA cleavage reaction for assaying endonuclease activity and inhibition. The assay can detect EcoRI endonuclease down to 5.0×10^{-4} U mL^{-1} with a detection range from 5.0×10^{-4} to 10 U mL^{-1}.[170]

Peptide functionalized gold nanoparticles were also used for the detection of proteins.[171] The term "peptide aptamer" has been coined to describe a "combinatorial protein molecule" consisting of a variable peptidic sequence inserted within a constant scaffold protein, were also used for the detection of proteins.[172] Bruylants and coworkers detected oncoprotein Mdm2 by functionalized the gold nanoparticles with the peptides that recognizes the target protein and forms a complex that induces aggregation of the AuNPs.[173]
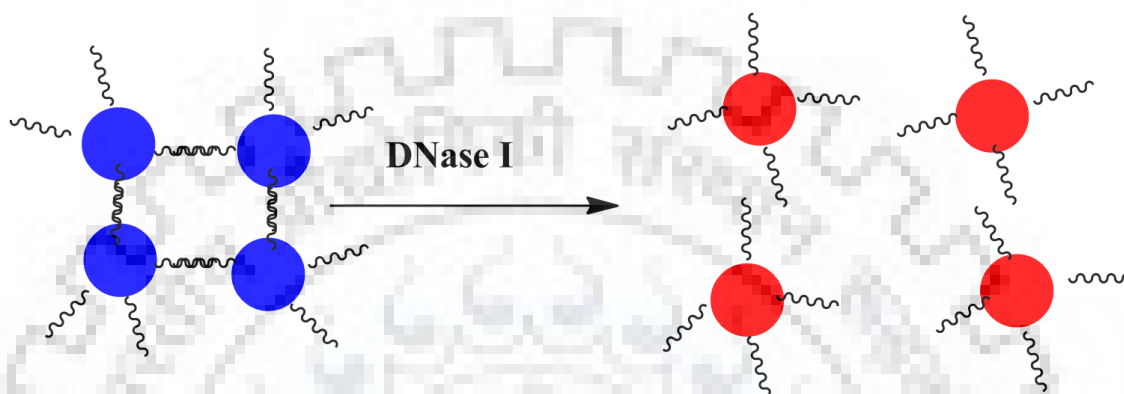
Figure 1.16 Illustration of the aggregation and dissociation of the DNA-AuNP probes by endonuclease inhibitors for colorimetric screening. The probes consist of gold nanoparticles (spheres) functionalized with oligonucleotides. The hybridization of oligonucleotide chains results in aggregation. Upon addition of DNaseI, the aggregates break resulting in formation of red solutions.

1.6.3 Detection of Ions

Colorimetric sensing for the detection of metal ions requires the attachment of chelating ligands on the AuNPs surface. The analyte ion induces the nanoparticle aggregation by forming multidentate interparticle complexes with chelating ligands. For example, AuNPs carrying 15-crown−5 moieties have been selectively used to detect the K^+ ion even in the presence of other physiological cations like Li^+, Cs^+, NH_4^+, Mg^{2+}, Ca^{2+}, and excess Na^+[174] and utilizing this method the Na^+ has been detected by 12-crown-4.[175] Trivalent cations like Fe^{3+}, Al^{3+}, Cr^{3+} and Ni^{2+} were detected using zwitterionic gold nanoparticles.[176,177] Li^+ were detected by utilizing phenanthroline functionalized 4 nm AuNPs,[178] Cr(III) and Cr(IV) were detected by sodium hyaluronate protected AuNPs.[179] Rao *et al*. utilized bifunctional calix[4]arene molecule bearing coumarin moiety attached to gold surface for Cu^{2+} sensing. [180] Mirkin and coworkers have employed DNA-functionalized AuNPs for the selective and sensitive detection of Hg^{2+}.[181]. DNAzyme directed assembly of AuNPs have been employed for the selective detection of lead.[182] Bovine serum albumin capped gold nanoparticles were used for the

detection of lead and mercury.[183] Cyanide and iodine ions were also detected by AuNPs in aqueous solution.[184-186]

1.6.4 Detection of other biomolecules

Geddes *et al.* have used dextran coated gold colloids for the detection of glucose. They used the tetravalent protein concanavalin A (Con A) that cross links dextran coated 20 nm gold particles and resuts in the red shift of SPR peak. Introduction of glucose breaks the cross linking by competitively biding with Con A and reversing the plasmon change.[187] The system has a wide range of detection and can potentially be useful to diagnose the blood glucose level in healthy people (3−8 mM) and in diabetics (2−40 mM). Uehara *et al.* functionalized gold nanoparticles with water soluble polymers [poly (N-nisopropylacrylamide-co-acryloyldiethyletriamine)] and were employed for the detection of glutathione. Addition of glutathione results in disassembly of the aggregated system with change in colour from blue to red.[188] Cysteamine modified gold nanoparticles were used for the detection of melamine.[189]

Lu and coworkers designed aptamer based sensor for detection of adenosine, consists of three functional systems two kinds of ssDNA−modified AuNPs and a linker DNA molecule that carries adenosine aptamer. Initially the gold nanoparticles were linked by the linker and are blue in color. The addition of the adenosine binds with the linker and disrupts the gold nanoparticle assembly producing the color change.[190] The adenosine was detected from the concentration of 0.3 to 2 mM. They have further extended the system for detection of cocaine, employed cocaine aptamer. Stevenon *et al.* have applied calorimetric assay for the detection of small molecules like ochratoxin A (1 nM), cocaine (1 nM) and 17β-estradiol (0.2 nM) using aptamer gold nanoparticle probes. Aptamer probes were formed by the adsorption of aptamers on the gold nanoparticle surface. The analytes were added and the interaction of target molecules with the aptamers resulted in desorption of aptamers which is dependent on the concentration of target molecule. The subsequent growth reaction in presence of reducing agent and gold salt result in the growth of nanoparticles into different morphologies and accompanied by color change.[192]

1.7 MORPHOLOGICAL CONTROL OF NANOPARTICLES

Nanoparticles display many unique properties and their properties are determined by their morphologies. Morphology includes both shape and surface properties of nanoparticles. The

morphological dependent properties have application in sensing (surface enhanced resonance scattering), imaging (dark field), and catalysis and biomedical (delivery platform).[4,5,192] To understand the full prospective of these nanomaterials it is important to reveal how to control the morphology of individual nanoparticles, precise spatial control of the position, orientation, and distances between multiple nanoparticles. Directed assembly methods are frequently used to meet these requirements but these methods rely on control of external variables, such as concentration, reaction time, pH, and solution temperature.[193] In contrast, high quality materials produced by nature under almost constant external variables e.g. seashells and pearls in the ocean are made from the same material under the same ambient conditions, yet they obtain different final structures in response to biological signals. By mimicking these biological processes one can also control the morphology of the nanoparticles. Role of the seed has also found to be important in controlling the morphologies of the nanoparticles. Seed initially formed could adopt different shapes and depending upon the reaction conditions such seeds could grow into large nanocrystals with well defined facets and specific shape. The variation in the shape that originates from the same type of the seed can be attributed to the degree to which particular facet is stabilized by the capping agent. Various methods to control the morphologies of nanoparparticles include the use of capping ligands like inorganic ions (e.g.; halides), organic molecules (e.g. citrate), polymers (e.g. polyvinyl pyro- lidine, DNA etc.) and proteins (e.g. streptavidin). Among them DNA acts as special capping agent because it is programmable and can be amplified that means we can systematically control its length, charge and functional groups. Moreover DNA is biocompatible, highly stable and cost effective over other polymers.[193,194]

Seed mediated methods are commonly used to prepare the nanocrystals with controlled morphologies.[195,196] In this approach preformed seeds are added to growth solutions containing molecular capping agents which selectively bind to certain facets and mediate the growth into different shapes. Lu's group reported that the DNA adsorbed on the gold nanospheres in a sequence dependent manner and guide their growth into nanospheres with Poly−T (T30) or nanoflowers with Poly−A (A30) or Poly−C (C30) (Figure 1.17).[197] Mechanistic studies point out that DNA binding affinity (dA > dG $\geq$ dC > dT) to the AuNP plays a major role in controlling different morphological processes. The adsorbed DNA on the AuNPs surface acted as template for the formation of flower-like gold nanoparticles. The gold nanoflower formation can result either from selective deposition of the reduced gold metal on

gold nanosurface where DNA acts as a template or due to uneven growth of the gold nanosurface occupied by DNA.
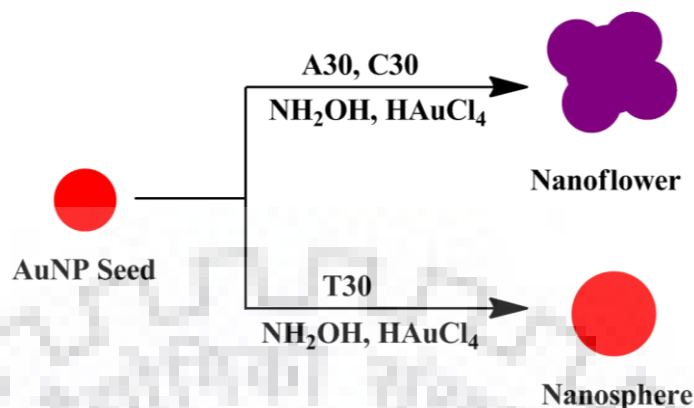
Figure 1.17 Shape-controlled growth of AuNP into Au nanoflowers and Au nanospheres from spherical seeds in the presence of A30, C30, or T30 DNA molecules.

Further they explore the effect of different DNA sequences oligo dA30 (A30), oligo dT30 (T30), oligo dC30 (C30) or oligo dG20 (G20) on the morphologies using nanoprism as a seed and developed a DNA "genetic code" for nanoparticle morphologies.[198] The formation of different morphological structures from gold nanoprism seed after growth reaction are summarized in the tabulated form.

Table 1: Summarizing the rules of different DNA bases on morphology of goldnanoprism seeds.

DNA	Morphological Effect
G20	Formation of flat hexagons
T30	Formation of six-pointed stars
A30	Formation of round rough plates
C30	Formation of round flat plates

Lu's group also provides the mechanistic insight for the DNA−guided control of nanomaterial morphologies using nanoprism as a seed and found that the shape depends on the binding affinity of DNA on gold nanoparticle surface and the concentration of DNA used for growth reaction. The binding affinity of DNA affects the DNA desorption from surface making it difficult for Au to deposit the positions where DNA can bind. Therefore, the bases with higher affinity (A and C) can kinetically trap the AuNPs at the nonagon shape during the early stage of the growth, whereas a base with a weaker affinity (G) could trap the shape only at a

later stage of the growth (i.e. hexagon). Thymine has the weakest affinity and allows the growth to all directions resulting in six−pointed stars.[199] Nam's group developed a method for controlling and Au core−nanogap−Au shell structures with various interior nanogaps and gold shell nanostructures based on the binding affinity of DNA bases to gold core.[200] Lu's group have also investigated the effect of different DNA sequences for modulating the geometrical and plasmonic properties of gold nanorods. The overgrowth resulted in the formation of structures varying from nanodumbbell to nanooctahedron and shapes in between.[201] They also reported the DNA templated syntheses of bimetallic Pd−Au nanoparticles from platinium nanocubes seeds into different morphologies like cuboctahedron with T10 and C10, rhombicuboctahedron with A10, and uneven shapes with G10.[202] Sim and coworkers anchored DNA onto gold nanoseed with various alignments to form gold nanocrystals with defined topologies like pushpin− star− and biconcave disc−like structures, as well as more complex jellyfish and flower−like structures.[203]

Peptides and amino acids have also been used in controlling the shape of the nanoparticles and provide improved solubility and biocompatibility.[204,205] Adsorption of small bio molecules like amino acids onto the surface of nanoparticles also offers a novel route for generation of nanoparticle assemblies with different architectures. Arginine were used to mediate the linear assembly of the gold nanoparticles.With increasing the concentrations of arginine to Au nanoparticles resulted in the formation of branched linear chains of the spherical nanomaterials.[206,207] Chen and co-workers used peptoids for morphological evolution of gold nanoparticles from spherical to highly branched coral shaped nanoparticles.[208] They engineered the peptoid sequences with hydrophobic and hydrophilic groups and generate different morphologies of nanoparticles like coral shaped, spherical and rough shape. Coral shape resulted from the strong hydrophobic peptoids that induced the formation of distorted nanorods during the early stage and finally got clustered to form spherical coral shaped nanoparticles. Lee's group synthesized chiral gold nanostructures using amino acids and peptides. They devised seed mediated method for forming the helicoidal shaped nanoparticles. As the first step, cubic and octahedral seeds were prepared and in the second step, cysteine or cysteine−based peptides with chiral conformations were used to control the optical activity, handedness and chiral plasmonic resonance of the nanoparticles.[209] In general the morphological control or plasmonic engineering of nanostructures can be built with plasmonic and non−building blocks and functional controllable modulators for eventual formation of plamonically engineered nanostructures (Figure 1.18).

Plasmonic Nanobuilding blocks

Modulators

Nanosphere

Nanorods

Nanocubes

Nanoprism

Nanoshell

2D Nanostructure

Small organic molecules
Host-Guest molecules
Metal chelators
Oligonucleotides
Amino acids
Peptides

Plasmonically engineered nanostructures

Core shell structures

Core gap shell structures

Branched structures

Cage structures
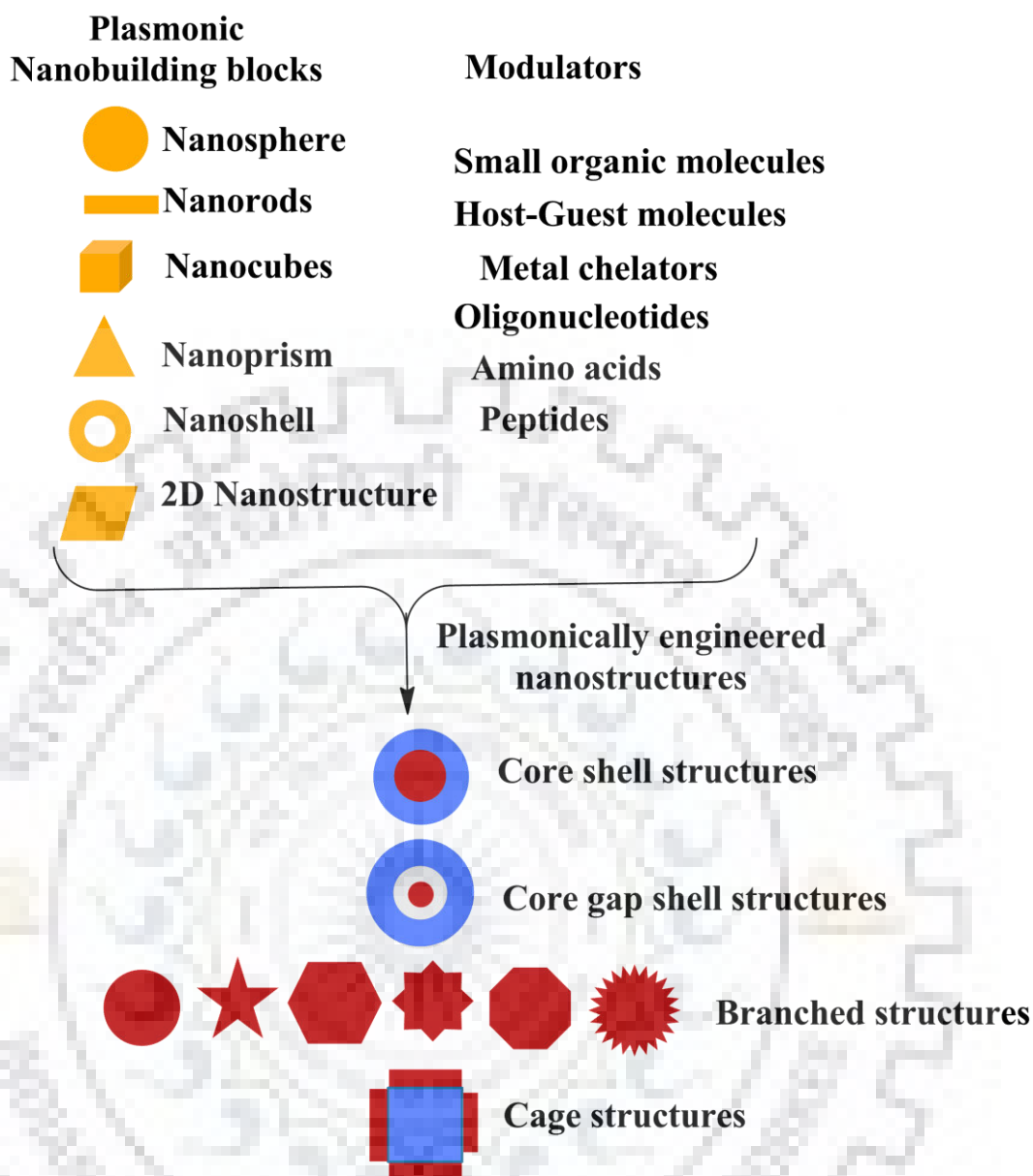
Figure 1.18 Combining plasmonic nanobuilding blocks and modulators to engineering particle morphology.

1.8 AGGREGATION OF NANOPARTICLES

Gold nanoparticles, prepared by the citrate reduction method are electrostatically stabilized by adsorbed citrate anions, which have negatively charged carboxyl groups that lead to the production of a surface zeta potential and provides stability to the nanoparticle. Reducing the absolute value of the zeta potential results in aggregation of nanoparticles via interparticle Van der Waal's attractive forces.[210] Analytes that can disrupt the citrate shell decrease the stability that ultimately leads to the aggregation of nanoparticles. This effect has been explored for colorimetric sensing utilizes the interparticle distance dependent property of surface

plasmon resonance. Aggregation of gold nanoparticles (AuNPs) can be utilized in chemical and biomolecular sensing as a sensitive and easy−to−visualize process. Molecular interactions can be monitored because they can control the dispersion and aggregation of the NPs leading to colorimetric change from pink to violet to blue. This process has been used in detection of various analytes.[211]

Organic molecules containing thiol and amine groups strongly promote the aggregation of nanoparticles and led to the formation of dual peak in the absorption spectrum.[212] Amino acids can induce the aggregation of the nanoparticles. Positively charged amino acids can cause the aggregation of the nanoparticles as they can decrease the zeta potential where uncharged and negatively charged amino acids do not alter the zeta potential and provides colloidal stability to the gold nanoparticles.[213] Arginine has been found to form the linear assembly of nanoparticles.[206] Cysteine promotes the spherical aggregation of the nanoparticles because of strong affinity of thiol with the gold that replaces the citrate molecules and forms the internanoparticle bridges because of hydrogen bonding between the carboxylate group on one nanoparticle with amine group on other nanoparticle (Figure 1.19).[214]

AuNP-based homogeneous assays mediated by hybridization with target DNA through changes in SPR resonance (colorimetric detection) and changes in hydrodynamic properties (dynamic light scattering) because of their good optical and chemical stability, and biocompatibility.[6] DNA can cause aggregation of gold nanoparticles induced by the non-crosslinking hybridization or by inter-crosslinking in presence of complementary strand at different salt concentrations (Figure 1.20).[215,216]
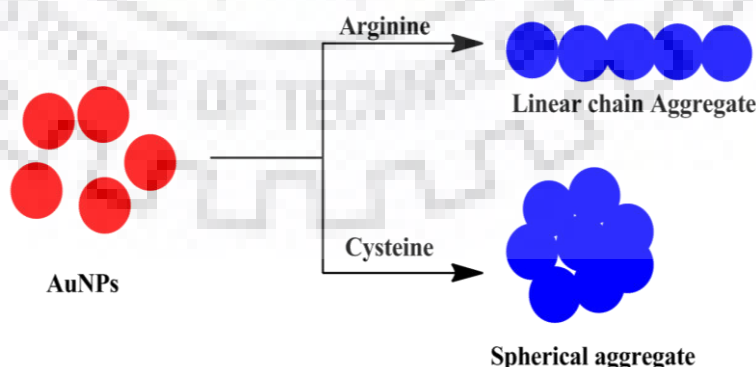
Figure 1.19 Linear and spherical aggregation of nanoparticles induced by amino acids.

DNA Functionalized AuNPs

Crosslink DNA   Complementry DNA
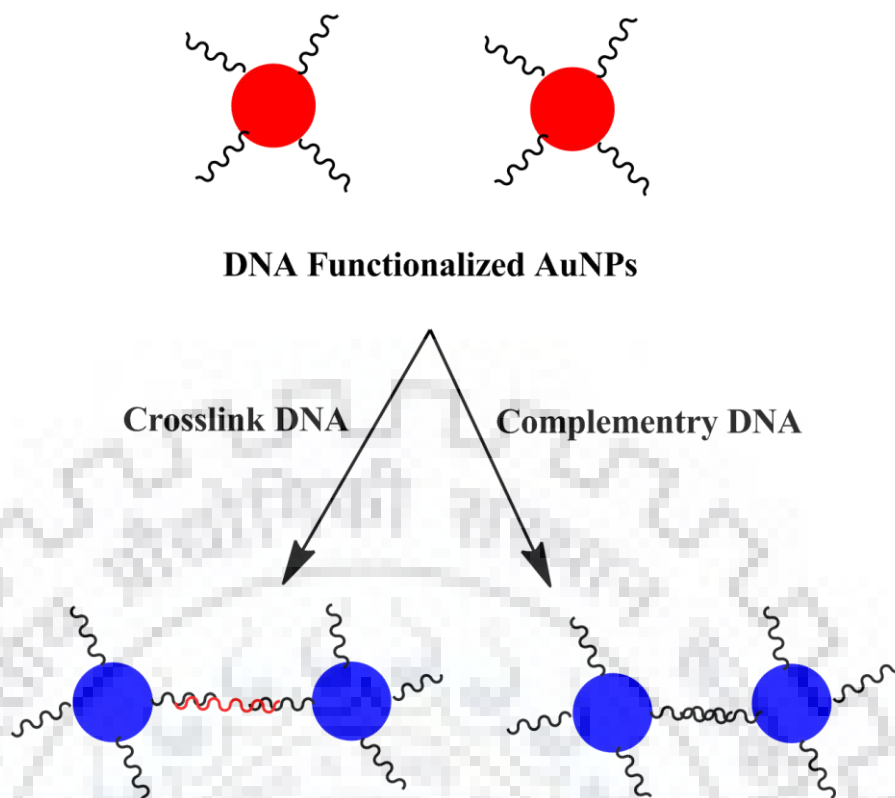
Figure 1.20 Schematic representation of the non-crosslinking and crosslinking aggregation of single-stranded DNA-functionalized gold nanoparticles (ssDNA−AuNPs).

Gold nanoparticles functionalized with thiol modified DNA can undergo aggregation process in presence of the complementary strand leads to color change from red to blue.[217] Mirkin's group first demonstrated the colorimetric detection based on gold nanoparticle aggregation to achieve a single mismatch detection in DNA sequence.[140] Mao and coworkers used ssDNA for assembling the gold nanoparticles into large structures by DNA hybridization using enzyme free target recycling scheme based on hairpin single strand displacement.[218] Recently Saiki and coworkers optimized surface modification and described AuNP dimerization induced by hybridization of two probe DNA with complementary target DNA molecule.[219]

1.9 BIMETALLIC NANOCOMPOSITES

Nanocomposites are solid materials that have multiple phase domains and at least one of these domains has a nanoscale structure.[220] Materials containing two or more different nanoscale functionalities are attractive candidates for advanced nanomaterials. Composite nanomaterials constructed with cores (inner material) and shells (outer layer material) both at nanoscale are broadly defined as core–shell nanoparticles (CSNs).[221] Core-shell nanoparticles have

evolved as potential materials for application as bifunctional nanomaterials for biomedical applications, catalysis and electrocatalysis.[222,223] Miscellaneous physical and chemical properties of the core shell interface and their components contribute to the complexity of the system and attracts to understand them. Different core shell gold nanostructures have been studied regarding their catalytic activity, surface plasmon resonance and other phenomena.[224-229] These can be modified with different reactive groups or functional moieties on the surface with enhanced stability and compatibility.[230-231] Controlling the functional peripheral properties can provide a platform for synthesizing next generation complex nanomaterials. The application for such materials depends on their nanostructure, composition, stability and dispersity of the particles under a range of different conditions. Therefore researchers have focused on the fabrication of nanocomposites to develop novelty in such materials.

1.10 GOLD IRON OXIDE NANOCOMPOSITES

Nanoparticles of iron oxide and gold have been broadly studied as individual systems: Fe_xO_y for its magnetic properties and Au for its optical and electronic properties as well as its desirable surface chemistry. Fe_xO_y nanoparticles are used as contrast agent in molecular imaging with negative contrast for MRI.[232,233] They can shorten the spin-spin proton relaxation time by accelerating the transverse relaxation of water protons.[234-236] Gold nanoparticles have been used in cellular optical imaging,[121] detection for DNA[137-145] proteins[156-168] and hyperthermia.[237,238] The plasmonic resonance peak of the Au nanoparticle gets shifted to the near infrared (NIR) region by tuning the proximities and its geometry. Therefore the combination of Au and Fe_xO_y nanoparticles are potential candidates for providing hybrid properties.

1.11 STRUCTURE OF GOLD–IRON OXIDE NANOCOMPOSITES

The structure of the Au–Fe_xO_y nanocomposites can be divided into two categories (1) Monodispersed nanoparticles and (2) Aggregates.

1.11.1 Monodispersed nanocomposites

These include core/satellite structures, core/shell structures, multi-layer composite structures, nanodumbbells and nanoflowers.

1.11.1.1 Core/satellite structures

This is one of the most common structures of the Au−Fe_xO_y nanocomposites. The structure possesses the single core with the attachment of numerous smaller particles i.e.satellites linking by covalent bonds or supramolecular interactions. Au@Fe_xO_y or Fe_xO_y@Au core/satellite structures acts as key intermediate for the conversion to core/shell or multilayer composites with discrete features.The core/satellite nanocomposites contain uncovered core which may be used for the further functionalization, more over the structure consists of numerous peripheral satellite nanoparticles of high surface area useful for catalysis.
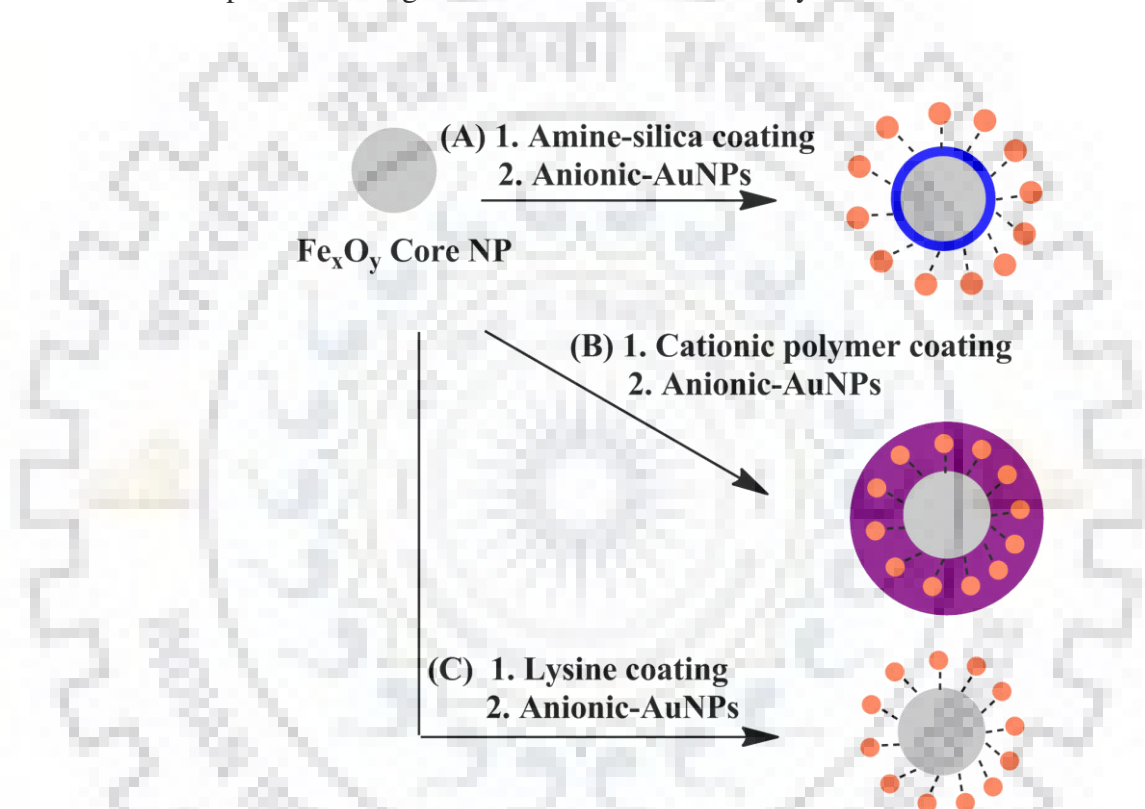
Figure 1.21 Schematic representations for preperation of Fe_xO_y@Au core/satellite structures using different linkers via electrostatic interactions. (A) Amine functionalised organosilica; (B) polymer; and (C) lysine.

The most commonly reported core/satellite structure is the Fe_3O_4@Au because of well established and facile syntheses of Fe_3O_4 core by solvothermal reaction and Au anions by reduction (chemical or photo).[239] Negatively charged citrate coated gold nanoparticles can be electrostatically attached to positively charged ammonium functionalized Fe_xO_y@SiO_2 nanoparticles (Figure 1.21A) or positively charged organic polymer resulting in Fe_xO_y@polymer@Au core/shell/ satellite nanocomposite and considered as more stable because of multivalent interactions (Figure 1.21B).[240] Carboxylate end of lysine can also be

attached to $\gamma-Fe_2O_3$ nanoparticles and the free amino group can serve as a template for *in situ* formation of Au nanoparticles in presence of $HAuCl_4$ and $NaBH_4$ forming $\gamma-Fe_2O_3$–lysine@Au core/satellite nanocomposites (Figure 1.21C).[241]

Tian *et al.*[242] used reversible addition fragmentation chain transfer (RAFT) technique to achieve Fe_3O_4@Au cluster (multi-core)/satellite nanocomposite structures. Fe_3O_4@SiO_2-RAFT–initiator nanocomposite initiates the polymerisation of styrene forming multiple Fe_3O_4@SiO_2 embedded poly (styrene) and the residual RAFT terminal is reducible to give the thiol functional group that again acts as a ligand to Au nanoparticle via strong Au–S bond.

1.11.1.2 Core/shell structures

Nanoparticles with a single core and fully covered with shell coating represent Core/shell nanocomposite. In contrast to core/satellite the surface of core is fully buried under the shell declining the properties of the core material and a low surface area to volume of the shell is obtained. The surface of the core/shell materials could be further functionalized with new ligands to give well defined structures. There are two different strategies to synthesize Fe_xO_y@Au core/shell composite structures either by coating a uniform Au layer on a Fe_xO_y@Au core/satellite composite or directly coating an Au layer on a Fe_xO_y core.[242]

The coating of an Au shell is achieved by reduction of $HAuCl_4$. The gold shell around the Fe_xO_y@Au core/shell composite could be formed by reducing Au^{3+} with reducing agent where the satellite Au nanoparticles on the Fe_xO_y core serves as nucleation sites for coating. This strategy is capable with a wide range of Fe_xO_y core from 6 to 100 nm [224-229] with different morphologies such as rice and cube.[244-246] Au shell could be directly formed on the Fe_xO_y core by modifying the core with functional groups that serves as templates for nucleation of gold. For example Fe_3O_4 nanoparticles (5–15 nm) synthesized by reduction of $Fe(acac)_3$ in 1,6-hexadecanediolin and capping agents oleic acid (OA) and oleylamine (OAm) where OAm acts as template to attach Au^{3+} ions to core.[247]

1.11.1.3 Multi-layer composite structures

Manipulating the scope of Au-Fe_xO_y nanocomposites by forming more layers of material over them in a view to synthesize "all in one" nanocomposites, common coating layer is the silica because of its stability. Tetraethylorthosilicate (TEOS) is typically used to coat silica by a sol-gel reaction. Huang *et al.* first coated the Fe_xO_y with silica layer followed by gold layer.[248]

Double layer gold shell was formed by again coating with silca layer followed by another coating of gold layer.[249] Coating of a silica layer followed by the selective itching of Fe_3O_4 core with $NaBH_4$, results in hollow type nanocomposites.[250] Figure 1.22 illustrates the formation of multi-layer Fe_xO_y@Au composites.
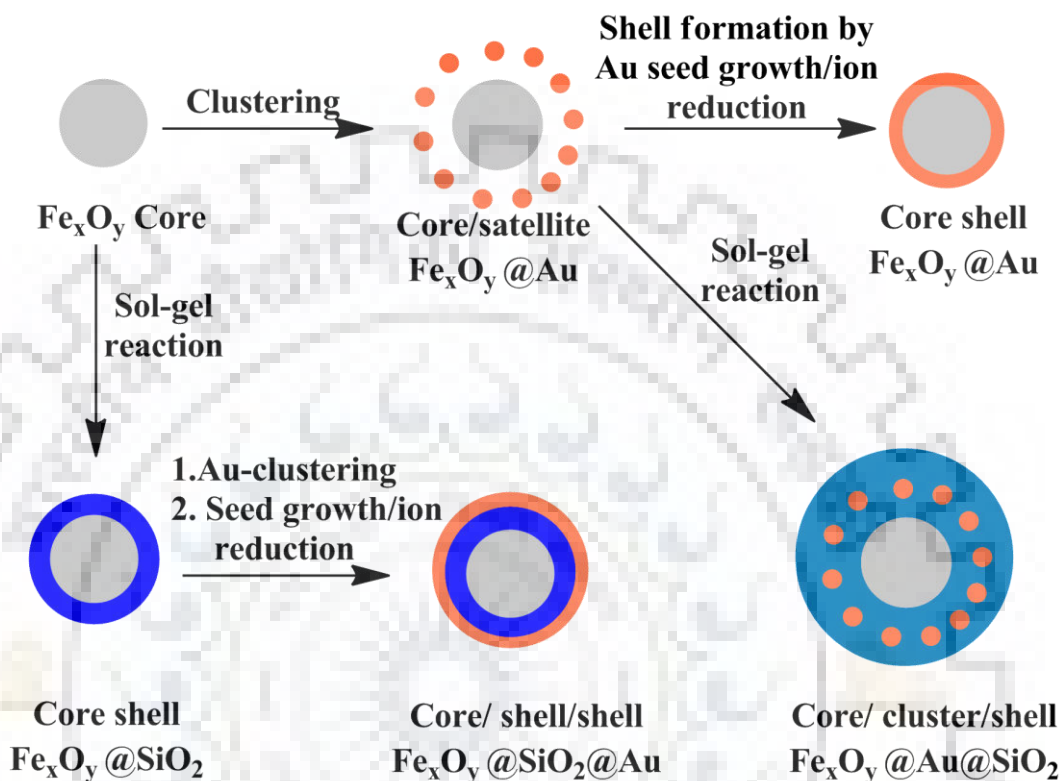
Figure 1.22 Schematic representations of the conversions of selected multi-layer Fe_xO_y@Au composites.

1.11.1.4 Nanodumbbells

Au-Fe_xO_y dumbbell nanocomposites are distinctly monodisperse nanoparticles composed of one Au nanoparticle and one Fe_xO_y nanoparticle bonded interfacially. There are generally two strategies for synthesis of Au–Fe_xO_y nanodumbbells, first involves the gold nanoparticles synthesis followed by deposition of the one Fe_xO_y on each Au nanoparticle and the second involves the simultaneous synthesis of Au nanoparticles and Fe_xO_y nanoparticles followed by complex formation. In the first strategy OA coated goldnanoparticles are first formed which are then made to react with iron complexes and the newly formed Fe_xO_y nanoparticles is deposited on Au surface (Figure 1.23A). The iron complexes generally used are iron pentacarbonyl [$Fe(CO)_5$] and iron–oleate complex [$(Fe(OL)_3$]. The metallic iron obtained from the decomposition of $Fe(CO)_5$ upon refluxing with Au nanoparticles, 1-octadecene, OA and OAm at 300^oC resulting in the formation of Au-Fe_xO_y dumbbell nanocomposites via air oxidation

(Figure 1.23B).[251] However when Fe(OL)$_3$ are used as precursor Au–Fe$_x$O$_y$ dumbbell nanocomposites are simply obtained by refluxing (Figure 1.23C). The second strategy involves the mixing all precursors in one pot to form the Au-Fe$_x$O$_y$ dumbbell nanocomposites.[252]
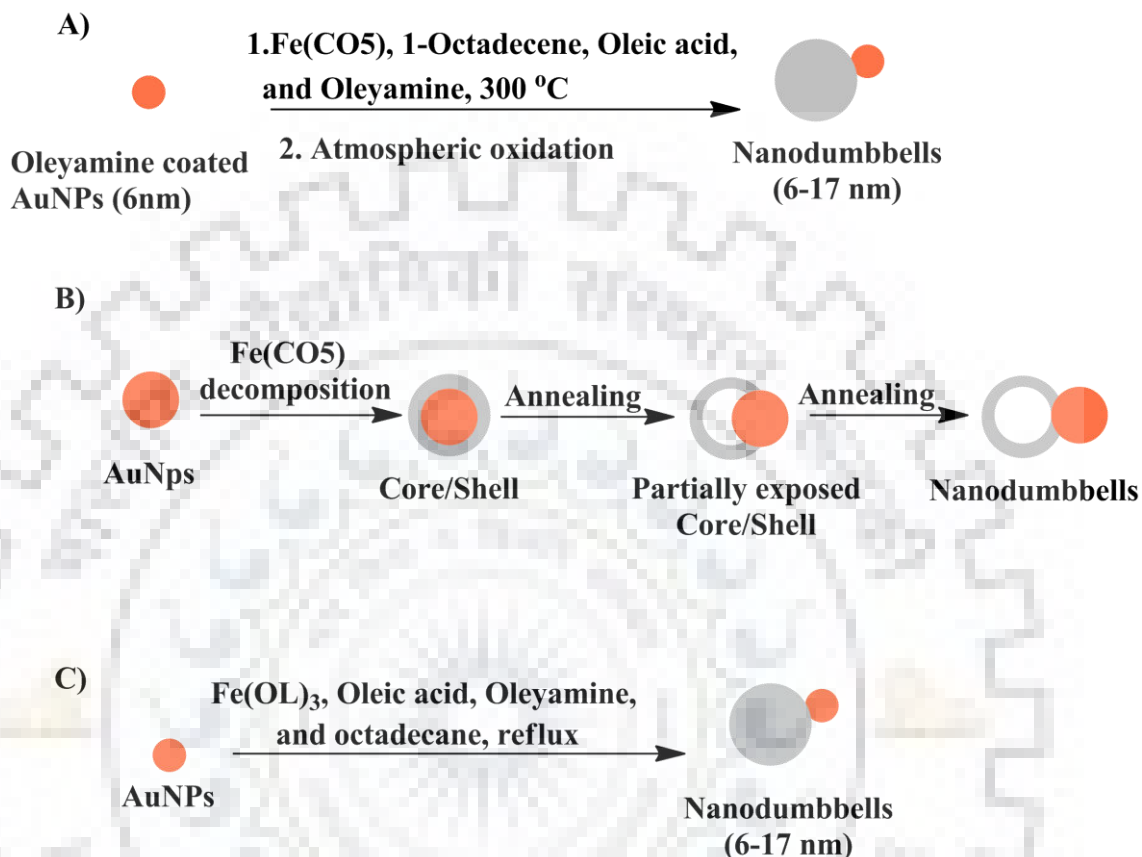
Figure 1.23 Formation conditions and mechanism of Au-Fe$_x$O$_y$ dumbbell nanocomposites.

1.11.1.5 Nanoflowers

Nanocomposites that look flower like with core and multiple pedals could be regarded as nanoflowers. One of the Au-Fe$_x$O$_y$ nanoflowers morphology is dumbbell shape where each flower is composed of one single Au core surrounded by few Fe$_x$O$_y$ nanoparticles of similar size.Their synthesis is similar to nanodumbbells mentioned above which involves the decomposition of Fe(CO)$_5$ and subsequent oxidation yields Au@Fe$_3$O$_4$ nanoflowers with Fe$_3$O$_4$ as pedals of 13.4 nm and gold core of 8 nm.[253] Grzybowski *et al.* showed that different stoichiometric ratio of Au and Fe precursors led to gradual morphological change from nanodumbbell to flower. With more iron precursor relative to Au the formation of nanoflowers was preferred with more pedals. Also increase in reaction time converted nanodumbbells to flowers.[254]

Feldman and coworkers synthesized Au-Fe$_x$O$_y$ nanoflowers by clustering from Fe$_3$O$_4$@Au core/shell nanoparticles. Presynthesized dextran coated Fe$_3$O$_4$ nanoparticles were dispersed in water and hydroxylamine and addition of HAuCl$_4$ resulted in deposition of gold on Fe$_3$O$_4$ core by subsequent reduction of dextran (Figure 1.24).[255]
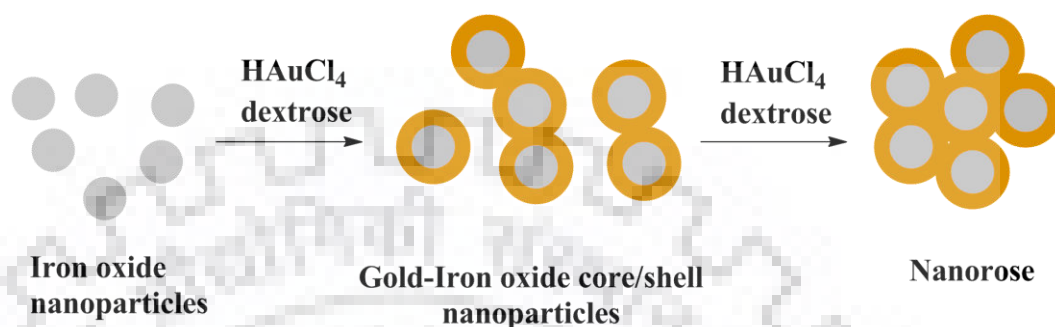
Figure 1.24 Formation mechanism of multi-core Au–Fe$_x$O$_y$ nanorose.

1.11.2 Aggregates

Au-Fe$_x$O$_y$ aggregate comprises random and polydispersed structures and there are generally two strategies for syntheses (1) radiation induced random aggregation, (2) self–assembly of Au and Fe$_x$O$_y$ nanoparticles via a polymer wrap. Nakagawa *et al.* developed the radiation induced method which involves the mixing of polyvinyl alcohol (PVA), presynthesized Fe$_3$O$_4$ nanoparticles and HAuCl$_4$ in an alcoholic solvent followed by irridation with electron beam or gamma radiation (ca. 6 kGy).[256]
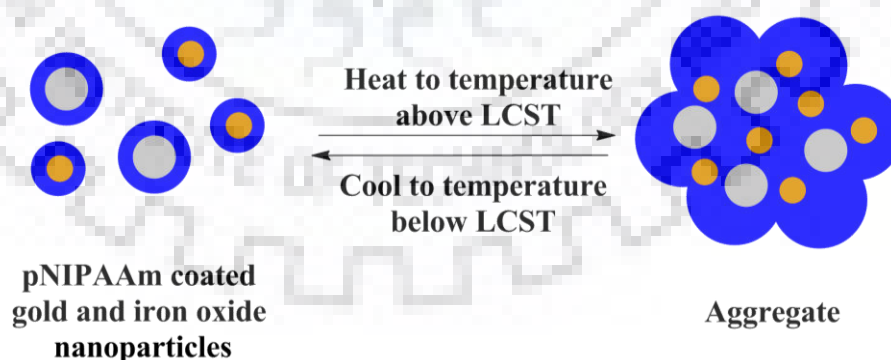
Figure 1.25 Aggregate formed from pNIPAAm-coated Au and Fe$_3$O$_4$ nanoparticles.

Stayton *et al*. brought Au nanoparticles and Fe$_3$O$_4$ nanoparticles together by thermally responsive polymer poly (N-isopropylacrylamide) (pNIPAAm) which serves as a binding unit, coated on Au nanoparticles and Fe$_3$O$_4$ nanoparticles. At temperature higher than the lower

critical solution temperature (LCST) the nanoparticles would aggregate and at temperature below LCST the nanoparticles disperse (Figure 1.25).[257]

1.12 MAGNETISM OF GOLD–IRON OXIDE NANOCOMPOSITES

Based on the response of the intrinsic magnetic dipole of magnetic nanoparticles (MNPs) and the net magnetization in presence and absence of an applied magnetic field, MNPs are typically classified as being either diamagnetic, paramagnetic, ferromagnetic, ferrimagnetic, and antiferromagnetic.[258] Diamagnetic materials (e.g. Au, Cu, Hg) do not have net magnetization in an applied field and are repelled by the magnetic field. Paramagnetic materials (Mg, Cr, Al) have net magnetisation only in the presence of applied field whereas ferromagnetic materials (Fe, Co, Ni, Fe_2O_3) have net magnetization in absence of magnetic field. In antiferromagnetic and ferrimagnetic materials the adjacent magnetic dipoles are oriented antiparallel to each other thus cancelling the net magnetization but atomic level magnetic dipoles are similar to ferromagnetic materials. When a ferromagnetic material is magnetized in an alternating magnetic field the magnetization will trace out a loop called hysterisis loop. The maximum possible magnetization in magnetic materials is called saturation magnetization and arises when all the magnetic dipoles are oriented along the magnetic field. The magnetization curve of the ferromagnetic or ferrimagnetic nanoparticles shows the saturation magnetization, remanent magnetization (induced magnetization remaining after magnetic field is removed) and coercivity (the intensity of an external field needed to force the magnetization to zero).

Iron oxide nanocomposites possess an inverse spinel structure and are favourable in constructing magnetic hybrid nanocomposites because of their intrinsic magnetic properties combined with their nanosize and surface effects. The magnetic Fe_xO_y nanocomposites exhibit high magnetic responses to external magnetic field and can be used for selective capture of target materials, recyclable nanocatalysis and magnetic–photonic purposes.[259-261] When the size of the Fe_xO_y is below the critical size (10–20 nm) and above the blocking temperature (bifurcation point in ZFC/FC plot) these nanocomposites show the super paramagnetic behaviour. Remanence or coercivity will be absent and aggregation behaviour will be negligible at room temperature.[262]

Au is essentially a diamagnetic material, although the examination of underlying Pauli and orbital paramagnetism has been recently reported.[263] The major drawback of the ferromagnetic metals is the chemical instability and calls for alternative that would resistance against external factors while maintaining magnetic properties. The most promising candidates

in this category are the transition metal oxides such as ferrites. Direct interaction between magnetic moment and non-magnetic counterpart inducing finite magnetization in Au due to spin polarization.[264] The most interesting property of Au-Fe_3O_4 nanoparticles is the exchange bias (EB).[265-267] EB usually arises due to interaction between ferromagnetic and antiferromagnetic (FeO) components of a system at their interface. When a ferromagnet is in close proximity to an antiferromagnet, the direct exchange interaction between a ferromagnet and antiferromagnet occurs and the moments in both can create unidirectional anisotropy which impedes the reversal of the ferromagnetic moment. The magnetization loop is shifted along the field axis manifested as EB. In the case of Au−Fe_3O_4 dumbbell nanoparticles exchange bias is induced due to charge transfer from gold.The charge transfer from gold partially reduces Fe_3O_4 to FeO at the Au-Fe_3O_4 interface resulting in the formation of Au−O bonds across the interface.[264,268]

1.13 APPLICATIONS OF GOLD−IRON OXIDE NANOCOMPOSITES

Selected applications of Au-Fe_xO_y nanocomposites include magnetic resonance imaging, drug delivery and catalysis.

1.13.1 Magnetic resonance imaging

Magnetic resonance imaging (MRI) is an noninvasive method for human *in vivo* imaging based on the alignment of hydrogen atoms under powerful magnetic field and can be generated by the relaxation process of the nuclei returning to the original state by the application of radio frequency pulse.[269,270] The relaxation process can be longitudinal relaxation (T_1-recovery) and transverse relaxation (T_2-decay). The difference in relaxation depends on the proton density of specimen and physiochemical nature of the tissue. Contrast agents are used to improve the differentiation between tissues. Au-Fe_xO_y nanocomposites are attractive materials for diagnostic images.[271,272] Fe_3O_4@Au core/shell nanocomposites exhibited a relatively lower transverse relaxivity (r_2) than other nanostructures such as dumbbell nanocomposites, because of the shielding effect based on the embedded Fe_3O_4 core inside an Au shell.[273,274] Superparamagnetic iron oxide nanoparticles work as T_2 negative contrast agents to shorten the T_2 relaxation parameters of water by resulting magnetic field gradients.[275] Magnetic iron oxide nanocomposites also act as T_1 contrast agents in MR imaging.[276,277]

1.13.2 Drug delivery for chemotherapy

Platinum based complexes like cisplatin, carboplatin and oxaliplatin are well known anti-cancer therapeutic agents.[278] Sun *et al.* reported dumbbell like Au-Fe$_3$O$_4$ nanoparticles as target specific nanocarriers for delivery of platin complexes into Her2–positive breast cancer cells with strong therapeutic effects (Figure 1.26A).[279]
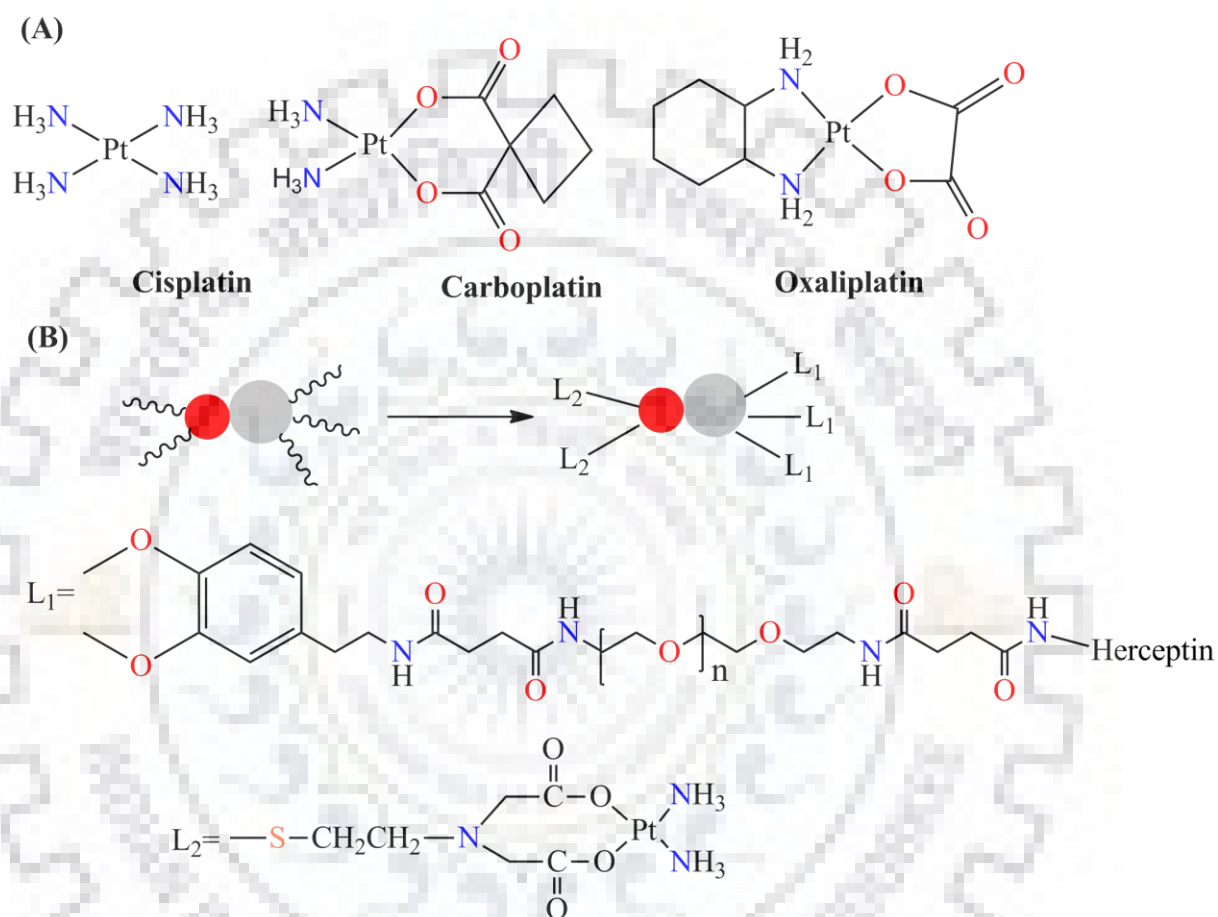
Figure 1.26 A) Structures of the common therapeutic platin complexes. (B) Schematic illustration of the dumbbell-like Au-Fe$_3$O$_4$ NPs coupled with Herceptin and a platin complex for target-specific platin delivery.

Researches have revealed that antigens get overexpressed on the surface of rapidly growing tumor cells and these antigents provide obvious target for specific antigen–antibody interaction.[280] The dumbbell like Au-Fe$_3$O$_4$ contains magnetic Fe$_3$O$_4$ NPs and optically active AuNPs and have the advantage over single component Fe$_3$O$_4$ NPs like the presence of Fe$_3$O$_4$ and Au surfaces facilitates the stepwise attachment of an antibody and a platin complex and serves both optical and magnetic probe for tracking of drug in biological system (Figure 1.26B).

Bhana *et al.* synthesized iron oxide nanoclusters and coated them with Au. A poly-ethylene glycol shell encapsulating a photosensitizing agent and the resulting Au@MNPs revealed in vitro decrease in cancer cells (KB-3-1 head and neck; SK-BR-3 breast) following a combined treatment of photothermal and photodynamic therapy. The magnetic targeting also allowed increased cellular uptake compared to biological drug only.[281] Lin and coworkers reported a chronological delivery of cisplatin codelivered by the iron oxide nanocarriers for anticancer efficacy.[282] Doxorubicin a well known anticancer drug were attached to magnetic nanoparticles by covalent or non–covalent approaches and its controlled release and clinical effects were studied.[283] The use of gold and iron oxide nanoparticles for doxorubicin delivery and cytotoxicity has been evaluated.[284] Gold nanoparticles were also loaded with the drug doxorubicin and the release was studied in presence of glutathione.[285]

1.13.3 Catalysis

Au nanoparticles have played an important role in several cayalytic reactions like hydrogenation, low temperature carbon monoxide oxidation, alcohol oxidation, alkene oxidation, reductive catalysis of chloro or nitro hydrocarbons and organic synthesis.[286-288] However high cost of materials, catalytic efficiency and time consuming centrifugation for recycling and reuse of catalyst are challenges faced for the Au-nanoparticle based catalytic reactions. Au-Fe_xO_y nanocomposites and their derivatives have been used as catalyst for carbon monoxide oxidations,[289-291] synthesis of hydrogen peroxide,[292] reduction of nitrophenols [289,2293,294] and reduction of hydrogen peroxide.[295] The Au-Fe_xO_y nanocomposites enable a better separation method for recycling of the catalyst using magnet. Due to the synergestic effect that occurs at the interface of Au and oxide support the reduction of nitrophenols was carried with high efficiency than that of pure gold.[294] It is believed that electronic structures of both the metal and oxide support are modified by electronic transfers along the interface that produces oxygen vacancies and acts as a active site for the oxygen absorption and activation. Moreover the nanocomposites can be successfully recycled and reused with 100% efficiency.

Electrocatalysts are important to increase rate of reaction and control of selectivity in many electrochemical processes like fuel production and consumption reactions. Electro-catalysts have been used for the hydrogen evolution reactions and oxygen evolution reaction.[295,296] Ongoing efforts are still in search for sustainable, clean and highly efficient energy generation to satisfy the energy needs of modern society. Among the various advanced technologies electrocatalysis for the oxygen evolution reaction (OER) plays a key role and

numerous new electro catalysts have been developed to improve the efficiency of gas evolution. Developing advanced nanoparticle catalysts with promoting effect of Au is an interesting strategy to improve the OER activity. Core-shell nanocomposites are of particular interest where Au core is surrounded by an OER−active transition metal oxide shell. Au substrates have been shown to enhance the OER catalytic activity of transition metal oxide films based on Fe, Ni, Co, and Mn.[297,298] In these cases Au was found to introduce the electronic effects,[298-303,304] provide lower kinetic energy barrier[300] and form bimetallic interfacial oxides leading to high OER activity.[298,299] Au iron oxides have been also used for the catalytic reduction of nitric oxide with carbonmonoxide,[305] nitrophenols[306-308] and CO oxidation.[309]

1.14 SCOPE OF THE WORK

Gold nanoparticles are the most commonly used candidates for fabricating SPR sensing strategies and offer a suitable platform for the selective binding and detection of biological targets. DNA has been used as a powerful tool for morphology control, spatial positioning and dynamic assembly of nanoparticles.[193] Thiol modified homo oligomers containing 30 deoxyribonucleotides were used for the syntheses of nanoflowers and nanospheres.[197] First time amine modified hetero oligomers containing 8 deoxyribonucleotides were studied (Chapter 2A) for the formation of nanoflowers and nanospheres and were utilized for the detection of DNA sequence of miRNA. Adsorption of bio molecules onto the surface of nanoparticles offers a novel route for generation of different architectures.[206-209] First time amino acids were studied (Chapter 2B) for the formation of different nanoarchitectures from spherical nanoparticles. The coral shape was selectively obtained from amino acid Met. DNA functionalized gold nanoparticles and peptide aptamers were utilized for the detection of proteins based on the aggregation.[156,164,165,171] First time a selective detection method for the amino acid Arg was developed (Chapter 3A) based on gold nanoflower methodology. The methodology was further extended for the detection of single Arg in a peptide sequence. Thornton et al. reported the hydrogen bonding interactions, van der Waals contacts and water mediated bonds between amino acids and different part of DNAs.[358] The interaction between amine modified DNAs and AApusc were exploited from time dependent growth of gold nanoparticles (Chapter 3B). The differential interaction creates selectivity among AApusc and can be differentiated at sub-molar concentration of DNA. Metal nanocomposites have attracted considerable attention because of their tunable physical and chemical properties. Gold iron oxide nanocomposites represent hybrid magneto-plasmonic nanoheterostructures have

applications in diagnostic imaging, drug delivery, catalysis and magnetism.[269-303] Au-Fe_xO_y nanocomposites were first time synthesized by Fe powder mediated reduction in presence of AuNP seed and sodium citrate (Chapter 4A) or tryptophan (Chapter 4b) as stabilizing agent in aqueous medium at room temperature. The synthesized nanocomposites showed variable exchange bias and were utilized for drug release, catalysts for nitroarenes reduction and electro chemical splitting of water.

The present thesis aims at investigating syntheses of gold based architectures after growth controlled reaction with bio molecules and development of facile syntheses for gold-iron oxide nanocomposites. The gold based nanomaterials were applied for the biomolecule detection, drug release and catalytic application.
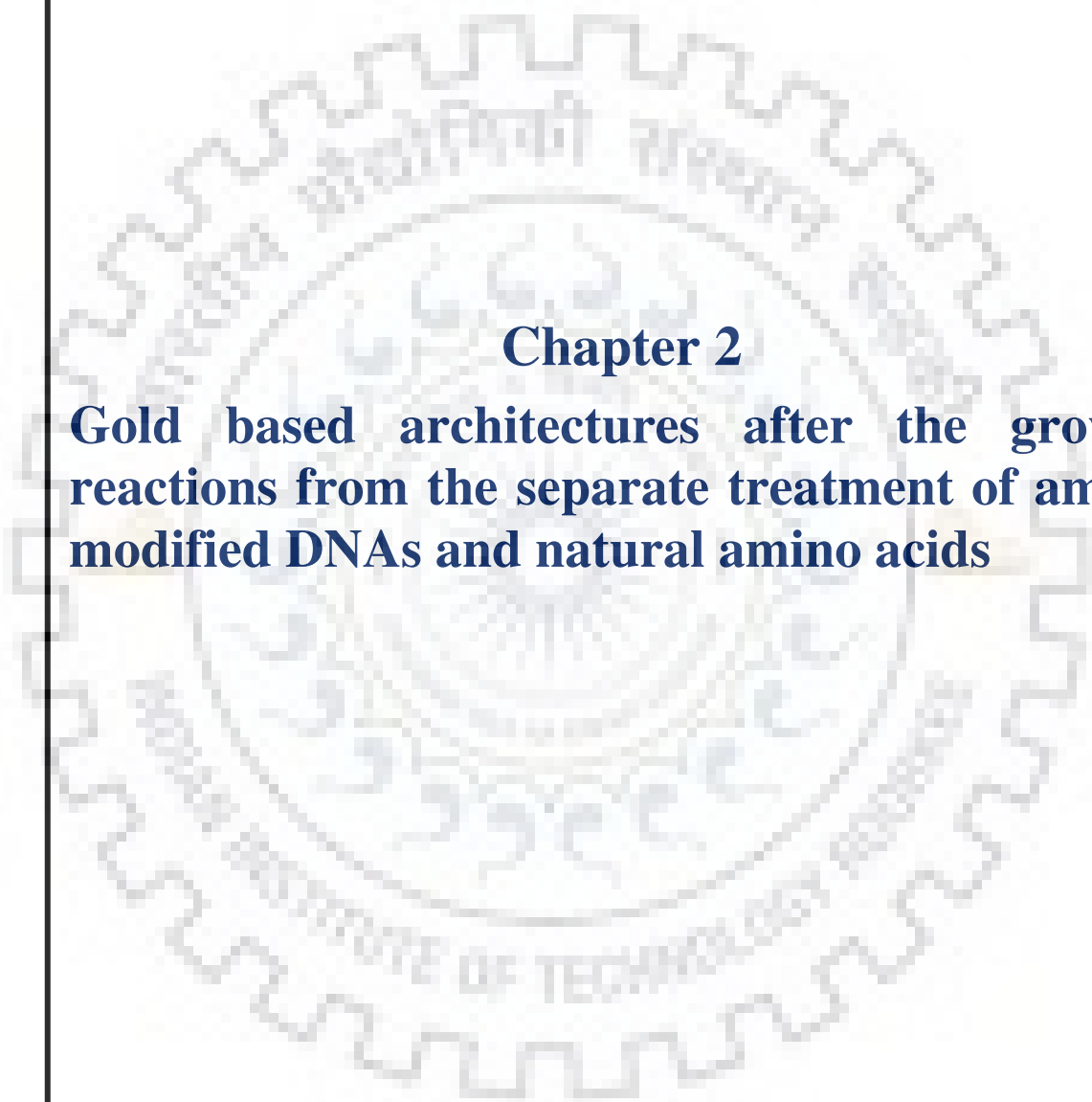
Chapter 2

Gold based architectures after the growth reactions from the separate treatment of amine modified DNAs and natural amino acids

2.1 INTRODUCTION

The surface modified nanoparticles with DNA strands show immense biomedical applications [310] including gene silencing.[311] In particular, the gold nanoflowers with DNA strands on the surface show high affinity for tumor cells with overexpressed nucleolin.[312] Lu *et al.* reported synthesis of highly stable gold nanoflower with thiol-modified nucleic acid strands (polyadenine, A30 and polycytosine, C30).[197] Further they have developed a wide range of nanoarchitectures using a variety of gold nanoplatform and DNA strands.[198,201] Growth-mediated thiol modified DNA functionalized nanostructures have been applied for the detection of natural products like ochratoxin A, cocaine and 17β-estradiol.[191] Haam and co-worker have used nanoflower like stellate gold nanoparticles functionalized with thiol based molecular beacon to detect different microRNAs.[152]

Amine functionalized DNAs, on the other hand, have been utilized for real time applications [313-315] including functional group transformation.[316] Amine-modified complementary DNAs with small molecule based dyes are crucial for the basic labelling of biomolecules.[317] This labelling is more effective for single strand DNAs without any secondary structures. Amine-modified staple strands have been applied for docking of antibodies into the cavities of DNA origami structure.[318]

This chapter is divided into two sections. Section A describes the growth reactions for detection of miRNA using amine modified DNA while Section B describes selective formation of coral shaped nanoarchitecture with methionine.

SECTION A

Amine-modified 8-mer single strand DNAs (Table 2.1) were used for the formation of gold nanoflowers or gold nanospheres. Growth-mediated gold nanoarchitecture formation was explored with 8-mer strands in order to avoid the complications of any secondary structure. Growth controlled reactions with two different DNAs strands PMR (amine-5'-ACATCAGT-3') and PML (amine-5'-GATAAGCT-3') were used for the formation of gold nanoflowers and nanospheres with different concentrations of gold nanoparticle seed in presence of mild reducing agents like hydroxylamine and hydroquinone (Scheme 2.1). The different nanostructures obtained after growth reaction were used for the detection of DNA sequence for miRNA.

Table 2.1: DNA sequences used in the experiments

S. No	Sequence	Name
1	**No DNA**	No DNA
2	**H_2NC_6-5′-ACATCAGT-3′**	PMR
3	**H_2NC_6-5′-GATAAGCT-3′**	PML
4	**H_2NC_6-5′-TCTTCTGT-3′**	MMR
5	**H_2NC_6-5′-GTTTTGCT-3′**	MML
6	**5′-ACATCAGT-3′-C_7NH_2**	PMR'
7	**5′-ACATCAGT-3′**	No mod
8	**H_2NC_6-5′-ACATCAGT-3′-C_7NH_2**	Both Mod
9	**H_2NC_6-5′-AAATCAGT- 3′**	PMA
10	**H_2NC_6-5′-ATATCAGT- 3′**	PMT
11	**H_2NC_6-5′-AGATCAGT- 3′**	PMG
12	**H_2NC_6-5′-ACA-3′**	PM3
13	**H_2NC_6-5′-ACAT-3′**	PM4
14	**H_2NC_6-5′-ACATC-3′**	PM5
15	**H_2NC_6-5′-ACATCA-3′**	PM6
16	**H_2NC_6-5′-ACATCAG-3′**	PM7
17	**H_2NC_6-5′-TCATCAGT-3′**	PMRTI
18	**H_2NC_6-5′-TTATCAGT-3′**	PMRT2
19	**H_2NC_6-5′-ACTTCAGT-3′**	PMRT3
20	**H_2NC_6-5′-ATTTCAGT-3′**	PMRT4
21	**H_2NC_6-5′-ACATCTGT-3′**	PMT5
22	**H_2NC_6-5′-ACAAAGCT-3′**	PMA2
23	**H_2NC_6-5′-ACATTGCT-3′**	MML'

Seed 0.15 nM

Seed $\xrightarrow[\text{HA, HAuCl}_4]{\text{PMR}}$ Gold nanosphere

Seed $\xrightarrow[\text{HA, HAuCl}_4]{\text{PML}}$ Gold nanosphere

Seed $\xrightarrow[\text{HQ, HAuCl}_4]{\text{PMR}}$ Gold nanoflower

Seed $\xrightarrow[\text{HQ, HAuCl}_4]{\text{PML}}$ Gold nanoflower

Seed 0.45 nM

Seed $\xrightarrow[\text{HA, HAuCl}_4]{\text{PMR}}$ Gold nanoflower

Seed $\xrightarrow[\text{HA, HAuCl}_4]{\text{PML}}$ Gold nanosphere

Seed $\xrightarrow[\text{HQ, HAuCl}_4]{\text{PMR}}$ Gold nanosphere

Seed $\xrightarrow[\text{HQ, HAuCl}_4]{\text{PML}}$ Gold nanosphere

HA= Hydroxylamine   **HQ= Hydroquinone**

Scheme 2.1 Formation of gold nanoflowers and nanospheres after adsorption of amine-modified 8-mer DNA sequences (PMR and PML) to gold nanoparticle seeds for controlled growth via Au(III) reduction with hydroxyl amine and hydroquinone.

2.2 EXPERIMENTAL SECTION

2.2.1 Chemicals and Materials

All the oligonucleotides used in the study were purchased from the GeneX India Bioscience Pvt. Ltd. Hydrogen tetrachloroaurate(III) trihydrate (HAuCl$_4$.3H$_2$O) were purchased from the Sigma Aldrich, Hydroxylamine hydrochloride (NH$_2$OH.HCl) were purchased from SISCO Research Laboratories, Sodium hydroxide and sodium chloride were purchased from Thomas Baker and trisodium citrate dihydrate was purchased from Merck chemicals.

2.2.2 Instrumentation

Absorption Spectroscopy: The absorbance measurements of the solutions were taken using the Synergy microplate reader (BIOTEK, USA) in the range of 400−800 nm wavelength.

Transmission Electron Microscopy (TEM): The Transmission Electron microscopy images (TEM) of gold nanoparticles were taken using FEI, Technai G2 20 S-TWIN. Image J softwear was used to calculate the average size of nanoparticles from TEM images.

Dynamic Light Scattering (DLS): Hydrodynamic diameters and ζ−potential of the gold nanoarchitectures were measured using Zetasizer Nano ZS90 (Malvern Instruments). DTS applications 7.03 software was used to analyze the data. All sizes reported here were based on

intensity average. For each sample, three DLS measurements were conducted with a fixed 11 runs and each run lasts 10s.

2.2.3 Apparent Binding constant (K_{app})

The apparent association constants for DNA sequences to the gold nanoparticle seeds were determined from the change in absorbance intensity due to addition of DNA (0.017 mM−0.127 mM) to gold nanoparticle seed. The K_{app} was obtained as intercept/slope ratio from the plot of $1/(\Delta A)$ against $1/[DNA]$. The more details are available in the literature.[319]

2.3 Synthetic Procedures

Synthesis of seed stock solution

20 mg (0.05 mmol) of $HAuCl_4$ was dissolved into 90 mL of Millipore water and refluxed with stirring. To the refluxing solution, 10 mL of 1% (w/v) trisodium citrate (0.3 mmol) was added. After some time, dark violet color was appeared. The color immediately changed to red. The reaction was further heated for 30 minutes and cooled at room temperature. The resulting mixture was characterized by UV−Vis spectroscopy and TEM. For use in further experiments the seed solution was diluted and absorbance was adjusted to 0.5 (1:1 diluted). The final volume in all the reactions was adjusted to 310 μL. The concentration of seed was calculated from the reported literature.[320]

Growth reactions of gold nanoparticles functionalized with DNA

Gold nanoparticles seed (0.15 nM, 0.21nM and 0.45 nM) were incubated with 0.6μM DNA for 30 minutes. 3 μL of 200 mM NH_2OH (adjusted to pH 5 with NaOH) or 3 μL of 200 mM hydroquinone was added to these solutions and stirred vigorously for 10 minutes. 5 μL of 0.8% (w/v) $HAuCl_4$ was added to these solutions to initiate the reduction reaction. The color change was observed within seconds.

Treatment of gold nanoparticles with NaCl

0.45 nM gold nanoparticle seed solutions were incubated with 0.6μM of DNA for 30 minutes. One reaction was setup in which no DNA was added. 3 μL of 200 mM NH_2OH (adjusted to pH 5 with NaOH) was added to these solutions and vigorously shaken for 10 minutes. 5 μL of 0.8% (w/v) $HAuCl_4$ was added to these solutions to initiate the reduction reaction. 0.1 M NaCl

was added to each of the solutions. Absorbance was recorded before and after the NaCl addition.

Growth reactions of gold nanoparticles with PMR and MMR by varying gold amount

0.45 nM of gold nanoparticle seed solutions were incubated with 0.6μM, PMR or MMR for 30 minutes. 3 μL of 200 mM NH_2OH (adjusted to pH 5 with NaOH) was added to these solu-tions and vigorously shaken for 10 minutes. Different amounts of 0.8% (w/v) $HAuCl_4$ 0.0 μL, 0.2 μL, 0.6 μL, 1.0 μL, 1.4 μL, 2.0 μL, 3.0 μL, 4.0 μL, and 5.0 μL were added to these solutions to initiate the reduction reaction.

Growth reactions of gold nanoparticle with lowering concentration of PMR

0.45 nM gold nanoparticle seed solution was incubated with different concentrations of PMR (65 nM, 130 nM, 195 nM, 260 nM, 325 nM, 390 nM, 520, nM and 650 nM for 30 minutes. 3 μL of 200 mM NH_2OH (adjusted to pH 5with NaOH) was added to these solutions and vigorously shaken for 10 minutes. 5 μL of 0.8% (w/v) $HAuCl_4$ was added to these solutions to initiate the reduction reaction.

Growth reactions of gold nanoparticle with increasing concentration of MMR

0.45nM gold nanoparticle seed solution was incubated with different concentrations of MMR (650 nM, 1625 nM, 19 nM, 3250 nM, 6500 nM and 9750 nM for 30 minutes. 3 μL of 200 mM NH_2OH (adjusted to pH 5with NaOH) was added to these solutions and vigorously shaken for 10 minutes. 5 μL of 0.8% (w/v) $HAuCl_4$ was added to these solutions to initiate the reduction reaction.

Detection of DNA Sequence for miR−21

100 μL of nanoflower or nanosphere (obtained from the above hydroxylamine based growth mediated synthesis with PMR and PML) seed was diluted with 200 mL of Millipore water. The solutions were incubated with different concentrations of miR-21, 20 pmol, 50 pmol, 100 pmol, 200 pmol for 30 minutes. 3 μL of 200 mM hydroquinone was added to these solutions and stirred vigorously for 10 minutes. 5 μL of 0.8% (w/v) $HAuCl_4$ was added to these solutions to initiate the reduction reaction. The color change from red to blue was observed within seconds.

2.4 RESULTS AND DISCUSSION

2.4.1 Synthesis and characterization

Growth reactions of gold nanoseeds were performed by incubating the amine modified DNA PMR and PML for 30 minutes. Hydroxylamine or hydroquinone as reducing agent was added and the reaction was vigorously shaken. $HAuCl_4$was added to complete the reduction reaction and the colour change was observed within seconds. The resulting solutions were characterized by the absorption spectroscopy and Transmission Electron Microscopy (TEM). Hydrodynamic radii and Zeta (ζ) potential of nanoparticles were measured by Dynamic Light Scattering (DLS).

2.4.2 Growth reaction with hydroxylamine

The reaction mixture reduced by hydroxylamine containing PMR sequence developed purple colour, whereas the solution containing PML sequence was red in color (Figure 2.1A).The absorption spectrum of the solution synthesised with PMR was substantially different from the seed solution. The surface plasmon resonance (SPR) peak maximum was red shifted to 550 nm (Figure 2.1 B) for PMR based growth reaction with respect to the SPR peak of seed solution at 521 nm. Along with the positional shift, broadening of the absorption peak was observed. In contrast, the absorption spectrum of the other solution containing PML was red shifted to 537 nm without any broadening (Figure 2.1 B). In both the cases, the intensities of the absorption were much higher in comparison to seed due to the growth of the gold nanoparticles in solutions. The absorption spectrum of the solution synthesised without any DNA showed slight red shift of 523 nm with enhanced intensity (Figure 2.1B).
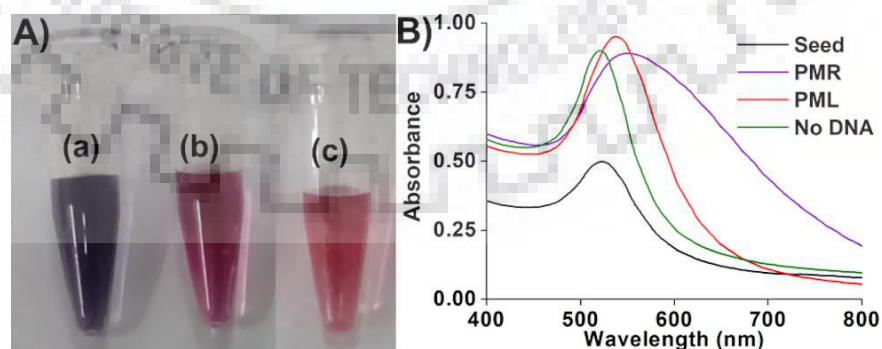
Figure 2.1 A) Color of gold nanoparticles after growth reaction in presence of (a) PMR, (b) PML (c) no DNA added to the seed solutions; B) absorbance spectra of these solutions.

The morphologies of the nanoparticles after growth reaction were confirmed from the TEM images. TEM images showed the nanoparticle synthesized with PMR sequence are flower shaped whereas nanoparticles synthesized without any DNA sequence and PML sequence were spherical in nature (Figure 2.2A–C).The morphology of nanoflowers was further checked under high resolution TEM (HR-TEM) imaging (Figure 2.2D).

The size distribution histograms of nanoparticles are shown in Figure 2.3 and the average size of the nanoparticles in absence of DNA was 15±1.8, while as in presence of PML and PMR were 18±4.8 and 20±4.5 respectively. The percentage of nanoflowers formation was 80%.
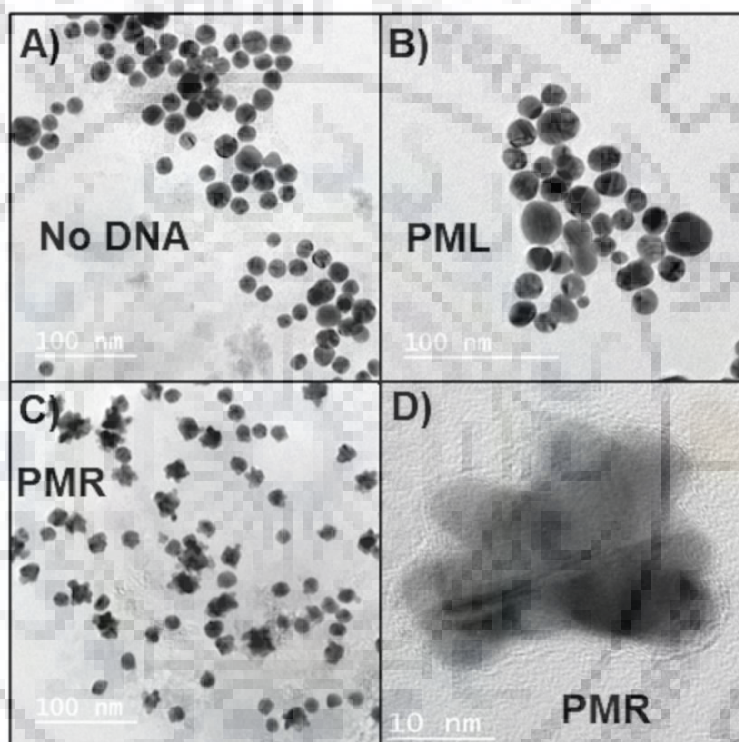
Figure 2.2 TEM images of gold nanoparticles after hydroxylamine-based growth reaction in the presence of A) no DNA, B) PML, and C) PMR; D) HRTEM of nanoflower after growth reaction in the presence of PMR.
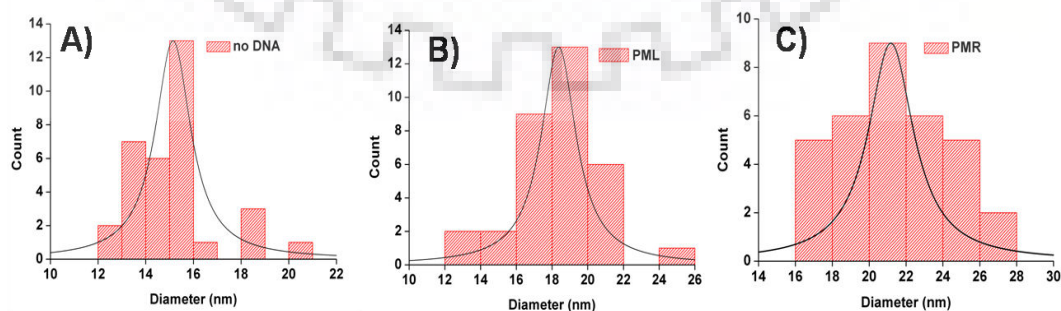
Figure 2.3 Size distribution histograms of gold nanoparticles after hydroxylamine-based growth reaction in the presence of A) no DNA, B) PML, and C) PMR.

2.4.3 Growth reaction with hydroquinone

These seed-mediated growth reactions with PMR and PML were further explored with comparatively milder reducing agent hydroquinone ($E° = -0.699$ V vs NHE) which is stronger than sodium citrate ($E° = -0.180$ vs NHE) and hydrazine ($E° = -0.230$ vs NHE) but weaker than sodium borohydride ($E° = -1.24$ vs NHE). The resulting solutions were red in color. The absorption spectra showed SPR peak at 530 nm with increase in intensity without any broadening (Figure 2.4).The morphologies of the nanoparticles checked by TEM images showed the nanoparticles were spherical in shape of almost identical sizes (Figure 2.5A−C) for both the sequences and in absence of DNA.
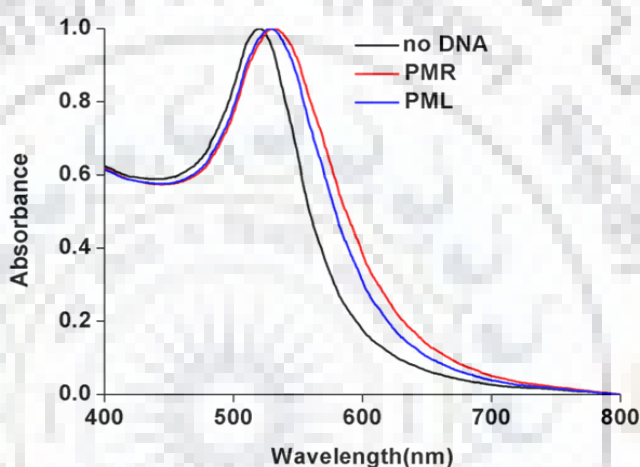
Figure 2.4 Normalized absorbance spectra of growth reactions in absence or presence of PMR and PML.
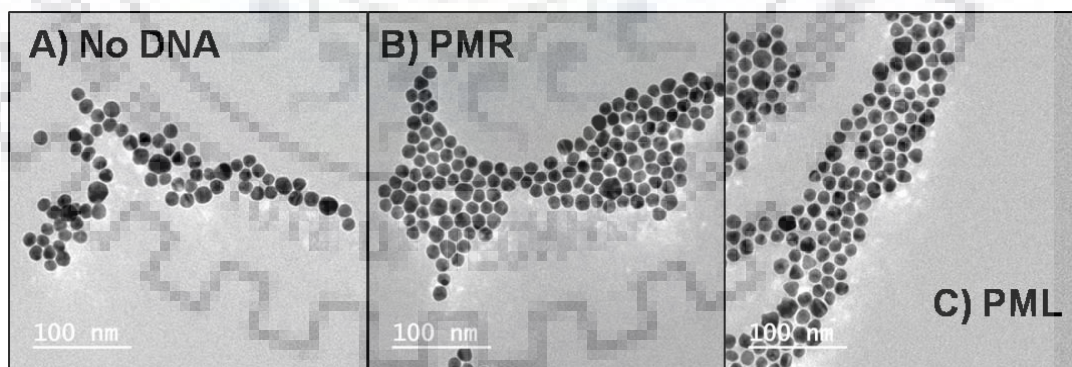
Figure 2.5 TEM images (A-C) of nanoparticles after reduction reaction by hydroquinone in presence of PMR, PML and no DNA conditions. Scale bar; = 100 nm.

The size distribution histograms of nanoparticles are shown in Figure 2.6 and the average size of the nanoparticles in absence of DNA was 15±20, while as in presence of PMR and PML were 16±1.7 and 15±1.9 respectively.
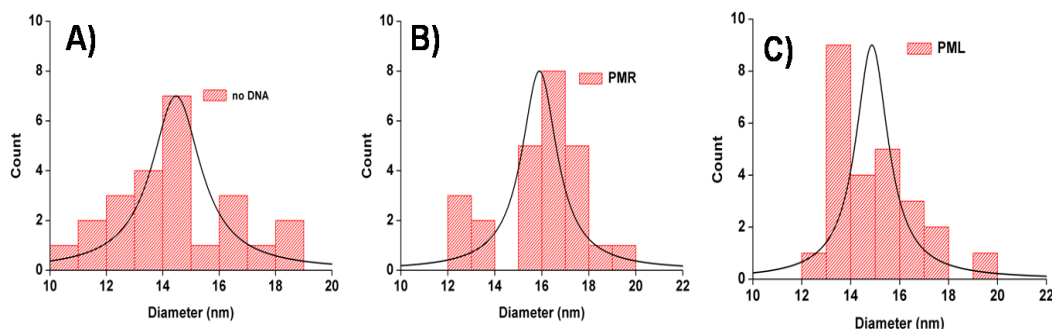
Figure 2.6 Size distribution histograms of gold nanoparticles after hydroquinone -based growth reaction in the presence of A) no DNA, B) PMR, and C) PML.

2.4.4 Seed variation methodology

The growth-mediated nanostructure formation was further explored with seed amount 0.15 nM, 0.21nM and 0.45 nM in presence of both the reducing agents. The seed variation treatment for PMR in presence of hydroxylamine showed red shift (530 nm to 555 nm) with increasing concentration of seed (Figure 2.7) while the reduction reaction in presence of hydroquinone for PMR showed significant red shift with decreasing the concentration of seed (Figure 2.8).

The growth reaction with PML and decreasing seed amount from 0.45 nM to 0.15 nM in presence of hydroxylamine showed negligible shift of the absorption maxima with broadening of the peak (Figure 2.9). Decreasing the seed concentration in presence of hydroquinone as reductant showed significant red shift in the absorption spectra (530 nm to 555 nm, Figure 2.10) for PML based reactions.
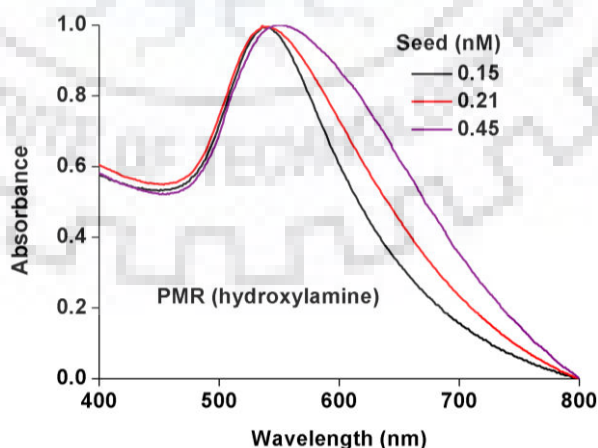
Figure 2.7 Normalized absorption spectra of nanosolutions prepared by different seed amounts after growth reaction by reduction with hydroxylaminein presence of PMR.
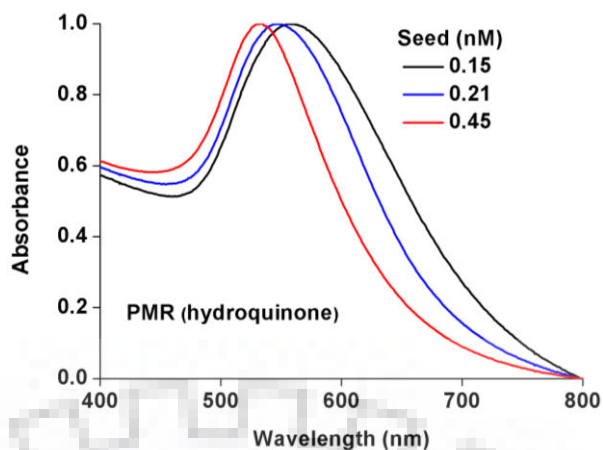
Figure 2.8 Normalized absorption spectra of nanosolutions prepared by different seed amounts after growth reaction by reduction with hydroquinone in presence of PMR.
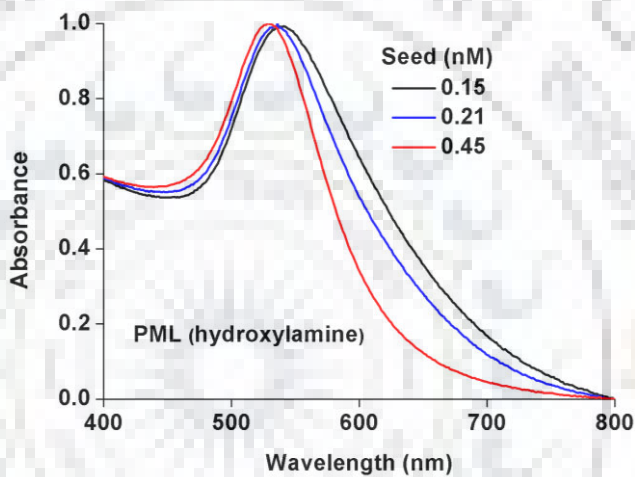
Figure 2.9 Normalized absorption spectra of nanosolutions prepared by different seed amounts after growth reaction by reduction with hydroxylamine in presence of PML.
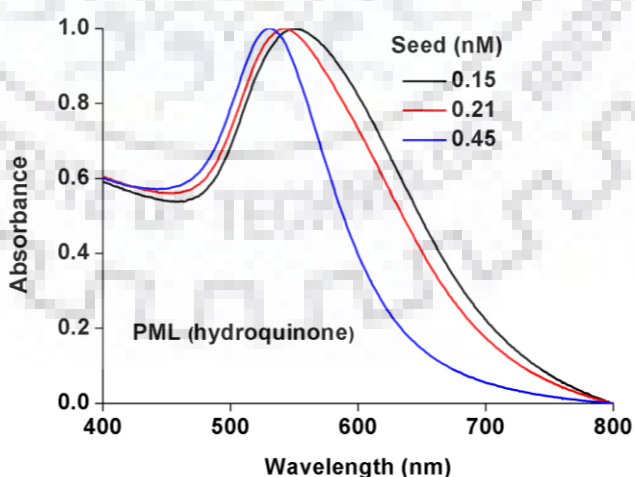
Figure 2.10 Normalized absorption spectra of nanosolutions prepared by different seed amounts after growth reaction by reduction with hydroquinone in presence of PML.

This trend in absorption spectra was similar to the previous report by Chan's group in the seed-mediated growth by hydroquinone based reduction without any DNA sequence.[48] TEM images of the nanoparticles after growth confirmed the formation of spherical nanoparticles at 0.21 nM and 0.15 nM for the combination of PMR and hydroxylamine and gold nanoflowers at 0.45 nM amounts for the combination of PMR and hydroxylamine (Figure 2.9 top). For hydroquinone based reaction in presence of PMR gold nanoflowers of large size was obtained at 0.15 nM seed amount and at 0.21 nM. TEM images showed spherical nanoparticles with decreasing size were obtained at 0.45 nM (Figure 2.11 bottom).
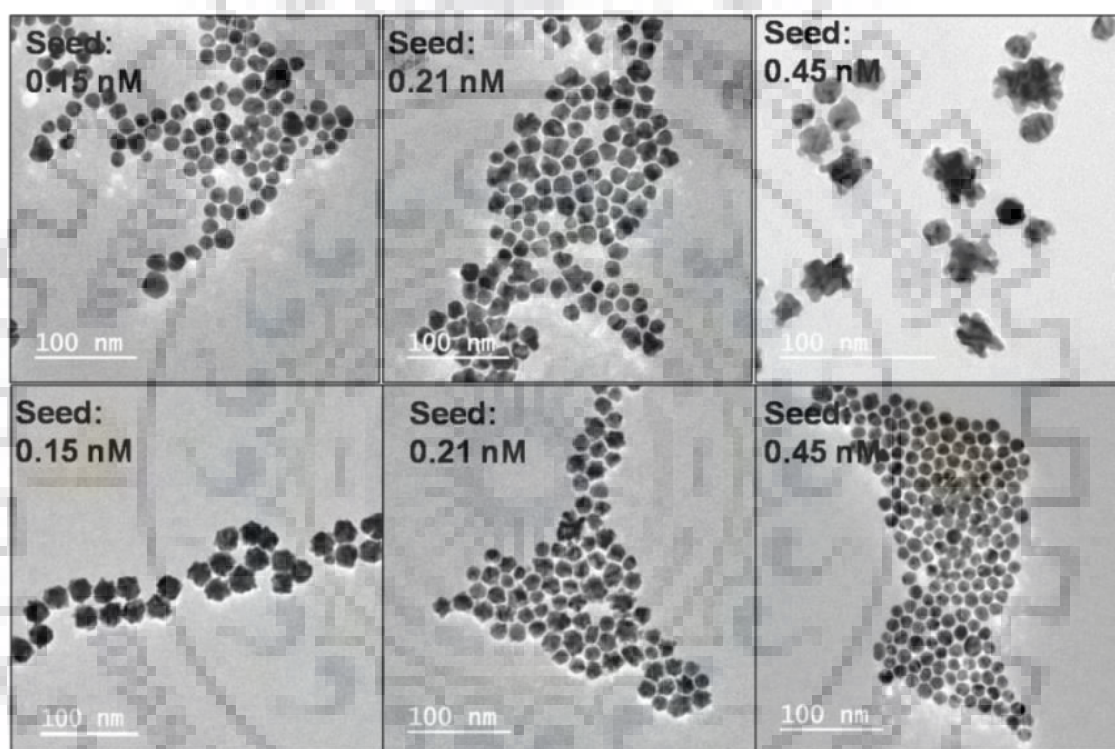
Figure 2.11 TEM images of gold nanoparticles after hydroxylamine (top) and hydroquinone-based (bottom) growth reactions with PMR in the different seed solutions.

The size distribution histograms of nanoparticles are shown in Figure 2.12 and 2.13. The average size of the nanoparticles for seed amount of 0.15 nM, 0.21 nM and 0.45 nM were 17±2.65 nm, 18±4.5 nm, 20±3.5nm after hydroxylamine based reduction reaction and 31±2.65 nM, 20±2.65 nM and 15±2.5nM after hydroxylamine based reduction reaction respectively.

In the case of hydroxylamine based reduction for PML TEM images showed spherical nanoparticles were formed. (Figure 2.14 top) whereas with hydroquinone based reaction nanoflowers of large size developed with seed amount of 0.15 nM and 0.21 nM (Figure 2.10 bottom). Seed amount of 0.45 nM developed nanospheres with size. Interestingly, with 0.15

nM seed concentration, the shape of the growth mediated gold nanoparticles for both the sequences finally showed gold nanoflower formation of larger size. The percentage of nanoflowers formed was 80% in all the cases.

The size distribution histograms of nanoparticles are shown in Figure 2.15 and 2.16. TEM analysis show slight increase in average size on decreasing seed amount was observed, 16±2.36 for 0.45 nM, 18±2.36 for 0.21 nM and 19±2.6 for 0.15 nM seed amount for hydroxylamine based reactions. For hydroquinone based reactions nanoflowers with average size of 35±4.2 nm and 31±3.9 nm were formed with seed amount of 0.15 nM and nanoparticles of 16±2.9 nm were formed with seed amount of 0.21 nm.
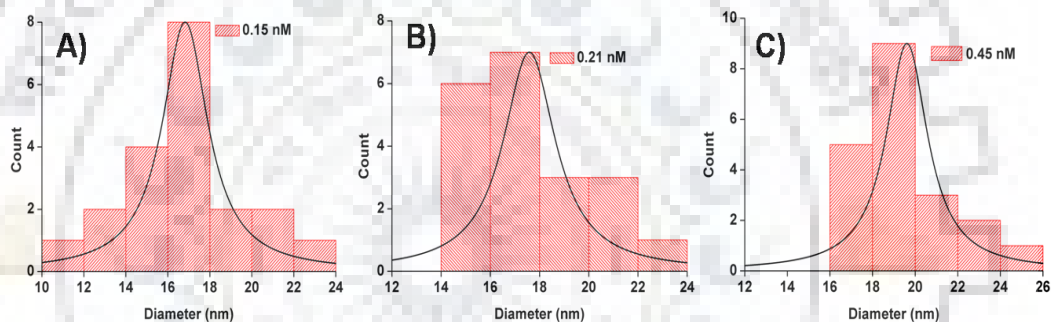
Figure 2.12 Size distribution histograms of gold nanoparticles after hydroxylamine based growth reaction with PMR at seed amount of (A) 0.15 nM and (B) 0.21 nM (C) 0.45 nM
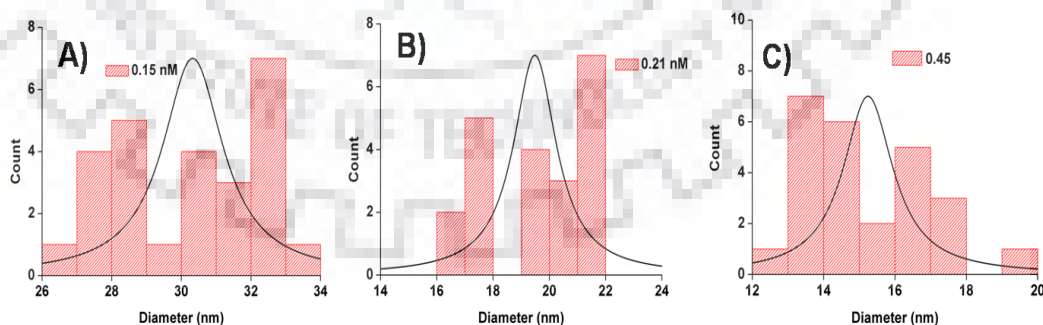
Figure 2.13 Size distribution histograms of gold nanoparticles after hydroxylamine based growth reaction with PMR at seed amount of (A) 0.15 nM and (B) 0.21 nM. (C) 0.45 nM.
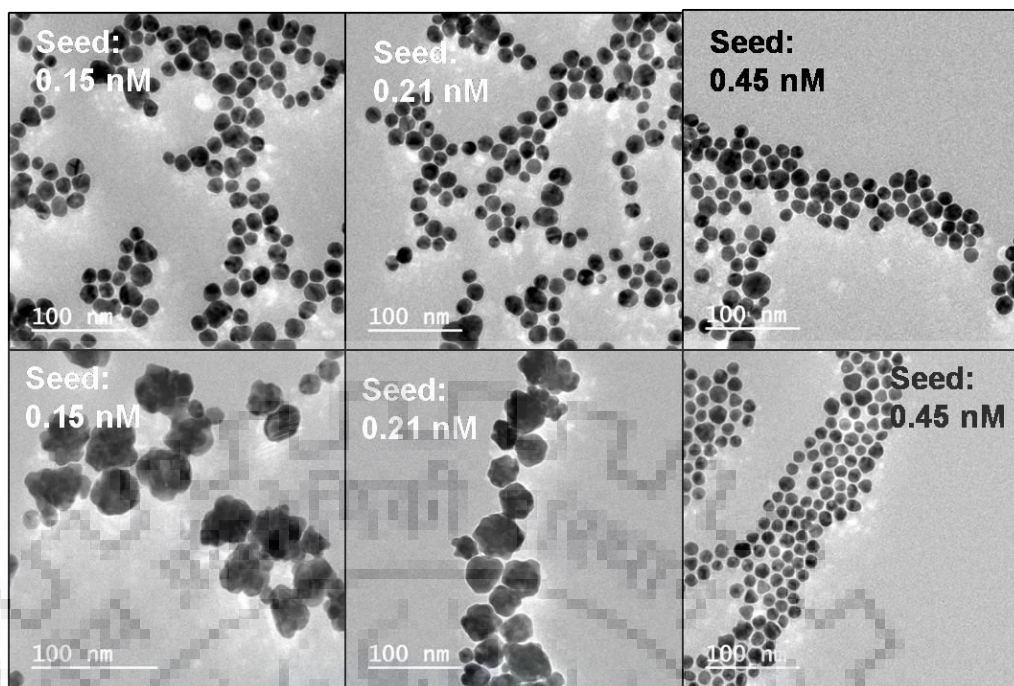
Figure 2.14 TEM images of gold nanoparticles after hydroxylamine (top) and hydroquinone-based (bottom) growth reactions with PML in the different seed solutions.
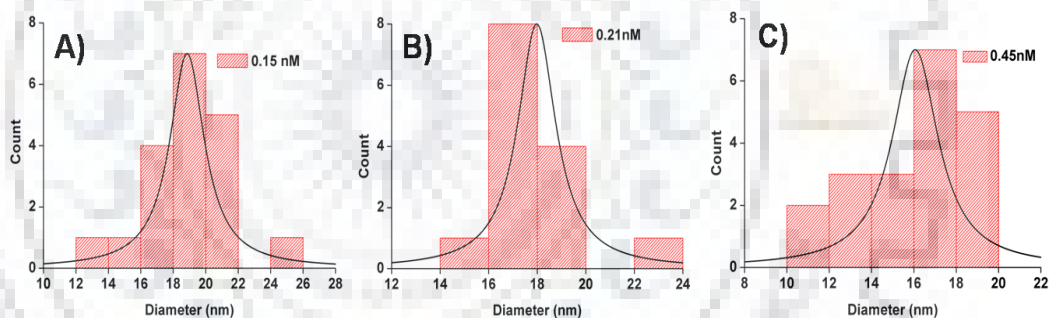
Figure 2.15 Size distribution histograms of gold nanoparticles after hydroxylamine based growth reaction with PML at seed amount of (A) 0.15 nM (B) 0.21 nM and (C) 0.45 nM.
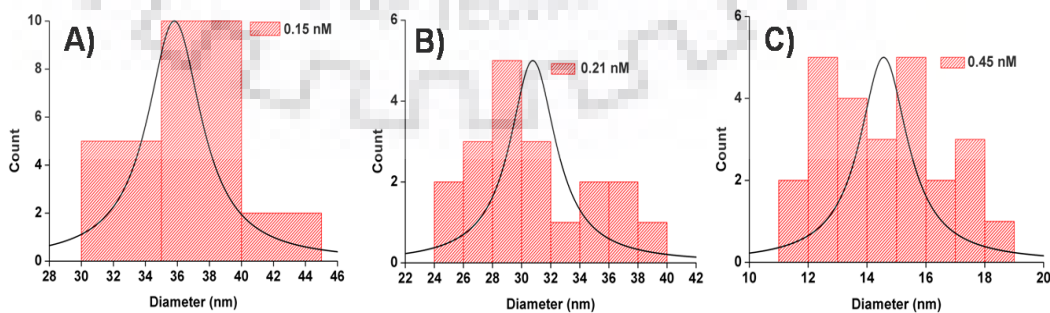
Figure 2.16 Size distribution histograms of gold nanoparticles after hydroquinone based growth reaction with PML at seed amount of (A) 0.15 nM (B) 0.21 nM and (C) 0.45 nM.

2.4.5 Reduction with mutated sequences and affinity dependence

In order to find out the origin of the nanoflower formation with the PMR sequence via hydroxylamine based reduction, nucleic bases of both the DNA strands were focused. Single strand DNAs with poly A and poly C sequences showed more adsorption on citrate stabilized gold nanospheres in comparison to DNA with poly T sequences.[197] To investigate this concept with DNA sequences, MMR (amine-5'-TCTTCTGT-3') and MML (amine-5'-GTTTTGCT-3'), sequences, were selectively chosen where all the adenine nucleic bases of PMR and PML were replaced with thymine. Growth reactions with hydroxylamine in presence of MMR and MML resulted in the red colored solutions. The absorption maxima were at 532 and 533 nm for the growth mediated nanoparticles synthesized in presence of MMR and MML respectively (Figure 2.17).

The morphologies of nanoparticle synthesized with MMR and MML sequences were spherical in nature. The nanospheres formation with MMR was further checked with HR-TEM (Figure 2.18A–C). A close look to the DNA sequences revealed ACA, GAT, TCT and GTT are the first three nucleic bases at the 5' amine-modified terminal of the PMR, PML, MMR and MML sequences respectively. The formation of the gold nanoflowers from PMR resulted from the higher adsorption of the terminal ACA sequence to the gold surface. The amine-modified end of PML, MMR and MML sequences contained mostly the mixed sequence with a smaller number of adenines and cytosines.
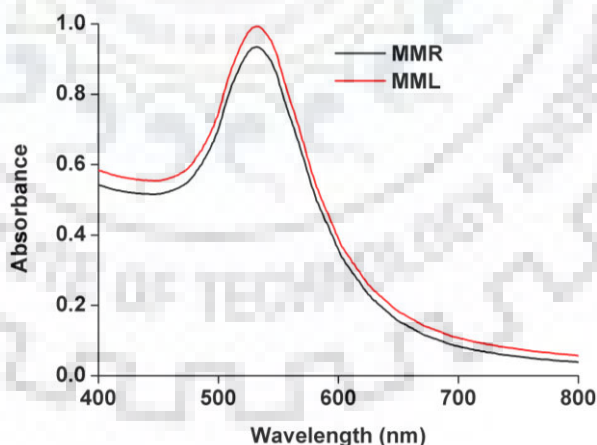
Figure 2.17 Absorption spectra of solutions after growth reaction in presence of MMR and MML.

The size distribution histograms of nanoparticles are shown in Figure 2.19. The average size of the nanoparticles were 19±4.8 nm and 20±4.08nm synthesized with MMR and MML respectively.
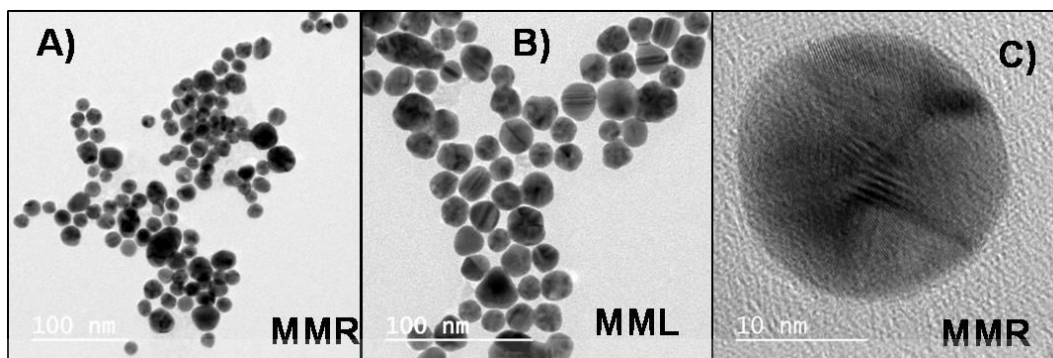
Figure 2.18 TEM images of gold nanoparticles from growth reactions after the treatment of MMR (A), MML (B) to the seed solutions; HR-TEM image of MMR (C).
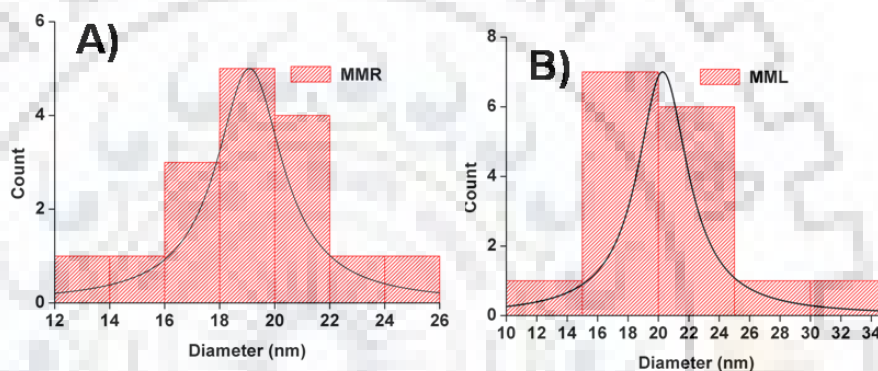
Figure 2.19 Size distribution histograms of gold nanoparticles from growth reactions after treatment of MMR (A) and MML (B).

2.4.6 Role of amine modified ACA terminal

For an in-depth understanding of the effect of the amine modified terminal ACA sequence dependent formation of nanoflowers, the effect of three sequences PMA (amine-5-AAAT CAGT–3'), PMG (amine-5-AGATCAGT-3') and PMT (amine-5'-ATATCAGT-3') were investigated. In these three sequences, the cytosine of 5' terminal ACA part of PMR sequence was mutated with adenine, guanine and thymine. Absorption studies (Figure 2.20) showed maximum red shift in case of PMA (562 nm) with terminal AAA sequence. The absorption maximum for PMG (552 nm) with terminal AGA sequence was observed almost at the same wavelength with respect to PMR. In the case of PMT with terminal ATA sequence, blue shift (526 nm) was observed. These results were consistent with the binding affinity of nucleic bases as A> C ≥ G > T.[321] TEM images (Figure 2.21A–C) showed the formation of gold nanoflower in the case of PMA and PMG. In the case of PMT, the nanoparticles were spherical in shape. The percentage of nanoflowers formed was 80%.
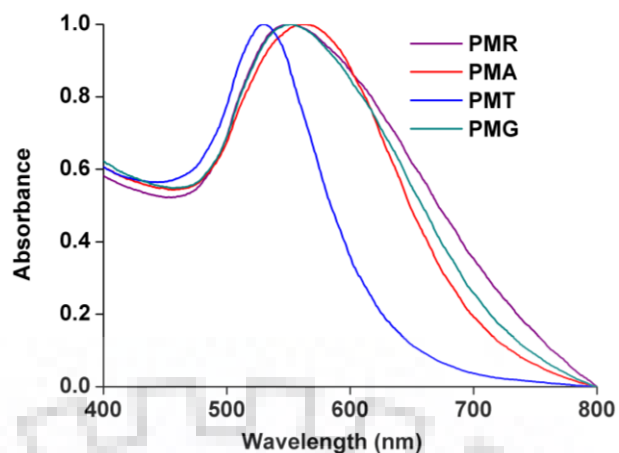
Figure 2.20 Normalized absorption spectra after growth reaction with the addition of PMT, PMA and PMG to the seed solutions.
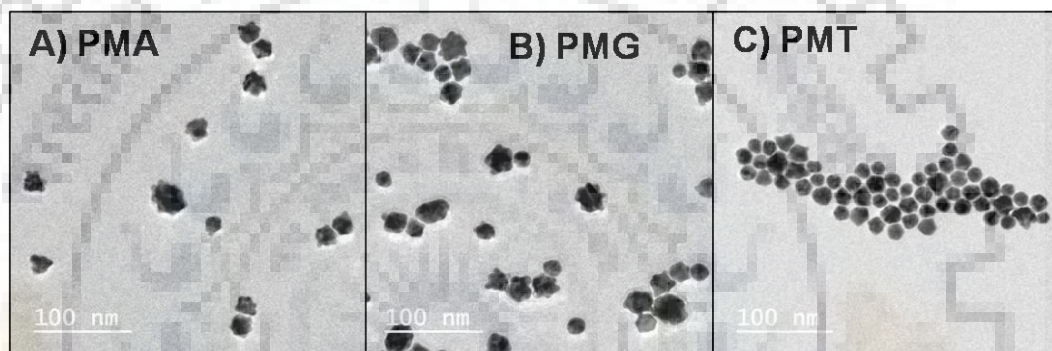
Figure 2.21 TEM images of gold nanoparticles after growth reaction with the addition of (A) PMA, (B) PMG and (C) PMT to the seed solutions. Scale bar: 100 nm.

The size distribution histograms of nanoparticles are shown in Figure 2.22. The average size of the nanoparticles synthesized with PMA and PMG were 24±3.58 nm and 25±4.6 nm. Average size of nanoparticles synthesized with PMT was 15±1.89 nm.
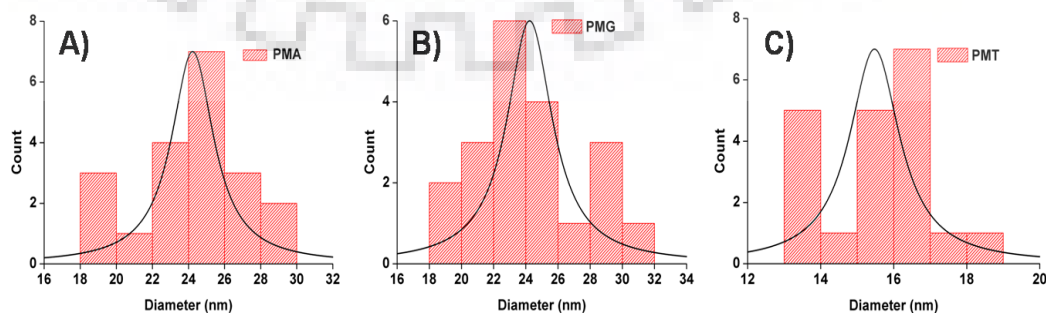
Figure 2.22 Size distribution histograms of gold nanoparticles after hydroquinone based growth reaction with PML at seed amount of (A) 0.15 nM (B) 0.21 nM and (C) 0.45 nM.

2.4.7 Effect of mutation

The sequence specific studies were further confirmed from the other possible partial thymine reached mutants of PMR. For this purpose, mutated sequences PMT1 (amine-5'-TCATCAGT-3'), PMT2 (amine-5'-TTATCAGT-3'), PMT3 (amine-5'-ACTTCAGT-3'), PMT4 (amine-5'-ATTTCAGT-3'), PMT5 (amine-5'-ACATCTGT-3') were chosen. Growth reactions with hydroxyl amine in presence of these DNAs were performed. Absorption studies (Figure 2.23A) from the synthesized nanoparticles using PMT1- PMT5 showed the maximum red shift for PMT5. This red shifted band was close to the SPR peak of PMR. In other cases, with PMT1-PMT4, the absorption maxima were restricted within 530–540 nm. However, the TEM analysis (Figure 2.23B) suggested that gold nanoflower structure cannot be obtained with a single adenine to thymine mutation in PMT5. The size distribution histograms of nanoparticles shows the average size of 17±2.69 nm nanoparticles were formed (Figure 2.24).

Interestingly in the case of MML' (amine-5'-ACATTGCT-3'), where ACA sequence was introduced as mutants around the 5' terminal of MMR, the synthesized nanoparticles showed absorption maximum (Figure 2.25A) similar to the PMT5. The TEM image (Figure 2.25 B) for MML' suggested the formation of gold nanospheres similar to that of PMT5. Partial adenine based mutation in PMA2 (amine-5'-ACAAAAGT-3') led to the formation of gold nanoflower (Figure 2.25A). The result with PMA2 confirmed that the sequence with amine modified polyadenine[197] was also responsible for nanoflowers formation.. Size distribution histograms (Figure 2.26) shows the average size of nanoparticles synthesized with MML' were 17.5±3.2 nm.
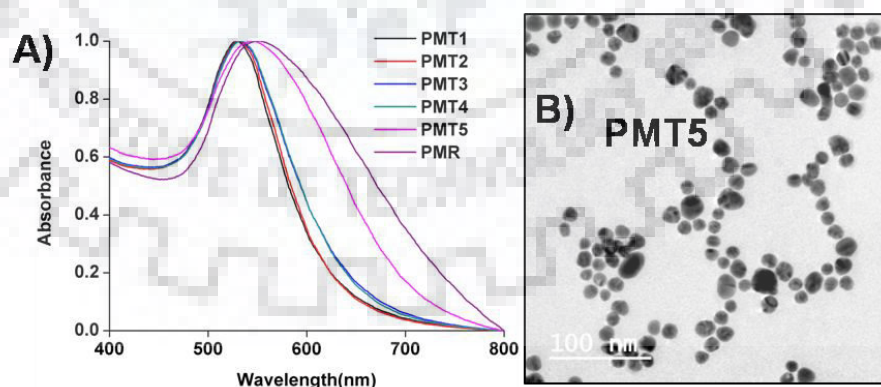
Figure 2.23 Normalized absorption spectra (A) of nanoparticle solutions synthesized with PMT1, PMT2, PMT3, PMT4, PMT5 and PMR; (B) Morphologies of gold nanoparticles from growth reactions after the treatment with PMT5.
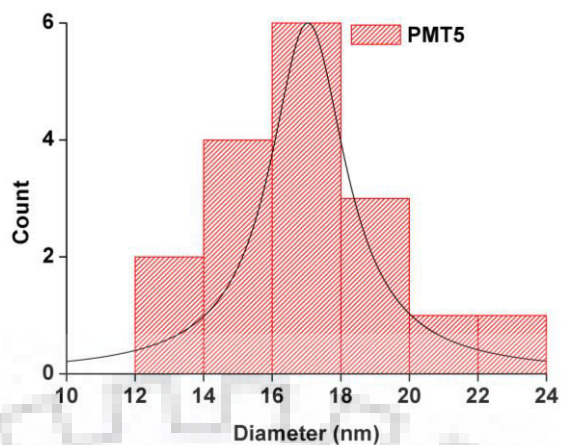
Figure 2.24 Size distribution histograms of gold nanoparticles synthesized with PMT5.
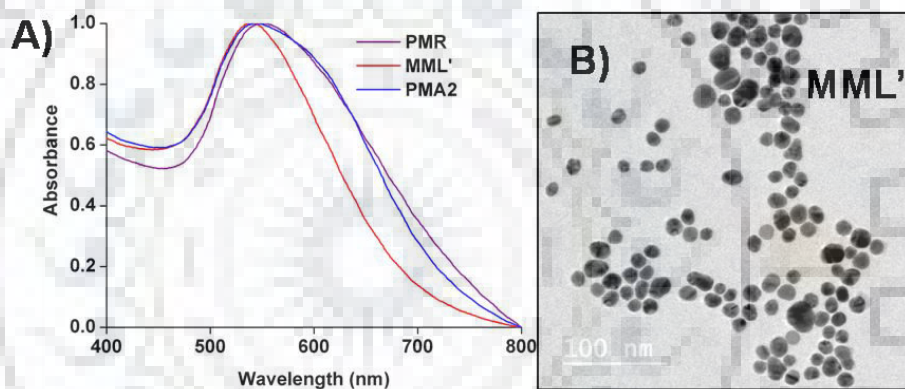
Figure 2.25 Normalized absorption spectra (A) of nanoparticle solutions synthesized with PMR, MML' and PMA2. (B) Morphologies of gold nanoparticles after growth reactions in presence of MML.
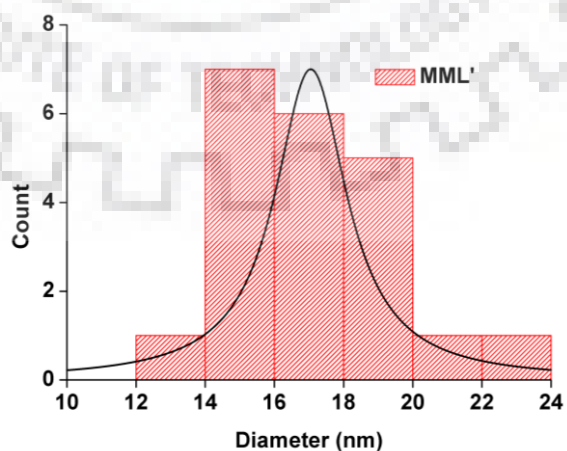
Figure 2.26 Size distribution histograms of gold nanoparticles synthesized with MML'.

2.4.8 Inevitability of amine functionalization at ACA Terminal

The necessities of amine functionalization in these sequences were checked via similar experiments with the sequence without any amine modification (No-Mod, 5'-ACATCAGT-3'), amine modification at 3' end (PMR',5'-ACATCAGT-3'-amine) and amine modification at both ends (Both-Mod, amine-5'-ACATCAGT-3'-amine). In all the cases the nucleic bases are common to that of PMR. Growth of nanoparticle in the presence of either No-Mod or PMR' sequences resulted in the development of purple color with absorption maxima at 541 nm and 539 nm respectively (Figure 2.27). In the case of Both-Mod sequence, absorption spectrum showed the maximum at 548 nm. However, the broadening was not that significant in comparison to the absorption spectrum in presence of PMR.
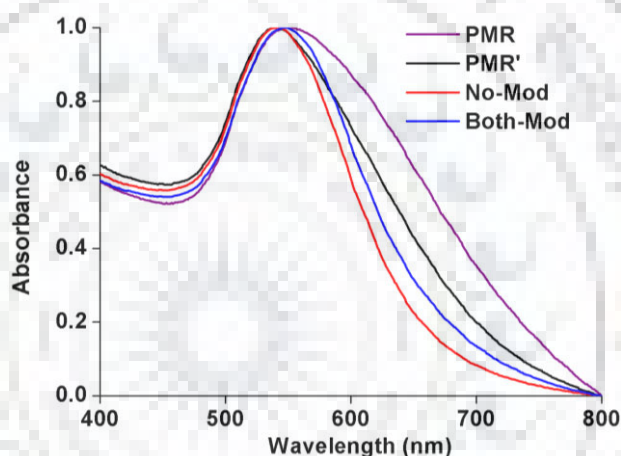
Figure 2.27 Normalized absorption spectra after growth reaction with the addition of PMR', No-Mod and Both-Mod to the seed solutions.

The morphology of the nanoparticles after the growth reactions was confirmed from the TEM images. TEM results suggested that among the three different possibilities explored, the formation of gold nanoflowers was observed only in the case of Both-Mod, where as spherical nanoparticles were observed in case of No-Mod and PMR'(Figure 2.28A–C). These results suggested that the inevitability of amine functionalization near the ACA sequence in PMR was responsible for the formation of the gold nanoflowers. The size distribution histograms of nanoparticles are shown in Figure 2.29. TEM analysis shows the average size of nanoflowers were 21±3.13 whereas spherical nanoparticles formed with PMR' and No-Mod have average size of 18±2.79 and 18±3.99 respectively. The percentage of nanoflowers formed was 90%.
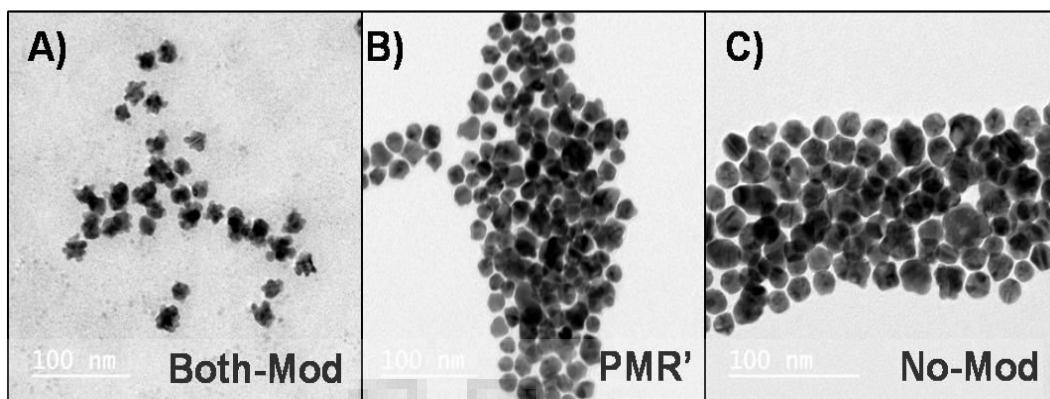
Figure 2.28 Morphologies of gold nanoparticles from growth reactions after the treatment of nanoseeds with Both-Mod (A), PMR'(C) and No-Mod (D) to the seed solutions.
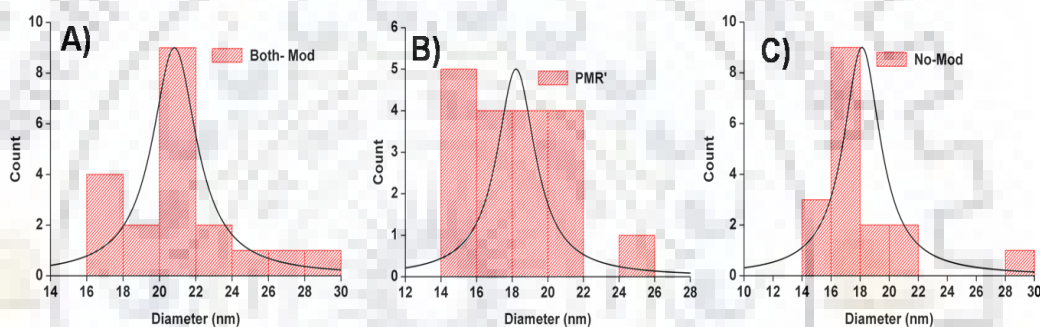
Figure 2.29 Size distribution histograms of gold nanoparticles after growth reaction in presence of PMR', No-Mod and Both-Mod.

2.4.9 Requirement of DNA length

The requirement of 8-mer sequences for the gold nanoflowers formation were confirmed by decreasing the length of PMR up to 3 mer. (PM3, amine–5'–ACA–3'; PM4, amine–5'–ACAT–3'; PM5, amine–5'–ACATC–3'; PM6, amine–5'–ACATCA–3'; PM7, amine–5'–ACATCAG–3'). The growth reactions in presence of 3–mer to 7–mer sequences were done and absorption studies confirmed the requirement of 8–mer sequence for gold nanoflower formation. A slight shift occurred in absorption maxima with increasing the length of DNA sequence upto 7–mer (Figure 2.30).
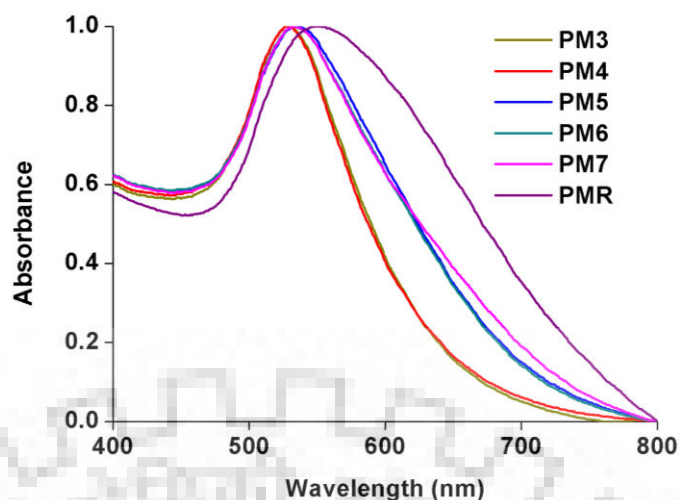
Figure 2.30 Normalized absorption spectra of nanoparticle solutions synthesized withPM3, PM4, PM5, PM6, PM7 and PMR.

2.4.10 Variation of DNA and gold

In another experiment, the PMR concentration was lowered in presence of constant amounts of seed, NH_2OH and $HAuCl_4$ to observe the change in absorption spectra for gold nanoflower formation. With increasing the amount of PMR, 65 nM to 650 nM a red shift and broadening was observed in the SPR peak (Figure 2.31) which ultimately led to the formation of nanoflower. The lower concentration of PMR led to spherical nanoparticles formation.
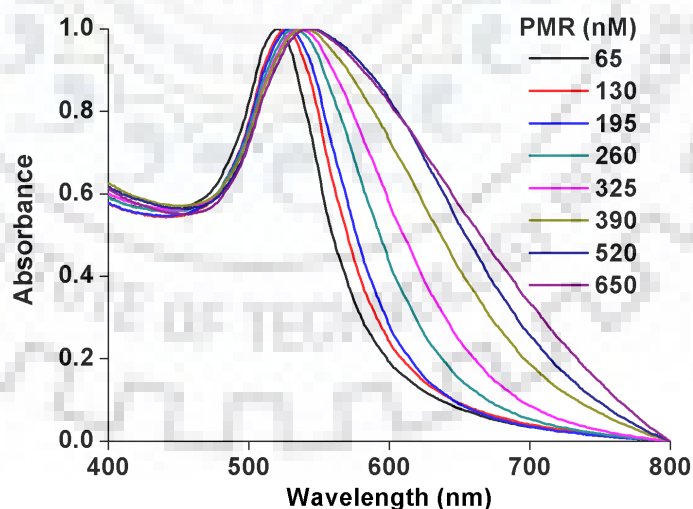
Figure 2.31 Normalized absorption spectra of nanoparticle solutions synthesized with decreasing concentration of PMR.
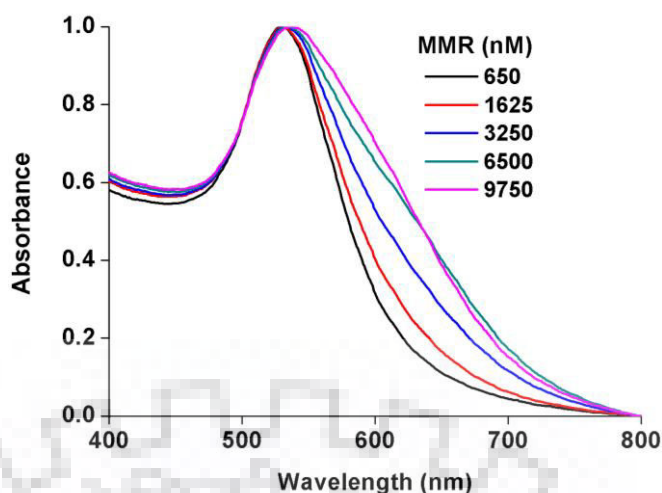
Figure 2.32 Normalized absorption spectra of nanoparticle solutions synthesized with increasing concentration of MMR.

Increasing the MMR concentration under similar conditions did not show any shift in SPR peak only broadening was observed (Figure 2.32). The MMR concentration was increased from 650 nM to 9750 nM. To provide further insight of gold nanoflower formation by PMR, varied amounts of $HAuCl_4$ was added to the mixture of PMR, incubated with gold nanoseeds and NH_2OH. Absorption studies (Figure 2.33) showed the red shift in the SPR peak with broadening and enhancement in intensity with increasing concentration of $HAuCl_4$. This process suggested the continuous development of gold nanoflowers from the spherical gold nanoparticle seed. However, no significant shift was observed in the case of MMR treatment with increasing the concentration of gold (Figure 2.34).
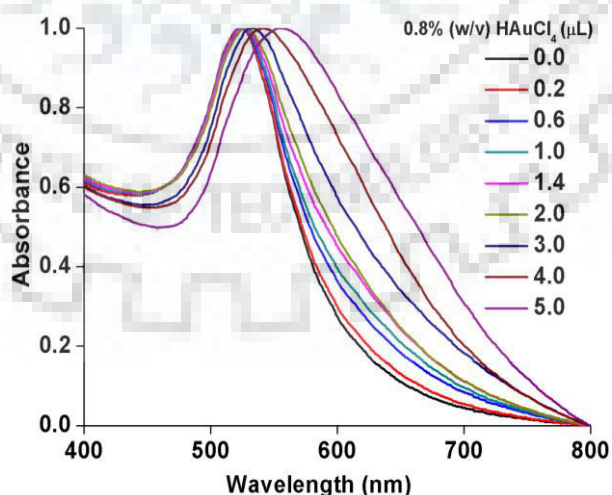
Figure 2.33 Normalized absorption spectra of PMR based growth solutions synthesized by increasing the amount of 0.8% (w/v) $HAuCl_4$.
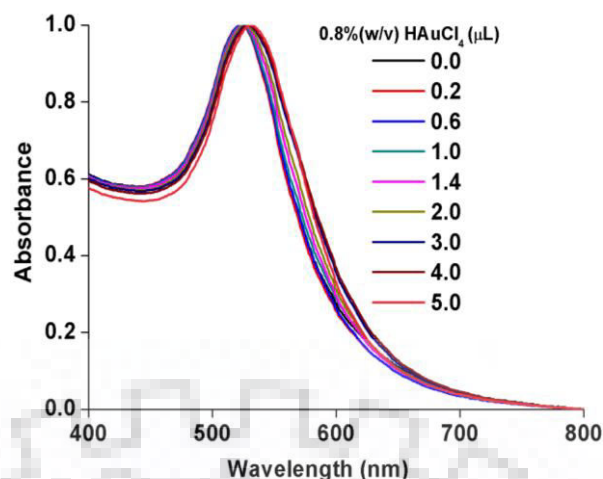
Figure 2.34 Normalized absorption spectra of MMR based growth solutions synthesized by increasing the amount of 0.8% (w/v) HAuCl₄.

2.4.11 Stability of nanosolutions

The stability of the synthesized gold nanosphere and nanoflower solutions were checked with 0.1M NaCl treatment. Gold nanoseeds were incubated with different DNA and the growth reactions were performed. After that 0.1 M NaCl solution was added and the aggregations of these nanoparticles were monitored by absorption studies (Figures 2.35 and 2.36). Aggregation takes place rapidly in case when no DNA, PML, MMR and MML were used for growth reactions. This is depicted by decrease in the intensity of absorption peak and appearance of dual peak in case of no DNA after salt treatment. For PMR based reactions light decrease in the absorption peak was observed after salt treatment suggesting a stable structure in solution (Figures 2.35).
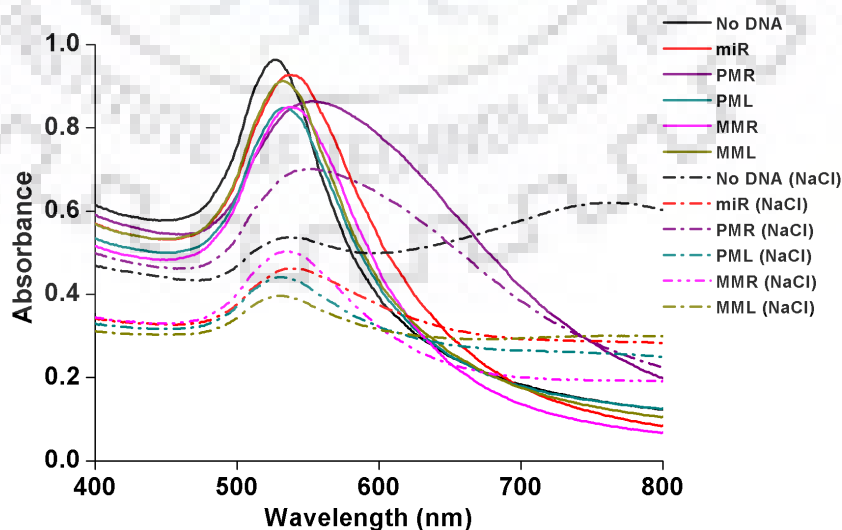
Figure 2.35 Absorption spectra of nanoparticle solutions with or without addition of NaCl (0.1M).
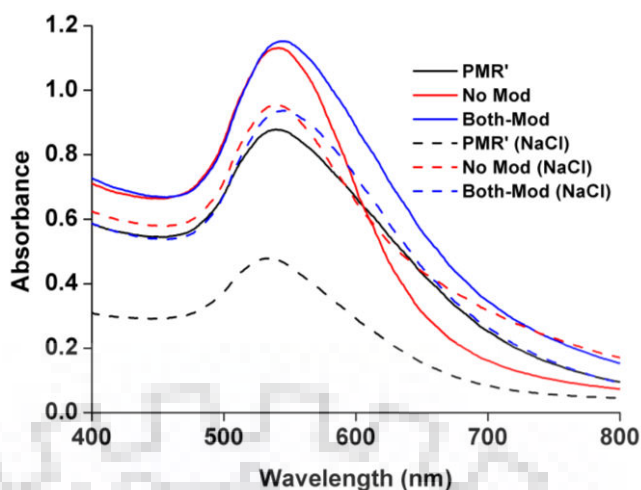
Figure 2.36 Absorption spectra of nanoparticle solutions with or without addition of NaCl (0.1M).

Similar results as of PMR were also observed for the gold nanosolutions synthesized with PMR', No-Mod and Both-Mod. In these cases, the common nucleic base sequence added to the gold surface prevented the aggregation (Figures 2.36). These results also conclude that the PMR and the related sequences have higher binding affinity to the gold nanosurface and resulted in the formation of stable structures which prevented the aggregation.

2.4.12 Apparent association constant

The adsorption affinity of the DNAs to the gold nanoparticle surface was further confirmed by calculating the apparent binding constant. The values suggested that the PMR has a very high binding affinity to the gold surface and apparent association constant was found to be 28 mM^{-1}. The apparent association constants for PML, MMR and MML sequences to the seed surface was calculated and values obtained were 7.5 mM^{-1}, 7.78 mM^{-1}and 7.0 mM^{-1} respectively (Figure 2.37).These values are much less compared to the value obtained from PMR. The results suggested that because of high binding affinity of PMR to gold nanoseeds resulted in the shape transformation of spherical gold nanoseeds to nanoflowers. The other three sequences have less binding affinity and restricted the formation of gold nanoflower after the growth reaction. The apparent constant value of PMR' No Mod, PMA, and PMG, were calculated to be 18.42 mM^{-1}, 14.81 mM^{-1}, 36.77 mM^{-1} and 25 mM^{-1}(Figure 2.38). The results also suggested that high adsorption affinity sequences resulted in the formation of nanoflowers where as low adsorption affinity sequences did not produce any shape transformation. The apparent association constant values of all DNAs are mentioned in Table 2.2. Similarly the apparent association constants of PMT and PMT5 were calculated and obtained values were 14.63 mM^{-1} and 21.05 mM^{-1} respectively (Figure 2.39).
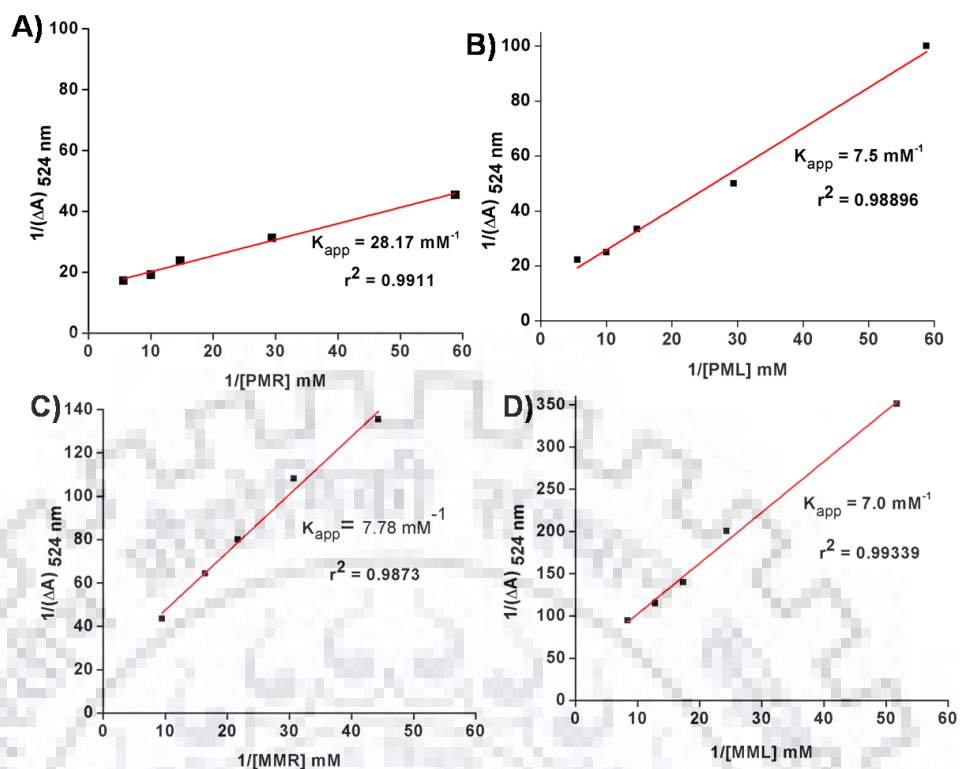
Figure 2.37 Apparent association constants for PMR (A), PML (B), MMR(C) and MML (D) with gold nanoparticle seed.
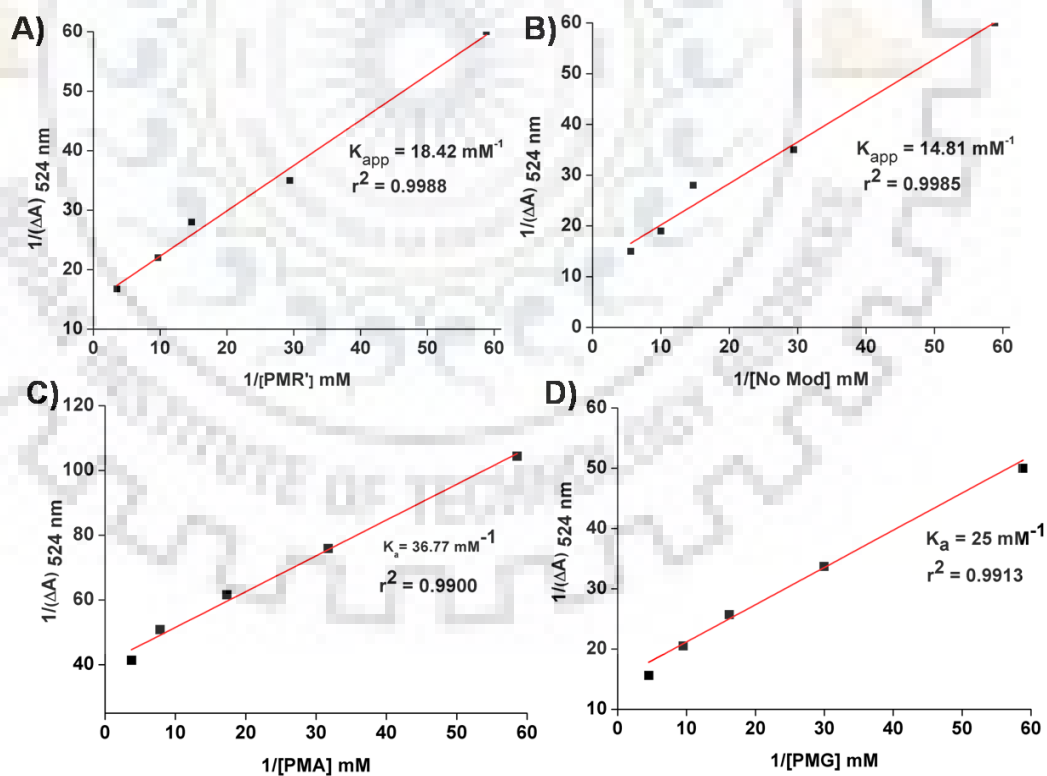
Figure 2.38 Apparent association constant for PMR' (A), No Mod (B), PMA (C) and PMG (D) with gold nanoparticle seed.
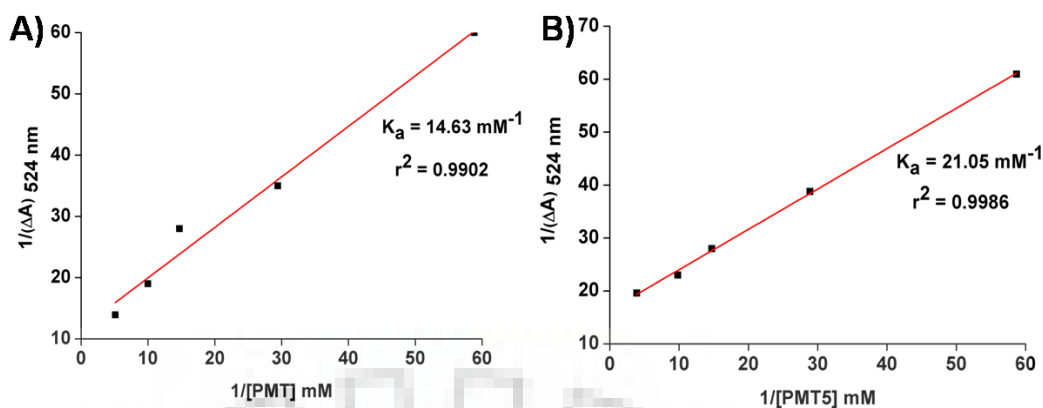
Figure 2.39 Apparent association constant for PMT (A) and PMT5 (B) with gold nanoparticle seed.

Table 2.2: Binding affinity constants of DNAs with gold nanoparticle seed

S. No	Name	Binding constant (mM^{-1})with gold AuNP seed (No reduction)
1	No DNA	-
2	PMR	28.2
3	PML	7.5
4	MMR	7.7
5	MML	5.0
6	PMR'	18.4
7	No mod	14.8
8	Both -Mod	31.8
9	PMA	36.8
10	PMT	14.6
11	PMG	25.0
12	PM3	17.4
13	PM4	18.9
14	PM5	20.5
15	PM6	21.5
16	PM7	22.9
17	PMRT1	6.5
18	PMRT2	3.8
19	PMRT3	10.7
20	PMRT4	8.8
21	PMT5	21.1
22	PMA2	35.8
23	MML'	24.7

2.4.12 DLS measurements

The size and zeta potential of the nanoparticles after growth reaction were confirmed from the DLS measurements. The size of the nanoparticles ranged within the limit of 17−26 nm and the maximum size were obtained with nanoflower architectures (Figures 2.40 and Table 2.3). The DLS measurement, which is suitable for spherical nanoparticles, shows the hydrodynamic diameters (Table 2.3) of the growth based spherical nanoparticles are comparable to that of TEM images. However, in the case of nanoflower, the hydrodynamic diameters are slightly higher in comparison to their TEM data. The monodisperity values increased for nanoflowers architectures or nanoparticles synthesized DNA containing common nucleobases as of PMR (Figures 2.41 and Table 2.3). The Surface charge (ζ-potentials), of the nanostructures, was restricted within a narrow limit for all the DNA sequences. These values were slightly more negative for the nanoflowers architectures (Figures 2.42 and Table 2.3).
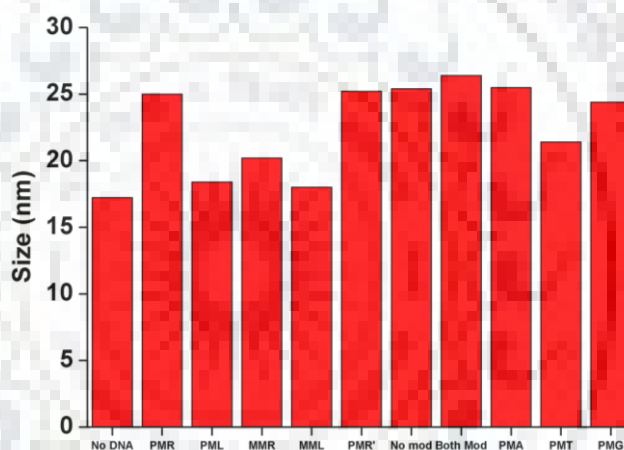
Figure 2.40 Size of gold nanoparticles after growth reaction synthesized in presence different DNAs.
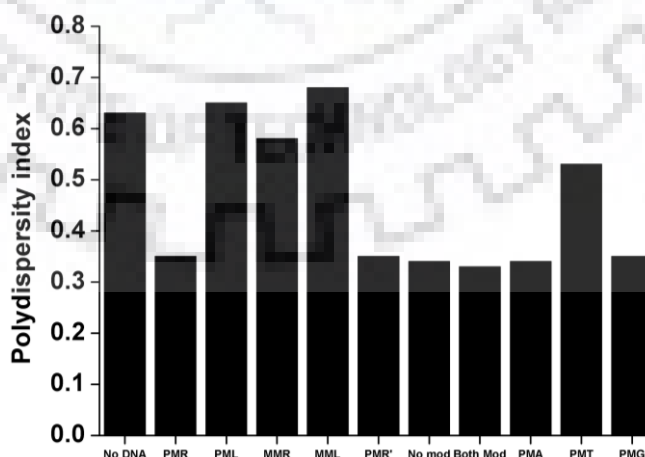
Figure 2.41 Polydispersity of gold nanoparticles after growth reaction synthesized in presence different DNAs.

71
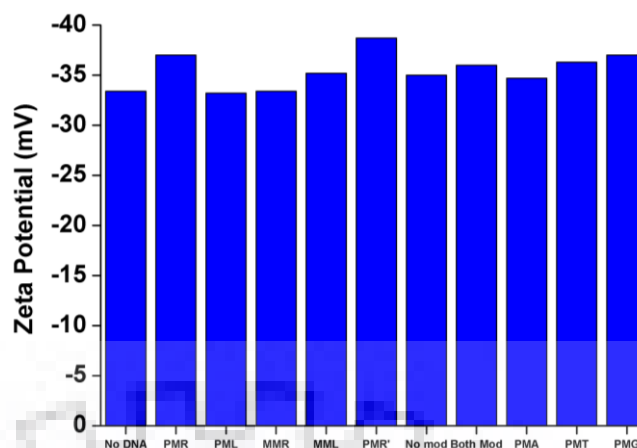
Figure 2.42 Zeta potential of gold nanoparticles after growth reaction synthesized in presence different DNAs.

2.4.13 Detection of DNA sequence for miRNA

The different nanostructures obtained from amine-modified 8-mer DNA based growth reactions were further employed for nanosensor studies. For this purpose, DNA sequence of miR-21, which is complementary for both PMR and PML were used. The hydroquinone based growth reactions with variable concentration of miR-21 DNA were performed separately with seeds like nanoflower and nanospheres, which were obtained from PMR and PML sequences respectively. The growth reaction in the presence of variable miR-21 resulted in sharp change in the maximum absorption wavelength (Figure 2.43) for the nanoflower seed.
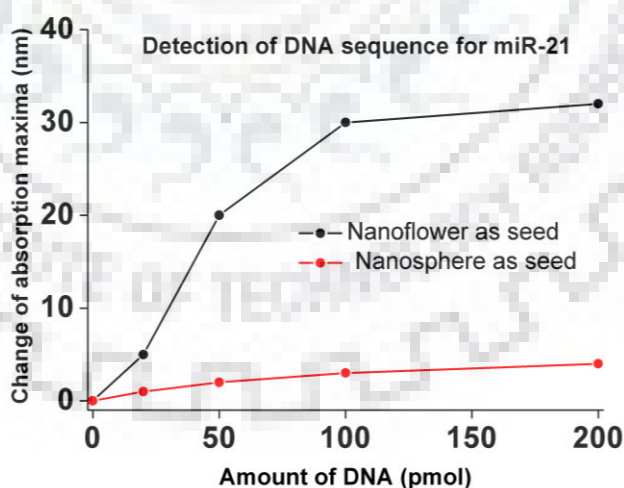
Figure 2.43 Change in the absorption maxima after growth reaction by concentration variation of DNA sequence for miR-21 in the presence of nanoflowers and nanospheres as seeds.

In the case of nanosphere seed, the growth reaction in presence of miR-21 DNA showed negligible shift under the similar experimental condition. The clear difference in the absorption

spectra with two different seed structures may be further extended to detection of miR-21 in biological samples.

Table 2.3: DLS measurements and Size of nanoparticles after growth reactions.

S. No	Name	Seed mediated growth by hydroxylamine reduction			
		Size* (nm)	ζ-Potential (mV)	PDI	Average Size** (nm)
1	No DNA	17.22	-33.4	0.63	15±1.8
2	PMR	25.0	-37.0	0.35	20±4.5
3	PML	18.40	-33.2	0.65	18±4.8
4	MMR	20.20	-33.4	0.58	19±4.8
5	MML	18.0	-35.2	0.68	20±4.04
6	PMR'	25.20	-38.7	0.35	18±2.79
7	No mod	25.40	-35.0	0.34	18±3.99
8	Both-Mod	26.40	-36.0	0.33	21±3.13
9	PMA	25.50	-34.7	0.34	24±3.58
10	PMT	20.40	-36.30	0.53	15±1.89
11	PMG	24.40	-37.0	0.35	25±4.61
12	PM3	20.0	-31.4	0.49	nd
13	PM4	20.70	-35.4	0.49	nd
14	PM5	22.50	-37.1	0.50	nd
15	PM6	23.0	-37.1	0.50	nd
16	PM7	23.30	-37.1	0.43	nd
17	PMT1	21.80	-32.6	0.49	nd
18	PMT2	21.30	-32.8	0.55	nd
19	PMT3	22.0	-33.0	0.55	nd
20	PMT4	22.0	-33.8	0.56	nd
21	PMT5	20.70	-36.2	0.43	17±2.69
22	PMA2	26.0	-32.0	0.47	nd
23	MML'	22.60	-34.3	0.45	17±3.2

* Size is hydrodynamic diameter of the nanoparticles

** Average size were obtained from the TEM analysis

2.5 CONCLUSION

In conclusion role of seed and reducing agents were established for the growth-mediated nanoflower formation with amine-modified DNAs. The variation of seed for hydroxylamine based reduction showed the formation of nanoflowers through the affinity of nucleobases. The growth-mediated formation of the nanoflowers confirmed the necessities of amine modification and affinity-based sequence at the same terminal of single-strand DNA. The nanoflowers were employed for the detection of DNA sequence of miRNA.

SECTION B

Preparation of metallic nanomaterials with a desirable shapes is of great interest and important in developing materials of nanobiotecnology.[322] Most of the unique properties of nanoparticles (NPs), like optical and catalytic properties, are derived from the NPs' morphologies, which include shape and surface characteristics.[323] Therefore many efforts have been put towards controlling the NP morphologies and to obtain methods that can control the morphology of NPs rationally and deliberately, is of significant challenge.[324] The role of ligands (halides or small molecules such as citrate and cetyltrimethylammonium bromide) have been investigated for controlling the NP morphologies[325,326] but despite the progress in this field it is still difficult to obtain the nanomaterials with systematic and prognostic morphologies.[327-329]

Bio molecules represent new structures employed for the fabrication, assembly, and subsequent use of nanomaterials for a variety of applications.[331-335] Sim *et al.* anchored DNA onto gold nanoseed with various alignments to form gold nanocrystals with defined topologies like pushpin- star- and biconcave disk-like structures, as well as more complex jellyfish and flower-like structures.[203] Peptoids have also been used for morphological evolution from spherical to highly branched coral shaped nanoparticles.[208] Lee's group have synthesized helicoid shaped chiral gold nanoparticles from amino acids to control the optical activity, handedness and chiral plasmonic resonance of the nanoparticles. The chiral molecules were added to the pre synthesized low indexed planes and get evolved into the high indexed nanoparticles.[209]. Dasgupta *et al*. also synthesized chiral gold nanoparticles with amino acids and showed surface chirality can affect the fibrillation of human serum albumin (HSA).[336] They have also shown the effect of silica nanoparticles on the amyloid fibrillation of lysozyme.[337] The present work describes the selective formation of coral shaped nanomaterials with methionine.

2.6 EXPERIMENTAL SECTION

2.6.1 Chemicals and Materials

All the reagent grade materials used unless specified were discussed in previous section of this chapter. L-aminoacids, glutathione oxidised, glutathione reduced, sodium thiosulfate, sodium sulphate and modified nucleic base [Ethyl-4-amino-2-(methylthio)-pyrimidin-5-carboxylatethioether] were purchased from Himedia Laboratories pvt. Ltd.

6- mercaptohexanoic acid, 3-mercaptopropionic acid, and $\alpha-$Lipoic acid were purchased from Sigma Aldrich. All solutions were prepared in millipore water. Aspartic acid, glutamic acid tyrosine and cysteine were prepared in 1N HCl. Stock solution of thioether modified nucleic base was prepared in DMSO. Lipoic acid was prepared in mixture of 1:1 ethanol water.

2.6.2 Instrumentation

Absorption spectroscopy, TEM and DLS measurements were done as described in earlier section of this chapter. Image J software was used to calculate the average size of nanoparticles on TEM images.

2.7 Synthetic Procedures

Synthesis of seed stock solution

The seed solution was prepared as previously mentioned in this chapter. The final volume of all the reactions was maintained at 340 µL. The nanoparticle concentration was calculated as previously mentioned.

Growth reactions of gold nanoparticles with amino acids at 9 mM

0.45 nM gold nanoparticles seed solutions were incubated with 9 mM of twenty different natural amino acids separately for 30 minutes. 3 µL, 200 mM NH_2OH (adjusted to pH 5 with NaOH) was added to these solutions and stirred vigorously for 10 minutes. 5 µL of 0.8% (w/v) $HAuCl_4$ was added to these solutions to initiate the reduction reaction. The colour change was observed within seconds.

Reaction with other molecules containing sulphur

0.45 nM gold nanoparticles seed solutions were incubated with 9 mM (glutathione oxidised, glutathione reduced, Sodium thiosulfate and sodium sulphate, 6−mercaptohexanoic acid, 3−mercaptopropionic acid Ethyl−4−amino−2− (methylthio)−pyrimidin-5-carboxylate, and Lipoic acid) for 30 minutes. 3 µL, 200 mM NH_2OH (adjusted to pH 5 with NaOH) was added to these solutions and stirred vigorously for 10 minutes. 5 µL of 0.8% (w/v) $HAuCl_4$ was added to these solutions to initiate the reduction reaction. The color change was observed within seconds.

Growth reactions of gold nanoparticles with amino acids at 50 µM

0.45 nM gold nanoparticles seed solutions were incubated with 50 µM amino acids for 30 minutes. 3 µL, 200 mM NH_2OH (adjusted to pH 5 with NaOH) was added to these solutions

and stirred vigorously for 10 minutes. 5 µL of 0.8% (w/v) HAuCl$_4$ was added to these solutions to initiate the reduction reaction. The colour change was observed within seconds.

Growth reactions of gold nanoparticles with different seed amount

Seed amounts ranging from 0.03 nM to 0.45 nM were incubated with 50 µM Arg, His and Met for 30 minutes. 3 µL, 200 mM NH$_2$OH (adjusted to pH 5 with NaOH) was added to these solutions and stirred vigorously for 10 minutes. 5 µL of 0.8% (w/v) HAuCl$_4$ was added to these solutions to initiate the reduction reaction. The color change was observed within seconds.

2.8 RESULTS AND DISCUSSION

2.8.1 Synthesis and characterization

Growth reactions of gold nanoseeds were performed by incubating with all natural amino acids for 30 minutes. Hydroxylamine as reducing agent was added and the reaction was vigorously shaken. HAuCl$_4$ was added to complete the reduction reaction and the colour change was observed within seconds.

2.8.2 Growth reaction with 9mM amino acid

The reaction mixture containing Asp, Glu, Cys and Tyr showed the instantaneous precipitation after the growth reaction. Arg, His, Ser, Phe, Met and Trp show blue color solution after the growth reaction and red color solutions were obtained for the Lys, Thr, Asn, Gln, Gly, Pro, Ala, Val, Ile and Leu (Scheme 2.2).
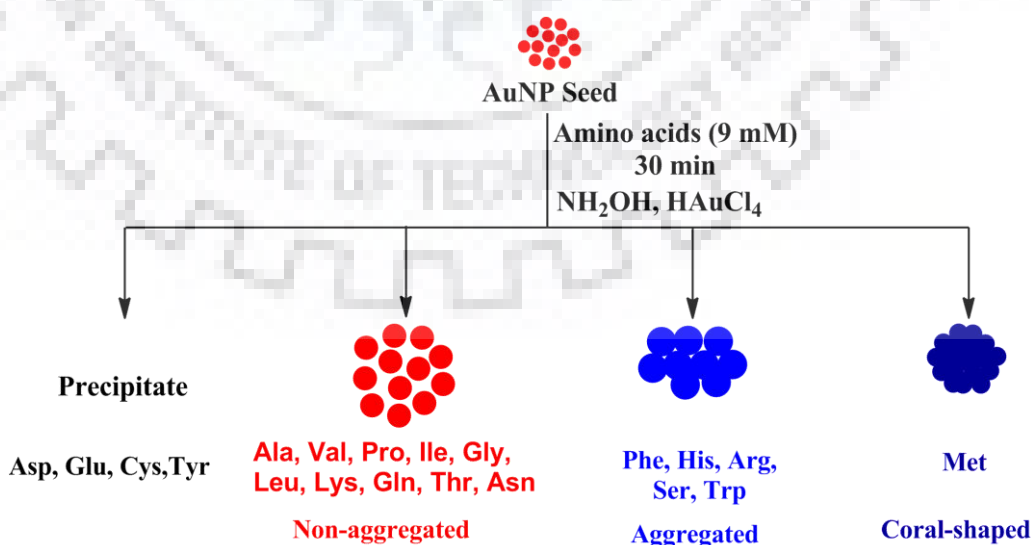
Scheme 2.2 Scheme for L-amino acid (9 mM) based growth reactions to form instantaneous precipitation, aggregated and non-aggregated gold nanoparticles.

The growth reactions with different amino acids were further characterized by absorption spectroscopy, TEM and DLS measurements.

The precipitated solutions did not develop any peak in absorption spectra (Figure 2.44).The absorption spectrum of the blue colored solutions showed the dual peak and the nature of the peaks were different in each case.(Figure 2.45) with Ser the peak was more red shifted whereas with Arg and His the peaks were broad. The red colored solutions showed single peak in absorption spectrum and the absorption maxima ranges between 530 nm to 540 nm(Figure 2.46).
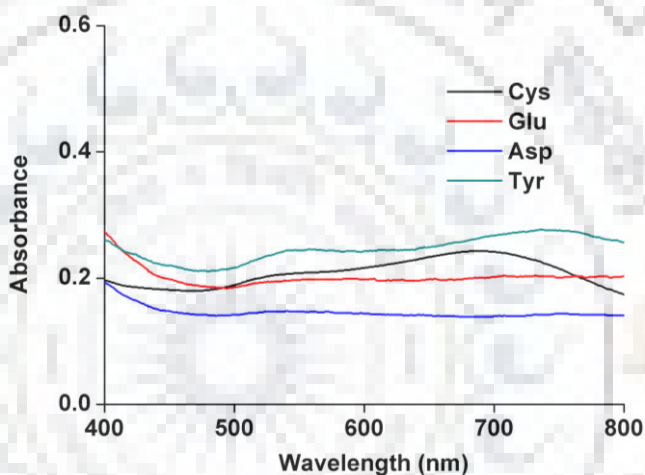
Figure 2.44 Absorption spectra of solutions contained precipitate after growth reactions in presence of Cys, Glu, Asp and Tyr.
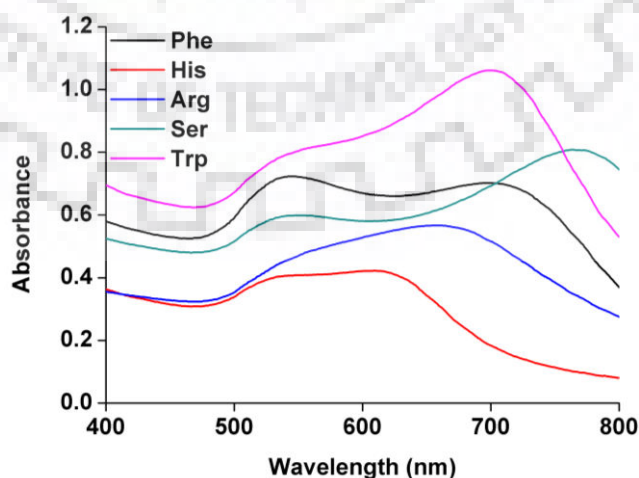
Figure 2.45 Absorption spectra of solutions after growth reactions in presence of Phe, His, Arg, Ser and Trp.
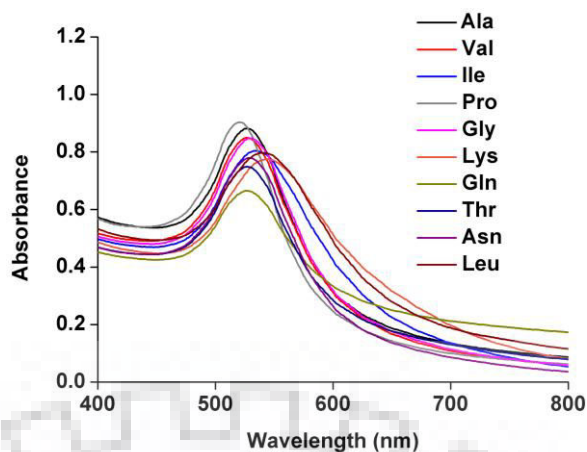
Figure 2.46 Absorption spectra of solutions after growth reactions in presence of Ala, Val, Ile, Pro, Gly, Lys, Gln, Thr, Asn and Leu.

The morphology of the nanoparticles after growth reaction in presence of different amino acids was confirmed from the TEM images. Among the five blue solutions Arg, His, Ser and Phe developed aggregates (Figure 2.47) while Met resulted in the formation of coral shaped nanoparticles (Figure 2.48). The red solutions with single absorption peak for Asn, Leu, Lys and Gln showed non aggregated nanoparticles (Figure 2.49).
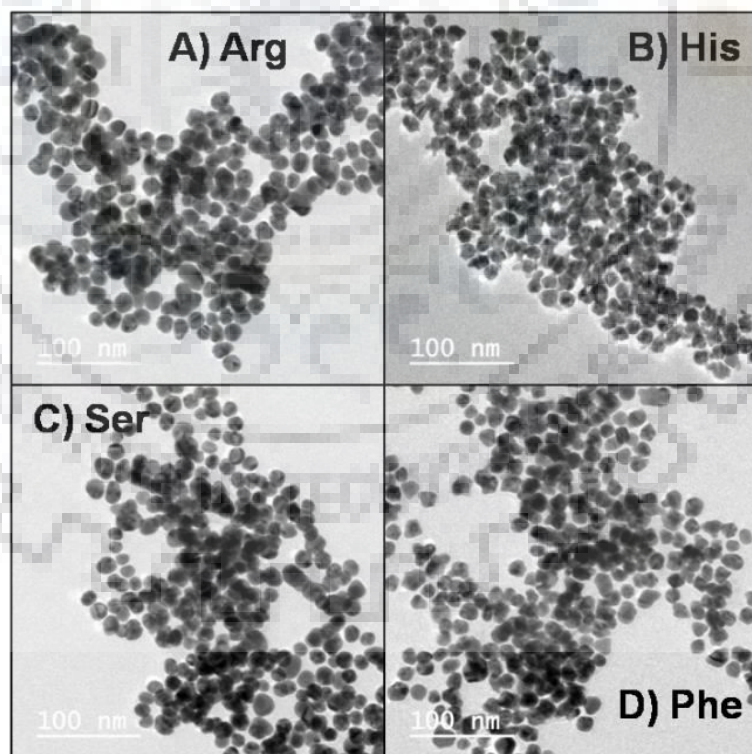
Figure 2.47 TEM images of aggregated gold nanoparticle after growth reaction in presence of A) Arg, B) His, C) Ser and (D) Phe.
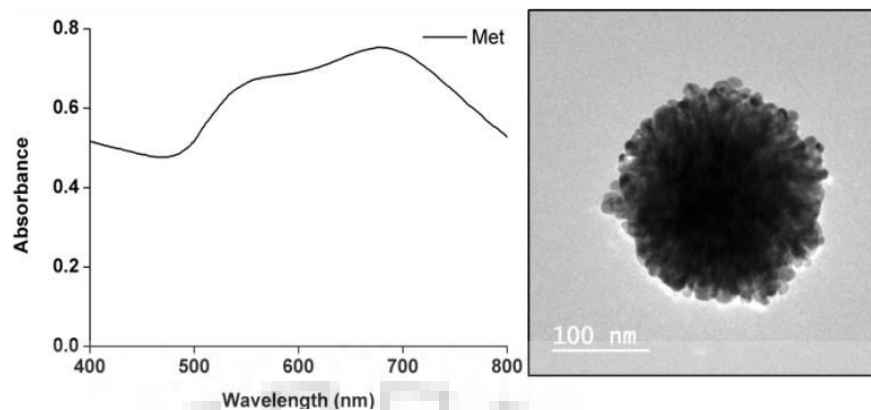
Figure 2.48 Absorption spectrum (left) and TEM images coral shaped nanoparticles formed after growth reaction in presence of Met.
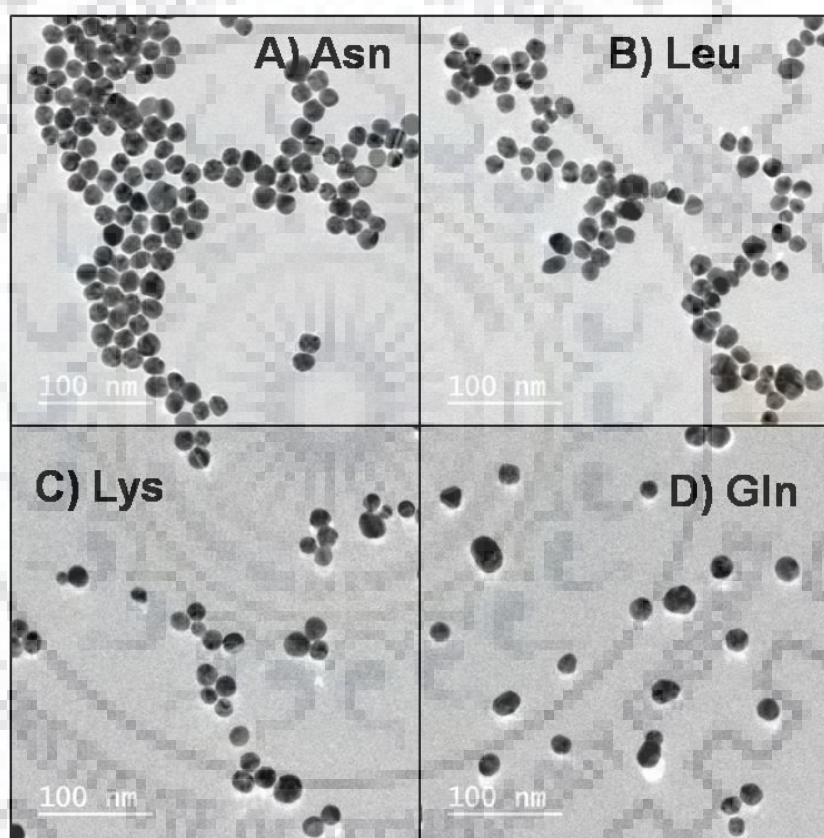
Figure 2.49 TEM images of non- aggregated gold nanoparticle after growth reaction in presence of A) Asn B) Leu, C) Lys and (D) Gln.

The size distribution histograms of the non-aggregated solutions are shown in Figure 2.50. The average size of the nanoparticles were found to be 20±3.58 nm, 20±1.9 nm, 20±2.37 nm and 25±6.3 nm synthesized in presence of Asn, Lys, Leu and Glu.
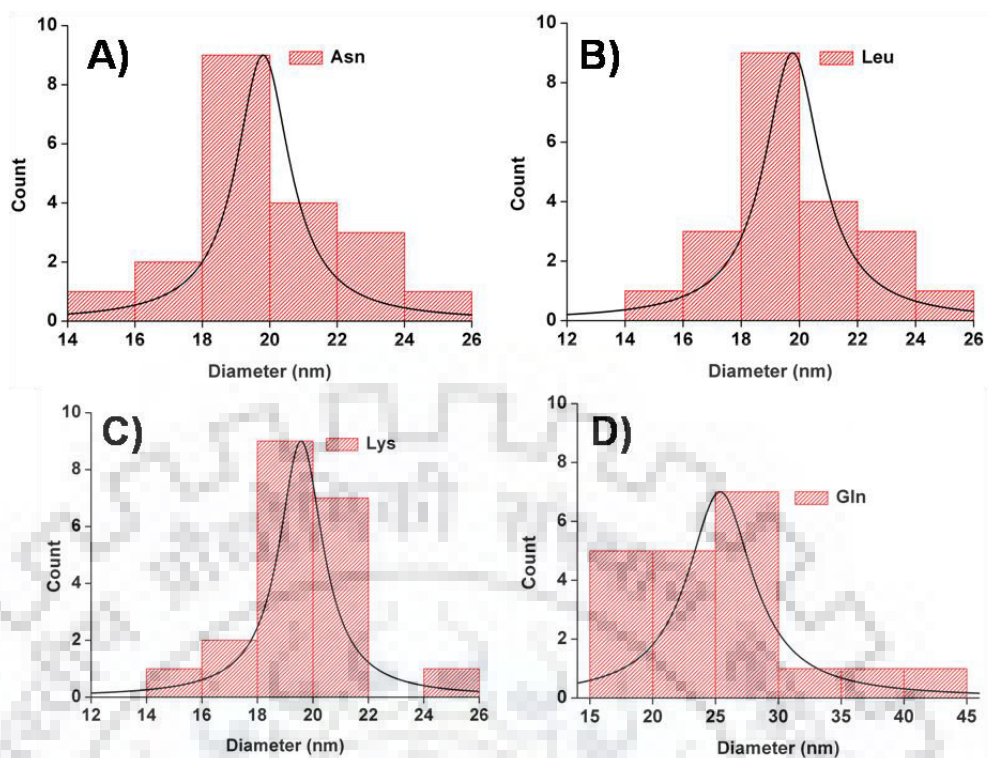
Figure 2.50 Size distribution of non- aggregated gold nanoparticle synthesized in presence of A) Asn B) Leu, C) Lys and (D) Gln.

The different binding energy, diffusion rates and packing characteristics of the ligands near the nanoparticle surface influences the final morphology to the nanoparticles during syntheses. For example thiols favour the growth of smaller size gold nanoparticles ranging from 1 to 10 nm.[330] weakly interacting ligands like citrate ions allows growth of colloidal particles ranging from 2 nm to 100 nm or beyond.[50] Amphiphilic ligands like CTAB acts as a stabilizing agent and shape directing agent because of differential adsorption to gold facets driving the growth to different anisotropic nanomaterials like gold nanorods, cubes and stars. According to the Derjagin- Landue and Verwey-Overbeek the colloidal stability of the gold nanoparticles is governed by the balance of the electrostatic repulsion against the van der Waals attraction between particles.[338] The zeta potential on the nanoparticle surface, established at the time of the nanoparticle synthesis by anionic citrate and citrate oxidation products electrostastically adsorbed on the nanoparticle surface is indicative of the electrostatic repulsion between nanoparticles that is required for the stability of the colloidal gold. Processes that reduce the absolute value of the zeta potential tend to result in nanoparticle aggregation. [339] Ala addition to the nanoparticle solution induces the slight red shift in the SPR peak. Ala amine group is able to bind to the gold nanoparticle surface replacing the weakly bound citrate molecules and carboxylic group protruding outside provides the colloidal stability to the nanoparticles without affecting the zeta potential.[213] This implicates that the terminal

carboxylic group on Ala as inhibitory to aggregation, by providing anionic surface after amine mediated replacement of citrate molecules. Val, Ile, Pro, and Gly also behave similar to Arg as they also have one carboxylic group which provides colloidal stability to the gold nanoparticles. All these amino acids have side chain that is neutral towards gold. Asp and Gln has amide group on their side chain that can interact with gold nanoparticles through nitrogen atom. In Asn and Gln due to tautomeric process the amine as well as imine groups competes for replacement of citrate molecules demonstrates no aggregation was seen. Ser and Thr has hydroxyl group in their side chain and their uptake on the surface of GNP occurs via this OH group. However the nature of interactions is different Ser has primary hydroxyl group whereas Thr has secondary hydroxyl group. Ser resulted in the aggregation by zwitterions interactions between adjacent amino acids. Lys side chain is a primary amine capable of binding to the gold nanoparticle surface but it has been shown that Lys addition at neutral pH does not really affect the Zeta potential,[213] hence no aggregation is observed after the reduction process. A linear assembly of gold nanoparticles was synthesized in presence of Arg, where Arg was able to weakly bind to a Au(111) surface via interactions with the guanidinium group of the side chain.[206] Arg is structurally similar to the Lys; its guanidium group has a pKa value of 12.10 which binds to the nanoparticle surface and the zwitterionic electrostatic interactions between the positively charged amine and negatively charged carboxylic acids placed in close proximity comes into existence and the naoparticles aggregates occurs. His side chain has a pKa value of 6.04 and can interact with the gold nanoparticle surface either by the imidazole ring where it can induce aggregations. Addition of Cys to the gold nanoparticles results in the aggregation due to formation of strong covalent bond with gold surface. The aggregation resulted from the inter nanoparticles bridges due to H- bonding of amine group on one nanoparticle surface with carboxylate group on another nanoparticle surface.[214] Phe has hydrophobic aromatic ring that interacts with the gold surface via π-metal intercalation and leads to aggregation. Glu, Asp and Tyr were not dissolved in acidic medium that caused precipitation of nanoparticles.

2.8.3 DLS measurements

The aggregation of the nanoparticles was further confirmed by measuring the size of the nanoparticles. Aggregated solution showed huge increase in the size than that of non-aggregated (Figure 2.51, Table 2.4).
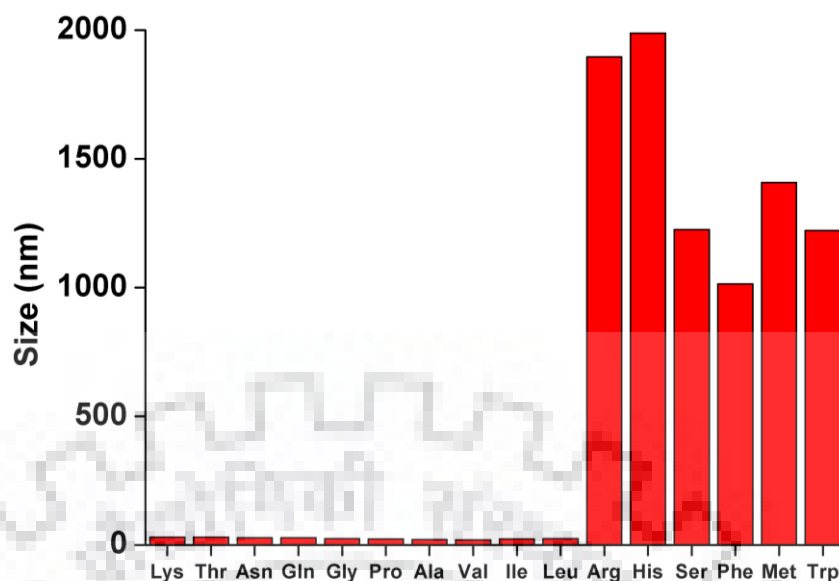
Figure 2.51 Size of gold nanoparticles after growth reaction synthesized in presence different amino acids at concentration of 9 mM.

The polydispersity values of red solutions remained almost constant except Ala and Val which showed increase in monodispersity. In case of blue solutions His showed increase in polydispersity whereas for Met and Trp monodispersity increased after growth reaction (Figure 2.52, Table 2.4). The zeta potential of nanoparticles remained almost same. However, Met incubated nanoparticles developed positive value probably due to some favourable interaction between thio ether functional group and gold nanoparticles (Figure 2.53, Table 2.4).
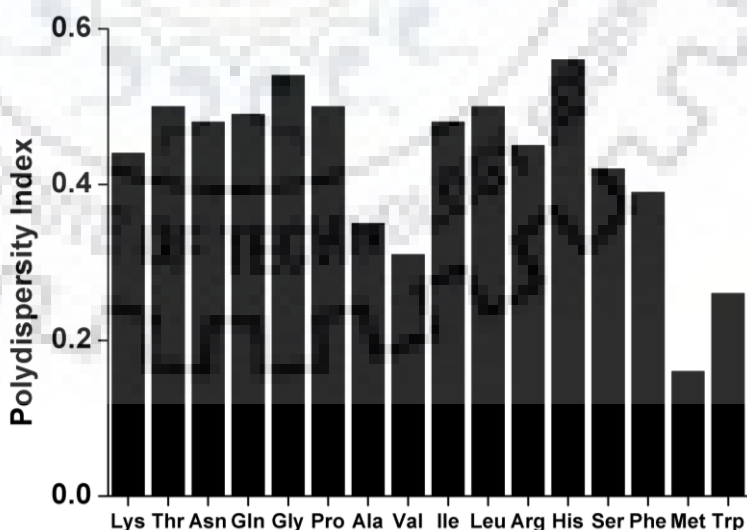
Figure 2.52 Polydispersity of nanosolutions after growth reaction synthesized with different amino acids.

Table 2.4: Size, Zeta potential and PDI values of nanoparticles measured after growth reactions.

Amino acid	Seed mediated growth by hydroxylamine reduction			
	Size* (nm)	ζ-Potential (mV)	PDI	Average Size ** (nm)
Lys	30.6	-28.6	0.44	20±1.9
Thr	30.0	-27.6	0.5	nd
Asn	28.2	-26.1	0.48	20±5.23
Gln	28.0	-28.9	0.49	25±6.3
Gly	24.0	-27.0	0.54	nd
Pro	23.0	-25.6	0.50	nd
Ala	20.6	-26.4	0.35	nd
Val	19.6	-27.0	0.31	nd
Ile	23.0	-27.0	0.48	nd
Leu	24.0	-30.2	0.50	20±2.37
Arg	1897	-22.8	0.45	nd
His	1989	-37.0	0.56	nd
Ser	1225	-20.8	0.42	nd
Phe	1015	-22.6	0.39	nd
Met	1408	3.26	0.16	nd
Trp	1221	-21.0	0.26	nd

*Size is the hydrodynamic diameter

**Average size determined from TEM images
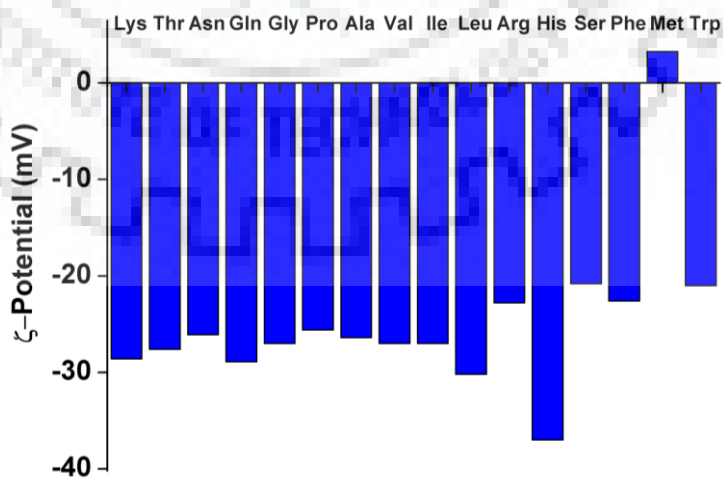
Figure 2.53 Zeta potential of nanoparticles after growth reaction synthesized with different amino acids.

2.8.4 Time dependent absorption for Met

To provide further insight to the coral formation, absorbance studies were performed by decreasing the incubation time for Met. With decreasing the incubation time the absorption spectra still showed the dual peak, however the absorption peak at 662 nm got red shifted with increasing the incubation time of five minutes with respect to zero minute. The absorption spectra did not show any shift with further increase in the incubation time (Figure 2.54).
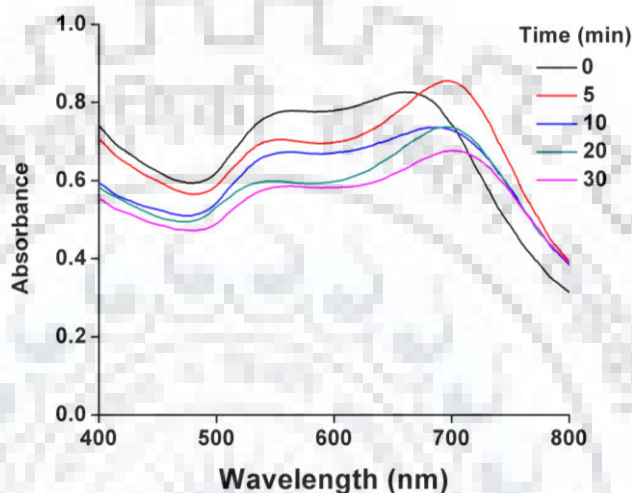
Figure 2.54 Absorption spectra of solutions after growth reactions prepared by incubated nanoseeds with Met for different time period.

TEM results of early stage suggested that the Met induced aggregation of nanoparticles to form small cluster like structures. The small clusters assemble randomly together into preorganised structure with irregular shaped structures and then finally grew into coral shape (Figure 2.55).
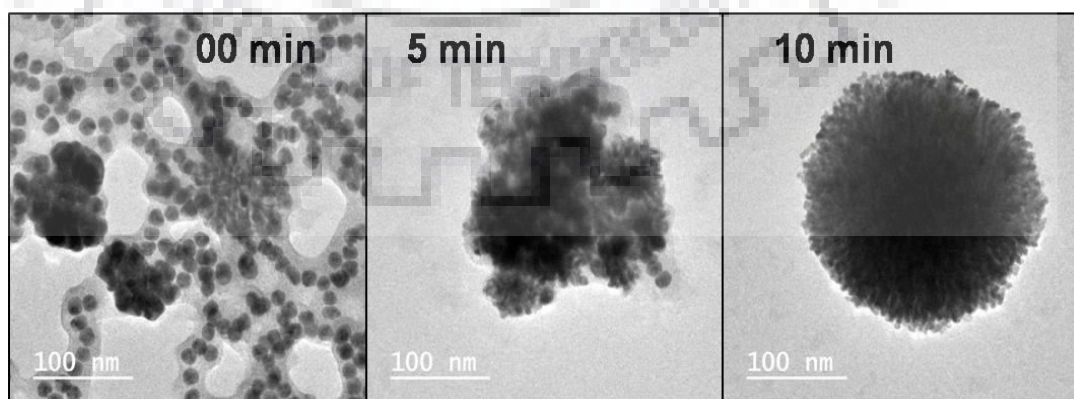
Figure 2.55 TEM images of intermediate nanostructures after growth reactions prepared by incubated nanoseeds with Met for different time period.

To understand the growth of coral formation UV-Vis analysis of the growth reaction were performed for 30 minutes. Absorption peak at 672 nm got red shifted with increase in intensity within 3 minutes. After that no shift was observed in the absorption spectra (Figure 2.56). The TEM results taken at different time intervals showed the size of the coral remained same. However the individual particle size increased with time (Figure 2.57).
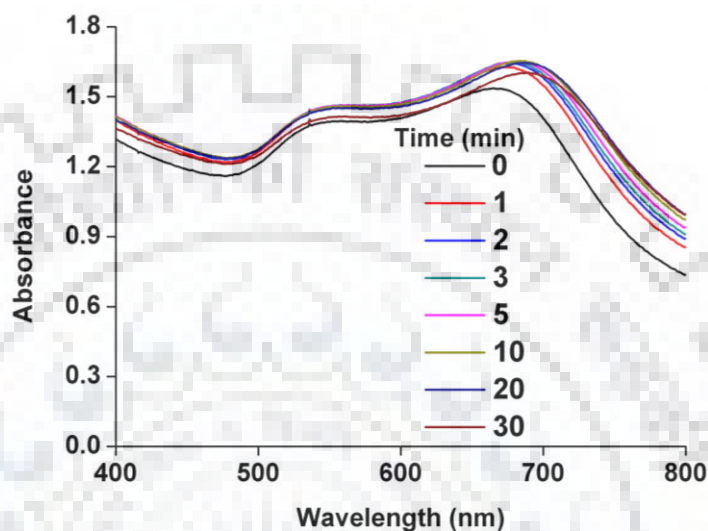
Figure 2.56 Time dependent absorbance data of coral growth prepared by incubated nanoseeds with Met for at different intervals of time.
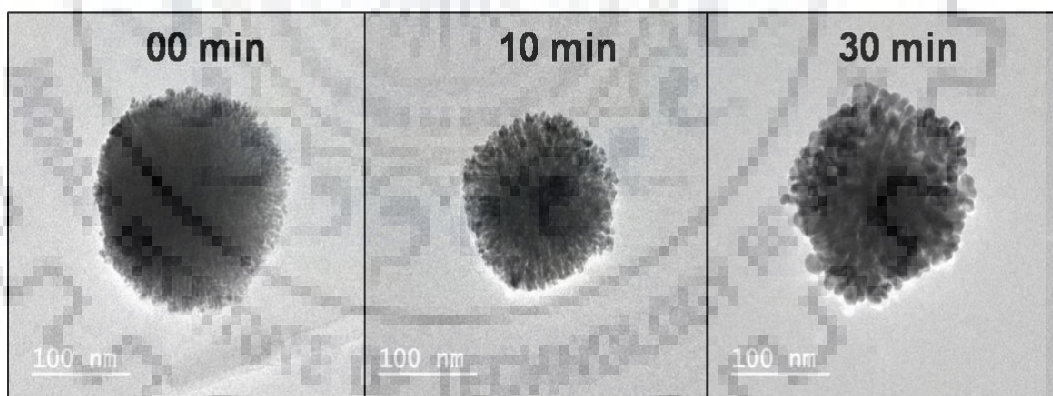
Figure 2.57 TEM images of nanostructures taken at 00 min, 10 min and 30 min after growth reaction.

2.8.5 Experiments with sulfur containing molecules.

In order to verify whether the coral formation is due to Met, control reactions were performed with bio molecules molecules like glutathione oxidized (GSSG) and glutathione reduced (GSH), organic aliphatic mercaptocompounds like 6–mercaptohexanoic acid, 3–mercaptopropionic acid, cyclic disulfide α–lipoic acid, cyclic thioether modified nucleic

base and inorganic salts like sodium sulphate and sodium thiosulfate. (Figure 2.58A, B). The solutions synthesized in presence of inorganic salts and α-lipoic acid were red in color (Figure 2.58A).where as solutions synthesized with glutathione oxidized and reduced forms were blue in color. 6– mercaptohexanoic acid and 3-mercaptopropionic acid developed precipitate. The absorption spectra showed single peak for red solutions whereas dual peak for blue colored solutions TEM images confirmed the formation of aggregated structures in case of glutathione oxidized (GSSG) and reduced (GSH) form while as non-aggregated spherical nanoparticles for lipoic acid (Figure 2.59A-C). Size distribution diagram of nanoparticles synthesized with lipoic acid are shown in Figure 2.60 and the average size calculated was 19±3.71 nm.
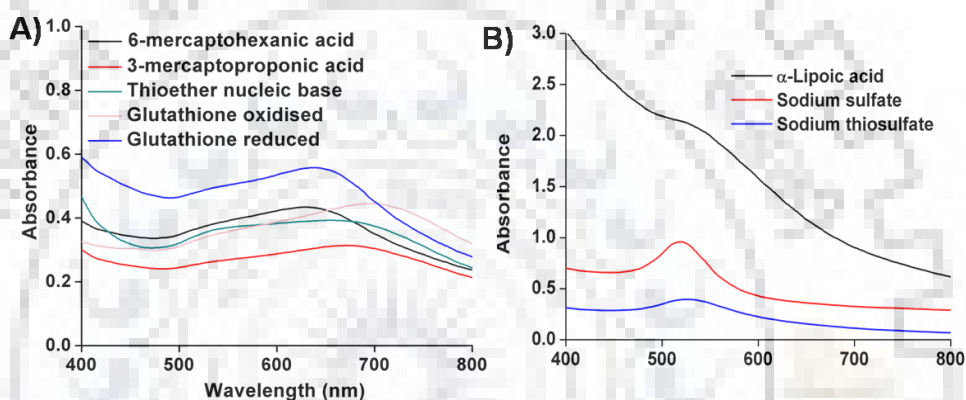
Figure 2.58 Absorption spectra of solutions after growth reactions prepared with different sulfur containing compounds.
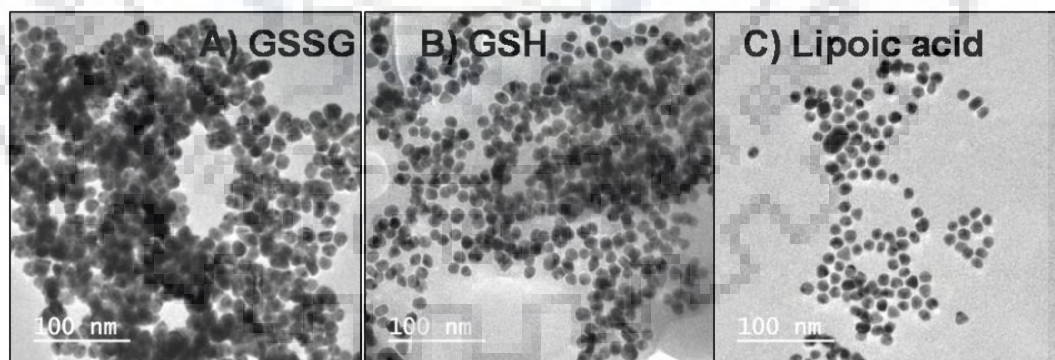
Figure 2.59 TEM images of nanoparticles after growth reaction synthesized with (A) Glutathione oxidised (B) Glutathione reduced and (c) α-Lipoic acid.

The presence of sulfur groups in these molecules allows them to covalently bind the gold nanoparticle surface change the zeta potential and can lead to aggregation of nanoparticles. It was also found that the molecules containing both thiol and amine group

promote the aggregation of nanoparticles because of cooperative functionalities. In the case of lipoic acid the molecules can replace the citrate from the gold nanoparticle surface but cannot decrease the negative charge significantly on gold surface thus cannot induce the aggregation. [212]
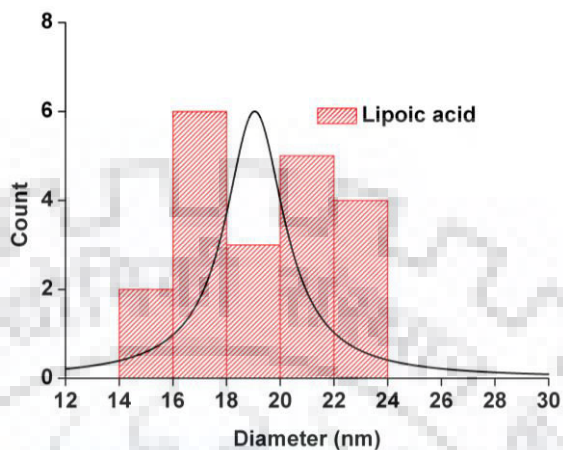
Figure 2.60 Size distribution histogram of nanoparticles synthysized in presence of lipoic acid.

2.8.6 Decreasing amino acid concentration

The growth reactions were further performed by decreasing the amino acid concentration in order to check the rapid aggregation and precipitation (Scheme 2.3).
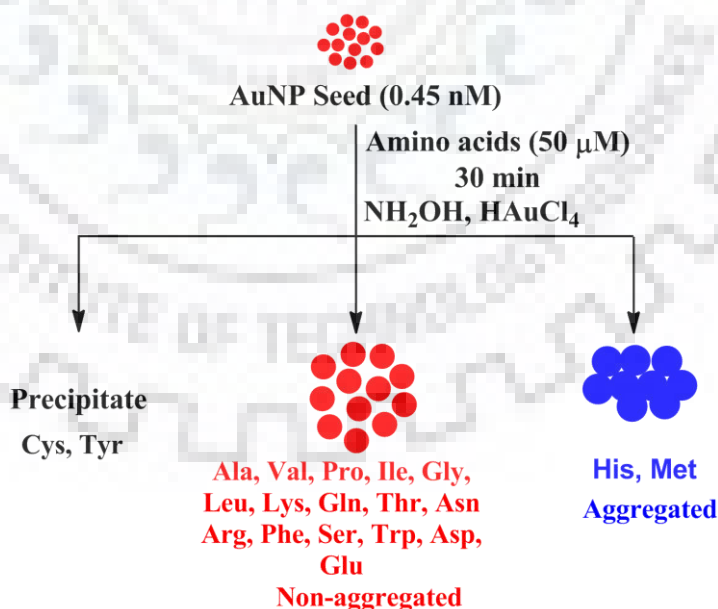
Scheme 2.3 Amino acids (50μM) based growth reactions to form instantaneous precipitation, aggregated and non-aggregated gold nanoparticles.

On decreasing the amino acid to 50 µM, among Cys, Tyr, Asp and Glu the precipitate was observed only with Cys, and Tyr (Figure 2.61A). Cys shows instantaneous precipitation. Among Phe, His, Arg, Ser, Trp and Met blue solutions were obtained for His and Met.(Figure 2.62) The rest amino acids developed red colored solutions as before.(Figure 2.61B) Precipitated solutions did not develop any peak in the absorption spectra while absorption spectra showed only single peak for red colored solutions, and dual peak was observed for blue colored solutions.

The morphology of the nanoparticles after growth reaction was confirmed from TEM images of three representative solutions Arg, Met and His. TEM images showed spherical non-aggregated nanoparticles for Arg based reaction whereas aggregated structure for His and Met based reactions. This confirmed that the coral formation from Met was inhibited at low concentration (Figure 2.63).
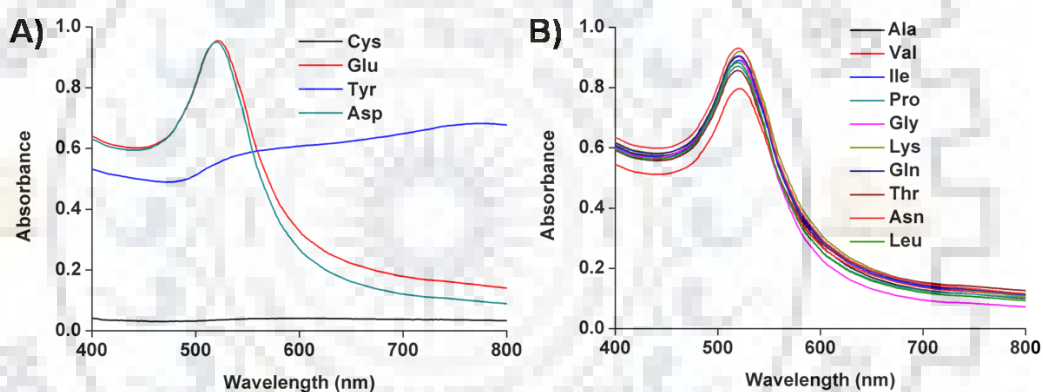
Figure 2.61 Absorption spectra (A) of solutions after growth reactions prepared in presence of Cys, Glu, Tyr and Asn and (B) Ala, Val, Ile, Pro, Gly, Lys, Gln, Lys, Gln, Thr, Asn and Leu.
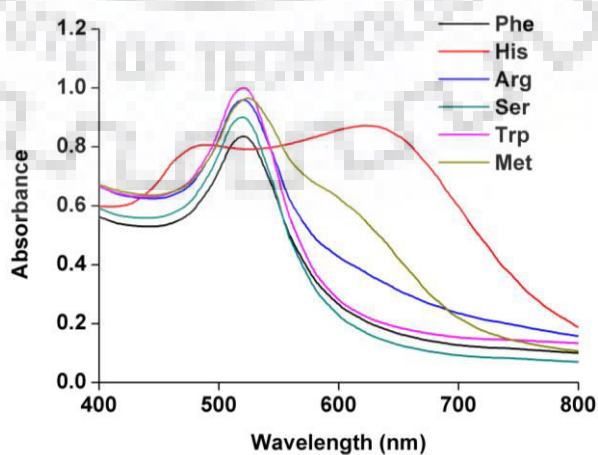
Figure 2.62 Absorption spectra of solutions after growth reactions prepared in presence of Phe, His, Arg, Ser, Trp and Met.
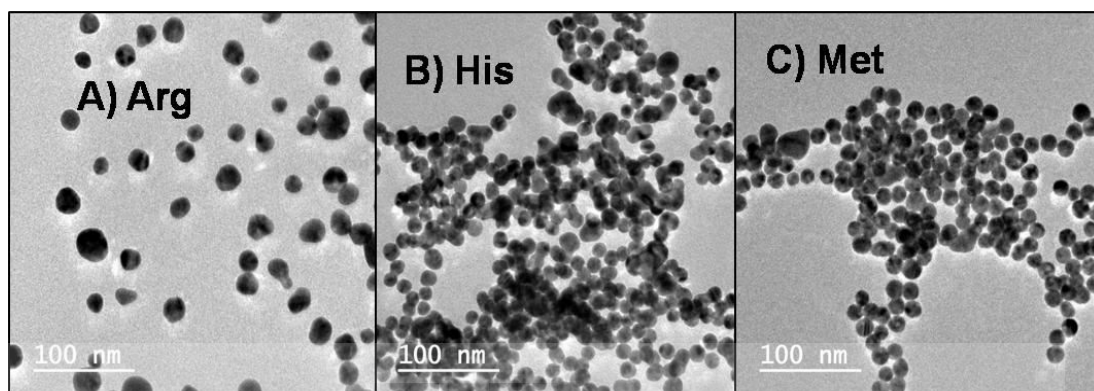
Figure 2.63 TEM images of non-aggregated and aggregated nanoparticles after growth reaction synthesized with (A) Arg (B) His and (C) Met.

2.8.7 Seed variation Methodology

The growth-mediated nanostructure formation was further explored with different seed amount within the range (0.03 nM to 0.45 nM) for three representative amino acids Arg, His and Met. In case of Arg the absorption spectra showed single peak and with increasing seed amount the intensity of the peak increased and at low seed amount 0.03 nM and 0.06 nM blue shift were observed (Figure 2.64). TEM results confirmed the formation of spherical non-aggregated nanoparticles and with increasing seed amount the size of the nanoparticles decreased (Figure 2.65). Size distribution histograms of nanoparticles at different seed concentrations are shown in Figure 2.66. The average size of the nanoparticles vary from 38±5.2, 26±2.77, 25±2.96, 20±3.71 for seed concentration of 0.06 nM, 0.15nM, 0.30 nM and 0.45 nM respectively.
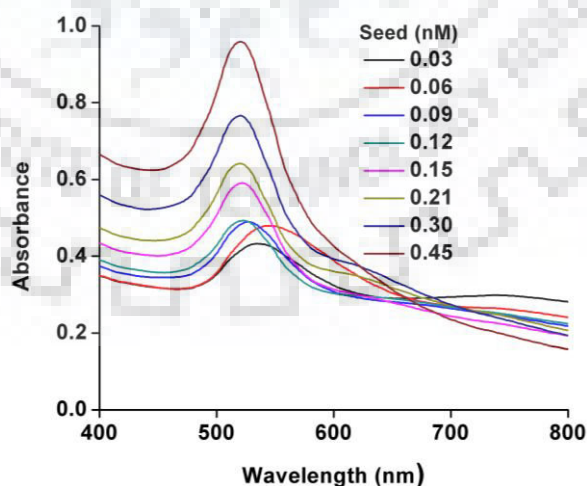
Figure 2.64 Absorption spectra of solutions after growth reactions prepared in presence of Arg with varying the seed amount.
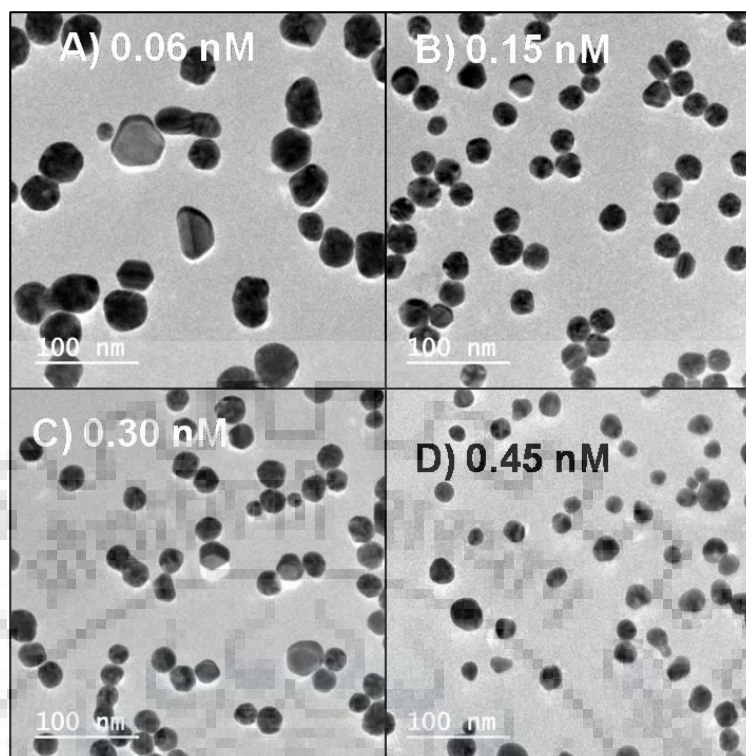
Figure 2.65 TEM images of nanoparticles after growth reactions prepared in presence of Arg with varying the seed amount.
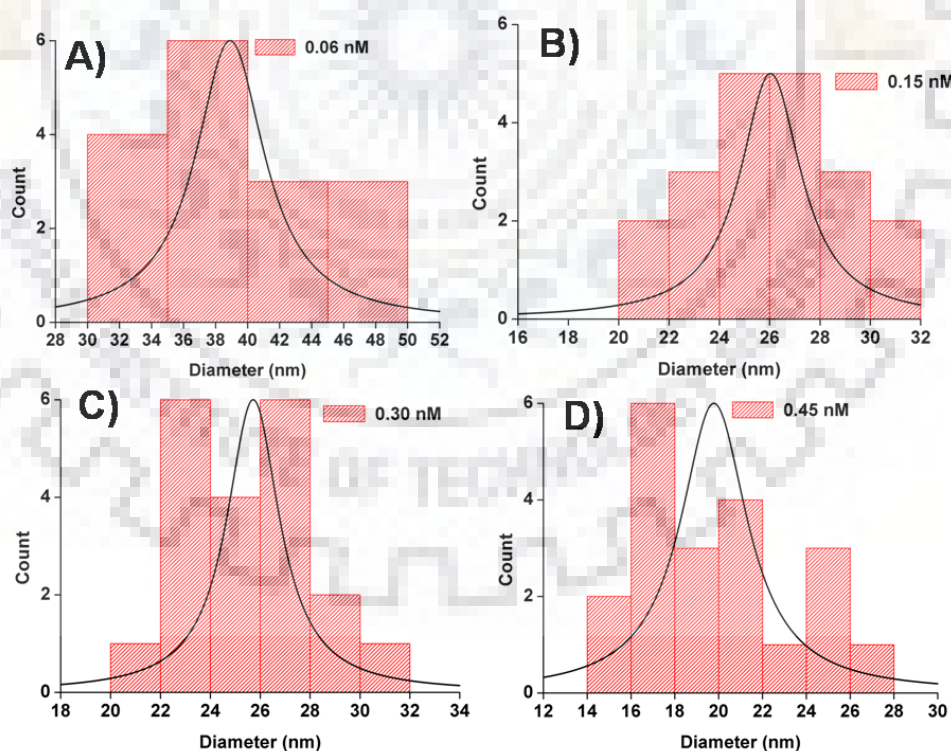
Figure 2.66 Size distributions of nanoparticles prepared in presence of Arg with varying the seed amount.

For His based reactions the absorption spectra developed two peaks and with increasing seed amount the peak intensity increased. The peak at longer wave length got blue shifted while no shift was observed for peak at lower wavelength (Figure 2.67). TEM images confirmed the formation of aggregated nanoparticles and with increasing seed amount the size of the nanoparticles decreased (Figure 2.68).
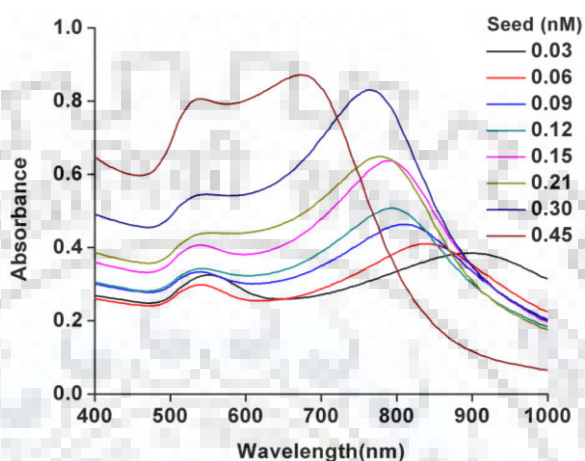
Figure 2.67 Absorption spectra of solutions after growth reactions prepared in presence of His with varying the seed amount.
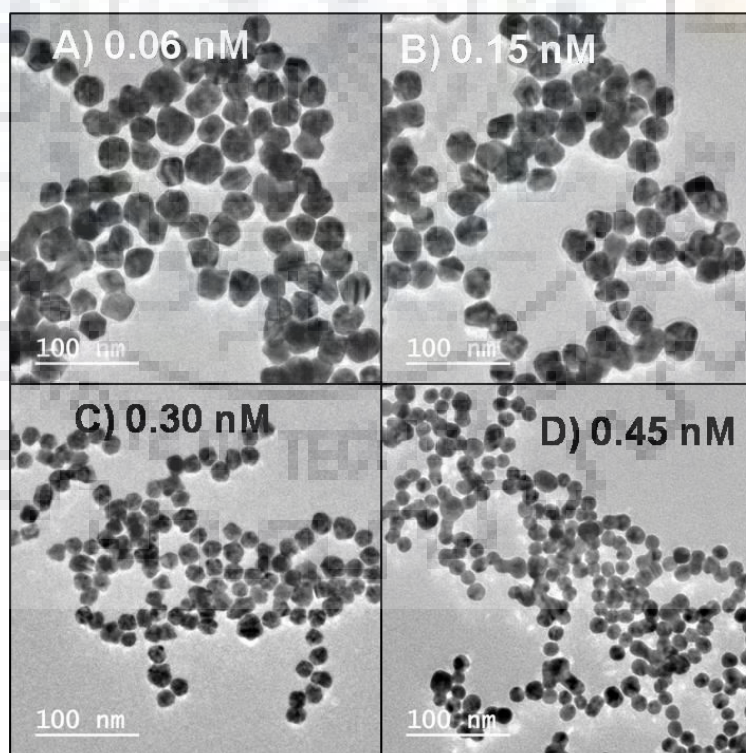
Figure 2.68 TEM images of nanoparticles after growth reactions prepared in presence of His with varying the seed amount.

Met based reactions also showed two peaks in the absorption spectra and with increasing seed amount the peak intensity increased with blue shift at longer wavelength (Figure 2.69). TEM images showed the formation of big network structures at low seed amount and aggregated nanoparticles with increasing seed amount. With increasing seed amount the size of the nanoparticle decreased (Figure 2.70).
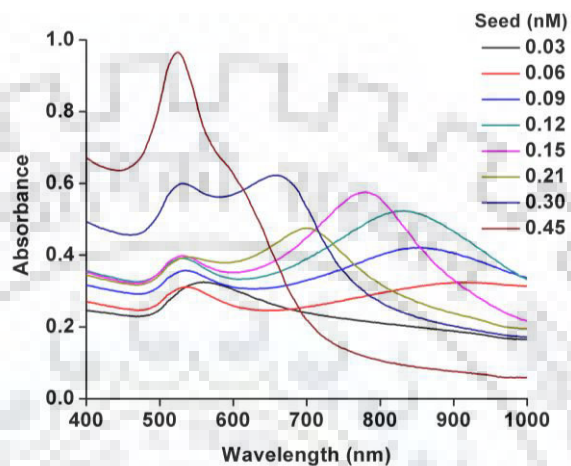
Figure 2.69 Absorption spectra of solutions after growth reactions prepared in presence of Met with varying the seed amount.
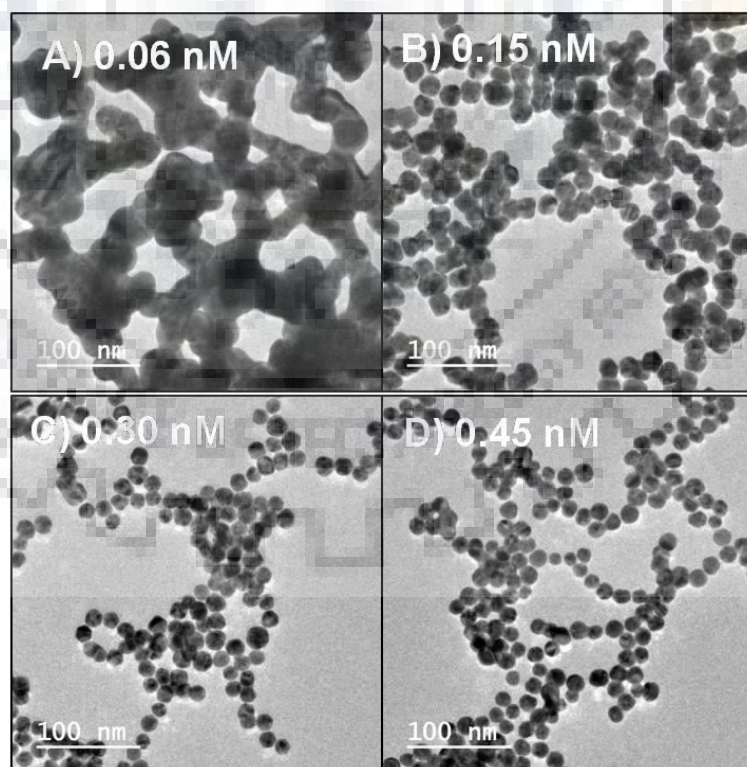
Figure 2.70 TEM images of nanoparticles after growth reactions prepared in presence of Met with varying the seed amount.

2.9 CONCLUSION

Growth reactions were performed with all natural amino acids using gold nanoparticles as seeds in presence of mild reducing agent hydroxylamine. These resulted in the formation of precipitate, aggregates, non-aggregates and coral shaped nanostructures. The formation of different structures was confirmed from the TEM images. The negative controlled reactions were done with few bio molecules, inorganic salts and sulphur containing organic molecules. These controlled reactions produced aggregated or non-aggregated nanoparticles. Aggregation and coral formation was again checked by lowering the concentration of amino acid. Coral formation was inhibited rather aggregated nanoparticles were developed. The growth reactions were further performed by varying the seed amount from 0.03 nM to 0.45 nM for Arg, His, and Met. Spherical non-aggregated, aggregated and network shaped nanostructures were obtained. TEM images showed decreasing trend of nanoparticle size with increasing seed amount.

Chapter 3

Growth reaction of gold nanoparticles after the combined treatment of amine modified DNAs and selected amino acids

3.1 INTRODUCTION

Interaction between gold nanoparticle and DNA has been well explored within last two decades.[340] Among the DNA based gold nanoarchitectures, gold nanoflower shows important biological application such as surface-enhanced raman scattering[341,342] which has been further exploited to live cell imaging. Gold nanoflower, originated from diverse pathways, have shown biological applications such as imaging of cellular alkaline phosphate,[343] in vivo inhibition of bacteria.[344] Quercetin-functionalized gold nanoparticle has been successfully explored for the detection of arginine, histidine, and lysine without any selectivity.[345] Dicoumarol and sodium chloride have been treated separately for the detection of cysteine by aggregation of gold nanoparticle.[346,347] Lee et al. developed chiral plasmonic gold nanoparticle from cubic seed controlled by amino acid and peptides.[209] The same group has also shown the growth of gold nanoparticle in the presence of peptide sequence containing five amino acids.[348] Currently, the biomolecule detection technology by gold nanoparticle solely depends on interactions of gold nanoparticle with either biomolecule or DNA or amino acids. However, so far gold nanoparticle has not been reconnoitered in the biomolecule detection process, where interactions between two biomolecules such as DNA and amino acids or peptides play a major role. The translocation of peptide through cell membrane is observed in the case of arginine-rich peptide.[349] In the same study, it has been reported that the replacement of arginine with lysine does not show translocation. However, Wu's group has shown the role of CGC nucleic bases at the end of the positively charged miniproteins containing either arginine or lysine for the equal uptake due to thiol−disulfide exchange on the cell surface.[350] Not only the uptake of peptide but also the release of peptide from late endosome to cytosol depends upon the threshold concentration of arginine in the peptide sequence.[351] Too-high concentration of arginine does not release the peptides from late endosomes.

The detection of arginine in peptide sequence is an active area of research over two decades. Among the arginine detection technique in peptide sequence, capillary electrophoresis, laser induced fluorescence was introduced to enhance the sensitivity of the benzoin based fluorogenic detection process[352], monolithic HPLC and aerolysin nanopore were also used for the estimation of Arg in the peptides.[353,354] Wu's group showed the role of CGC nucleic bases at the end of the positively charged miniproteins containing either arginine or lysine for the equal uptake due to thiol-disulfide exchange on the cell surface.[355]The strong interaction between arginine and DNA has explored its usage as positively charged amino acid in protamines for DNA packaging.[356]

This chapter is divided into two sections. Section A describes the role of amine modified DNA for detection of single Arg over Lys substitution in peptide while section B describes the role of amine modified for differentiation of polar uncharged side chains amino acids.

SECTION A

Gold nanoflowers were developed from spherical gold nanoparticle seed with the help of amino acids and amine modified DNA. This was further applied to differentiate the 3_{10}-helical and α-helical peptides containing lysine and arginine respectively. The substitution of lysines by arginines of 3_{10}-helical Ac-(AAAAK)$_3$A-NH$_2$(KKK) peptide led to the formation of the α-helical Ac-(AAAAR)$_3$A-NH$_2$(RRR) peptide.[357] In the present study, gold nanoflowers were developed from spherical gold nanoparticle seed with the help of amino acids and amine modified DNA sequence to develop an easy technique for the detection of α- helical peptide sequence RRR, where all the lysines of 3_{10}-helical KKK peptide were replaced with arginine (Scheme 3.1). Further the method was successfully extended for the detection of single lysine to arginine substitution in peptide closest to the carboxy terminal of Ac-AAAAKAAAAKAAAARA-NH$_2$ (KKR) peptide. The conformational change in the helicity due to single arginine substitution at lysine residue [357] played the crucial role in the detection process.
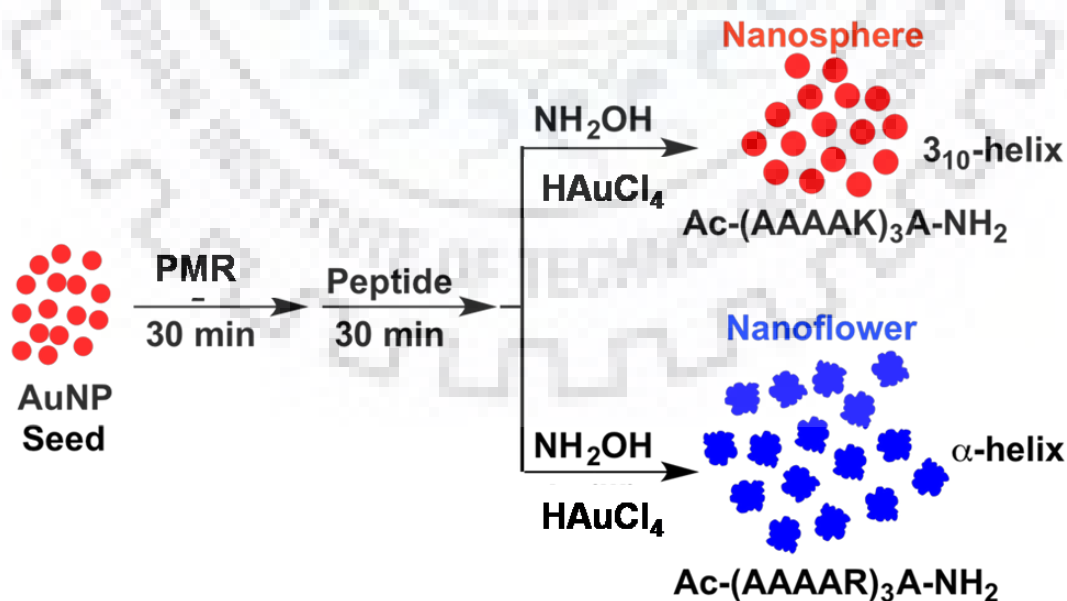
Scheme 3.1 Selective formation of gold nanoflowers after adsorption of PMR to gold nanoparticle seeds with Arg or Arg containing peptides.

3.2 EXPERIMENTAL SECTION

3.2.1 Chemicals and Materials

All the reagent grade materials used unless specified were discussed previously. L-amino acids were purchased for Himedia Laboratories pvt. Ltd. The peptides were purchased from GL Biochem (Shanghai) Ltd. The amino acids solutions were prepared in a 1:1 mixture of ethanol and water. Aspartic acid, glutamic acid and tyrosine were prepared in 1:1 mixture of ethanol and 1N HCl, whereas cysteine was prepared in 1N HCl. Amino acids at low concentration were prepared by taking stock from high concentration and diluting in millipore water. The peptide solutions were prepared in pure millipore water.

3.2.2 Instrumentation

Absorption spectroscopy, TEM and DLS measurements were done as previously described. Circular dichroism spectra of growth solutions from peptides were measured with a J-1500 CD spectropolarimeter at 25 °C. The spectra were collected from 195 to 255 nm by using a 10 mm path length quartz cuvette while keeping the high tension (HT) voltage less than 500 V for reliability. The data were accumulated from three repeated runs, and a smoothing process was done.

3.3 Synthetic Procedures

Synthesis of seed stock solution

The seed solution was prepared as previously mentioned. The seed solution was diluted to adjust the absorbance at 0.5. The final volumes of the reactions were adjusted to 340 μL in all cases.

Growth reactions of gold nanoparticles with PMR and L-amino acids

300 μL gold nanoparticles seed solutions were incubated with 0.6 μM DNA for 30 minutes. 9 mM amino acid was added and further incubated for 30 minutes. 3 μL, 200 mM NH_2OH (adjusted to pH 5 with NaOH) was added to these solutions and stirred vigorously for 10 minutes. 5 μL of 0.8% (w/v) $HAuCl_4$ was added to these solutions to initiate the reduction reaction. The color change was observed within seconds.

Growth reactions of gold nanoparticles with L-amino acids at low concentration

300 μL gold nanoparticles seed solutions were incubated with 50 μM amino acids for 30 minutes. 3 μL, 200 mM NH_2OH (adjusted to pH 5 with NaOH) was added to these solutions

and stirred vigorously for 10 minutes. 5 µL of 0.8% (w/v) HAuCl$_4$ was added to these solutions to initiate the reduction reaction. The color change was observed within seconds.

Growth reactions of gold nanoparticles with PMR and L-amino acids at low concentration

300 µL gold nanoparticles seed solutions were incubated with 0.6 µMPMR for 30 minutes. 50µM amino acids was added and further incubated for 30 minutes. 3 µL, 200 mM NH$_2$OH (adjusted to pH 5 with NaOH) was added to these solutions and stirred vigorously for 10 minutes. 5 µL of 0.8% (w/v) HAuCl$_4$ was added to these solutions to initiate the reduction reaction. The color change was observed within seconds.

Growth reactions of gold nanoparticles with PMR and peptide

300 µL gold nanoparticles seed solutions were incubated with 0.6 µM DNA for 30 minutes. Peptide (0.5 µM, 1 µM, 2 µM or 3 µM) were added and further incubated for 30 minutes. 3 µL, 200 mM NH$_2$OH (adjusted to pH 5 with NaOH) was added to these solutions and stirred vigorously for 10 minutes. 5 µL of 0.8% (w/v) HAuCl$_4$ was added to these solutions to initiate the reduction reaction. The color change was observed within seconds.

3.4 RESULTS AND DISCUSSION

3.4.1 Synthesis and characterization

Growth reactions were performed by incubating the gold nanoseeds with 0.6 µM PMR before addition of amino acids. Hydroxylamine as reducing agent was added and the reaction was vigorously shaken. HAuCl$_4$was added to complete the reduction reaction. The synthesized solutions and nanoparticles were characterized by absorption spectroscopy, TEM and DLS measurements.

3.4.2 Selectivity for nanoflower formation

The growth reactions which were performed in presence of different amino acids showed different extent of aggregated or non-aggregated gold nanoparticles. The results developed selectivity between the Arg and Lys in the growth reaction; however the detection of Arg was not selective by this method. In order to develop a tool for the detection of Arg, the earlier growth reactions with all natural amino acids were further explored in presence of PMR (Scheme 3.2).
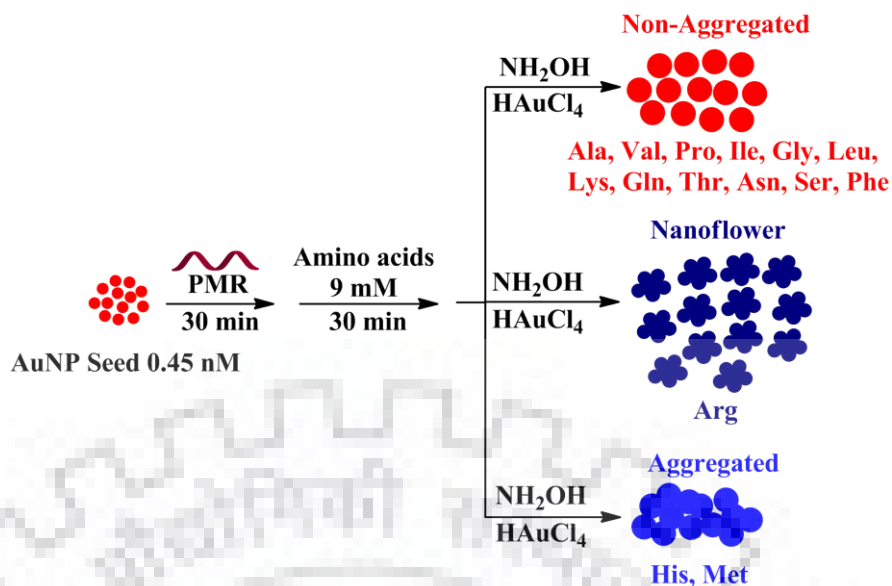
Scheme 3.2 Growth reactions in presence of PMR and amino acids showing formation of non-aggregated, nanoflowers or aggregated nanoparticles.

Asp, Glu, Cys and Tyr did not produce any change in presence of PMR, still resulted in precipitation and precipitation was instantaneous in case of cysteine. Precipitated solutions did not develop absorption peak or very weak intensity peak was observed (Figure 3.1).
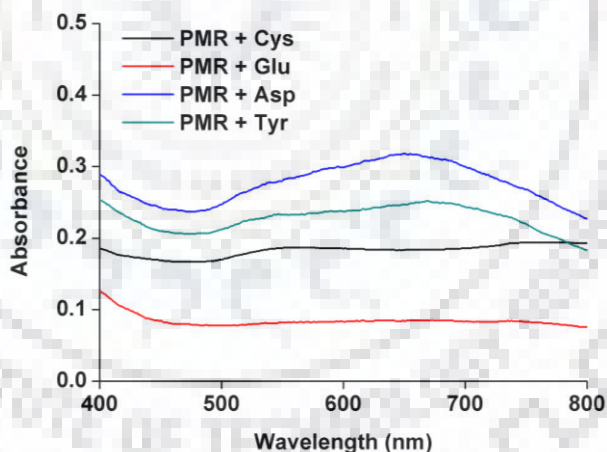
Figure 3.1 Absorption spectra of precipitated solutions.

Introduction of PMR generated red color for Phe, Ser and Trp based reactions which were blue in absence of PMR. However, in the case of Arg and Met the solutions were still blue colored even after the treatment of PMR. Absorption spectra showed dual peak for blue colored solutions whereas single peak for red colored solutions (Figure 3.2). All other amino acids resulted in red color after the growth reaction in presence of PMR and showed single peak in

absorption spectrum (Figure 3.3). This developed selectivity among the Arg, His, Ser, Phe, Met and Trp.
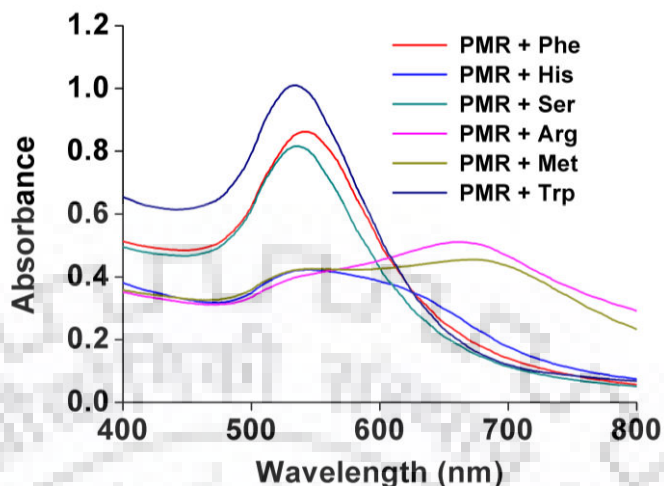
Figure 3.2 Absorption spectra of growth solutions synthesized in presence of PMR and Phe, His, Ser, Arg, Met and Trp.
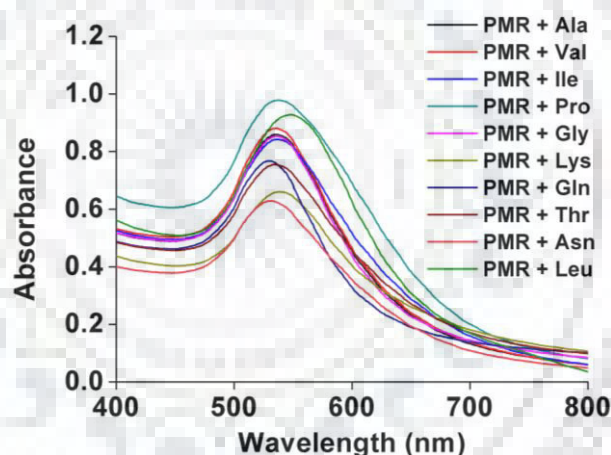
Figure 3.3 Absorption spectra of red solutions synthesized in presence of PMR and amino acids.

The morphology of the nanoparticles after the growth reaction was confirmed from TEM images. Among the blue solutions combined treatment of PMR and Arg showed the gold nanoflower architecture (Figure 3.4A). The gold nanoflower which was obtained after growth reaction with PMR sequence cannot be formed in presence of amino acids. A comparison of the interaction between the amino acids and DNA bases and backbone shows the interactions are very high between the DNA and Arg compared to other amino acids (Table 3.1)[358]. The strong interaction between Arg and PMR sequence was responsible for the formation of the nanoflowers. However, in the case of His and Met, there were aggregation of gold nanoparticle

after the growth reaction (Figure 3.4 B and C). In the case of Ser, Phe, Lys, and Leu the excess amount of amino acids could replace the PMR from the gold nanoparticle surface. Therefore, gold nanoflower could not be obtained after the growth reactions from the combination of PMR with these amino acids (Figure 3.5A-D).
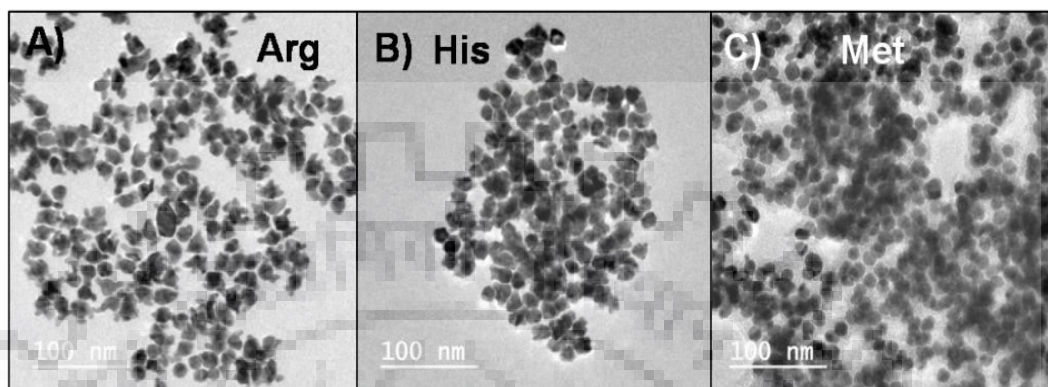
Figure 3.4 TEM images of gold nanoflowers, A) Arg, aggregate B) His and C) Met after growth reaction synthesized with PMR incubated nanoseeds. Scale bar: 100 nm
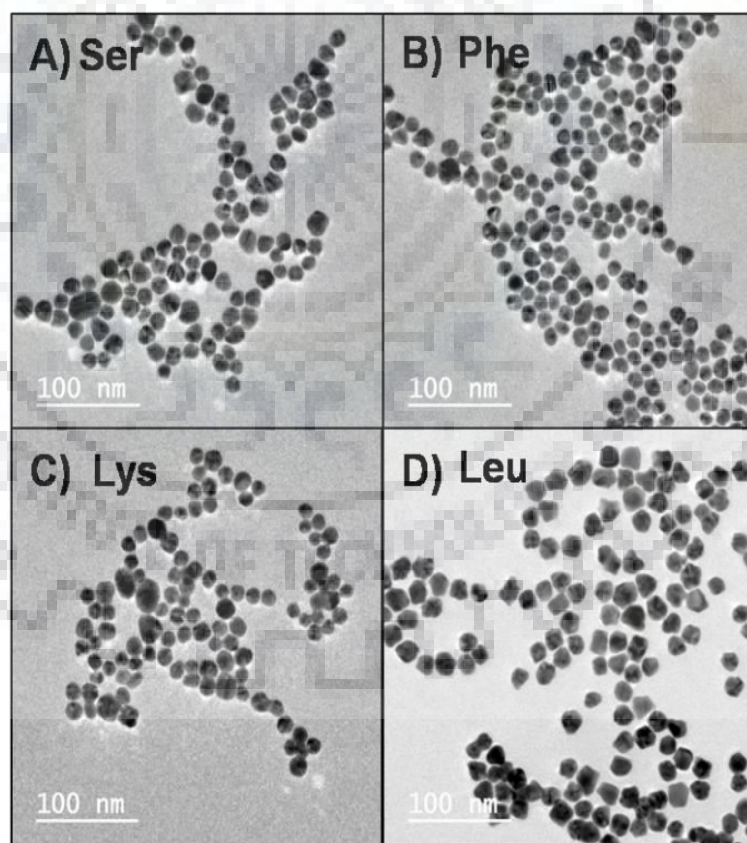
Figure 3.5 TEM images of non-aggregate nanoparticle A) Ser B) Phe C) Lys and D) Leu after growth reaction synthesized with PMR incubated nanoseeds. Scale bar: 100 nm.

Size distribution histograms of the nanoflowers and nanospheres are shown in Figure 3.6 and 3.7. TEM analysis showed the average size of nanoflowers are 20±2.98 nm and nanoparticles synthesized with Ser, Phe, Lys and Leu have average size of 17±2.67 nm,17±3.16 nm, 19±3.36 nm, and 20±2.22 nm.
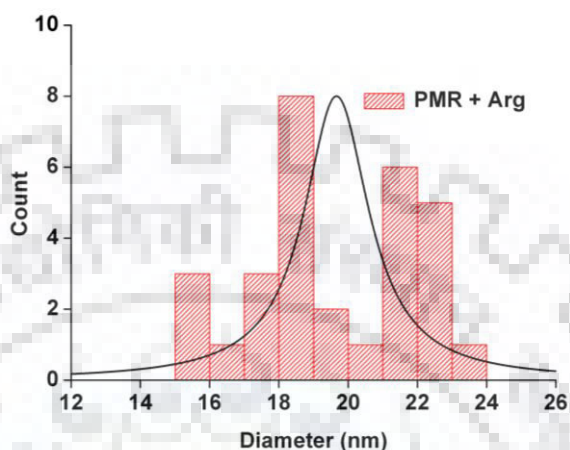
Figure 3.6 Size distribution histograms of the nanoflowers synthesized with Arg in presence of PMR.
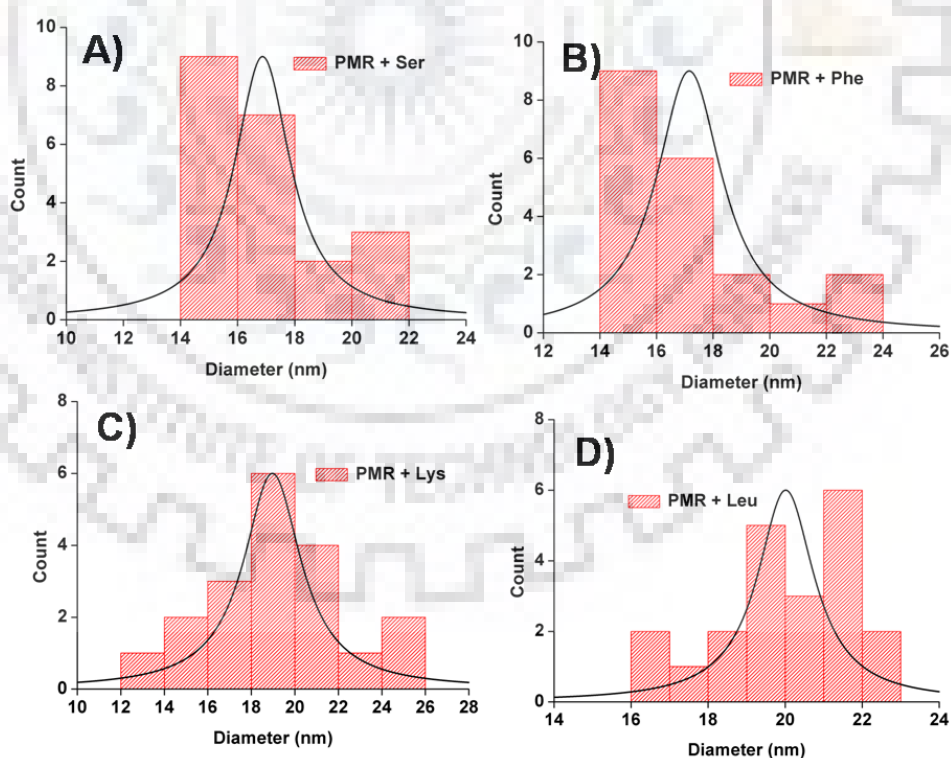
Figure 3.7 Size distribution histograms of the nanoparticles synthesized with Ser, Phe, Lys and Leu in presence of PMR.

Table 3.1: Distribution of hydrogen bonds between amino acid and DNA base or backbone group. In parentheses are the number of hydrogen bonds that would be expected from purely the random docking of amino acids to DNA.[358]

Amino acids	DNA Bases					DNA backbone	Total
	Thymine	Cytosine	Adenine	Guanine	Sugar		
Arg	24 (2.5	8 (2.0)	19 (4.2)	98 (4.0)	8 (1.9)	218 (49.9)	375 (64.7)
Lys	9 (4.4)	6 (3.4)	4 (7.4)	30 (7.1)	3(3.2)	109 (86.7)	165(112.6)
Ser	3(3.0)	2(2.2)	1(5.0)	12(4.6)	2(2.1)	91(57.3)	113(74.4)
Thr	5(2.4)	3(2.0)	4(4.2)	-(4.0)	1(1.8)	79(49.2)	92(63.9)
Asn	7(3.6)	10(2.7)	18(6.0)	7(5.8)	3(2.6)	43(70.7)	88(91.8)
Gln	2(2.2)	2(1.7)	16(3.8)	6(3.6)	2(1.7)	42(44.8)	70(58.1)
Gly	1(3.2)	4(2.4)	-(5.4)	6(5.1)	1(2.4)	29(63.3)	41(82.2)
His	-(0.8)	1(0.6)	1(1.5)	12(1.4)	-(0.7)	26(18.3)	40(23.7)
Tyr	-(1.2)	2(1.0)	-(2.1)	1(2.0)	1(1.0)	35(25.7)	39(33.4)
Ala	1(2.5)	1(2.0)	-(4.2)	1(4.0)	-(1.9)	17(49.8)	20(64.6)
Glu	-(3.8)	10(3.0)	1(6.5)	1(6.2)	-(2.9)	6(76.2)	18(99.0)
Ile	-(0.7)	-(0.5)	-(1.3)	3(1.2)	-(0.6)	11(15.9)	14(20.7)
Asp	-(4.5)	5(3.4)	2(7.5)	2(7.2)	-(3.3)	2(88.3)	11(114.7)
Val	-(1.2)	-(1.0)	-(2.0)	-(2.0)	-(0.9)	8(24.5)	8(31.8)
Cys	-(0.2)	1(0.2)	-(0.5)	-(0.5)	-(0.3)	4(6.7)	5(8.7)
Phe	-(0.6)	-(0.5)	-(1.1)	1(1.1)	-(0.5)	4(14.4)	5(18.6)
Leu	-(1.5)	-(1.1)	-(2.6)	-(2.5)	-(1.2)	5(30.8)	5(40.0)
Met	1(0.4)	-(0.3)	-(0.7)	-(0.7)	-(0.3)	3(9.1)	4(11.8)
Trp	-(0.3)	-(0.2)	-(0.7)	-(0.6)	-(0.3)	3(8.7)	3(11.3)
Pro	-(3.5)	1(2.7)	-(6.0)	-(0.6)	-(2.6)	-(70.0)	1(90.9)
Total	53(42.5)	56(33.0)	66(73.4)	180(69.4)	21(32.2)	735(860.3)	1,111(1.111)

3.4.3 Selective detection of arginine

The strategy required further improvement in order to develop selective detection of Arg via growth mechanism. The concentration of amino acids was lowered to 50 μM after the treatment with 0.6 μM PMR. Among Asp, Glu, Cys and Tyr, only Cys showed the precipitation, others resulted in red colored solutions (Figure 3.8). The reduction reaction in presence of Ala, val, Ile, Pro, Gly, Lys, Gln, Thr, Asn and Leu also developed red color and showed single peak in the absorption spectra (Figure 3.9).
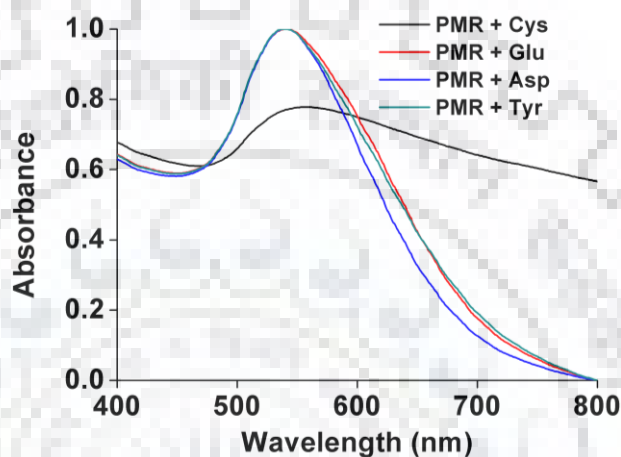
Figure 3.8 Normalized absorption spectra of precipitated or non-aggregated nanoparticle solutions after growth reactions synthesized with PMR incubated nanoseeds.
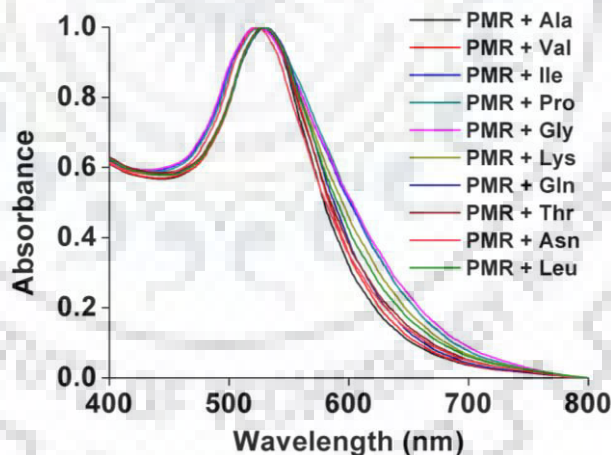
Figure 3.9 Normalized absorption spectra of non-aggregated nanoparticle solutions after growth reactions synthesized with PMR incubated nanoseeds.

Interestingly, within Arg, His and Met, blue colored solution was only obtained from Arg case. The combination of 0.6 μM PMR and 50 μM of remaining amino acids produced red colored solution (Figure 3.10). The absorbance of blue solution obtained with Arg was broad in nature and was similar to the earlier report of gold nanoflower solution.[197] The TEM images

showed the formation of gold nanoflower only in case of Arg (Figure 3.11A). In the case of His and Met, spherical gold nanoparticle were formed after growth reaction (Figure 3.11B and C).
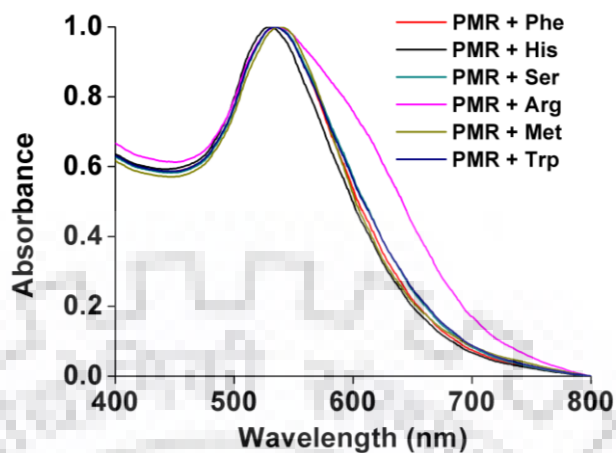
Figure 3.10 Normalized absorption spectra of non-aggregated nanoparticle solutions after growth reactions synthesized with PMR incubated nanoseeds.
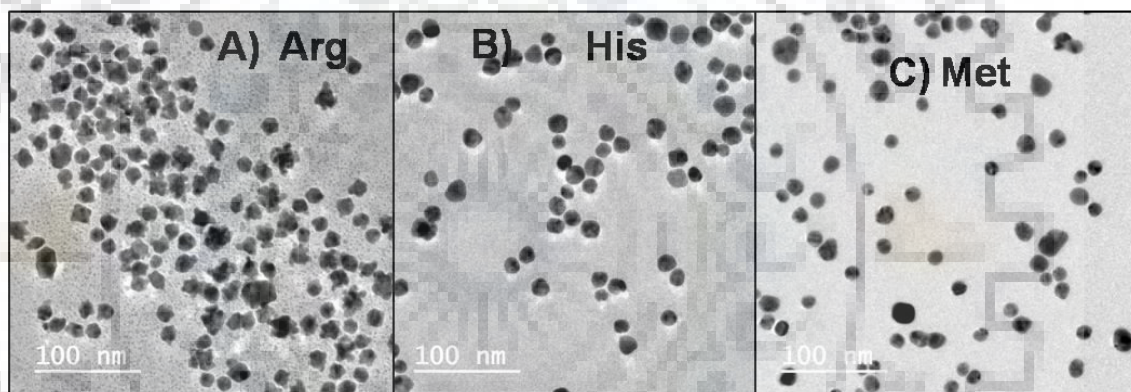
Figure 3.11 TEM images of gold nanoflowers (A), spherical nanoparticle (B) and (C) after growth reaction synthesized with PMR incubated nanoseeds in presence of Arg, His, and Met. Scale bar: 100nm.
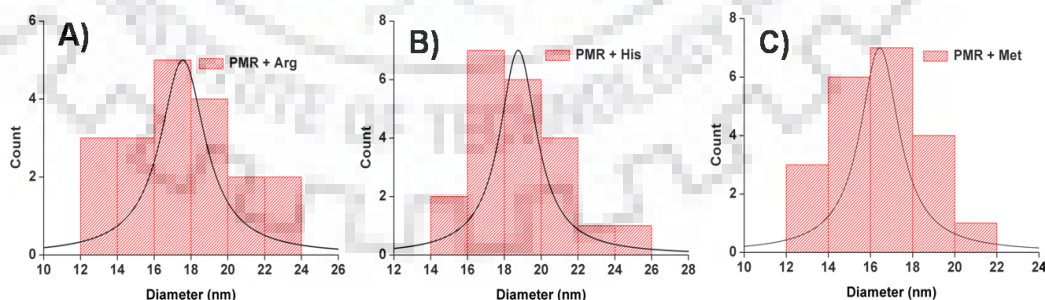
Figure 3.12 Size distribution histograms of the nanoparticles synthesized with Arg, His and Met at concentration of 50 μM in presence of PMR.

Size distribution histograms of the nanoflowers and nanospheres are shown in Figure 3.12. TEM analysis showed the average size of nanoparticles were 17± 2.50 nm, 18±2.93 nm, 16±3.11 nm synthesized with Arg, His, and Met in presence of PMR.

3.4.4 Detection of arginine in peptide

The gold nanoflower based selective detection of Arg from the growth reaction in presence of PMR was further extended to the determination of Arg in peptide sequence. The positive charge in Arg was mostly compared with Lys residue in terms of cellular as well as cytosolic entry of peptide containing these amino acids. Two peptides KKR and RRR were targeted, where three Lys residues in one peptide were replaced with three Arg residues. Interestingly, these three changes in the amino acid residues not only maintained the charge uniformity of the peptide sequence but also showed two completely different structural configurations, 310-helical configuration with three Lys and α-helix configuration with three Arg in the peptide sequences.[357] The same report showed the increasing global helicity of the peptide series in the order of KKK **<** RKK < KRK < KKR < RRR on the basis of circular dichroism data. RKK, KRK, and KKR, was chosen where the substitution closest to the carboxy terminal in KKR is the major factor in the change of helical configuration.[357]

Formation of gold nanoflowers was checked from the combination of 0.6 μM PMR and 0.5 μM to 3 μM range of three peptides KKK, KKR and RRR. Gold nanoseeds were first treated with 0.6 μM PMR for 30 min and then further incubated with peptides for another 30 min before performing the growth reaction with hydroxylamine and Au (III) salt. The growth reactions in absence of PMR resulted in either red colored solutions or precipitate (Figure 3.13A, 3.14A and 3.15A) whereas the growth reactions in presence of PMR and peptide were red (Figure 3.13B) or blue in colour and showed red shift solution with increasing concentration of either KKR or RRR (Figure3.14B and 3.15B).
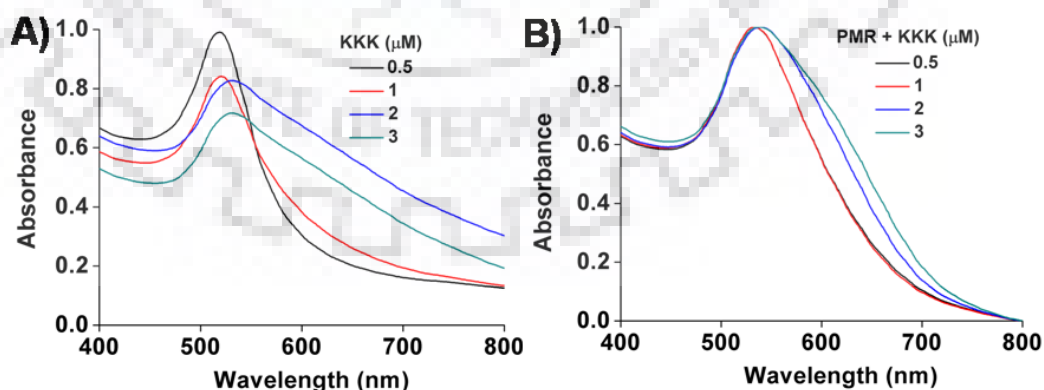
Figure 3.13 (A) Absorption spectra of the nanosolutions after growth reactions in presence of peptide KKK at different concentrations. (B) Normalized absorption spectra of growth reactions in presence of PMR and peptide KKK at different concentrations.
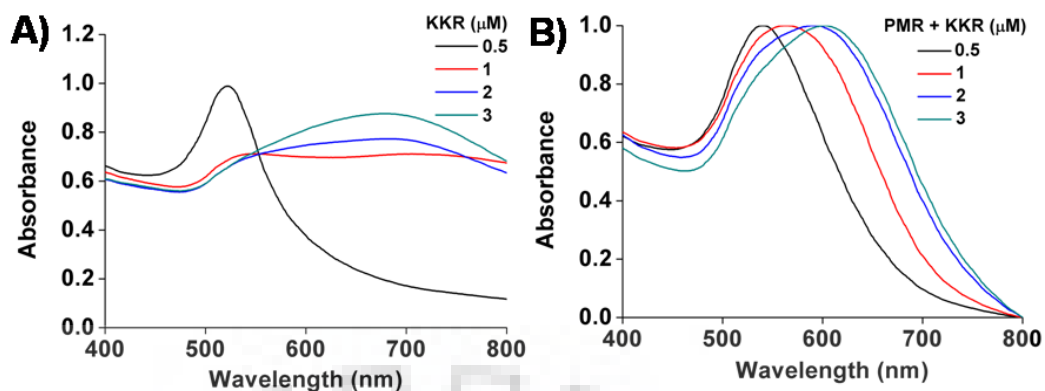
Figure 3.14 (A) Absorption spectra of the nanosolutions after growth reactions in presence of peptide KKR at different concentrations. (B) Normalized absorption spectra of growth reactions in presence of PMR and peptide KKR at different concentrations.
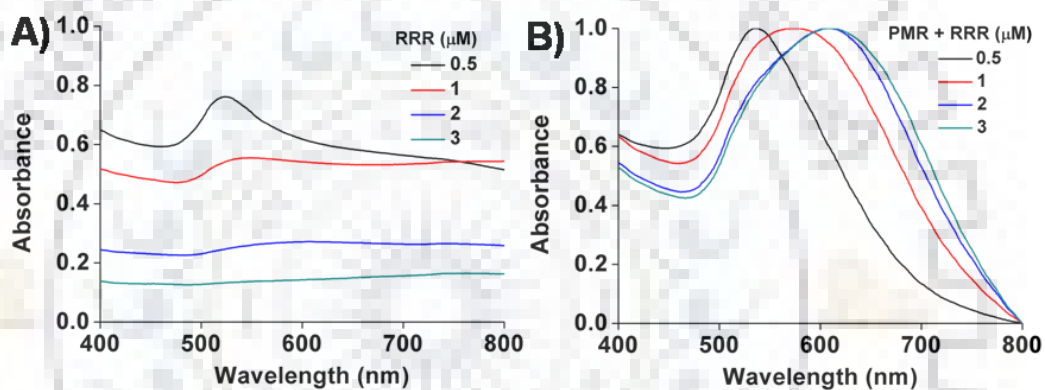
Figure 3.15 (A) Absorption spectra of the nanosolutions after growth reactions in presence of peptide RRR at different concentrations. (B) Normalized absorption spectra of growth reactions in presence of PMR and peptide RRR at different concentrations.

The change in the absorption maxima was plotted for these five peptides which confirmed the detection of single Arg to Lys in peptide and the solution color changed from red to blue (Figure 3.16A, inset).In the case of RKK and KRK, the color was shifted from red to violet (Figure 3.16A) and confirmed the gradual change in color due to the change in peptide configuration. The morphology of the red and blue solutions was confirmed from TEM images. TEM images showed the formation of spherical nanoparticles in presence of KKK whereas nanoflowers in presence of KKR or RRR (Figure 3.16B-D).

Size distribution histograms of the nanoflowers and nanospheres are shown in Figure 3.17. TEM analysis showed the average size of nanoparticles were 15± 2.27 nm, 19±3.06 nm, 17±2.66 nm synthesized with KKK, RRR, and KKR in presence of PMR.
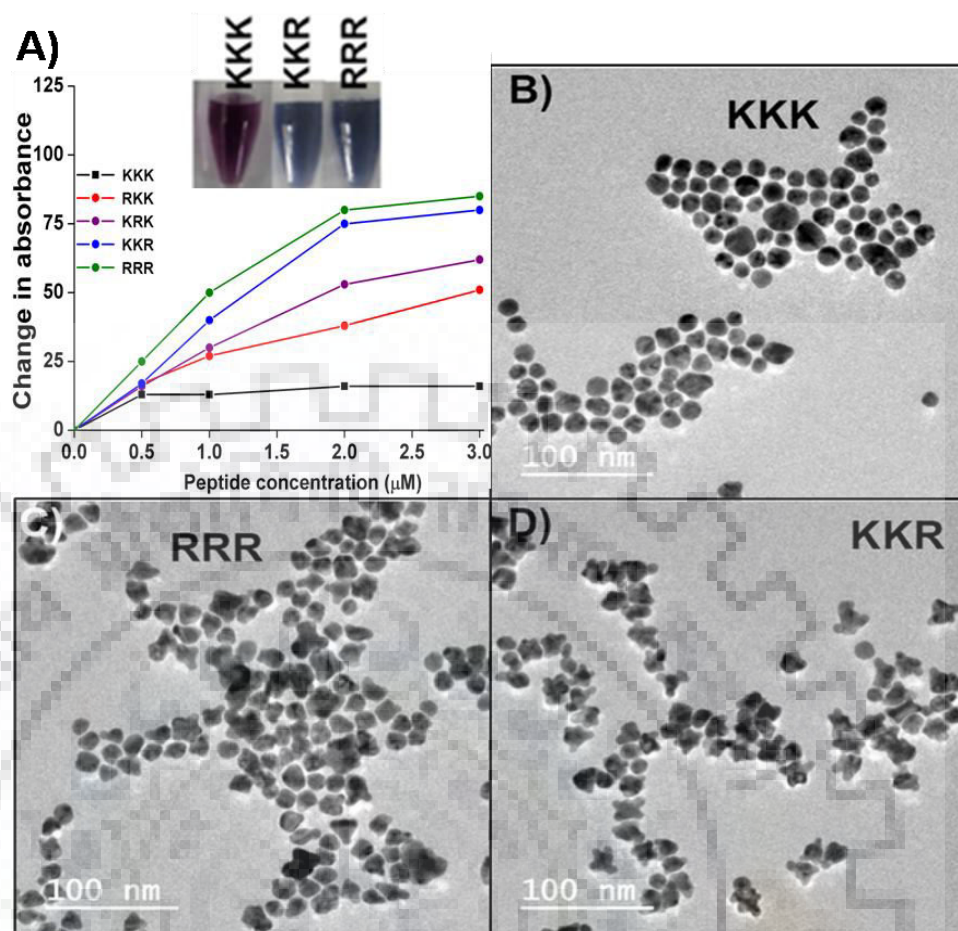
Figure 3.16 Change of absorption maxima wavelength during after the growth reactions in presence of 0.6 μM PMR and different concentration of peptides and (inset) the color of the solutions after the growth reaction with 3 μM peptide (KKR, RRR and KKK) concentration and B-D) TEM images of gold nanoflower and spherical gold nanoparticles after the growth reaction in presence of 3 μM peptides KKK, RRR and KKR. Scale bar for B-D: 100 nm
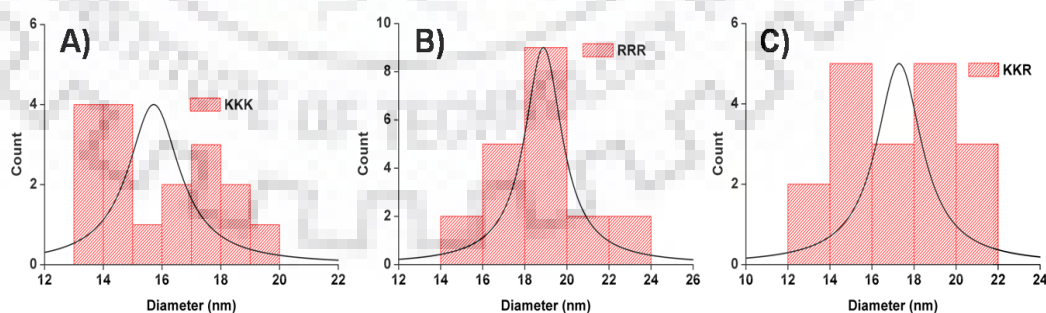
Figure 3.17 Size distribution histograms of the nanoparticles synthesized with KKK, RRR, and KKR in presence of PMR.

The change of the peptide configuration was further confirmed by taking the Circular dichroism (Figure 3.18) spectra of the peptide based solutions after growth reaction at 100 μM. The structural change of the peptides from KKK, KKR, and RRR are clear from the mean

residual ellipticity of CD spectra at 222 nm. However, the change of ellipticity for RKK, KRK, and KKR are close to each other. The change in the ellipticity was observed similar to the ellipticity of the free peptides even at high concentration after growth reaction.
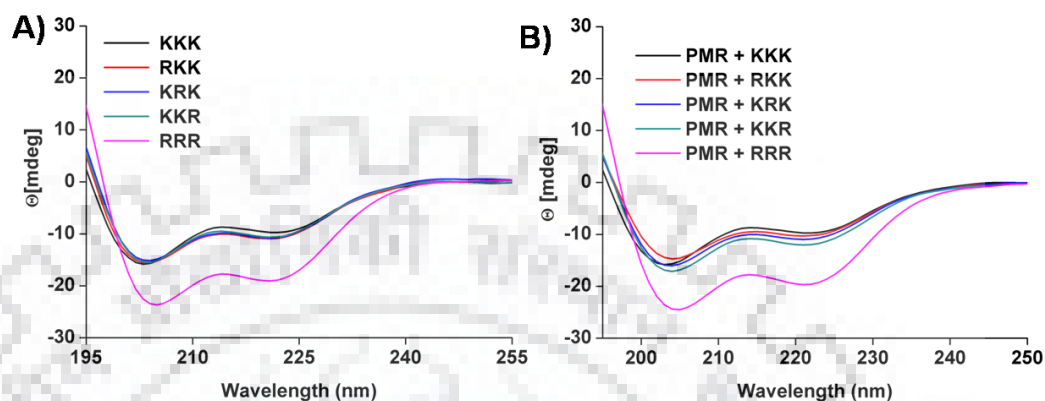
Figure 3.18 CD spectra of solutions of pure peptides (A) after the growth reactions (B). Concentration of peptide was 100 μM.

3.4.5 DLS Measurements

The aggregation process was further confirmed from measuring the size of the nanoparticles. The blue solutions developed large sized nanoparticles which confirmed the formation of aggregated nanoparticles (Figure 3.19, Table 3.2). On decreasing the concentration of amino acid to 50 μM the aggregation was stopped.
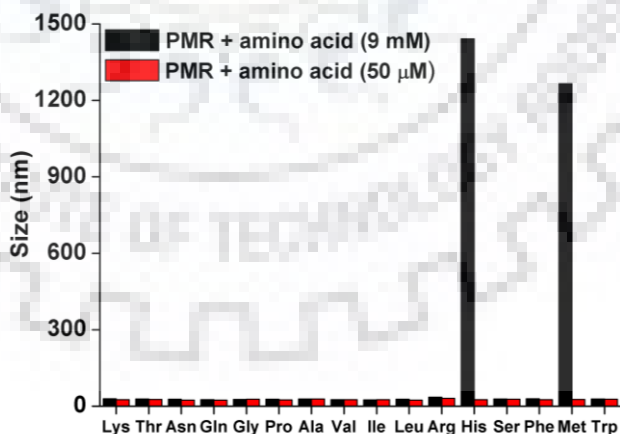
Figure 3.19 Size of nanoparticles after growth reaction synthesized in presence of PMR with different amino acids at concentration of 9 mM and 50 μM.

The polydispersity of the growth solutions was almost the same at both 9 mM and 50 μM. The PDI values were high for the His and Arg than other amino acids (Figure 3.20, Table 3.3)
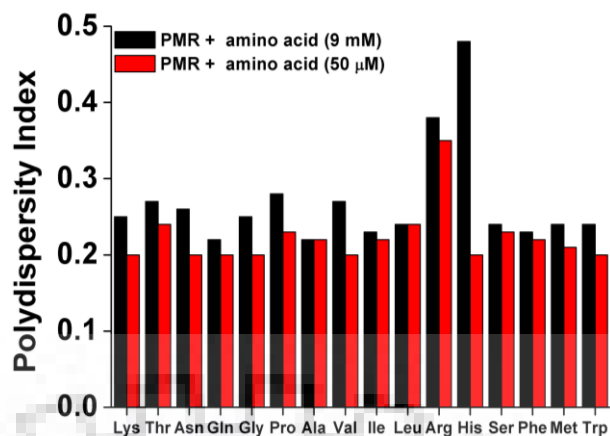
Figure 3.20 Polydispersity of nanoparticles after growth reaction at concentration of 9 mM and 50 µM of amino acids.

Table 3.2: Size, zeta potential and PDI values of nanoparticles after growth reaction in presence of PMR and amino acids.

Amino acid	Size* (nm) of nanoparticles after growth reaction	
	9 mM	**50 µM**
Lys	29.2	25.5
Thr	28.3	25.9
Asn	27.6	24.0
Gln	25.86	24.0
Gly	26.7	26.8
Pro	27.2	24.2
Ala	28.8	27.7
Val	25.4	25.7
Ile	24.3	25.8
Leu	26.8	24.0
Arg	35.0	30.4
His	1442.0	25.5
Ser	28.0	27.5
Phe	29.4	25.7
Met	1266.0	26.3
Trp	27.8	27.3

*Size is the hydrodynamic diameter of nanoparticles.

Table 3.3: PDI values of nanoparticles after growth reaction in presence of PMR and amino acids.

Amino acid	PDI values	
	9 mM	**50 μM**
Lys	0.25	0.20
Thr	0.27	0.24
Asn	0.26	0.20
Gln	0.22	0.20
Gly	0.25	0.20
Pro	0.28	0.23
Ala	0.22	0.22
Val	0.27	0.20
Ile	0.23	0.22
Leu	0.24	0.24
Arg	0.38	0.35
His	0.48	0.2
Ser	0.24	0.23
Phe	0.23	0.22
Met	0.24	0.21
Trp	0.24	0.20

The zeta potential of the growth controlled nanoparticles at 50 μM was almost same at 9 mM of amino acid. (Figure 3.21, Table 3.4)
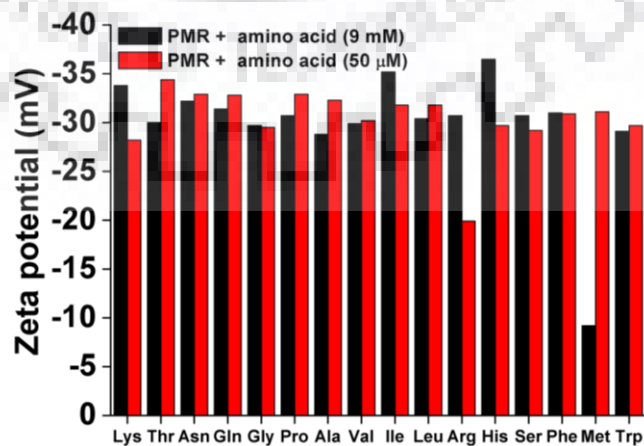
Figure 3.21 Zetapotential of nanoparticles after growth reaction at concentration of 9 mM and 50 μM of amino acids.

Table 3.4: Zeta potential of nanoparticles after growth reaction in presence of PMR and amino acids.

Amino acid	Zeta potential (mV)	
	9 mM	**50 μM**
Lys	-33.8	-28.2
Thr	-30.0	-34.4
Asn	-32.2	-32.9
Gln	-31.4	-32.8
Gly	-29.7	-29.5
Pro	-30.7	-32.9
Ala	-28.8	-32.3
Val	-29.9	-30.2
Ile	-35.2	-31.8
Leu	-30.4	-31.8
Arg	-30.7	-19.9
His	-36.5	-29.7
Ser	-30.7	-29.2
Phe	-31.0	-30.9
Met	-9.2	-31.1
Trp	-29.1	-29.7
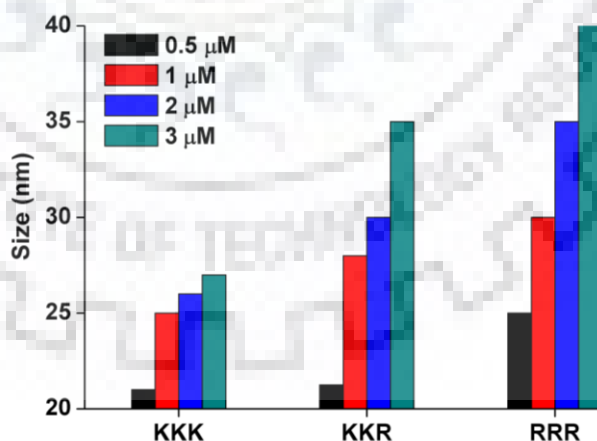
Figure 3.22 Size of the nanoparticles of the solutions after growth reactions in presence of PMR and peptide KKK, KKR and RRR at different concentrations.

In case of peptide based reaction the hydrodynamic radii of nanoparticles increased after growth reaction with combination of PMR and increasing concentration of the peptide (Figure 3.22, Table 3.5). The PDI values of the solutions after the growth reaction decreased

with increasing concentration of peptides (Figure 3.23, Table 3.6). However the ζ-potentials of the gold nanoparticles after the growth reaction remained almost constant in all the peptides (Figure 3.24, Table 3.7).

Table 3.5: Size of nanoparticles after growth reaction in presence of PMR and peptide at different concentrations.

Peptide	*Size(nm) after growth reactions			
	0.5µM	1µM	2µM	3µM
KKK	25.0	25.0	26.0	27.0
KKR	21.3	28.0	30.0	35.0
RRR	25.0	30.0	35.0	40.0

* Size is the hydrodynamic diameter of the nanoparticles.
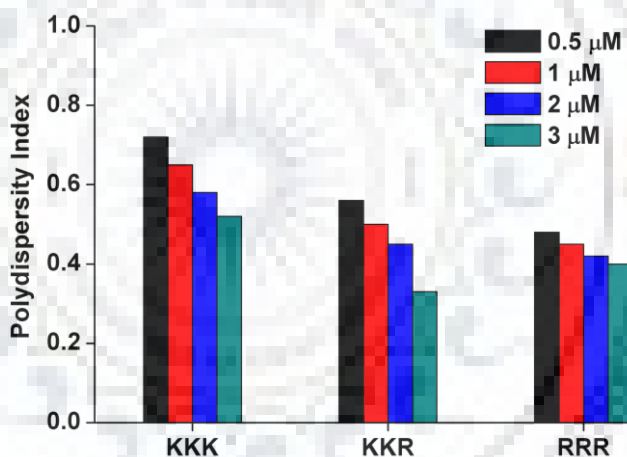
Figure 3.23 Polydispersity of the nanoparticles of the solutions after growth reactions in presence of PMR and peptide KKK, KKR and RRR at different concentrations.

Table 3.6: PDI values of nanoparticles after growth reaction in presence of PMR and peptide at different concentrations.

Peptide	PDI valued after growth reactions			
	0.5µM	1µM	2µM	3µM
KKK	0.72	0.65	0.58	0.52
KKR	0.56	0.50	0.45	0.33
RRR	0.48	0.45	0.42	0.40
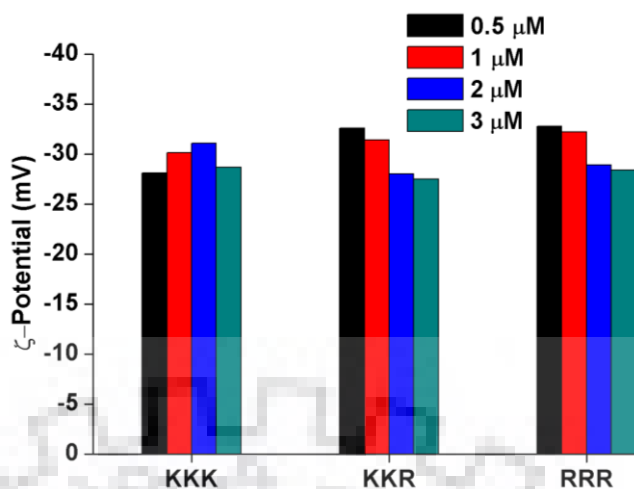
Figure 3.24 Zeta potential of the nanoparticles after growth reactions in presence of PMR and peptide KKK, KKR and RRR at different concentrations.

Table 3.7: Zeta potential of nanoparticles after growth reaction in presence of PMR and peptide at different concentrations.

Peptide	Zeta potential (mV) after growth reactions			
	0.5μM	1μM	2μM	3μM
KKK	-28.1	-30.1	-31.1	-28.7
KKR	-32.6	-31.4	-28.0	-27.5
RRR	-32.8	-32.2	-28.9	-28.4

3.5 CONCLUSION

Gold nanoflower based strategy were developed to detect the substitution of Lys to Arg in the peptide sequence. The interference from other amino acids was sequentially nullified and the detection of the peptide was performed within 3 μM concentration range. The detection strategy was guided by the strongest interaction between arginine and DNA sequence. The amine modified DNA sequence was chosen for its unique property of gold nanoflower formation during the growth reaction in presence of gold nanoparticle seed. The methodology was further explored for the single substitution of Lys by Arg in the peptide sequence.

SECTION B

Bio-enabled strategies are an effective approach to nucleate, grow, stabilize, activate and organize inorganic nanoparticles in aqueous media.[359] Amino acids play an important role in the development of chirality of gold nanoparticle via growth-mediated synthesis.[209] This growth-based material development was considered as milestone in the development of device, which can control the light rotation.[360] Chemiluminescence based silver nanoparticle was explored to differentiate the group of selected amino acids, where Thr has been only considered among the amino acids containing polar uncharged side chain- Ser, Thr, Asn and Glu (AA$_{pusc}$).[361] Another differentiation methodology involves interaction with serum albumin, intracellular uptake and cytotoxicity among another group of selected amino acids, where Ser was the only amino acids from the AA$_{pusc}$.[362]

DNA-protein interaction is the basic understanding of complex biological systems.[363] This interaction is quite different from covalent interaction even for the case of specific DNA binding proteins.[364] The theoretical predictions [365] as well as experimental proofs [366] of DNA-protein interactions are quite evident in recent time literature. The weak interactions, which are responsible for DNA-protein interactions specifically through the amino acids within proteins, are van der Waals contact, hydrogen bonding and water mediated bonding interactions. These weak interactions between these amino acids and different part of DNAs and their critical contributions were earlier reported by Thornton and coworkers.[358] Scheraga and coworkers carried out the interaction between amino acids containing the polar uncharged side chain and DNA computationally with the help of physics based potentials.[367]

Although there are few theortical models [368,369] for differentiating the AA$_{pusc}$ there is no experimental methodology to differentiate their interactions with DNA. The target of the work was to differentiate the amino acids containing the polar uncharged side chain, Ser, Thr, Arg and Glu (AA$_{pusc}$). To assess the differentiation, interaction between amine modified DNAs– PMR, MMR and AA$_{pusc}$ were studied from time dependent growth of gold nanoparticles. The amino acids were differentiated based on their van der Waals interaction with the DNAs (Scheme 3.3).
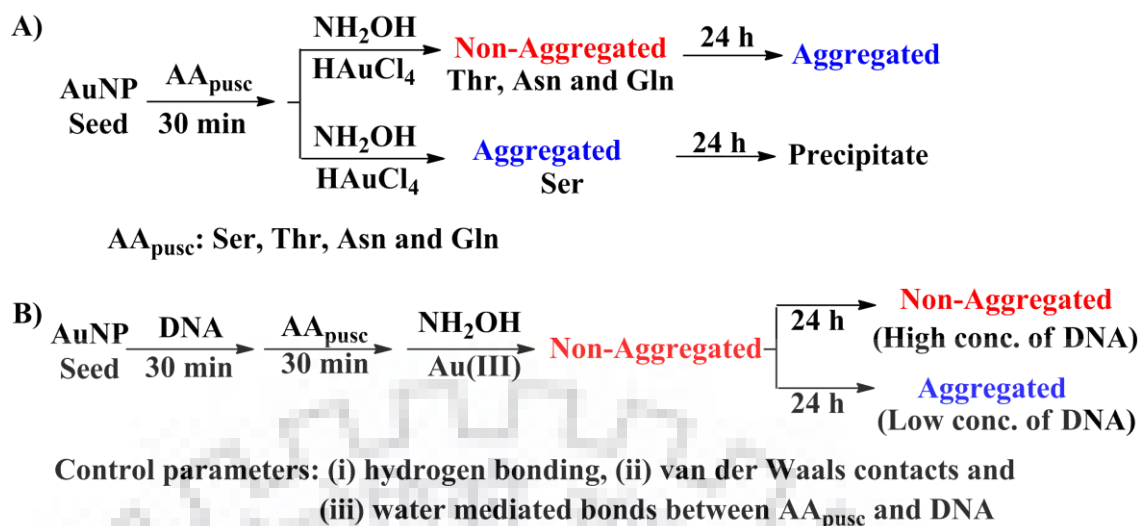
Scheme 3.3 (A)Separation of Ser from other three amino acids by growth reaction of AuNP seed; (B) growth reaction of AuNP seed in presence of different concentrations of DNAs and AA$_{pusc}$ for time dependent studies of aggregation vs non-aggregation.

3.6 EXPERIMENTAL SECTION

3.6.1 Chemicals and Materials

All the reagent grade materials used unless specified were discussed previously.

3.6.2 Instrumentation

Absorption spectroscopy, TEM and DLS measurements were done as described in the earlier section of this chapter. The UV-Vis absorbance for 24 h was monitored with a time interval of one hour.

3.7 Synthetic Procedures

Synthesis of seed stock solution

The seed solution was prepared as previously mentioned. The seed solution was diluted and absorbance was adjusted to 0.5 for use in further reactions. In all reactions the final volume was maintained to 340 μL.

Growth reactions of gold nanoparticles with L-amino acids

340 μL gold nanoparticles seed solutions were incubated with 9 mM amino acid for 30 minutes. 3 μL, 200 mM NH$_2$OH (adjusted to pH 5 with NaOH) was added to these solutions and stirred vigorously for 10 minutes. 5 μL of 0.8% (w/v) HAuCl$_4$ was added to these solutions to initiate the reduction reaction.

Growth reactions of gold nanoparticles with DNA and L-amino acids

340 μL gold nanoparticles seed solutions were incubated with DNA (600 nM) for 30 minutes. 9 mM amino acid was added and further incubated for 30 minutes.3 μL, 200 mM NH_2OH (adjusted to pH 5 with NaOH) was added to these solutions and stirred vigorously for 10 minutes. 5 μL of 0.8% (w/v) $HAuCl_4$ was added to these solutions to initiate the reduction reaction.

3.8 RESULTS AND DISCUSSION

3.8.1 Synthesis and characterization

Growth reactions of AuNP seeds were performed by incubating with AApusc for 30 minutes. Hydroxylamine as reducing agent was added and the reaction was vigorously shaken. $HAuCl_4$ was added to complete the reduction reaction and the color change was observed within seconds. The resulting solutions were characterized by absorption spectroscopy, TEM, and DLS measurements.

3.8.2 Time dependent growth reaction with amino acid

Time dependent growth reactions were studied with AA_{pusc}. Among these Ser based reaction demonstrated a change in color from red to blue whereas red color was maintained for Thr, Asn and Gln after addition of gold. The growth solutions were kept at room temperature and colors of the red solutions turned blue gradually with time whereas blue solution settled as precipitate. Such visual color changes were consistent with the aggregation and non aggregation of gold nanoparticles. The absorption spectra showed a single peak for red solutions whereas dual peak was observed for blue solutions after gold addition (Figure 3.25).
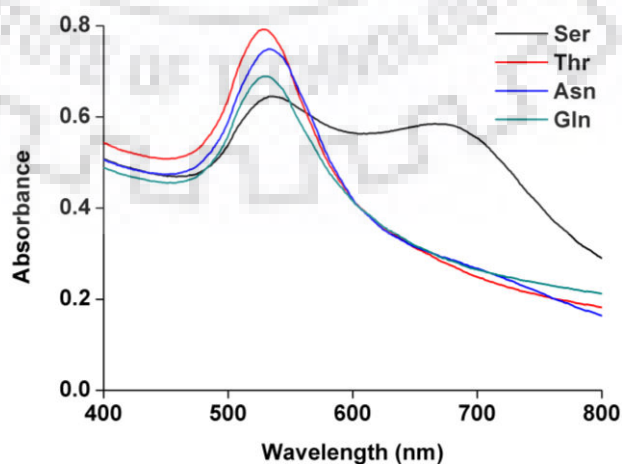
Figure 3.25 Absorption spectra of solutions after growth reactions in presence of Ser, Thr, Asn and Gln.

The absorption of the solutions was again checked after 24 hours Thr, Asn and Gln developed dual peak whereas decrease in intensity of peak was observed for Ser based reaction (Figure 3.26).
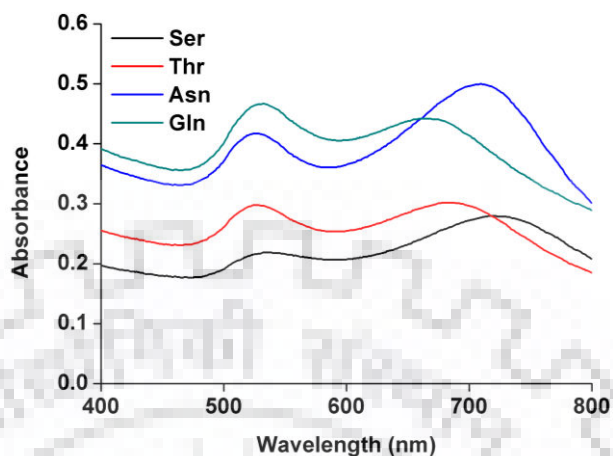
Figure 3.26 Absorption spectra of solutions after growth reactions in presence of Ser, Thr, Asn and Gln taken after 24 h.
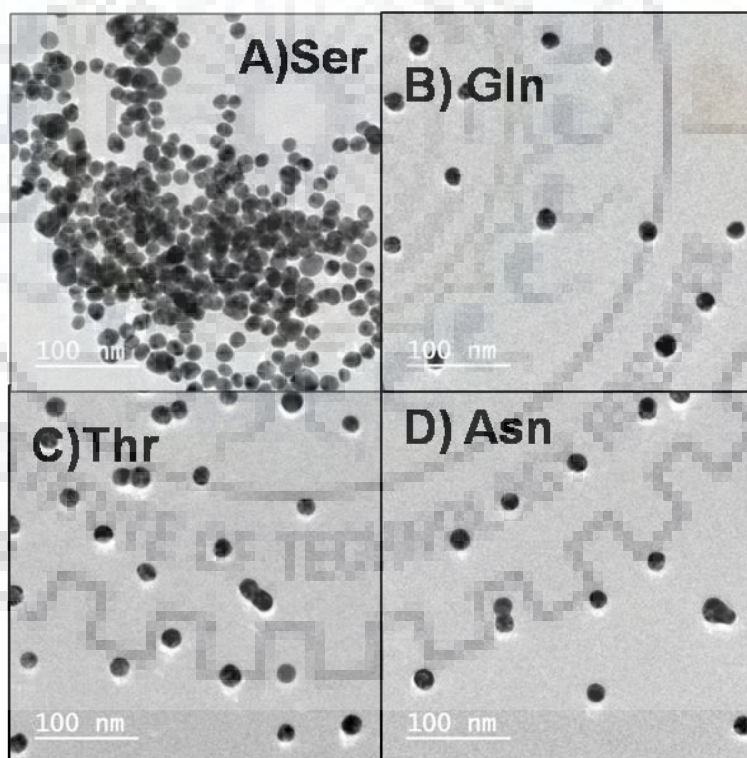
Figure 3.27 TEM images of nanoparticles after growth reactions in presence of Ser, Thr, Asn and Gln taken at 0 h.

TEM images confirmed the formation of non-aggregated nanoparticles for red solutions and aggregated nanoparticles for blue solutions (Figure 3.27) at 0 h. This created selectivity

among these amino acids where Ser was differentiated from the other three amino acids within AA$_{pusc}$. The TEM results after 24 h showed the formation of aggregated nanoparticles for Thr, Asn and Gln based reactions after 24 h (Figure 3.28). Size distribution histograms of the non-aggregated nanoparticles were shown Figure 3.29. TEM analyses showed the average size of the nanoparticles were 17±3.69 nm, 20±2.28 nm and 17±3.34 nm synthesized with Glu, Thr and Asn respectively.
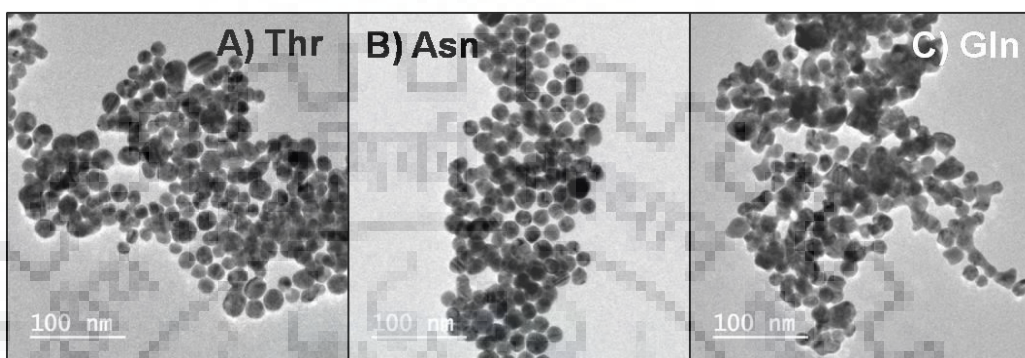
Figure 3.28 TEM images of nanoparticles after growth reactions in presence of Thr, Asn and Gln taken after 24 h.
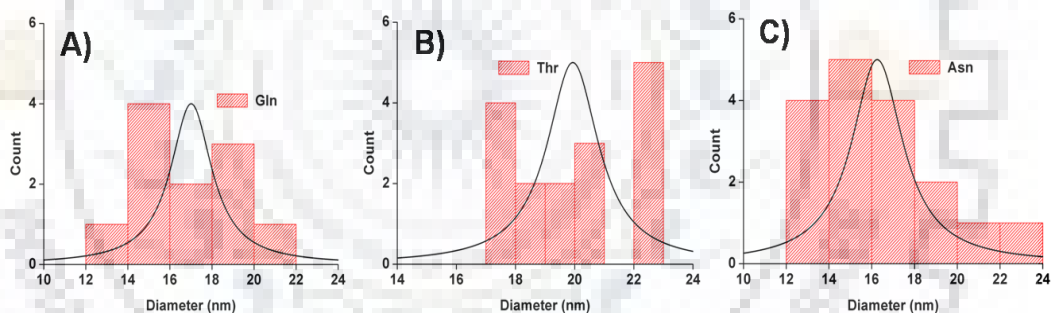
Figure 3.29 Size distribution histograms of nanoparticles after growth reactions in presence of Gln, Thr, and Asn.

3.8.3 Time dependent growth reaction with DNA and amino acid

In order to differentiate Thr, Asn and Gln within AA$_{pusc}$, 600 nM amine modified DNA (PMR) was introduced in to the growth solution prior to the AA$_{pusc}$ addition. The affinity of the growth was affected in the presence of PMR. In all the cases red solutions were obtained after the addition of gold. The absorption spectra showed single peak in all the cases (Figure 3.30A). The red colour was maintained for next 24 h. The absorption was again checked after 24h, no shift in the absorption peak was observed (Figure 3.30B). The results suggested that PMR inhibited the aggregation in all the cases. TEM results also confirmed the inhibition of

aggregation in these growth controlled reactions. TEM images were taken after 24 hours and spherical nanoparticles were formed in all cases (Figure 3.31).
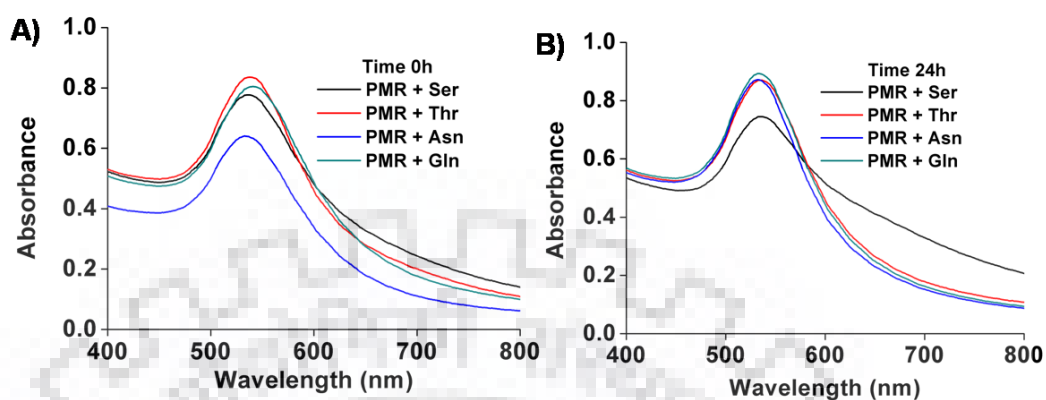
Figure 3.30 Absorption spectra of solutions after growth reactions in presence of PMR and AA$_{pusc}$ at 0 h and 24 h.
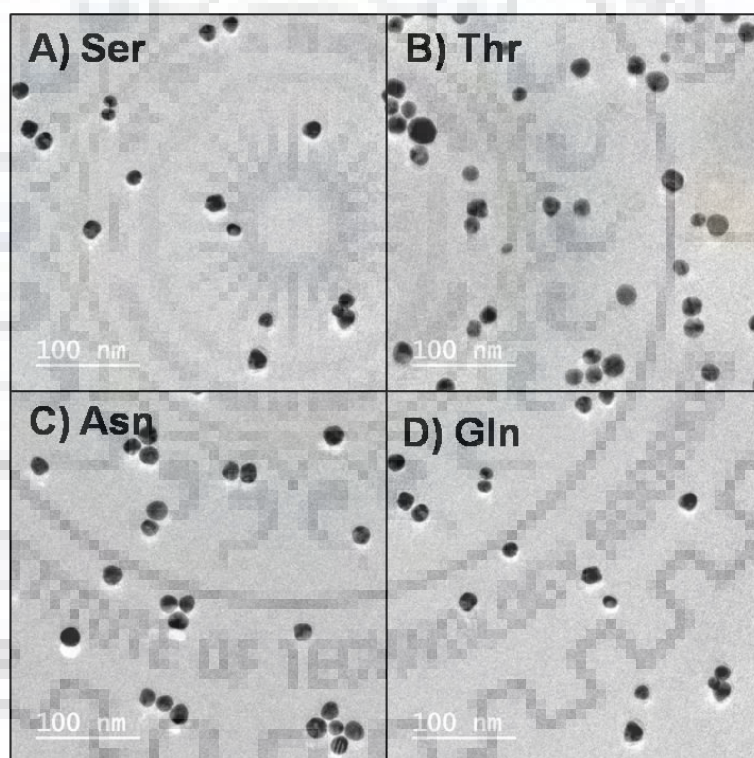
Figure 3.31 TEM images of nanoparticles after the growth reaction in presence of PMR and AA$_{pusc}$ after 24 h.

Size distribution histograms of the nanoparticles were shown Figure 3.32.The nanoparticles average size of the nanoparticles were 16±2.68 nm, 17±2.45 nm, 18±2.89 nm and 16±2.30 nm synthesized with Ser, Thr, Asn and Glu respectively in presence of PMR.
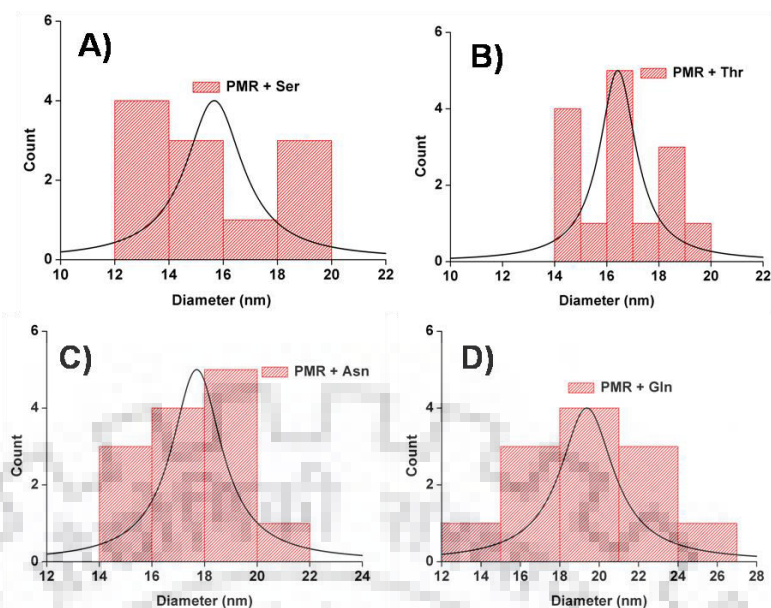
Figure 3.32 Size distribution histograms of the nanoparticles synthesized with Ser, Thr, Asn and Glu in presence of PMR.

The introduction of thymine in presence of adenine of the amine modified DNA sequence was reported to control the shape of the growth mediated product of AuNP in absence of any amino acid.[136] Further the growth reactions were done by incubating the nanoseeds with MMR before addition of amino acids. The growth reaction in presence of Ser gradually developed blue colour with time. The growth reactions with Thr, Asn and Gln developed red color after addition of gold and the red color was maintained for another 24 h (Figure 3.33A).Absorption spectra showed development of dual peak after 24 h in case of Ser based reaction whereas single peak was observed for Thr, Asn and Gln even after 24 h (Figure 3.33B). The intensity of the dual peak was very low. TEM images confirmed the aggregated nanoparticles for Ser based reactions while non-aggregated nanoparticles for Thr, Asn and Gln based reactions (Figure 3.34).
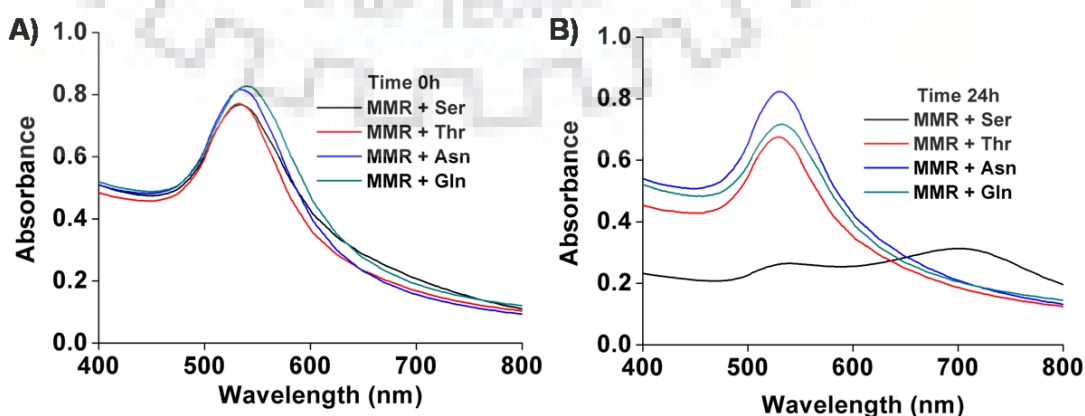
Figure 3.33 Absorption spectra of solutions after growth reactions in presence of MMR and AA$_{pusc}$ at 0 h (A) and 24 h (B).
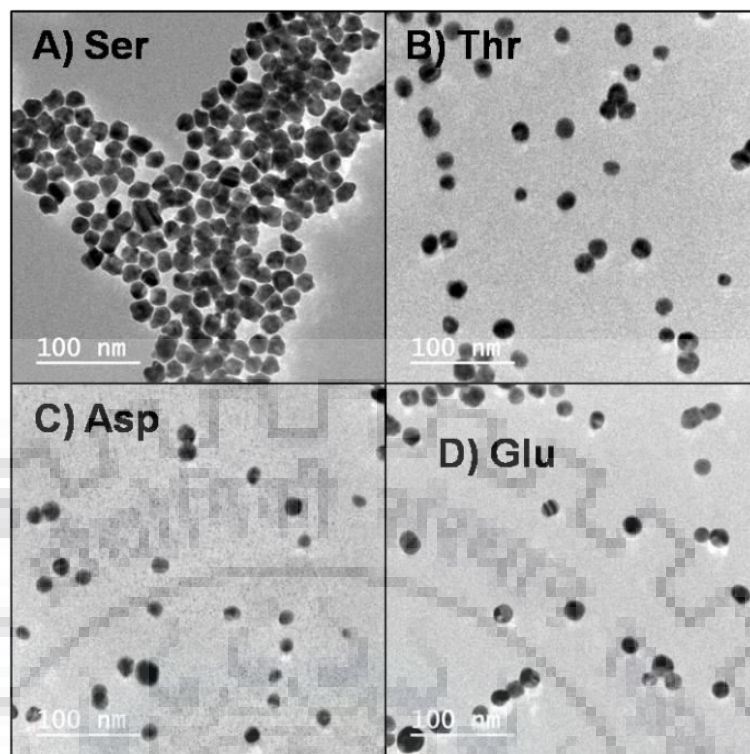
Figure 3.34 TEM images of nanoparticles after the growth reaction in presence of MMR and AA$_{pusc}$ after 24 h.

Size distribution histograms of the nanoparticles were shown in Figure 3.35. TEM analysis showed the average sizes of the nanoparticles synthesized with Thr are 19±2.12 nm, with Asn are 15±3.13 nm and with Glu are 18±2.39 nm
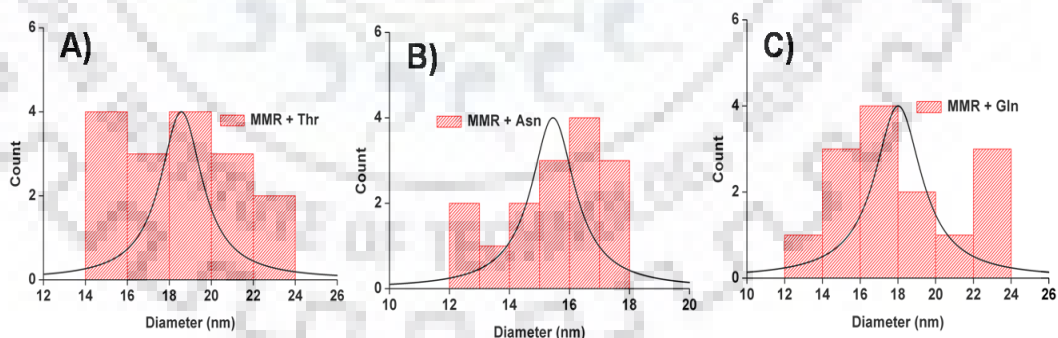
Figure 3.35 Size distribution histograms of the nanoparticles synthesized with Thr, Asn, and Glu in presence of MMR.

3.8.4 Time dependent absorption of growth reactions

The time dependent growth of the nanoparticles was monitored for period of 24 h. The spectral changes for Ser based reaction showed decrease in intensity without changing the position of peaks over a period of 24h. This diminishing factor was attributed to precipitation of the

materials as the reaction proceeded. Absorption spectra analysis for Thr, Asn and Gln showed decrease in intensity for SPR at 527 nm with the development of new absorption peak at longer wavelength (around 700 nm) over period of 24 h (Figure 3.36). Comparison of the absorption spectra for Thr, Asn and Gln suggested the aggregation process was slow in case of Glu than that of Asn and Thr. The absorption analysis of the growth reactions in presence of PMR and AA_{pusc} did not show any shift in the absorption peak over a period of 24 h rather a slight increase in intensity occurred suggested the aggregation process were stopped by the DNA (Figure 3.37). Reactions in presence of MMR and AA_{pusc} also did not show any shift in SPR peak for Thr, Asn and Gln based reaction but for Ser based reaction development of second peak at longer wavelengths gradually occurred with time and after 12 h the intensity of the peak started decreasing (Figure 3.38).
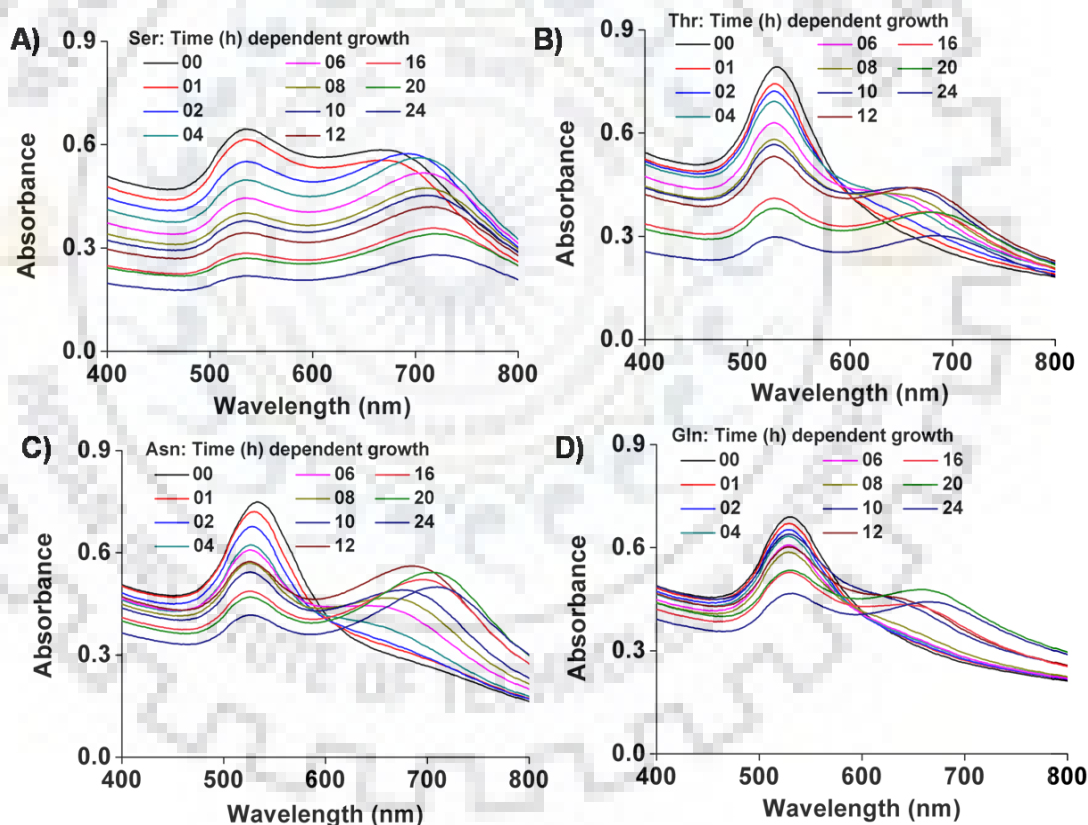
Figure 3.36 Time dependent absorption spectra of solutions after growth reactions in presence of AA_{pusc} over a period of 24 h.
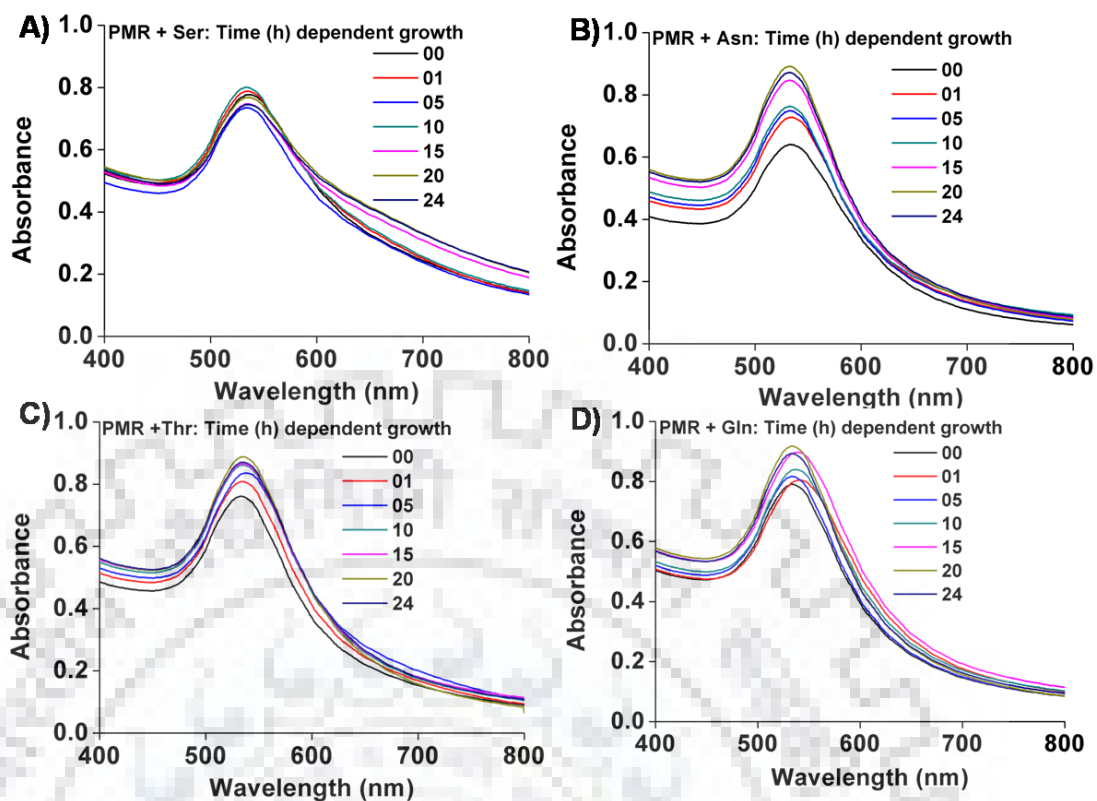
Figure 3.37 Time dependent absorption spectra of solutions after growth reactions in presence of PMR and AA$_{pusc}$ over a period of 24 h.
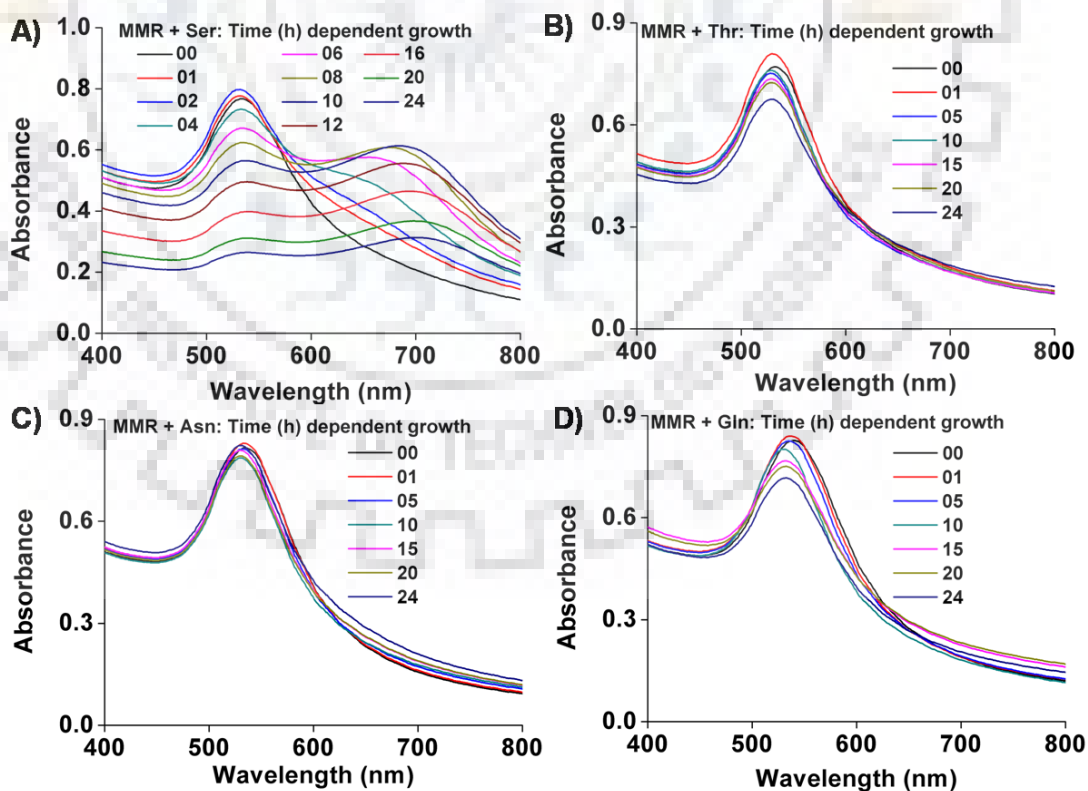
Figure 3.38 Time dependent absorption spectra of solutions after growth reactions in presence of MMR and AA$_{pusc}$ over a period of 24 h.

3.8.5 DLS measurements

To address the change in size of nanoparticles DLS measurements of the nanoparticle solutions were conducted over a time period of 12 hours. The average size of the nanoparticles increased with time and the increase was sharp in case of Ser based reaction than for Thr, Asn, and Gln. DLS spectra suggested average size of the nanoparticles for Ser based reaction increased sharply within one hour and continued to increase up to five hours and after that size remained constant (Figure 3.39A, Table 3.8). For Thr, Asn and Gln based reactions increase in the size was also observed but not so sharp over a period of four hours and after that size increased sharply and the aggregation process followed a sigmoid pattern (Figure 3.39 B, C, D Table 12).The change in size for the combination of PMR and AA_{pusc} was not observed with time confirmed the inhibition of aggregation (Figure 3.39A–D). But the change of sizewas observed for the combination of MMR and Ser with time (Figure 3.39A). Initially the size increased slowly for 2 hours and then sharply increased with time indicated the slow rate of aggregation. The combination of MMR and other three amino acids (Thr, Asn and Gln) also did not show any change in the size (Figure 3.39B–D).
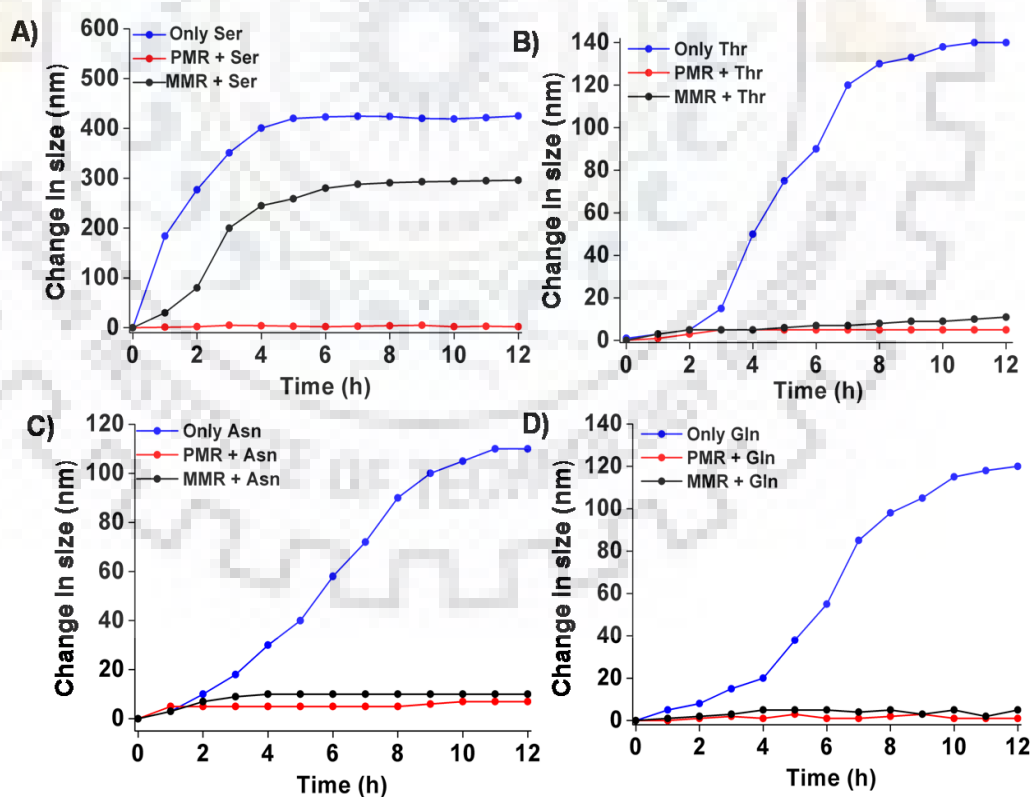
Figure 3.39 DLS analysis of the growth reactions in presence or absence of DNA over a time period of 12 h.

Table 3.8: Size of nanoparticles after growth reaction over time period of 12 h.

Time (h)	*Size (nm) of nanoparticles after growth reaction			
	Serine	**Threonine**	**Aspargine**	**Glutamine**
0	335	525	525	525
1	519	527	528	530
2	461	530	535	533
3	535	540	543	540
4	582	575	555	545
5	420	597	565	563
6	604	615	583	580
7	608	645	597	610
8	609	655	615	623
9	605	658	625	630
10	604	663	630	640
11	607	665	635	643
12	610	665	635	645

*Size is the hydrodynamic diameter of nanoparticles.

The polydispersity was almost constant with respect to time for Ser based reactions and the PDI values increased in presence of DNA. The polydispersity was higher with combination of PMR and Ser (Figure 3.40, Table 3.9).
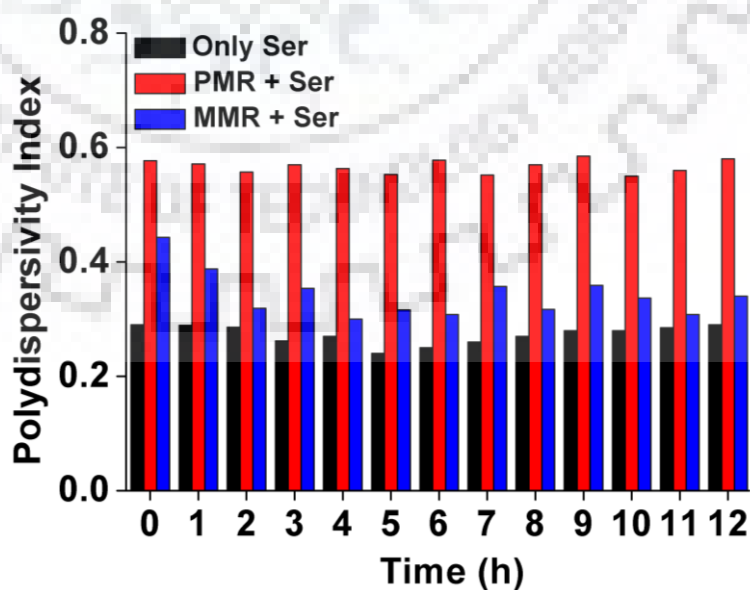
Figure 3.40 Polydispersity of the growth solutions after growth reaction for Ser based reaction over a time period of 12 h.

Table 3.9: PDI values of Ser based reactions.

Time (h)	PDI values		
	Only Ser	**PMR +Ser**	**MMR+ Ser**
0	0.30	0.58	0.44
1	0.29	0.571	0.39
2	0.29	0.56	0.32
3	0.26	0.57	0.35
4	0.27	0.56	0.30
5	0.24	0.55	0.32
6	0.25	0.58	0.31
7	0.26	0.55	0.36
8	0.27	0.570	0.32
9	0.28	0.59	0.359
10	0.28	0.55	0.34
11	0.29	0.56	0.31
12	0.29	0.58	0.34

The surface charge (zeta potential) also remained constant with respect to time. The zeta potential values were high for the combination of PMR and Ser and decreased for the combination of MMR and Ser and only Ser based reaction (Figure 3.41, Table 3.10)
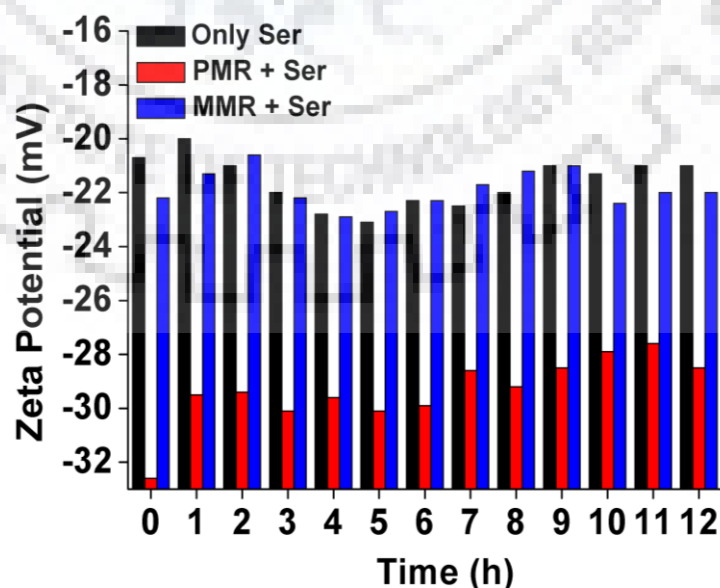
Figure 3.41 Zeta potential of the nanoparticles after growth reaction for Ser based reaction over a time period of 12 h.

Table 3.10: Zeta potential of nanoparticles for Ser based reactions.

Time (h)	Zeta potential (mV)		
	Only Ser	**PMR + Ser**	**MMR + Ser**
0	-20.7	-32.6	-22.2
1	-20	-29.5	-21.3
2	-21	-29.4	-20.6
3	-22	-30.1	-22.2
4	-22.8	-29.6	-22.9
5	-23.1	-30.1	-22.7
6	-22.3	-29.9	-22.3
7	-22.5	-28.6	-21.7
8	-22.0	-29.2	-21.2
9	-21.0	-28.5	-21
10	-21.3	-27.9	-22.4
11	-21.0	-27.6	-22.0
12	-21.0	-28.5	-22.0

The monodispersity increased with respect to time in case of only Thr based reaction while the polydispersity increased with respect to time for combination of PMR and Thr and the PDI values remained constant for combination of MMR and Thr (Figure 3.42, Table 3.11).
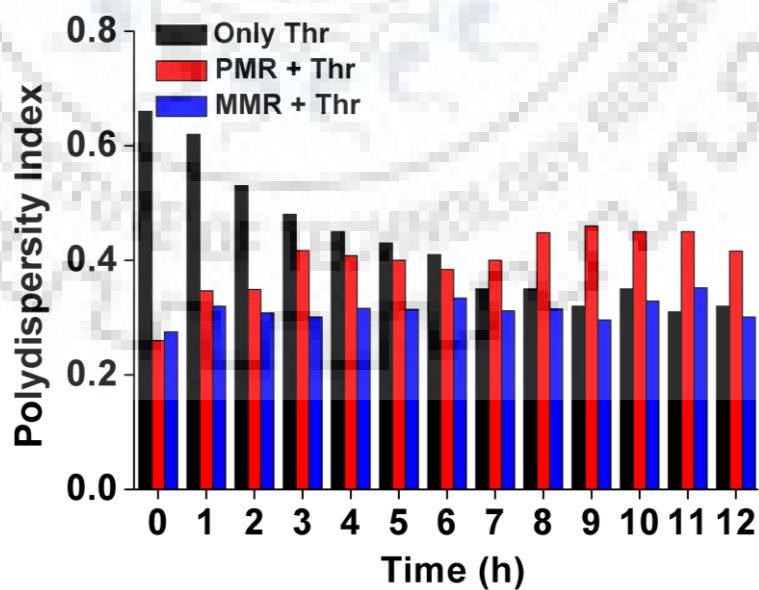
Figure 3.42 Polydispersity of the growth solutions after growth reaction for Thr based reaction over a time period of 12 h.

Table 3.11: PDI values of Thr based reactions.

Time (h)	PDI values		
	Only Thr	**PMR +Thr**	**MMR+ Thr**
0	0.66	0.26	0.28
1	0.62	0.35	0.32
2	0.53	0.35	0.30
3	0.48	0.417	0.30
4	0.45	0.40	0.32
5	0.43	0.40	0.31
6	0.41	0.39	0.33
7	0.35	0.4	0.31
8	0.35	0.44	0.32
9	0.32	0.46	0.30
10	0.35	0.45	0.30
11	0.31	0.45	0.36
12	0.32	0.416	0.30

The zeta potential decreased with respect to time for only Thr based reaction while the zeta potential was constant for the combination of DNA and Thr with respect to time. The zeta potential values were high for the combination of DNA and Thr and low for only Thr based reaction (Figure 3.43, Table 3.12).
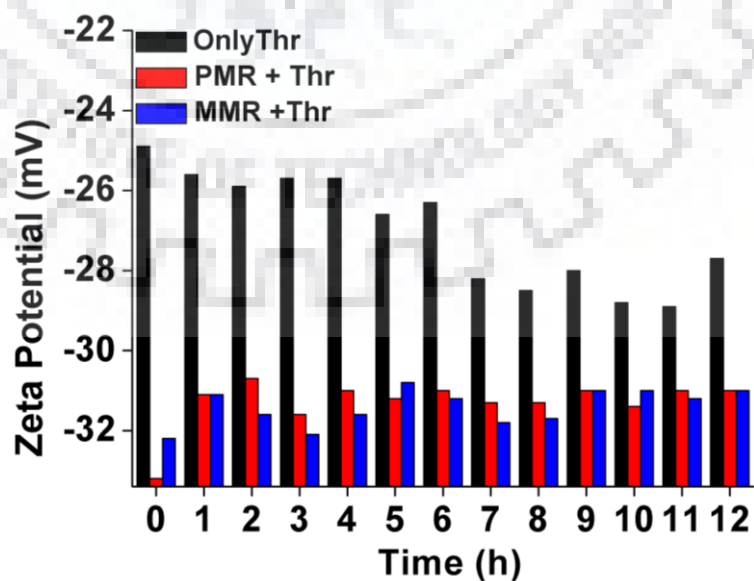
Figure 3.43 Zeta potential of the nanoparticles after growth reaction for Thr based reaction over a time period of 12 h.

Table 3.12: Zeta potential of nanoparticles for Thr based reactions.

Time	Zeta potential (mV)		
	Only Thr	**PMR + Thr**	**MMR + Thr**
0	-24.9	-33.2	-32.2
1	-25.6	-31.1	-31.1
2	-25.9	-30.7	-31.6
3	-25.7	-31.6	-32.1
4	-25.7	-31	-31.6
5	-26.6	-31.2	-30.8
6	-26.3	-31	-31.2
7	-28.2	-31.3	-31.8
8	-28.5	-31.3	-31.7
9	-28	-31	-31
10	-28.8	-31.4	-31
11	-28.9	-31	-31.2
12	-27.7	-31	-31

The polydispersity was almost constant with respect to time for only Asn based reactions and increased in presence of DNA. The PDI values were higher with combination of DNA and Asn (Figure 3.44, Table 3.13).
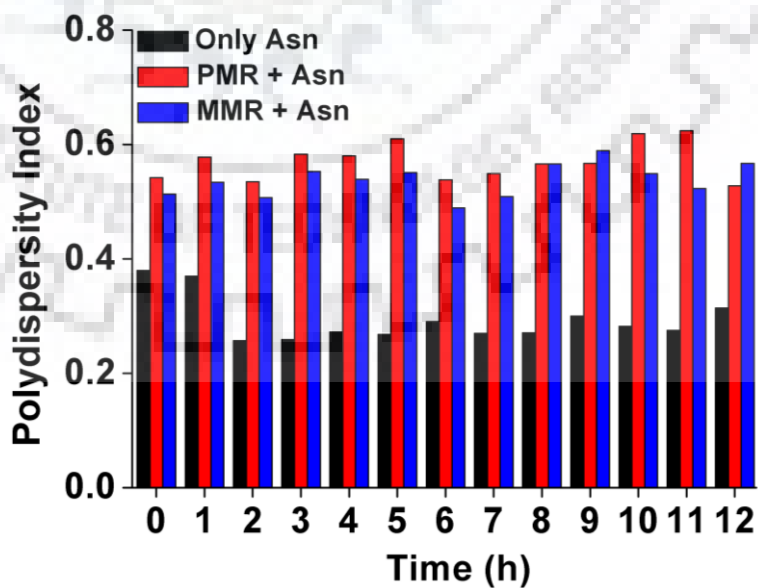
Figure 3.44 Polydispersity of the growth solutions after growth reaction for Asn based reaction over a time period of 12 h.

Table 3.13: PDI values of Asn based reactions.

Time (h)	PDI values		
	Only Asn	**PMR + Asn**	**MMR+ Asn**
0	0.38	0.54	0.51
1	0.37	0.58	0.53
2	0.257	0.53	0.50
3	0.26	0.58	0.55
4	0.27	0.58	0.54
5	0.27	0.61	0.55
6	0.29	0.54	0.49
7	0.27	0.55	0.50
8	0.27	0.56	0.57
9	0.30	0.57	0.59
10	0.28	0.62	0.55
11	0.27	0.62	0.52
12	0.31	0.53	0.57

The change in the zeta potential was observed for the combination of PMR and Asn or only Asn based reaction but was constant for the combination of MMR and Asn with respect to time. The zeta potential value decreased for the combination of MMR and Asn (Figure3.45, Table 3.14).
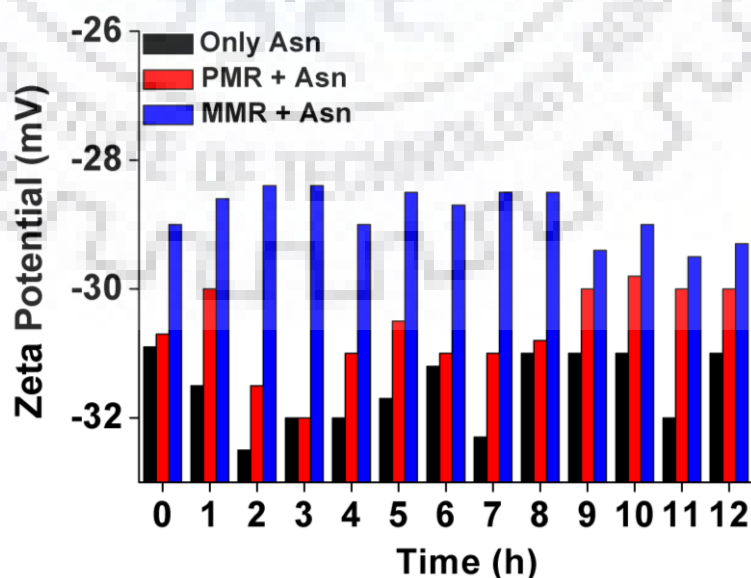
Figure 3.45 Zeta potential of the nanoparticles after growth reaction for Asn based reaction over a time period of 12 h.

Table 3.14: Zeta potential of nanoparticles for Asn based reactions.

Time (h)	Zeta potential (mV)		
	Asn	**PMR + Asn**	**MMR + Asn**
0	-30.9	-30.7	-29.0
1	-31.5	-30.0	-28.6
2	-32.5	-31.5	-28.4
3	-32.0	-32.0	-28.4
4	-32.0	-31.0	-29.0
5	-31.7	-30.5	-28.5
6	-31.2	-31.0	-28.7
7	-32.3	-31.0	-28.5
8	-31.0	-30.8	-28.5
9	-31.0	-30.0	-29.4
10	-31.0	-29.8	-29.0
11	-32.0	-30.0	-29.5
12	-31.0	-30.0	-29.3

The combination of DNA and Gln showed increase in the polydispersity and remained constant with respect to time for all Gln based reactions. The PDI values were higher for the combination of PMR and Gln (Figure 3.46, Table 3.15). The zeta potential remained almost constant for all Gln based reactions (Figure 3.47, Table 3.16).
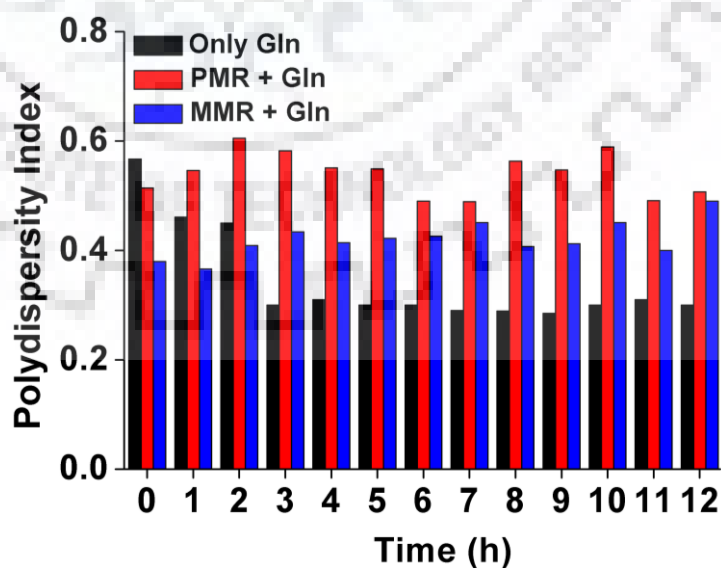
Figure 3.46 Polydispersity of the growth solutions after growth reaction for Gln based reaction over a time period of 12 h.

Table 3.15: PDI values of Glu based reactions.

Time (h)	PDI values		
	Only Gln	**PMR + Gln**	**MMR+ Gln**
0	0.57	0.51	0.38
1	0.46	0.54	0.37
2	0.45	0.60	0.40
3	0.3	0.58	0.43
4	0.31	0.55	0.41
5	0.3	0.55	0.42
6	0.3	0.49	0.42
7	0.29	0.49	0.45
8	0.29	0.56	0.40
9	0.28	0.55	0.41
10	0.30	0.59	0.45
11	0.31	0.49	0.40
12	0.30	0.50	0.49
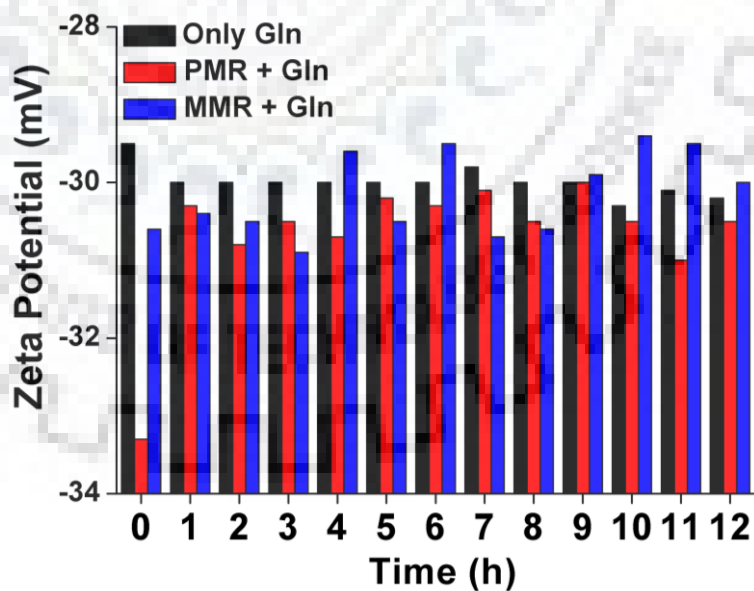
Figure 3.47 Zeta potential of the nanoparticles after growth reaction for Gln based reaction over a time period of 12 h.

Table 3.16: Zeta potential of nanoparticles for Glu based reactions.

Time (h)	Zeta potential (mV)		
	Glu	**PMR + Glu**	**MMR + Glu**
0	-29.5	-33.3	-30.6
1	-30.0	-30.3	-30.4
2	-30.0	-30.8	-30.5
3	-30.0	-30.5	-30.9
4	-30.0	-30.7	-29.6
5	-30.0	-30.2	-30.5
6	-30.0	-30.3	-29.5
7	-29.8	-30.1	-30.7
8	-30.0	-30.5	-30.6
9	-30.0	-30.0	-29.9
10	-30.3	-30.5	-29.4
11	-30.1	-31.0	-29.5
12	-30.2	-30.5	-30.0

3.8.6 Sensitivity of DNA for controlling the aggregation.

Thronton et al. investigated the anino acid DNA interactions and found that two-third of the interactions involve the van der Waals contact compared to one sixth each for hydrogen bonding and water mediated bonds.[358] In order to rationalize the aggregation difference for 600 nM PMR and MMR with 9 mM Ser, we compared the weak interactions between DNA and Ser. Among the three types of weak interactions, hydrogen bonding and water-mediated bonding affinities do not vary between thymine and adenine with Ser (Table 3.1 and 3.17).[358] However, the van der Waals contact, which is negligible in the case of adenine-Ser interaction, shows significant interaction in thymine-Ser case (Table 3.18).[358] This van der Waals contact was responsible for slow aggregation from the combination of MMR and Ser. In order to confirm the presence of van der Waals contact in the time dependent aggregation process with Ser, we lowered down the concentration of PMR to favor the aggregation. On the other hand, we increased the concentration of MMR to inhibit the aggregation in presence of Ser. In the case of PMR, addition of 60 nM DNA solution was required for the aggregation of AuNP after 12 h from the growth reaction, while for MMR, we required 8 μM solution to inhibit the process (Figure 3.48 and Table 3.19). The effective concentration of Ser, which was

required for the aggregation in each case, could be achieved only after fulfilling the requirement of van der Waals contact between Ser and adenine or thymine. Among weak interactions, van der Waals contact [238] between DNA and amino acid is known to cover two-third of all interactions for thermodynamic stability.

Table 3.17: Distribution of water-mediated bonds between amino acid Ser, Thr, Asp, Glu and DNA component.[358]

Amino acids	DNA Bases				DNA backbone		Total
	Thymine	Cytosine	Adenine	Guanine	Sugar	Phosphate	
Ser	7 (8.5)	14 (8.9)	- (10.4))	24 (17.5))	41(67.1	144 (88.7)	230 (201.1)
Thr	-(8.9)	5 (9.3)	11 (10.8)	42 (18.3)	74(70.1)	153 (92.7)	285 (210.2)
Asn	9 (9.8)	6 (10.2)	21 (11.9)	14 (20.1)	84(77.1)	102 (102.0)	236 (231.0)
Glu	13 (8.7)	6 (9.1)	26 (10.6)	36 (18.0)	76(68.7)	77 (90.9)	234 (206.1)

Therefore, 100 times higher concentration of MMR with respect to PMR concentration was justified for the aggregation process in presence of Ser due to more van der Waals contact between Ser and thymine. In order to check the effect of van der Waals effect among the other amino acids of AApusc family, the concentration of PMR and MMR were lowered down from 600 nM to observe the aggregation process. The critical concentrations (Figure 3.48), which were required for the aggregation process after 12 h, have been summarized in Table 3.19.

Table 3.18: Distribution of vander waals contacts between amino acid Ser, Thr, Asp, Glu and DNA component.[358]

Amino acids	DNA Bases				DNA backbone		Total
	Thymine	Cytosine	Adenine	Guanine	Sugar	Phosphate	
Ser	3 (1.7)	4 (2.2)	5 (3.6))	7 (3.5))	2 (1.6)	56 (42.1)	77 (54.7)
Thr	1 (1.5)	2 (1.9)	4 (3.1)	- (3.0)	- (1.4)	52 (36.2)	59 (47.0)
Asn	3 (2.1)	5 (2.7)	12 (4.5)	10 (4.3)	4 (1.9)	46 (52.0)	81 (67.5)
Gln	2 (1.3)	6 (1.7)	3 (2.8)	5 (2.7)	-(1.2)	37 (44.8)	53 (58.1)

Table 3.19 Concentration of minimum amount of amine modified DNAs required for the aggregation after 12 h of growth reactions in presence of 9 mM AA_{pusc}.

AA_{pusc}	Concentration of PMR	Concentration of MMR
Ser	60nM	7μM
Thr	0.4pM	4nM
Asn	30pM	3pM
Gln	4nM	30 nM

The concentration of PMR, which were required for aggregation with amino acids of AA_{pusc} family, follows the order Thr < Asn <Gln< Ser. This trend is simply follow the reverse order (Thr > Asn >Gln> Ser) of van der Waals contact between DNA and amino acids of AA_{pusc} family.[238] The significant difference of PMR concentration in the cases of Gln and Ser could be rationalized with the help of the size of these two amino acids.
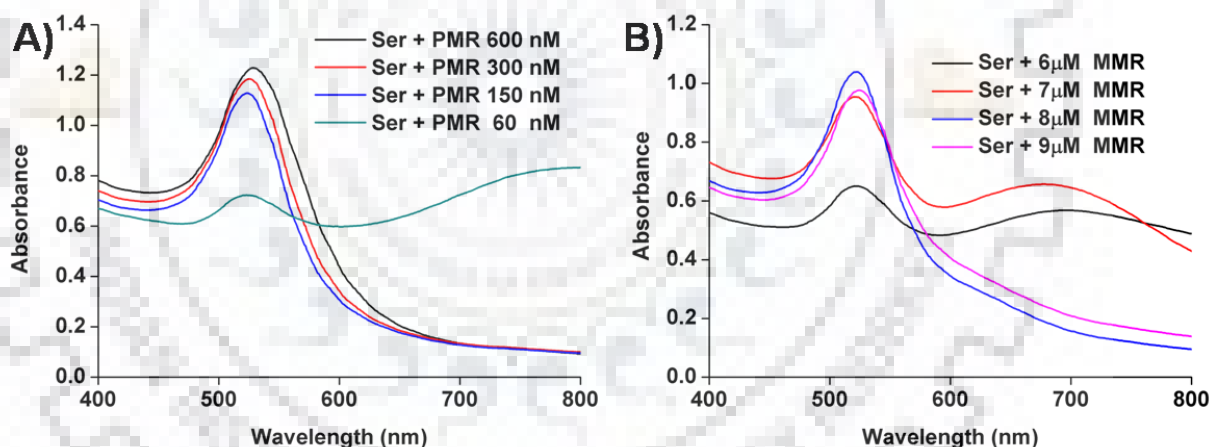
Figure 3.48 Absorption spectra after growth reaction with different concentrations of DNA in presence of Ser after 12h.

On the other hand, the concentration MMR, which was required for the amino acids of AApusc family, did not follow the similar strategy to that of PMR. In the case of Thr, the concentration of MMR was 10^4 times more with respect to PMR concentration (Figure 3.49 and Table 3.18). The concentrations of MMR were 117 and 7.5 times higher respectively with respect to PMR concentration for Ser and Gln. This trend is due to significant difference of van der Waals contact between adenine and thymine with these amino acids. Upon mutation from adenine to thymine, the order of van der Waals contacts show the trend Thr > Ser >Gln, which is similar to our observation. Interestingly, in the case of Asn, the MMR concentration was

found to be 10 times less than PMR concentration in the critical amount measurement for aggregation process. This is also similar to the theoretically predicted trend of Asn, where van der Waals contact decreases from adenine to thymine modification.[358]
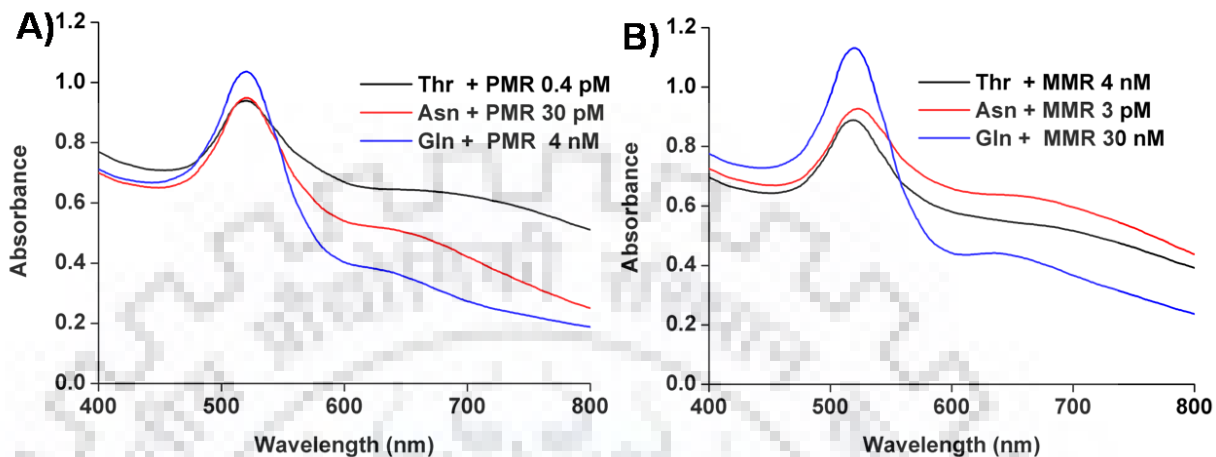
Figure 3.49. Absorption spectra after growth reaction with different concentrations of DNA in presence of Thr, Asn and Gln after 12h.

3.9 CONCLUSION

Growth-controlled reactions of gold nanoparticles with amino acids containing polar uncharged amino acids were investigated. The growth of gold nanoparticle resulted in aggregation either instantly or with time depending upon the nature of amino acids. The effect of the amine modified DNAs in order to control the aggregation of the gold nanoparticles after the growth reactions were systematically studied. The van der Waals contact between amino acids and nucleic bases such as adenine and thymine were explored for the controlled aggregation process of gold nanoparticle at sub-nanomolar concentration of amine modified DNAs The current strategy was successfully applied for the differentiation of four amino acids containing polar uncharged side chains via time dependent aggregation process in presence of super or subnanomolar concentration of two amine modified DNAs, where adenine in PMR sequence had been replaced with thymine in MMR.

Chapter 4

Gold iron-oxide nanocomposites for doxorubicin release and catalyst for oxygen evolution reactions

4.1 INTRODUCTION

Unequivocally nanotechnology plays crucial role in the upsurge of contemporary material science as well as biomedical research.[370] Among the Au-metal oxide nanocomposites, Au-Fe_xO_y have been implemented in diagnostic imaging[269−277], drug delivery[278−285] and catalysis[292−303]. The preparation of these Au nanocomposites often involved the utilization of Au nanoparticle seeds.[371] In the case of Au-Fe_xO_y nanocomposite synthesis, the most commonly used technique is the attachment of gold and iron oxide nanoparticles with organic or inorganic polymeric support followed by modular surface modifications.[372] In situ preparation of Au-Fe_xO_y nanocomposites generally involves reduction of Au(III) on Fe_xO_y core as the platform.[373] Alternate routes include the use of iron pentacarbonyl or iron-oleate as iron source at elevated temperature in inert atmosphere along with the gold nanoparticle as core in the composite.[374]

This chapter is divided into two sections. Section A describes the citrate stabilized Au-Fe_xO_y nanocomposites with variable exchange bias catalytic properties and drug release while Section B describes tryptophan stabilized Au-Fe_xO_y as catalysts for oxygen evolution reactions.

SECTION A

Exchange bias (EB) effect in the nanodomain [265−267] is a well-known phenomenon. Materials with EB has been successfully used in memory devices.[265−267] EB usually arises due to interaction between ferromagnetic and antiferromagnetic components of a system at their interface.[375] In the case of nanomaterials, several factors like size, crystallinity, oxidation state of the constituent elements play important roles in the EB strength.[375,376] In recent times, among gold nanocomposites, EB effect has been reported in Au-Fe_3O_4 core-shell[377] and nano-dumbbell.[378] Presence of FeO phase is quite common for such Au-Fe_3O_4 nanomaterials,[378,379] where the EB arises due to the interface of the antiferromagnetic FeO and ferromagnetic Fe_3O_4. This FeO phase is generally obtained as a reduced product of Fe_3O_4. In the present work, a facile synthetic route was proposed to vary Fe_xO_y compositions in a regulated fashion and thereby achieving control over exchange bias and coercivity with respect to variation of both iron content and temperature. Despite there being a handful of literature reports available on the skilful synthetic strategies of Au-metal oxide nanocomposites, there are no reports on a generalized synthetic methodology that could be utilized for the preparation of Au-Fe_xO_y nanocomposites with variable Au : Fe, more so

under amicable reaction conditions thereby achieving control over exchange bias, with respect to variation of both iron content and temperature.

4.2 EXPERIMENTAL SECTION

4.2.1 Chemicals and Materials

All reagent grade materials used unless specified were discussed previously. Iron powder was purchased from Himedia chemicals and nitro amines were purchased from sigma Aldrich. All glassware and stirrer bars were washed with freshly prepared aqua regia (mixture of 1:3 volume ratio of nitric acid: hydrochloric acid) then with Millipore water and dried in oven before use.

4.2.2 Instrumentation

Absorption Spectroscopy: Nanocomposite solutions were characterized using UV-Vis spectrometer (UV-1601, Shimadzu). Absorbance measurement was taken over 400-800 nm wavelength range.

Infrared Spectroscopy (IR): Nanocomposites were characterized using KBr pellets with Thermo Nikolet Nexus FT-IR spectrometer, with 50 scans and were reported in cm^{-1}.

Transmission Electron Microscopy (TEM): The TEM images were taken as described earlier.

Field Emission Scanning Electron Microscope (FE−SEM): The FE-SEM (Carl ZEISS Ultra plus Gemini, Germany) was employed to analyze the morphological features where all the samples were prepared by drop casting the solution on silicon wafers at 30 kV. The EDX analysis was carried out at least three different areas of the spot.

X-ray Photoelectron Spectroscopy (XPS): XPS experiment was performed with PHI 5000 Versa Prob II, FEI Inc. and C60 sputter gun have been used for characterization. The chemical states of the nanocomposites were characterized by XPS with mono chromatized Al K (α) excitation (h = 1486.6 eV). The C 1s (284.8eV) was used as a reference to calibrate the peak X-ray Photoelectron Spectroscopy (XPS) with Auger Electron Spectroscopy (AES) module positions of the elements. Gaussian method was used for curve fitting.

Superconducting quantum interference device (SQUID): The magnetization measurements (ZFC and FC) were performed using SQUID magnetometer (MPMS XL, Quantum Design Ever cool) at a field of 1000 Oe. Field dependent and zero field magnetization (M-H) measured after field cooling in 50 kOe from 300K to corresponding temperature.

HPLC analysis: HPLC analysis was performed with Shim-pack GSW 5µm C18 (4.15 × 250 mm) column (SHIMADZU) using an HPLC system (Shimadzu LC-2010AHT) in isocratic mode. The eluent used was 0.1% formic acid in acetonitrile with flow rate of 0.5 mL/min. The yield of the amine derivatives were calculated with respect to the area ratio of the synthesized product and the pure amine products obtained from Sigma-Aldrich.

DLS measurements: The DLS measurements were done as described earlier.

4.3 Synthetic Procedures

Synthesis of seed stock Solution

The seed solution was prepared as previously mentioned. Seed solution per mL was calculated as per method available in the literature.[380]The final volume in all reactions was maintained to 203 mL.

Syntheses of nanocomposites 1–5

Five different solutions were prepared. Each solution contained 20 mg (0.05 mmol) $HAuCl_4$ in 200 mL of Millipore water. To these solutions, four different seed amount 22.5×10^4/ mL, 45×10^4/ mL, 90×10^4/ mL, 180×10^4/ mL and 900×10^4/ mL were added respectively. In each of five solutions, additional 2 mL 10% (w/v) solution of trisodiumcitrate dihydrate (0.07 mmol) and 20 mg iron powder (0.35 mmol) were added to produce nanocomposite**1–5**. All these five reaction mixtures were stirred at room temperature for 75 min and filtered.

Syntheses of nanocomposite 6 and 7

Two solutions contained 20 mg (0.05 mmol) $HAuCl_4$ dissolved in 200 mL of Millipore water. To this were added 0.07 mmol of 10% (w/v) solution of trisodiumcitrate dihydrate and 200 mg iron (3.5 mmol) powder. Two different seed amount 900×10^4/ mL and 22.5×10^4/ mL were added to produce nanocomposite 6 and 7 respectively. The reaction mixtures were stirred at room temperature for 75 minutes followed by filtration.

Syntheses of nanocomposite 8 and 9

Two solutions contained 20 mg (0.05 mmol) $HAuCl_4$ in 200 mL of Millipore water. To these were added seed amount of 900×10^4/mL, and 200 mg (3.5 mmol) iron powder. 0.028 and 0.021 mmol of trisodiumcitrate dihydrate were added to obtain nanocomposite8 and 9 respectively. The reaction mixtures were stirred at room temperature for 75 minutes and filtered.

Catalytic reactions

The catalytic reactions with Au-Fe$_x$O$_y$ catalysts were carried out using nitroarenes (0.5 µmol), NaBH$_4$ (20 µmol) and 100 µL catalyst (2 mg /mL) in water (total volume 3.0 mL) for 20

minutes at room temperature. The reaction was centrifuged to remove the catalyst and supernatant was used for the analysis. The yield of the amine derivatives was calculated with respect to the area of pure amine products shown by black lines.

Host-Guest Chemistry

Doxorubicin solution was prepared by dissolving doxorubicin hydrochloride in dichloromethane containing excess of triethylamine (molar ratio of Dox.HCl to triethylamine1:3) in dark. After sonication and subsequent evaporation the final solution was prepared in methanol. 1.0 mL aqueous suspension of four $Au\text{-}Fe_xO_y$ nanocomposites (4 mg/mL) was stirred with 100 µM doxorubicin solution for 24 h at room temperature. Excess drug were removed by centrifugation and the nanocomposite suspension were prepared in 1 mL water. A 500 µL of each of the four $Au\text{-}Fe_xO_y$ nanocomposites solutions prepared above was mixed with 500 µL sodium acetate buffer containing 10 mM GSH and the pH was adjusted to 4.6. The solution was stirred vigorously for 24 h and then centrifuged. The four different supernatants were analysed with respect to the absorbance of standard doxorubicin under identical conditions.

4.4 RESULTS AND DISCUSSION

4.4.1 Synthesis and characterization

The nanocomposites **1–9** were synthesized by seed mediated approach using gold nanoparticles as seed, sodium citrate as stabilizing agent and Fe powder as metal source and reducing agent. The solutions were stirred for 75 minutes to complete the reaction.

$$HAuCl_4.3H_2O + Fe(0) \xrightarrow[\substack{\text{Aqueous medium} \\ \text{Room temp. stirring} \\ \text{75 minutes}}]{\substack{\text{AuNP seed} \\ \text{Sodium citrate}}} Au\text{-}Fe_xO_y \text{ (1-9)}$$
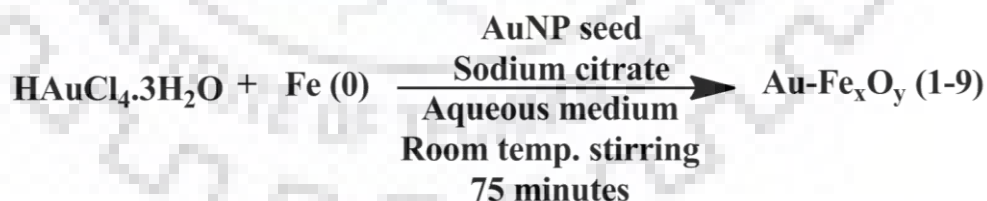
Scheme 4.1 Syntheses of $Au\text{-}Fe_xO_y$ (**1–9**) nanocomposites in presence of gold nanoparticles as seed, sodium citrate as stabilizing agent and Fe as reducing agent and metal source.

The resultant nanocomposites were characterized by absorption (visible) and vibrational (IR) spectroscopy, FE-SEM, TEM, powder X-ray diffraction (PXRD), XPS and SQUID measurements.

4.4.2 Seed variation methodology

Variable seed concentration in the presence of sodium citrate (0.07 mmol), Fe (0.35 mmol) and chloroauric acid (0.05 mmol) developed violet color in different solutions within 75 min of room temperature reaction in aqueous medium. Absorption spectra (Figure 4.1) showed development of plasmonic band for **1** (λ_{max} = 550 nm and seed concentration 22.5 x 10^4/mL) in comparison to the reaction in absence of seed suggested the formation of nanocomposites.
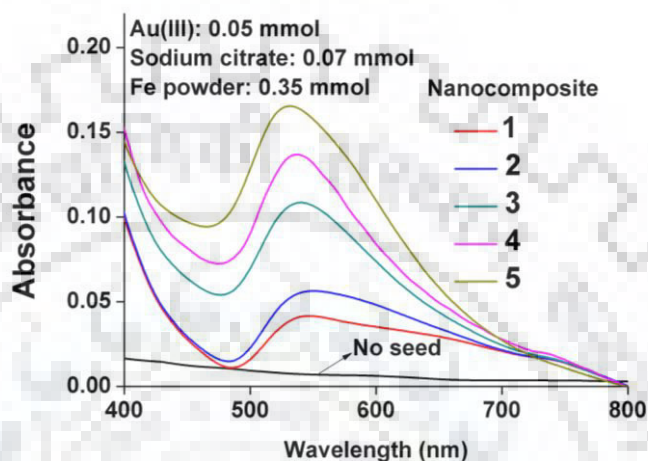
Figure 4.1 Absorption spectra of nanocomposites **1** (22.5 x 10^4/mL), **2** (45 x 10^4/mL), **3** (90 x 10^4/mL), **4** (180 x 10^4/mL), and **5** (900 x 10^4/mL) synthesized by using different concentration of seed (in parentheses) during the reduction of Au (III) by Fe powder in presence of sodium citrate.
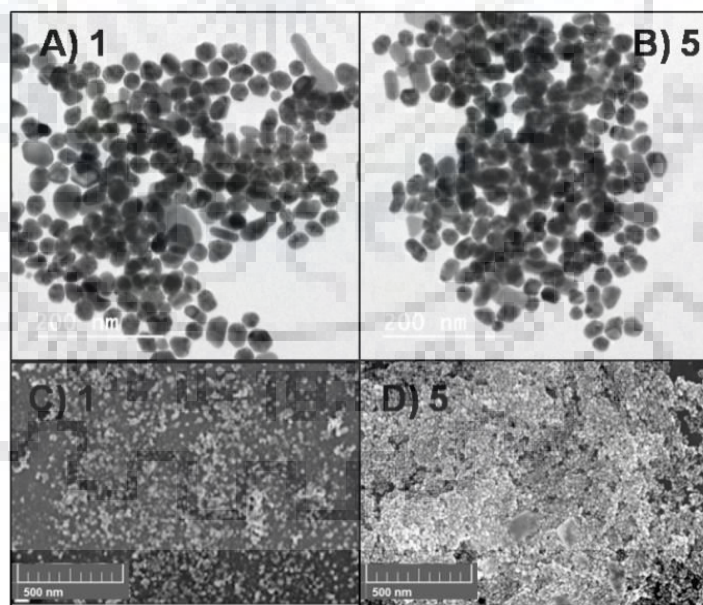
Figure 4.2 TEM (upper) and FE-SEM (lower) images of nanocomposite**1** and **5**.

The addition of more seed resulted in the enhanced coloration with appearance of colour immediately and the reaction was completed within 10 minutes. With increasing seed

amount from 22.5 x 10⁴/mL to 900 x 10⁴/mL blue shift in the absorption maxima was observed for **1** to **5** (550 nm to535 nm). The formation of nanocomposite **1** and **5** were further confirmed from FE-SEM and TEM images (Figure 4.2).

Seed variation methodology with increase in the concentration of Fe (3.5 mmol) led to rapid (~10 minute) appearance of violet colour in the reaction mixture for **6** and **7**. The absorption spectra did not show any appreciable shift in the plasmonic bands only increase in the intensity occurred. (Figure 4.3) The formation of nanocomposites was further confirmed from TEM and FE-SEM images (Figure 4.4).
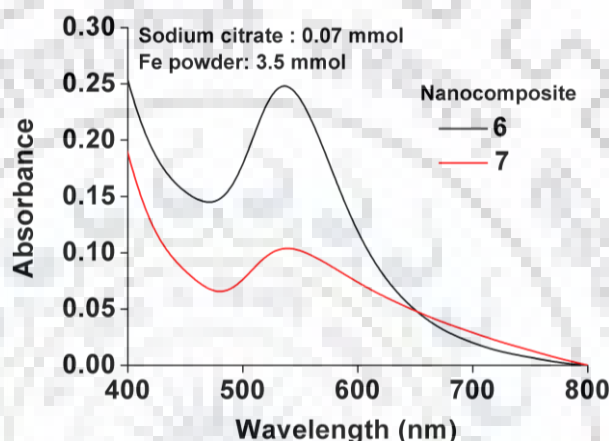
Figure 4.3 Absorption spectra of nanocomposites **6** (900 x 10⁴/mL) and **7**(22.5 x 10⁴/mL) synthesized by using seed different concentration (in parentheses) during the reduction of Au (III) by increasing the Fe powder in presence of sodium citrate.
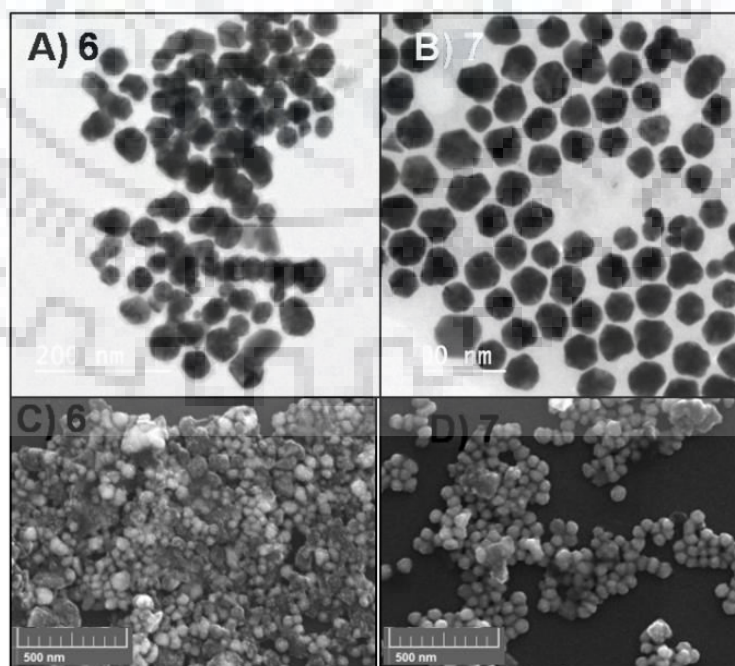
Figure 4.4 TEM (upper) and FE-SEM (lower) images of nanocomposite **6** and **7**.

4.4.3 Role of metal

The role of the metal was verified by performing the reaction in absence of metal powder with seed concentration of 900 x 10^4/mL and sodium citrate 0.035 mmol, no visible colour generation occurred confirming the role of metal in redox reaction (Figure 4.5).
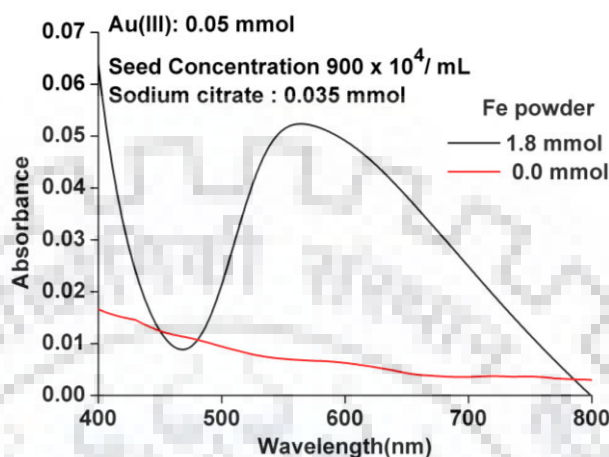
Figure 4.5 Absorption spectra in presence and absence of iron powder.

4.4.4 Decreasing Sodium Citrate concentration

In order to rule out the competitive reduction of Au(III) by sodium citrate, the amount of the sodium citrate were decreased from 0.07 mmol to 0.007 mmol for Au-Fe_xO_y nanocomposites preparation at a constant seed concentration of 900×10^4/mL and Fe powder 3.5 mmol. The red shift of ~100 nm in the absorbance (Figure 4.6) compared to **6** were observed with lowering of sodium citrate amount to 0.028 mmol and 0.021 mmol for **8** and **9**.
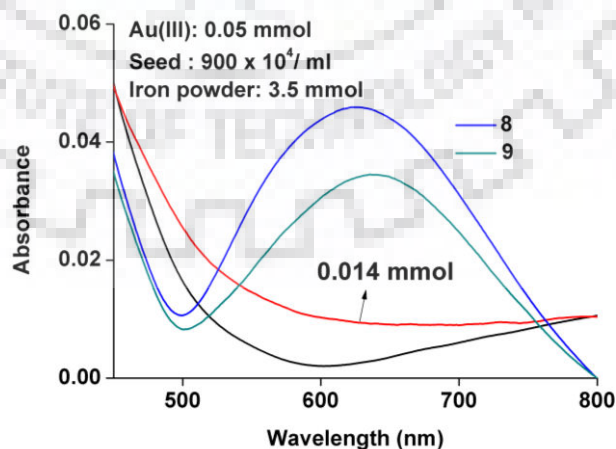
Figure 4.6 Absorption spectra of nanocomposites **8** (0.028 mmol), and **9** (0.021mmol) synthesized by using different concentration of sodium citrate (in parentheses) during the reduction of Au(III) by Fe powder in presence of gold nanoparticle as seed.

Further lowering of citrate concentration did not produce any visible color from the reaction mixture within 75 min stirring at room temperature. The results suggested that threshold amount of 0.021 mmol of sodium citrate required as stabilizing agent in the reduction process to synthesize the Au-Fe$_x$O$_y$ nanocomposites. The formation of nanocomposites **9** was confirmed from TEM and FE-SEM images (Figure 4.7).TEM images also confirmed the increase in size for **9**.
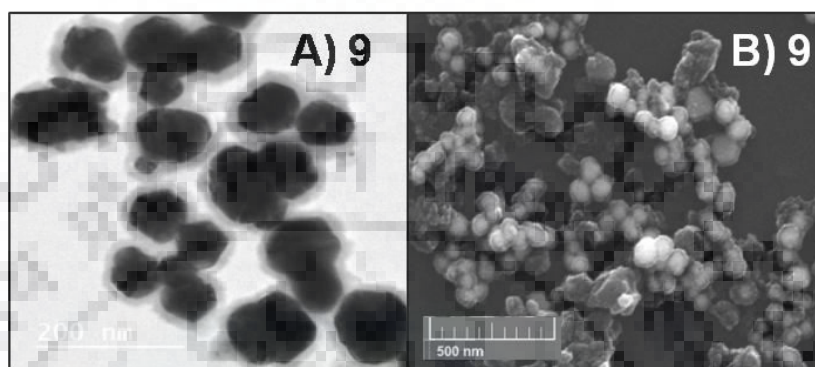
Figure 4.7 TEM (A) and FE-SEM (B) images of nanocomposite **9**.

4.4.5 Composition of nanocomposites

EDX analysis and elemental mapping via FE-SEM confirmed the composition of these nanocomposites (Figure 4.8–4.10). In the synthesis, the metal powder engaged in redox reaction between Au(III)/Au(0) and Fe(II)/Fe(0) couple, in addition to playing the role of simple metal source, led to the formation of Au-metal oxide nanocomposites.

(a)	(b)	(c)	(d)
FE-SEM	**EDX plot**	**Au-mapping**	**Fe-mapping**
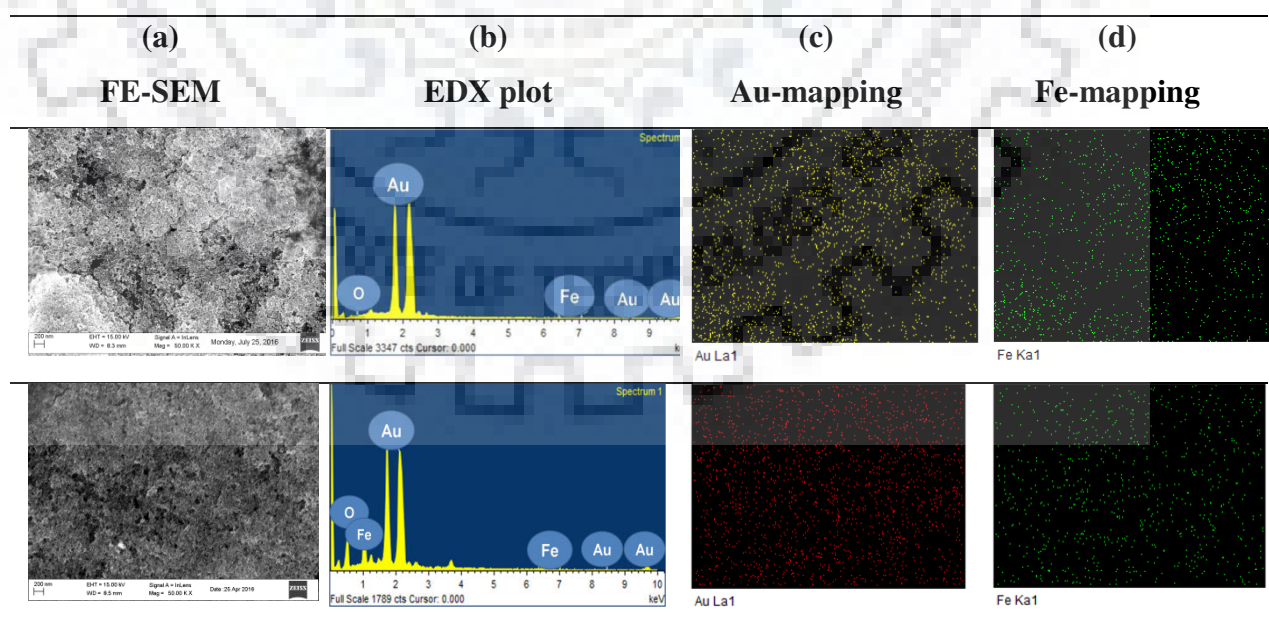
Figure 4.8 FE-SEM images (a), EDX plot (b), EDX mapping of Au (c), and EDX mapping of Fe (d) for nanocomposites **1** and **5**.

EDX analysis (Figure 4.8) showed incorporation of Fe in the nanocomposites **1** is sparse, and Au:Fe ratio up to 1:0.01 in **5** was obtained. Increase in the concentration of Fe (3.5 mmol) for **6** and **7** led to 50 times enhancement of iron content in **6** with Au : Fe = 1:0.5 and in **7**, 25 times enhancement of iron content occurred with Au : Fe = 1:0.16, comparison to **5** (Figure 4.9).

(a)	(b)	(c)	(d)
FE-SEM	**EDX plot**	**Au-mapping**	**Fe-mapping**
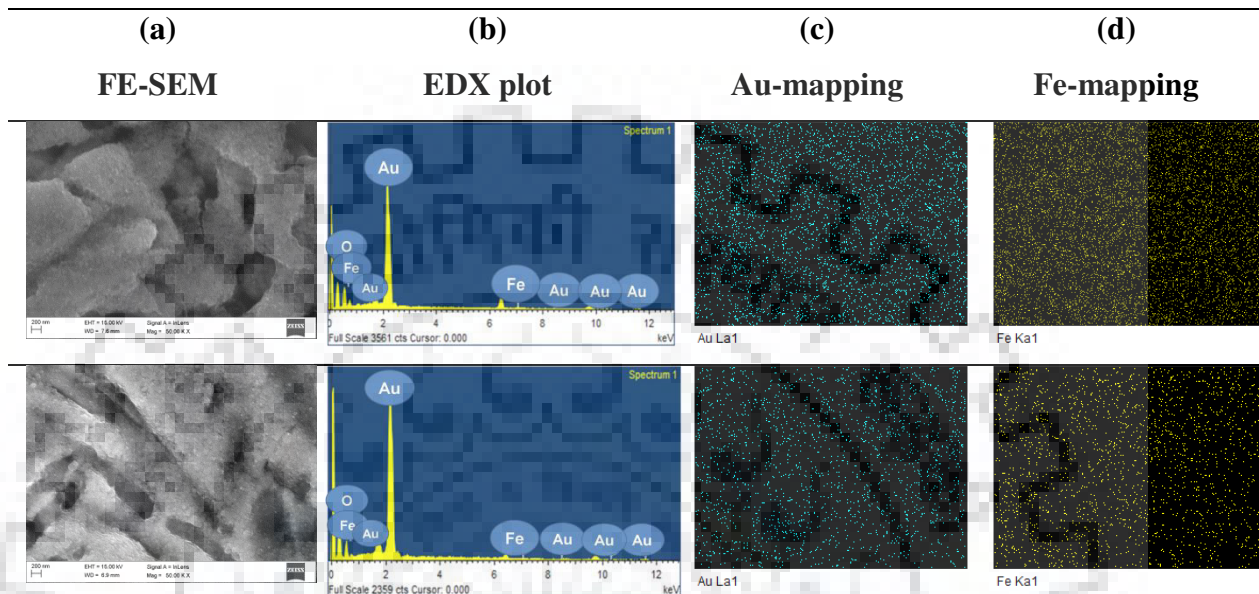
Figure 4.9 FE-SEM images (a), EDX plot (b), EDX mapping of Au (c), and EDX mapping of Fe (d) for nanocomposites **6** and **7**.

(a)	(b)	(c)	(d)
FE-SEM	**EDX plot**	**Au-mapping**	**Fe-mapping**
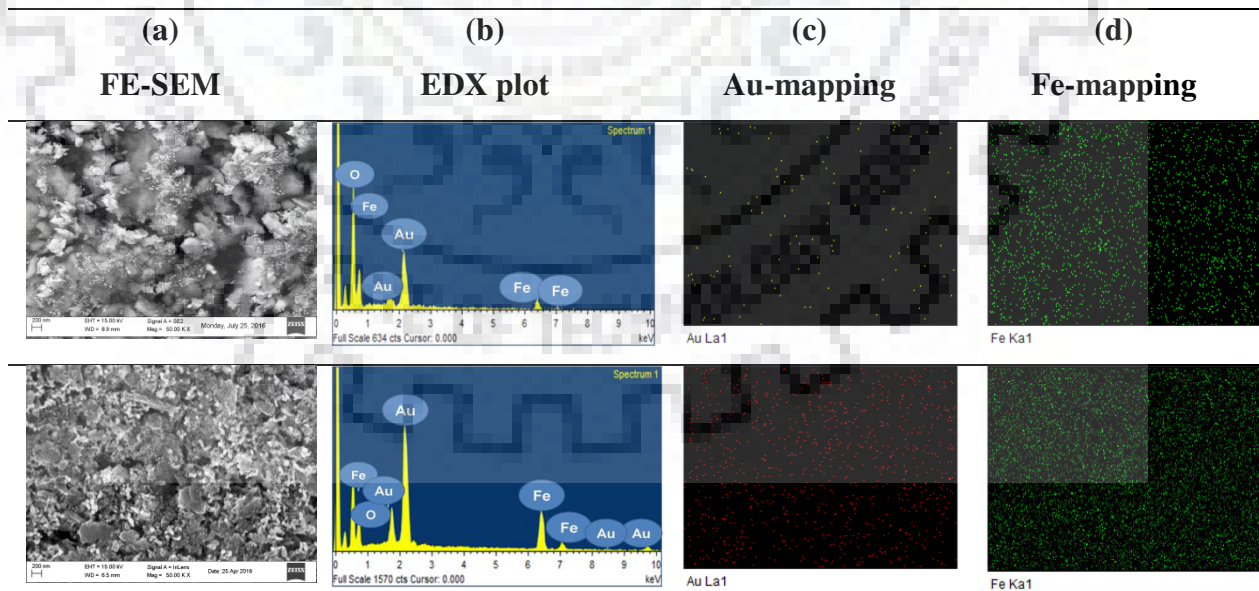
Figure 4.10 FE-SEM images (a) EDX plot (b), EDX mapping of Au (c), and EDX mapping of Fe (d) for nanocomposites **8** and **9**.

Decreasing the sodium citrate concentration increased the iron content in the nanocomposites. Decreasing in sodium citrate to 0.028 mmol from 0.07 in **8** increased the Au:

Fe to 1:1 whereas further decrease of citrate amount to 0.021 mmol in **9** increased the Au: Fe ratio to 1:1.9 (Figure 4.10).

4.4.6 Powdered X-ray Diffraction

The nanocomposites **5, 6, 7,** and **9** were further characterized by PXRD. Only the characteristic peaks of Au (0) was observed for **5**, **6**, **7**, and **9** suggesting amorphous nature of Fe_xO_y.[381] The diffraction peaks at 38.3°, 44.2° and 154.5°, were attributed to gold, which can be indexed to 111, 200 and 220, lattice planes of gold in a cubic phase, respectively (Figure 4.11).
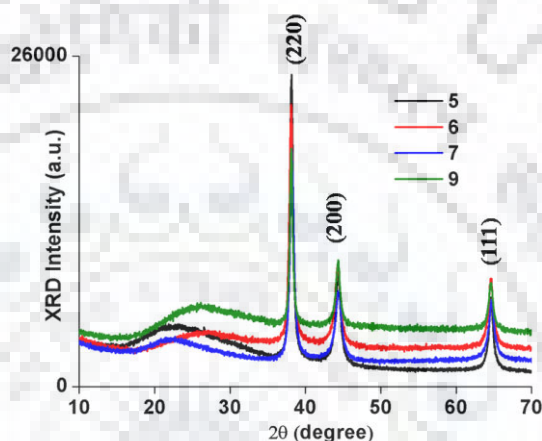
Figure 4.11 Powder X-ray diffraction pattern of nanocomposite **5, 6, 7,** and **9**, the peaks are due to Au (0).

4.4.7 X-ray Photoelectron Spectroscopy

The chemical compositions of the $Au\text{-}Fe_xO_y$ nanocomposites obtained from EDX analysis was further confirmed by XPS analysis. (Figure 4.12) This also revealed the oxidation states of different elemental species present in $Au\text{-}Fe_xO_y$ nanocomposites. Binding energy studies confirmed the peaks of Au $4f_{7/2}$,[382] Fe $2p_{3/2}$ and $2p_{10/2}$, [383] and O 1s [384] at 83.0, 710, 724.15 and 530 eV respectively in these nanocomposites. The combinations of XPS peaks for each species suggested the formation of $Au\text{-}Fe_xO_y$ in the nanocomposites. Detailed analysis of the XPS spectra in the range 705–715 eV (Figure 4.13 and 4.14) for Fe_xO_y nanocomposites showed the presence of a peak at around 709–710 eV due to Fe_3O_4 ($2p_{3/2}$) and another one at 710–721 eV due to Fe_2O_3 ($2p_{3/2}$). [385] The characteristic satellite peak at around 719 eV in samples **5** and **9** indicated the predominant presence of Fe_2O_3.[385,386] On the contrary, this peak was absent in **6** and **7**, thus indicating the predominance of Fe_3O_4. Further studies for **5** and **9** revealed the presence of shoulder at around 721 eV and 710.5 eV respectively. Cumulatively, these data suggested the presence of mostly $\gamma\text{-}Fe_2O_3$ in **5** and $\alpha\text{-}Fe_2O_3$ in **9**.[386]
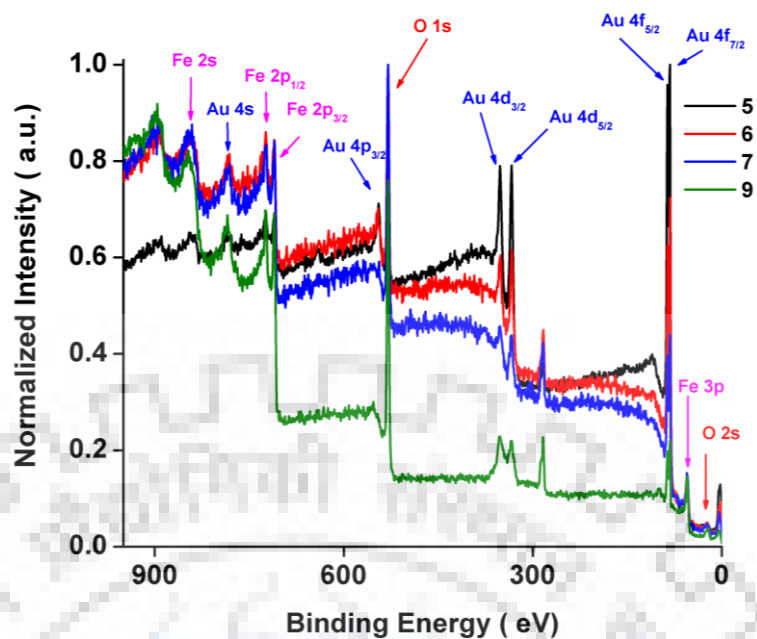
Figure 4.12 XPS spectra with binding energy 0 to 950 eV of nanocomposites **5, 6, 7,** and **9.**
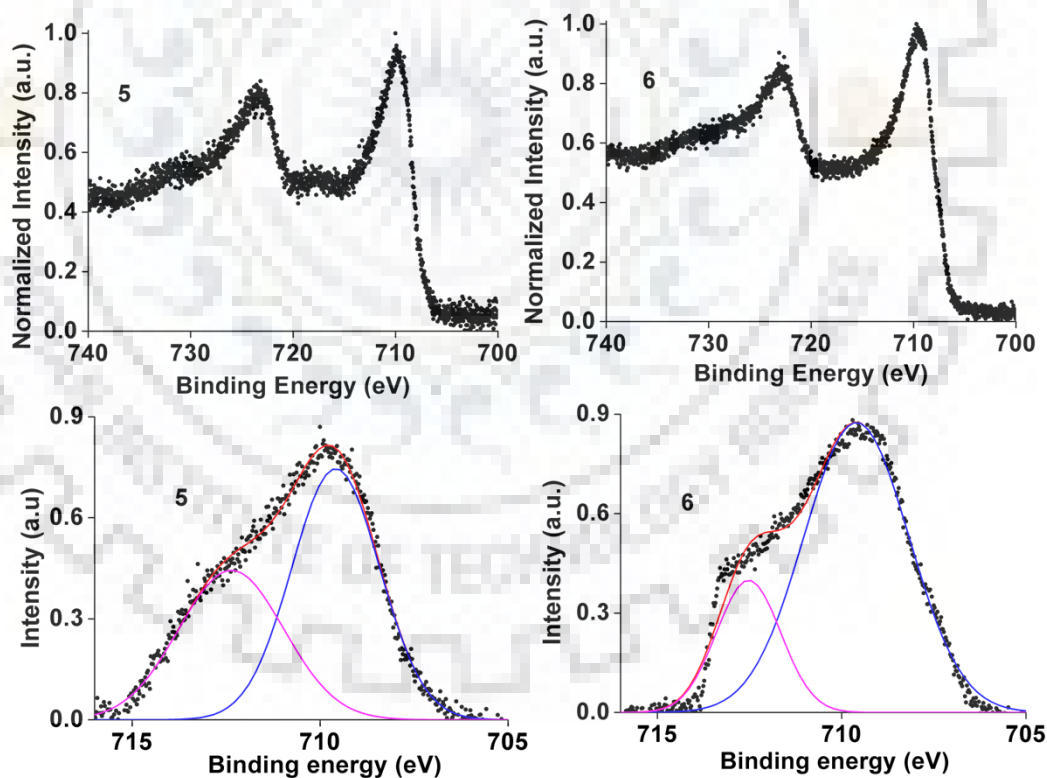
Figure 4.13 XPS spectra with binding energy (top) 700 to 740 eV and (bottom) back ground subtracted spectra from 705 to 725 eV for nanocomposites **5** and **6**.
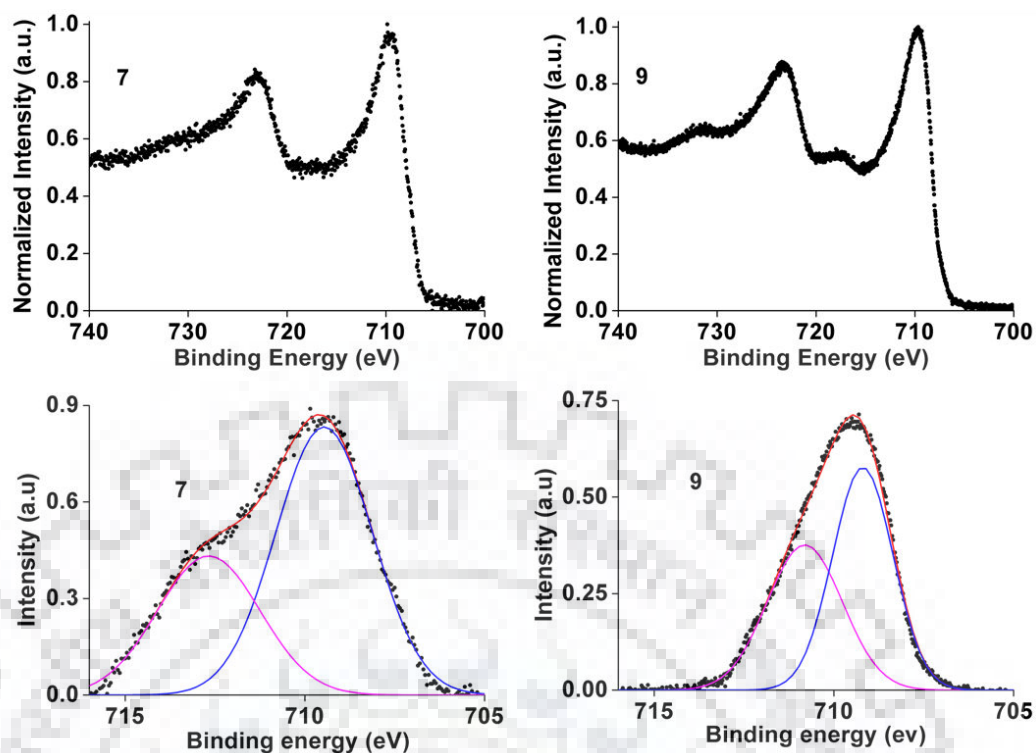
Figure 4.14 XPS spectra with binding energy (top) 700 to 740 eV and (bottom) back ground subtracted spectra from 705 to 725 eV for nanocomposites **7** and **9**.

4.4.8 FTIR Spectroscopy

The IR spectra, of the nanocomposites **5, 6, 7** and **9** which range between 450-500 cm^{-1}(Figure 4.15) suggested the formation of α-Fe$_2$O$_3$ in the samples **6, 7, 9** and predominantly γ-Fe$_2$O$_3$ in sample **5**. The α-Fe$_2$O$_3$nanoparticles shows characteristic peak at 478 cm^{-1} and are assigned to Fe-O functional groups while as γ-Fe$_2$O$_3$ shows peak at 580 cm^{-1} [387]
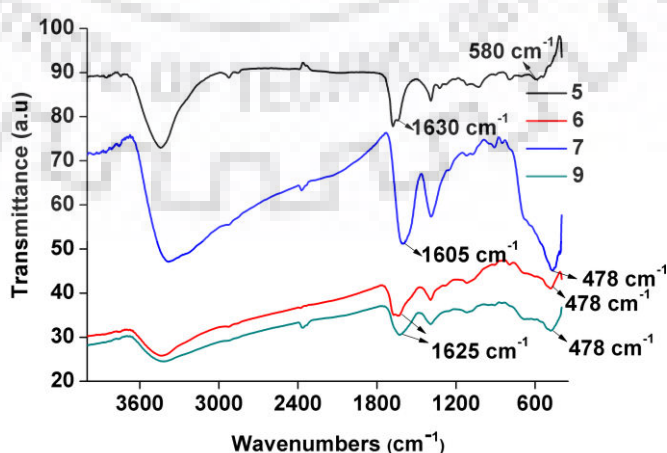
Figure 4.15 FT-IR spectra of nanocomposite **5, 6, 7,** and **9**.

4.4.9 Magnetic Properties

Magnetic properties of the nanocomposites **5**, **6**, **7** and **9** were analyzed (Figure 4.16). The ZFC and FC of the samples **6**, **7** and **9** (Figure 4.16A) started diverging from around 250-300K, and a blocking temperature was evident at around 25–37K (T$_B$), similar to earlier reports on gold-iron oxide nanoparticles.[388]However, unlike this earlier report, no downturn in M vs T curve was observed at 190K.[388] Instead, a downturn in M vs T between 15–20K was observed for the samples **6**, **7** and **9**. However, in the case of **5** (Figure 4.16B), neither any blocking temperature nor any downturn was observed and the ZFC and FC diverged throughout the experimental temperature range. Moreover, the ZFC magnetization for **5** showed slight increase at low temperature.
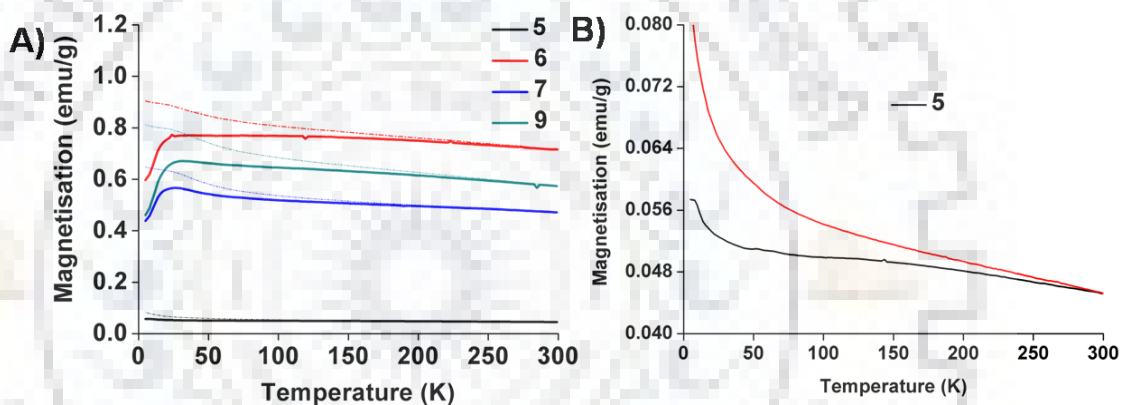
Figure 4.16 A) ZFC (solid)–FC (dotted) magnetization plots for samples **5**, **15**, **7** and **9**; (B) blow up of the ZFC-FC for sample **5**.

There arouse a slight hump in the ZFC of M–T curves for all the samples around 120K signifying the Verwey transition of Fe$_3$O$_4$.[388] Both the ZFC and FC magnetization at high temperature for all the samples were found to flatten off in the M vs T curves at a value which increased progressively from **5**→**7**→**9**→**6** (Figure 4.16A). A similar effect was observed in the M vs H plots at high temperatures 100K (Figure 4.17), where the magnetization for sample **5** saturated to a low value, while the high field magnetization increased progressively from **5**→**7**→**9**→**6** (or **5**→**7**→**6**→**9** depending on field). This suggested the presence of superparamagnetic behavior in samples **6**, **7** and **9** above T$_B$. Notably, the M–H plots at 50K (Figure 4.18) showed little hysteresis for samples **6**, **7** and **9** in comparison to M–H plots at 5K (Figure 4.19), confirmed that the blocking temperature T$_B$ lies below this value. The correspondence of the blocking temperature T$_B$ (Table 4.1) with the high temperature superparamagnetic background of magnetization in the M–T plots for different samples

5→7→9→6 was similar to that reported in Fe_2O_3–Fe_3O_4 nanocrystals.[389] However, unlike this case, the order of their samples was also directly correlated to the sample size, showing that this mechanism was different from a non interacting anisotropy driven picture
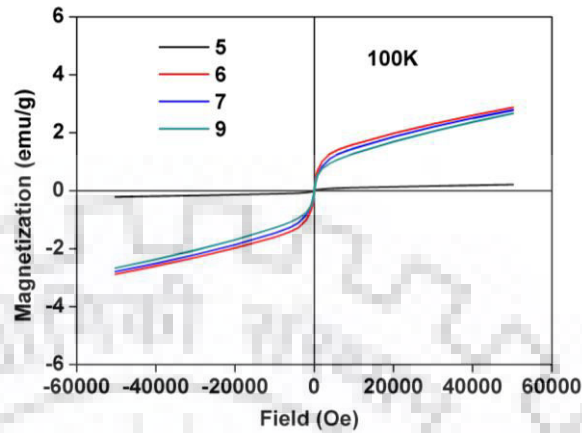
Figure 4.17 Field cooled magnetization versus field (*M-H)* curves for nanocomposites **5**, **6**, **7** and **9** at 100K.
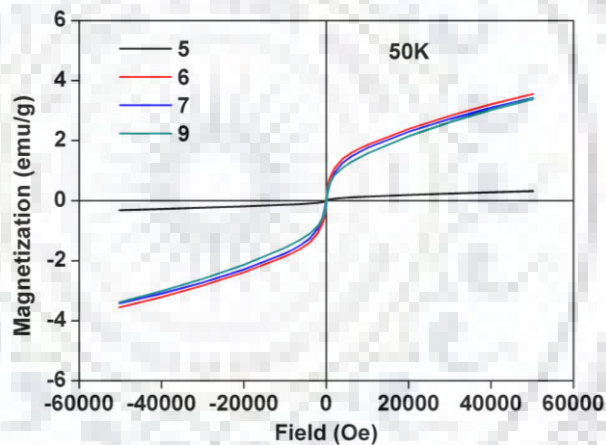
Figure 4.18 Field cooled magnetization versus field (*M-H)* curves for nanocomposites **5**, **6**, **7** and **9** at 50K.
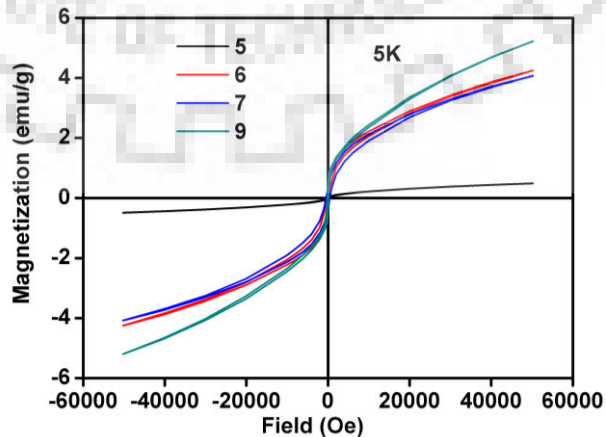
Figure 4.19 Field cooled magnetization versus field (*M-H)* curves for nanocomposites **5**, **6**, **7** and **9** at 5K.

156

Table 4.1: Comparison of blocking temperatures, sizes and their ratio for different nanocomposites.

Sample	T_B (K)	V^a (10^4 nm^3)	T_B/V (10^{-3} K/nm^3)
5	0	3.08	0
6	37	104.21	0.2152
7	215	15.23	0.1710
9	32	17.99	0.02915

[a]volumes have been calculated from the data of TEM images and considering the shapes as ellipsoids

The downturn in M−T curves for samples **6**, **7** and **9** can thus be attributed to the Morin transition in haematite into a low temperature antiferromagnetic state. Although the value of T_{Morin} was about 260 K for bulk samples, it strongly depended on particle size, and was known to be suppressed dramatically for sizes from 30-100 nm.[390–393] The transition was pushed to below 5K for nanoparticles of size 10−20 nm or less [391,393] which was possibly the case for our sample **5**. Consequently, sample **5** at the lowest measured temperatures (about 5K) contained weakly ferromagnetic (canted AFM) haematite above the Morin transition (along with ferromagnetic maghemite), and hence showed an upturn in the ZFC curves (Figure 4.16B). Since no downturn was observed at 190 K in any of the samples, hence presence of antiferromagnetic FeO was ruled out, unlike other reported cases.[388,394]

The EB was found to increase progressively from the samples **7**→**6**→**9** at 5K. (Figure 4.20A). Also, for these three samples, the EB decreased monotonically as temperature increased. The EB for sample **5** at 5K was coincident with sample **7**, while it showed an anomalous behaviour at high temperatures. The EB in all the samples arouse from the interaction between the AFM haematite and the FM magnetite phases as reported before in α-Fe_2O_3/Fe_3O_4 nanocomposites. [395] The EB for samples **6**, **7** and **9** almost disappeared at 50K, consistent with the suppressed T_{Morin} at 15−20K. Such a suppression of T_{Morin} and corresponding disappearance of EB above 40K was observed in nanostructured haematite thin films.[393] The coercivity at 5K increased progressively from samples **5**→**7**→**6**→**9** (Figure 4.20B). The coercivity of samples **6**, **7** and **9** decreased monotonically with increase in temperature, running almost parallel to each other, while sample **5** showed an anomalous behavior at high temperatures.

Sample **5** had no low temperature blocking, indicating that T_B=0 for this case (probably due to small particle size). It also had a very small moment at low temperature due to mostly unblocked character, small particle size and small overall amount of iron. The origin of the high temperature anomaly in EB and coercivity in nanocomposite **5**, was due to the presence of unblocked Fe_3O_4, γ-Fe_2O_3 and α-Fe_2O_3, the last one having residual weak ferromagnetic

(canted AFM) correlations above the Morin transition temperature.
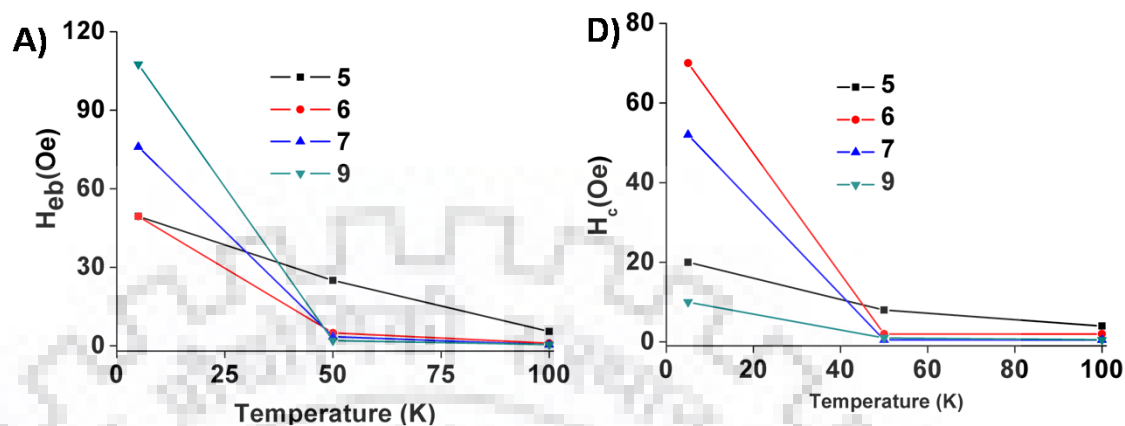
Figure 4.20 A) Exchange bias and B) Coercivity for samples **5**, **6**, **7** and **9** at different temperatures.

4.4.11 DLS measurements

The hydrodynamic radii of the nanocomposites decreased from **1** to **7** whereas **9** showed increase in the size (Figure 4.21A, Table 4.2).
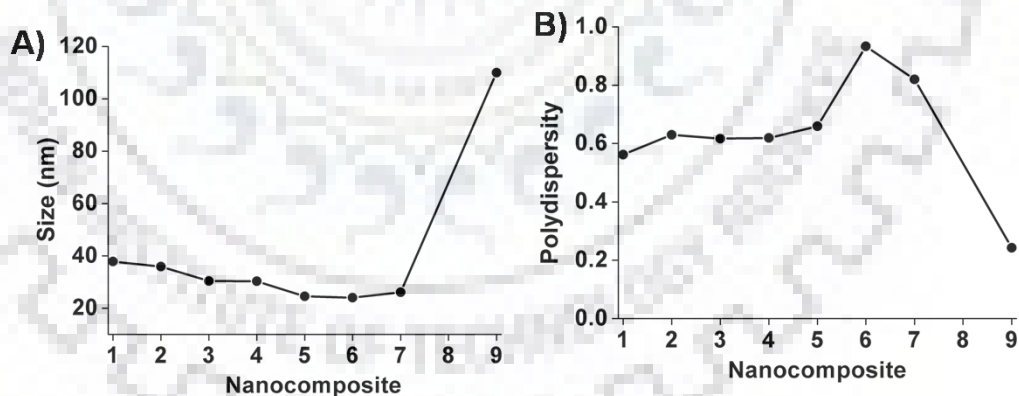
Figure 4.21 Size (hydrodynamic diameter) (A) and polydispersity (B) of nanocomposites **1** to **9**.

The polydispersity of nanocomposites increased with increase in seed amount however monodispersity increased for **9** (Figure 4.21B, Table 4.2). Zeta potential remained almost constant for **1** to **4** and decreased for **5** and **6** and then again started increasing for **7** and **9** (Figure 4.22 Table 4.2).
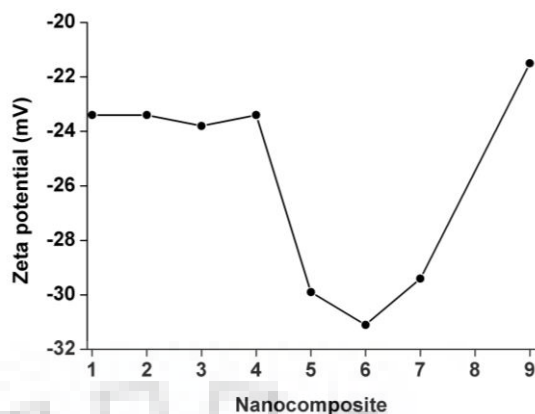
Figure 4.22 Zeta potential of nanocomposites **1** to **9**.

Table 4.2: Size, Zeta potential and PDI values of nanocomposites

Nanocomposite	Size(nm)	PDI	Zeta potential(mV)
1	37.4	0.56	-23.4
2	35.9	0.63	-23.4
3	30.4	0.61	-23.8
4	30.3	0.61	-23.4
5	24.5	0.66	-29.9
6	24.0	0.93	-31.1
7	26.1	0.82	-29.4
9	110.0	0.24	-21.1

4.4.10 Catalytic reactions

The nanocomposites **5**, **6**, **7** and **9** were utilized as catalysts for the conversion of nitroarenes. The conversion of 4–NP (4–nitrophenol) through absorption spectroscopy for different nanocomposites was reported as model catalytic reaction as the absorbance change of this reagent was simplistic to monitor.[308] The yield of amine products was monitored not only for 4–NP, but also for other nitroarenes through HPLC for **5**, **6**, **7** and **9** as catalysts (Table 4.3, Figure 4.23 and 24). The results have been also compared with other catalysts (**C1-C12**) reported in literature (Table 4.3).[308,396–407]. A control reaction was set in absence of catalyst for 4-NP and a negligible change in the absorbance spectra was observed over a period of 30 minutes (Figure 4.25)

In this study, 98% free amine derivatives from the reactions were isolated. Unreacted nitroarenes and hydroxylamine derivative as side product were also identified in the reaction mixture. Similar to these studies, repetitive reduction cycles of 4–NP with more than 90%

conversion for each reaction cycle up to 8 cycles (Figure 4.26) in presence of catalyst **5** suggested the stability and reusability of **5** in the reaction condition.

Table 4.3: Catalytic reaction[a] and yields (%) of amines from nitroarene.

Nitro-arenes	5Fe	6Fe	7Fe	9Fe	C1	C2	C3	C4	C5	C6	C7	C8	C9	C10	C11	C12	C12
	% Yield of amine				% Conversion of nitroarenes												
A	95	83	13	14	95	99	98	92	99	>95	>95	100	>95	-	-	-	-
B	90	40	15	65	-	-	93	-	-	-	-	-	-	-	-	-	-
C	65	75	66	57	-	-	94	-	-	-	-	-	-	-	-	-	-
D	75	95	65	85	-	-	-	-	91	-	-	-	-	-	-	-	-
E	95	95	85	50	-	-	-	-	-	-	-	-	-	>99	-	-	-
F	70	98	80	85	-	-	-	-	-	-	-	-	-	-	97	-	-
G	55	71	70	53	-	-	-	-	-	-	-	-	-	-	-	76	-
H	90	81	75	90	-	-	-	-	-	-	-	-	-	-	-	-	98
I	66	62	90	95	-	-	-	-	-	-	-	-	-	-	-	-	98
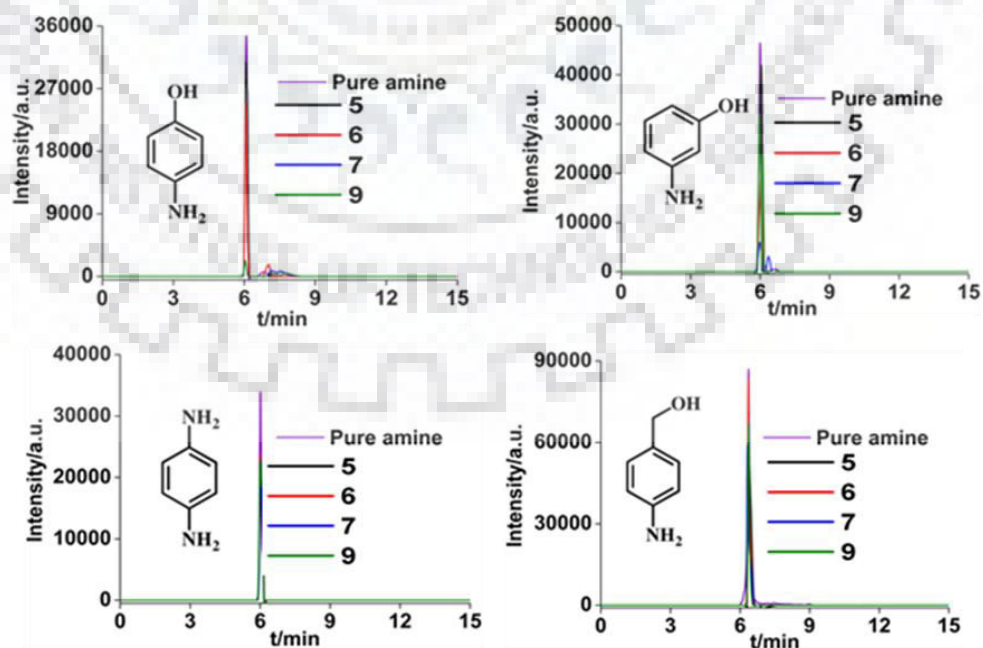
Figure 4.23 HPLC analysis of the catalysis reaction of nitroarenes in presence of selective Au-Fe_xO_y catalysts.
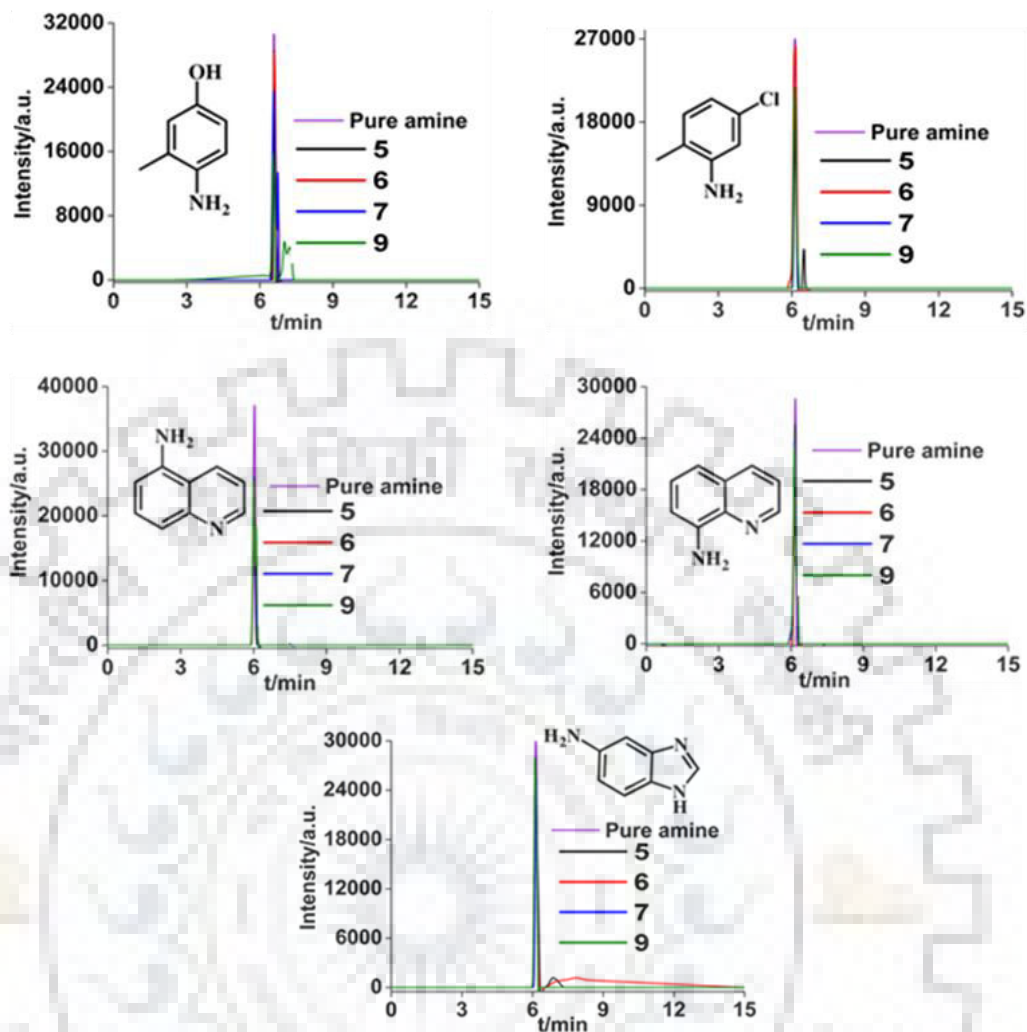
Figure 4.24 HPLC analysis of the catalysis reaction of nitroarenes in presence of selective Au-Fe$_x$O$_y$ catalysts.
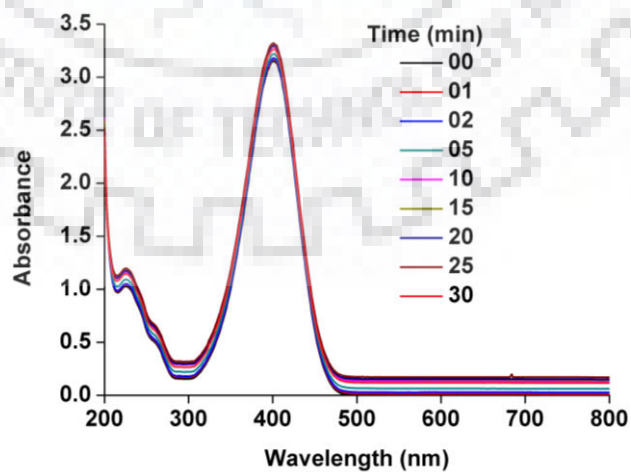
Figure 4.25 Absorption spectrum for 4-NP reduction at room temperature in absence of catalyst.
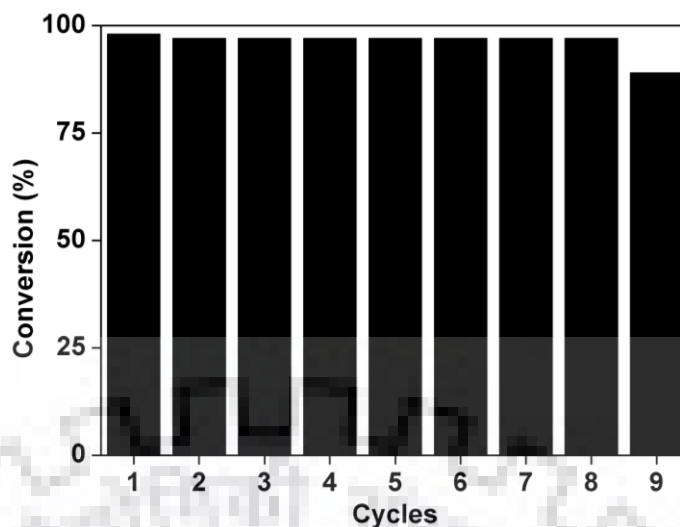
Figure 4.26 Recyclability of catalyst **5** for 4-NP reduction at room temperature.

4.4.12 Host Guest Chemistry

The nanocomposites **5**, **6**, **7** and **9** were used as a host for a well known small molecule cancer drug doxorubicin. Aqueous suspensions of the nanocomposites were treated separately with doxorubicin for the uptake of the guest. The uptake of the guest was monitored after 24 h by the absorption of doxorubicin in the solution (Figure 4.27).
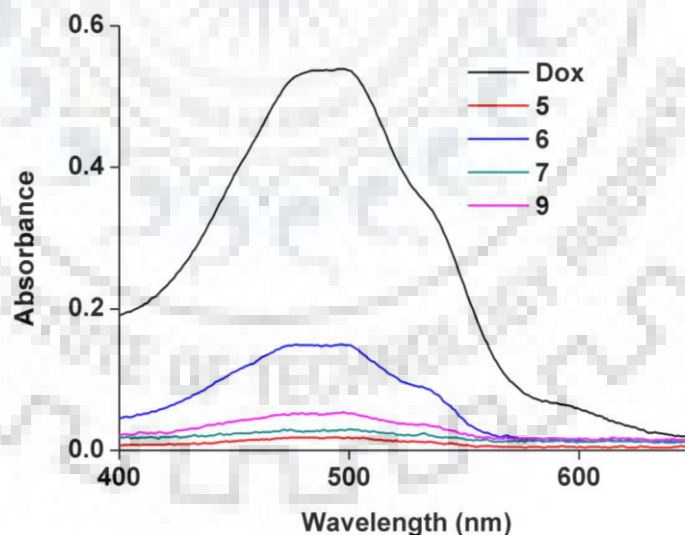
Figure 4.27 Absorption spectra taken showing uptake of doxorubicin by the nanocomposites **5**, **6**, **7** and **9**.

The maximum uptake was observed in case of **5** (Table 4.4). The uptake was further confirmed from the change in morphology of the nanocomposite in FE-SEM (Figure 4.28).
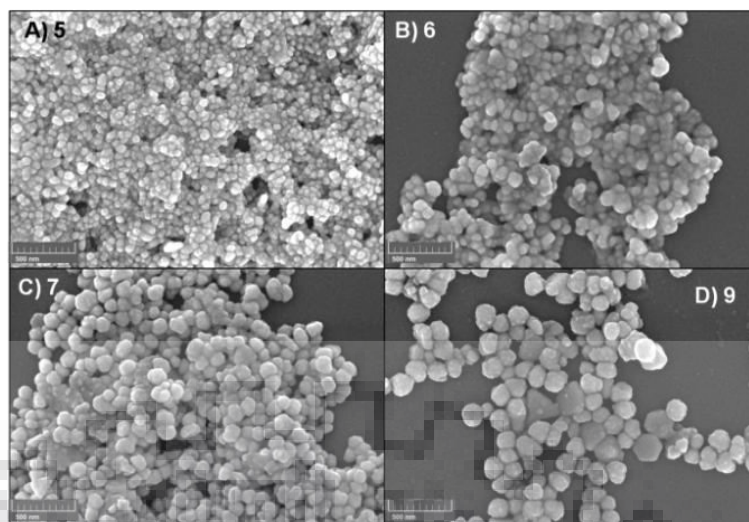
Figure 4.28 FE-SEM images of the nanocomposites **5**, **6**, **7** and **9** taken after uptake of doxorubicin.

The release of doxorubicin guest was the most challenging task in the case of cancer cell biology. The release was initially tried in the common cell culture. However the release of doxorubicin as guest was not significant in this medium. In order to facilitate the process, the release was further checked in phosphate acetate buffer pH 4.6 containing glutathione (Figure 4.29). The release of **5** was 91%, maximum among the nanocomposites (Table 24). The morphologies of the nanocomposites after release of doxorubicin were checked by FE-SEM (Figure 4.30).
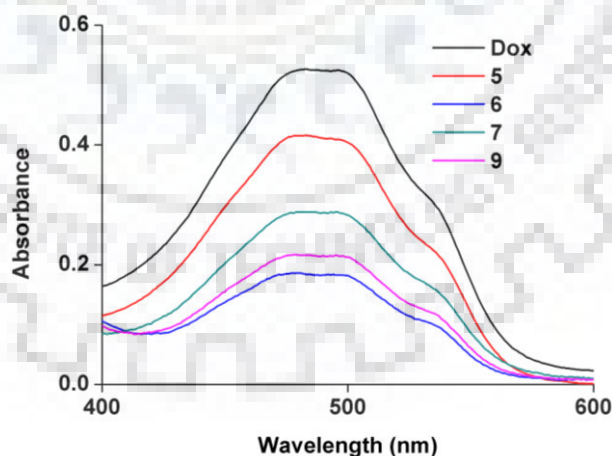
Figure 4.29 Absorption spectra showing release of doxorubicin by the nanocomposites **5**, **6**, **7** and **9** at pH 4.6.
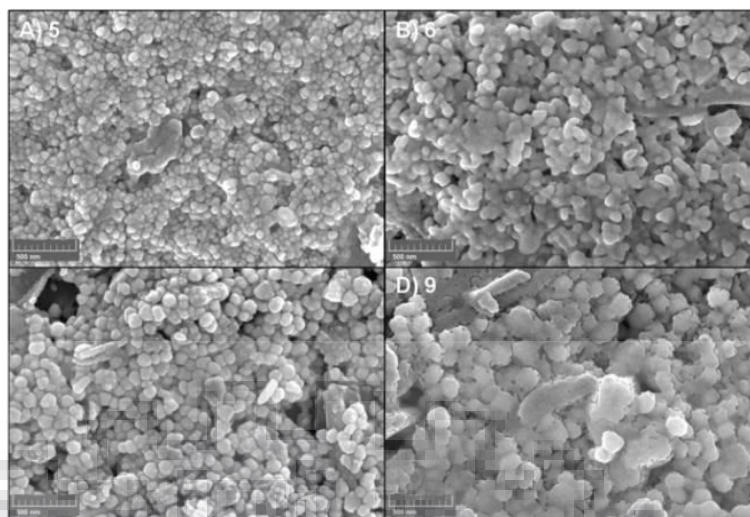
Figure 4.30 FE-SEM images of the nanocomposites **5**, **6**, **7** and **9** taken after release of doxorubicin.

Table 4.4: Host-guest chemistry of doxorubicin with Au-Fe$_x$O$_y$

Nanocomposite (4 mg/mL)	Uptake % (after 24 h)	Release % (after 24 h)
5	91	91
6	72	42
7	94	60
9	90	43

4.5 CONCLUSION

Facile route for syntheses of Au-Fe$_x$O$_y$ nanocompositeswere achieved by Fe powder reduction at room temperature in aqueous with regulated Au : Fe ratio, for controlling the exchange bias.It was possible to vary the Fe content in the Au-metal oxide nanocomposites by proficiently playing around the concentrations of seed, reducing agent and stabilizing agent. The exchange bias in all samples, arouse from the interaction between FM Fe$_3$O$_4$ and AFM α-Fe$_2$O$_3$, could be controlled using the variation of gold-iron content. The nanocomposites were used as catalysts for nitroarene reduction and acts as hosts for the drug doxorubicin.

SECTION B

Electrochemical splitting of water into hydrogen and oxygen is no doubt a matter of significant interest for the scientific community recently because of its potential applications in renewable energy technology.[261] In this regard, metal nanocomposites have attracted considerable attention because of their tunable physical and chemical properties.[409-411] So far, the combination of Au nanoparticles (AuNPs) with three first row transition metal oxides (Co, Ni, and Mn) has been reported to exhibit promising OER activity in recent literature. [412-414] Au$-$Fe$_x$O$_y$ nanocomposite has been explored only once by Jaramillo's group as an OER catalyst. [304] However, a handful of Au$-$Fe$_x$O$_y$ nanocomposites with interesting catalytic and magnetic properties have been well explored recently. An alternative method of water splitting involves the use of photocatalysts. Photocatalysts materials consists additional components associated with them called as cocatalysts which catalyze electrochemical redox reactions.[415] In photocatalytic reactions, the photocatalysis can thus be considered to be electrocatalysis where electrocatalyst components induce the redox reactions driven by the potential shifts caused by the photocatalyst. The photocatalytic activity depends upon the physiochemical properties of the photocatalyst, nature of the active site (cocatalyst) and reaction conditions.[416] Most metal oxide, sulfide and nitride photocatalysts consist of metal with d^0 and d^{10} configurations. Some transition metals and oxides like noble metals Pt, Rh, Au, NiO and RuO$_2$ function as cocatalysts for the H$_2$ evolution[417] Metal oxides consists of d^0 metal cations (Ti^{4+}, Zr^{4+}, Nb^{5+}, Ta^{5+} and W^{6+}), group four elements, group five elements and group six have reasonable water splitting activity under UV light only and d^{10} metal oxides include Ga3+, In3+, Ge4+, Sn4+ and Sb5.[417,418] Representative photocatalysts with d^0 or d^{10} electronic configurations include La-doped NaTaO$_3$ and Zn-doped Ga$_2$O$_3$,[417] and both exhibit extremely high photocatalytic activities during overall water splitting in the deep UV region. New photocatalysts like such as oxynitrides and oxysulfide behave as photocatalysts under visible light thus becoming important.[419,420] A cocatalyst can be vital to obtaining highly efficient overall water splitting by promoting charge separation and suppressing charge recombination by extracting photogenerated electrons and holes. Oxides of Co, Fe, Ni, Mn, Ru and Ir were used as O$_2$-evolution cocatalysts [418]. Various bimetallic cocatalysts have also been developed like Ni/NiO core$-$shell [421], Rh/Cr$_2$O$_3$ core$-$shell [422] and Rh$_{2-x}$Cr$_x$O$_3$[423].

This work demonstrates the establishment of the one-pot seed-mediated synthetic method for Au$-$Fe$_x$O$_y$ nanocomposites at room temperature in an aqueous medium using L$-$tryptophan

as a stabilizing agent and iron powder as the reducing agent. Tryptophan were used for the first time to stabilize transition metal oxide and noble metal nanocomposites, considering its strong electron donating properties and water solubility during the stabilization of gold nanoparticles.

4.6 EXPERIMENTAL SECTION

4.6.1 Chemicals and Materials

All the materials unless specified were discussed previously. Potassium hydroxide was purchased from Thomas Baker, Nafion solution and FTO glass electrode from sigma aldrich.

4.6.2 Instrumentation

The synthesized nanocomposites were characterized by absorbance spectroscopy, IR spectroscopy, TEM, FE−SEM, PXRD, DLS and XPS as described in earlier section of this chapter.

4.7 Synthetic Procedures

Synthesis of Seed Stock Solution

The seed solution was prepared as previously mentioned. The final volume in all reactions was maintained at 101 mL.

Calculation of seed particle per mL:

Seed solution per mL was calculated as previously mentioned.

General syntheses of nanocomposites in presence of amino acids

For gold−iron oxide nanocomposites stabilized with different L-amino acids, 25 different solutions were prepared. Each solution contained 10 mg (25 μmol) $HAuCl_4$, 450×10^9 AuNP seed/ mL in 100 mL of Millipore water. To these solutions, 5 μmol of 20 different amino acids were added. Finally, 10 mg (18 μmol) of iron powder was added to all the solutions for the syntheses of nanocomposites. The generation of the surface plasmon resonance (SPR) peak was studied in each case to monitor the formation of nanocomposite containing gold.

Syntheses of nanocomposites 10–17

For gold−iron oxide nanocomposites with variable seed concentration, nine different solutions were prepared. Each solution contained 10 mg (25 μmol) $HAuCl_4$ in 100 mL Millipore water. To thesesolutions, eight different seed amounts, 90×10^9, 180×10^9, 270×10^9, 3150×10^9, 450×10^9, 540×10^9, 1530×10^9, and 720×10^9/mL were added for the syntheses of nanocomposites**10−17** respectively. In each of these solutions, an additional 50 μL solution of

tryptophan (5 µmol in 1:1 mixture of water and ethanol) and 10 mg (18 µmol) iron powder were added. All these reaction mixtures were stirred at room temperature for 60 min and then filtered. The filtrate was concentrated by evaporation and **10−17** nanocomposites were obtained as solid materials from the filtrate after 3 days. After discarding the supernatant solutions, the solid nanocomposites were further dried under vacuum before characterization. One negative control reaction was prepared without any AuNP as seed.

Syntheses of nanocomposite 18−21

For gold−iron oxide nanocomposites with variable iron concentration, five different reactions were prepared. Each solution contained 10 mg (25 µmol) $HAuCl_4$, 90×10^9/mL, seed and 50µL solution of tryptophan (5 µmol in 1:1 mixture of water and ethanol) in 100 mL Millipore water. Iron powder amounts of 20 mg (315 µmol), 30 mg (54 µmol), 40 mg (72 µmol), and 50 mg (90 µmol) were added for the syntheses of nanocomposites **18−21**, respectively. All these reaction mixtures were stirred at room temperature for 60 min and then filtered. The filtrate was concentrated by evaporation, and **18−21**nanocomposites were obtained as solid materials from the filtrate after 3 days. After discarding the supernatant solutions, the solid nanocomposites were further dried under vacuum before characterization. One negative control reaction was prepared without any iron powder.

Syntheses of nanocomposite 22−25

For gold−iron oxide nanocomposites with variable iron concentration, five different reactions were prepared. Each solution contained 10 mg (25 µmol) $HAuCl_4$, 540×10^9/mL seed, and 50 µL solution of tryptophan (5 µmol in 1:1mixture of water and ethanol) in 100 mL Millipore water. Iron powder amounts of 20 mg (36 µmol), 30 mg (54 µmol), 40 mg (72 µmol) and 50 mg (90 µmol) were added for the syntheses of nanocomposites **22−25**, respectively. All these reaction mixtures were stirred at room temperature for 60 min and then filtered. The filtrate was concentrated by evaporation, and **22−25** nanocomposites were obtained as solid materials from the filtrate after 3 days. After discarding the supernatant solutions, the solid nanocomposites were further dried under vacuum before characterization. One-negative control reaction was prepared without any iron powder.

Electrochemical Measurements

The electrochemical experiments were performed in a three-electrode electrochemical cell at room temperature with a 660D CH instrument potentiostat. A standard calomel electrode (SCE) was used as the reference electrode. The working electrode was nanomaterial-coated FTO

plates. Pt wire was used as the counter electrode. A KOH amount of 1.0 M (pH ~13.0) was used as the electrolytes. The nanomaterial/FTO working electrode was prepared as follows: 10 mg of nanomaterials was added into 0.2 mL EtOH; 0.2 mL water and 0.06 mL 5% Nafion solution and ultra sonicated for 30 min to prepare the ink; and then 20 μL of ink was loaded onto the FTO plate. The catalyst loading area was maintained as ~10 cm^2. Then, the plate was dried at room temperature for 24 h. Linear scan voltammograms (LSV) were recorded at a scanning rate of 50 mV/S. The electrochemical impedance spectroscopy (EIS) tests were carried out in a N_2-saturated 1.0 M KOH (pH ~13.0) solution at 0.5 V (vs SCE). Potentials were converted to RHE for comparison. The EIS spectra were obtained in a frequency range of $0.1-10^5$ Hz with an amplitude value of 5 mV. The charge transfer resistance (R_{ct}) was determined by fitting the Nyquist plot to a Randles equivalent circuit. Faradic efficiency was calculated on the basis of the volume of the oxygen collected per area of electrode at their corresponding onset potentials for 5 h , and the theoretical number of moles of the gas per area of electrode was calculated using the ideal gas law ($nO_2 = PV/RT$). Finally, the nO_2 was converted to photocurrent density (using photocurrent density = 4 ×nO_2 × F, where F is the Faraday constant, which is 0.0.096487 C/μmol). Amounts of oxygen produced were 45.3, 47.4, 60.3, and 56.3 mmol for nanocomposite**10**, **15**, **21**, and **25** respectively (after blank subtraction), which was obtained from the calibration curve. The total accumulated charge during 5 h of electrolysis was found to be 20.8, 25.3, 25.3, and 23.9 C (after blank subtraction) for **10**, **15**, **21**, and **25** respectively.

4.8 RESULTS AND DISCUSSION

4.8.1 Synthesis and Characterization

The nanocomposites **10–25** were synthesized by seed mediated approach using gold nanoparticles as seed, tryptophan as stabilizing agent and Fe powder as metal source and reducing agent. The solutions were stirred for 60 minutes to complete the reaction.

$$HAuCl_4.3H_2O + Fe\,(0) \xrightarrow[\substack{\textbf{Aqueous medium}\\\textbf{Room temp. stirring}\\\textbf{60 minutes}}]{\substack{\textbf{AuNP seed}\\\textbf{Tryptophan}}} Au\text{-}Fe_xO_y\ (10\text{-}25)$$
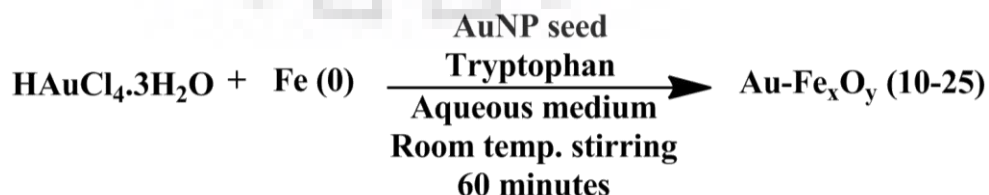
Scheme 4.2 Syntheses of Au-Fe$_x$O$_y$ (**10–25**) nanocomposites using tryptophan as stabilizing agent and Fe powder as metal source and reducing agent.

The resultant nanocomposites were characterized by absorption (visible) and vibrational (IR) spectroscopy, field emission scanning electron microscopy (FE-SEM), transmission electron microscopy (TEM), powder X-ray diffraction (PXRD), X-ray photoelectron spectroscopy (XPS) and DLS measurements.

4.8.2 Selectivity of tryptophan

The seed-mediated syntheses of the $Au-Fe_xO_y$ nanocomposites were performed in the presence of highly water-soluble L–amino acids to investigate their role as a stabilizing agent for the nanocomposites. Among the 16 different amino acids, only the solution containing tryptophan developed a violet color accompanied by the formation of surface plasmon resonance (SPR) band at 555 nm, indicating the formation of gold nanomaterials (Figure 4.31).
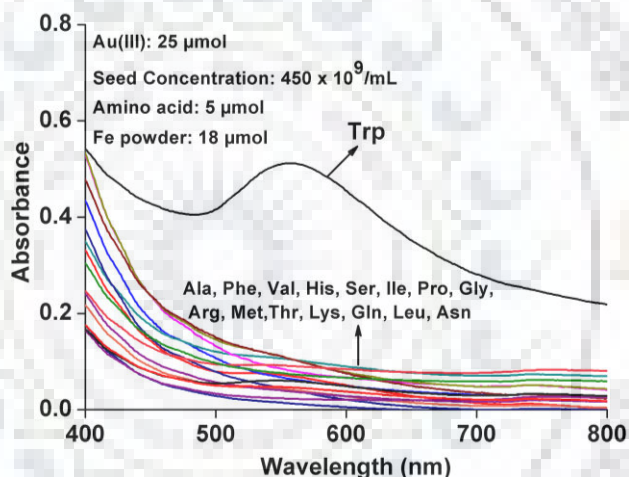
Figure 4.31 Selectivity of tryptophan as a stabilizing agent: absorption spectra after the redox reaction between Au(III) and Fe(0) in the presence of AuNP as a seed and different L-amino acids as the stabilizing agent.

Out of 20 essential amino acids, 4 amino acids could not be utilized because of their poor solubility in an aqueous medium. Under the same reaction condition, other 15 amino acids except tryptophan did not show any color change even after prolong reaction time, demonstrating the function of tryptophan as the stabilizing agent for the nanomaterial. The indole moiety of tryptophan, which is absent in other amino acids, creates the difference in the interaction with gold nanoparticle. The oxygen of carboxylic acid group and nitrogen of indole were responsible for the additional stabilization of gold nanomaterial. [424] Moreover the other amine nitrogen of tryptophan, which generally did not interact with gold, can interact with iron oxide for the stabilization of nanomaterial.

4.8.3 Variation of tryptophan

To find out the threshold amount of tryptophan required for nanomaterial formation, absorption experiment was performed with varying tryptophan concentrations (Figure 4.32). Absorption profile showed that a threshold amount of 2 μmol tryptophan was required for the development of the characteristic plasmonic band for the nanomaterials. Further increment in the tryptophan concentration up to 8 μmol did not show any significant alteration in the SPR band.
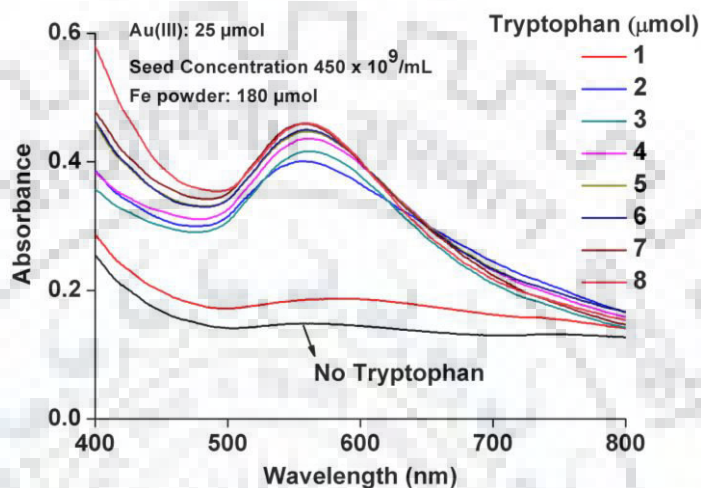
Figure 4.32 Absorption spectra of nanocomposites with varying tryptophan concentrations (1-8 μmol).

4.8.4 Seed variation methodology

Seed variation methodology was applied to investigate the role of seed solution for the syntheses of nanomaterials (**10−17**) by varying seed amounts from 90×10^9/mL to 720×10^9/mL (Figure 4.33) during the reduction of Au(III) in the presence of a constant amount of the reducing and stabilizing agent.

With increasing seed amount, the intensity of the SPR band increased with a slight blue shift. The absorption intensity remained almost unaltered after 540×10^9 mL^{-1} of seed solution. The same redox reaction in the absence of seed solution did not show the appearance of the SPR band. This observation confirmed the requirement of the AuNP seed in the nanomaterial synthesis.

The nanocomposites **10** and **15** were further characterized by TEM and FE−SEM images (Figure 4.34). The gold nanoparticles were deposited on the iron oxide layer in the Au−Fe$_x$O$_y$ nanocomposites **10** and **15**.
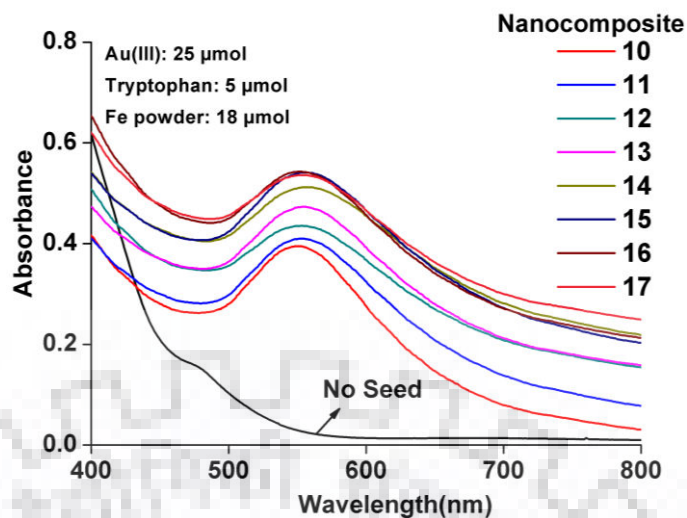
Figure 4.33 Absorption spectra of nanocomposites **10** (90×10^9/mL), **11** (180×10^9/mL), **12** (270×10^9/mL), 13(360×10^9/mL), **14** (450×10^9/mL), **15** (540×10^9/mL), **16** (630×10^9/mL) and **17**(720×10^9/mL) synthesized using different concentration of seed during the reduction of Au (III) by Fe powder in presence of tryptophan.
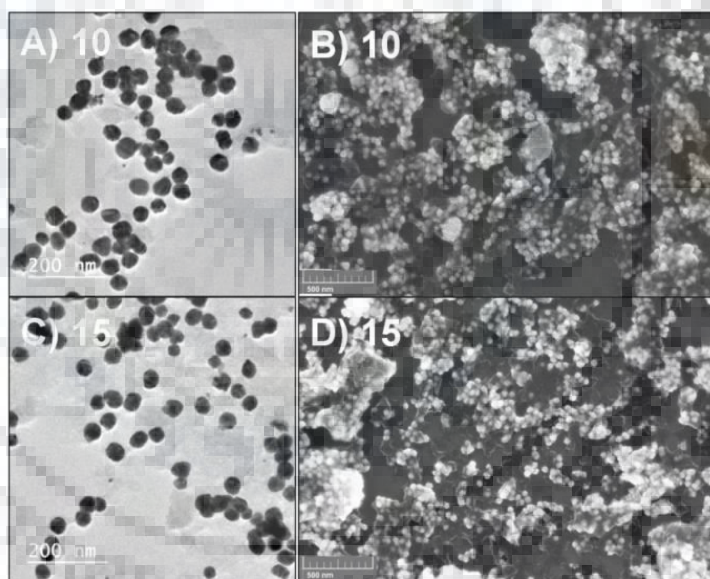
Figure 4.34 TEM (A, C) and FE–SEM (B, D) images of composites **10** and **15**. Scale bars in TEM: 200 nm and FE–SEM: 500 nm.

4.8.5 Variation of iron

The effect of variation of iron powder compared with the iron amount used for 10 and 17 nanocomposite syntheses was also explored with two different seed concentrations .In the absence of iron powder, no SPR band was developed confirming the vital role of metal powder in the reduction process (Figure 4.35 and 4.36).
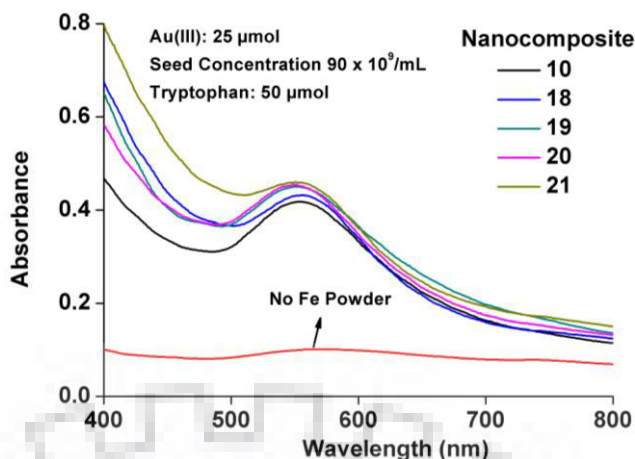
Figure 4.35 Absorption spectra of nanocomposites synthesized with increasing iron amount (in parentheses), **10** (18 μmol), **18** (36 μmol), **19** (54 μmol), **20** (72 μmol) and **21** (90 μmol) at seed amount of 90×10^9/mL.
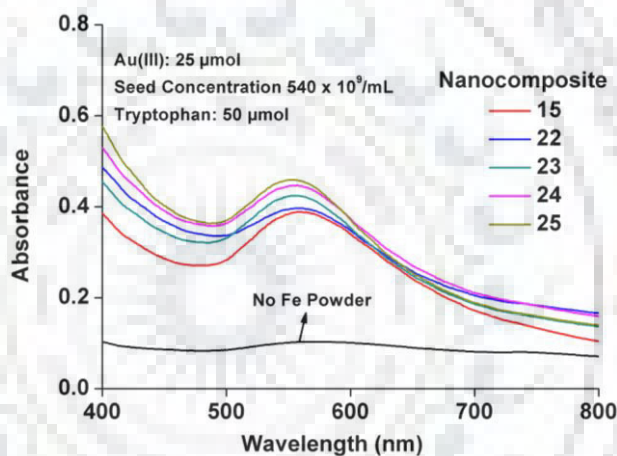
Figure 4.36 Absorption spectra of nanocomposites synthesized with increasing iron amount(in parentheses),.and 540×10^9 mL^{-1} of seed amount, **10** (18 μmol), **18** (36 μmol), **19** (54 μmol), **20** (72 μmol) and **21** (90 μmol) at seed amount of 90×10^9/mL .

With a fixed seed and tryptophan amount, increasing the iron amount (from 18 μmol to 90 μmol) resulted in the formation of nanocomposites, exhibiting clear SPR peak at 555 nm With 90×10^9 mL^{-1} of seed amount, the addition of a variable iron amount resulted in the formation of nanocomposites **10**, **18**, **19**, **20**, and **21** (Figure 4.35) whereas with 540×10^9 mL^{-1} the addition of a variable iron amount resulted in the formation of nanocomposites **15**, **22**, **23**, **24** and **25** (Figure 4.36).

Nanocomposites **21** and **25** were taken as representative materials for further characterization purpose. The TEM and FE-SEM images (Figure 4.37) clearly confirmed the deposition of gold nanoparticles on the iron oxide layer.
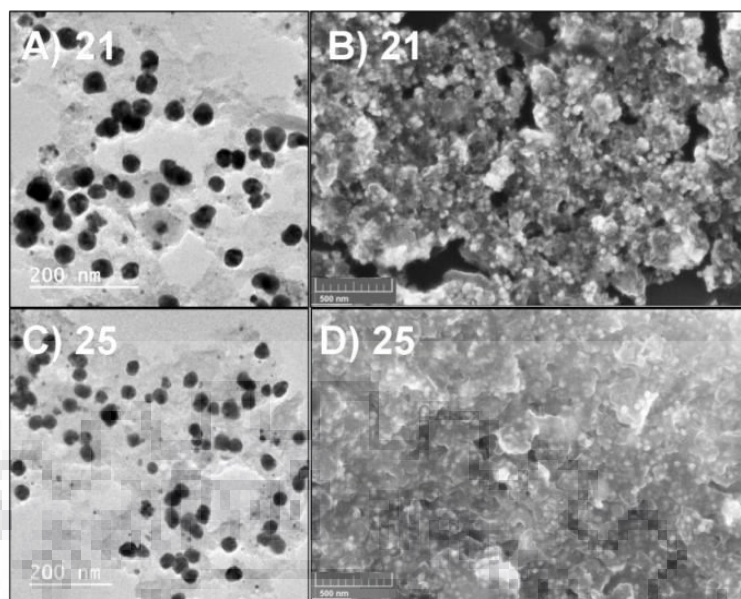
Figure 4.37 TEM (A, C) and FE–SEM (B, D) images of composites 10 and 15. Scale bars in TEM: 200 nm and FE–SEM: 500 nm.

4.8.6 DLS measurements

Zeta potential and polydispersity of the nanocomposites were measured from DLS measurements. The surface charge (ζ-potential) of nanocomposites **10** to **17** increased (Figure 4.38A) with increase of seed amount (Table 8). The polydispersity index (PDI) trend (Figure 4.38B) suggested monodispersity increased with the increase of seed concentration. (Table 25)
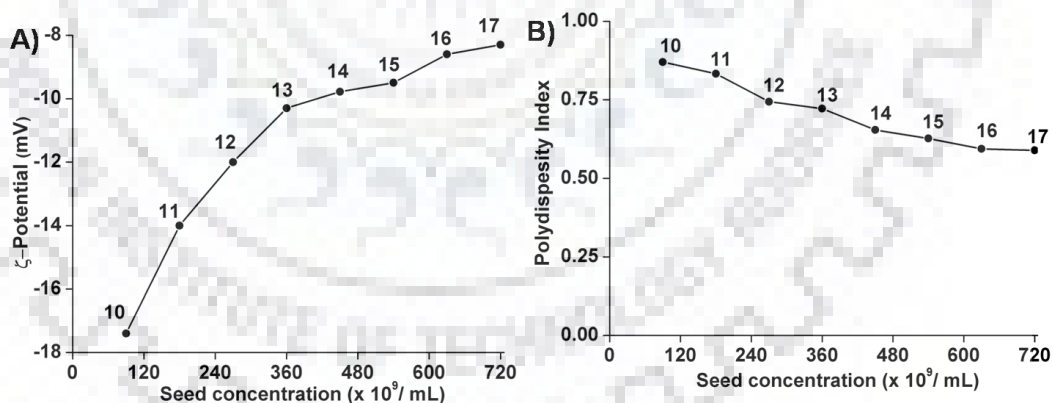
Figure 4.38 ζ-potentials (A) and Polydispersity (B) of nanocomposites **10–17**.

ζ -potential and monodispersity also increased for **18** to **25** (Figure 4.39A and B) with increase in concentration of iron amount in the presence of low seed concentration. However, in the case of higher seed concentration, surface charge densities and polydispersity were almost constant for **22** to **25** with the increasing concentration of the iron amount (Table 4.5).
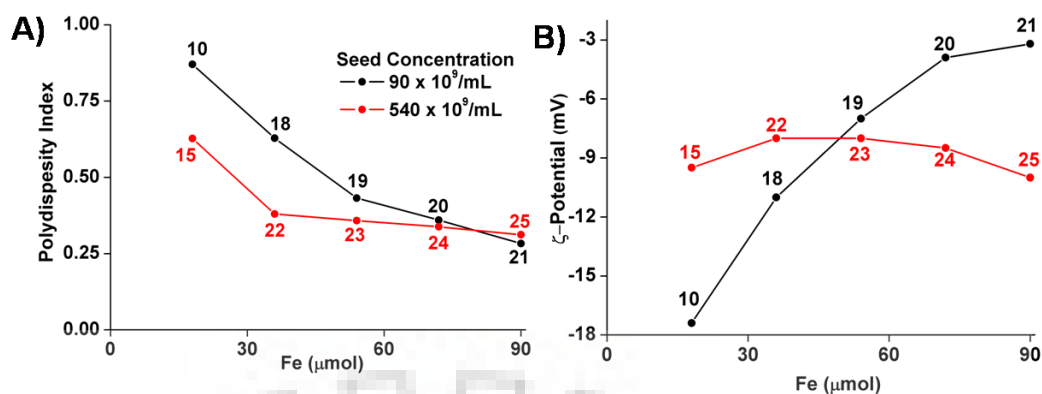
Figure 4.39 ζ-potentials and PDI of nanocomposites **18–22**.

Table 4.5: PDI and Zeta potential values of nanocomposites

Nanocomposite	PDI	Zeta potential(mV)
10	0.87	-17.4
11	0.83	-14.0
12	0.74	-12.0
13	0.72	-10.3
14	0.65	-9.8
15	0.63	-9.5
16	0.61	-8.6
17	0.60	-8.3
18	0.63	-11.0
19	0.43	-7.0
20	0.36	-4.0
21	0.30	-3.2
22	0.40	-8.0
23	0.36	-8.0
24	0.33	-8.5
25	0.31	-10.0

4.8.7 Elemental composition

The chemical components within the nanocomposites **10**, **18**, **19**, **20**, and **21**were further confirmed from elemental mapping, EDX, and EDX line scanning via FE−SEM. These results clearly showed that the metal powder, which has participated in the redox reaction, served the role of reagent in the nanocomposite formation. The presence of nitrogen confirmed the participation of tryptophan in the nanocomposites. This EDX analyses (Figure 4.40) showedthe poor incorporation of iron in the nanocomposites **10** with Au : Fe ratio 1: 0.05 whereas iron

content increased in **15** with Au : Fe ratio 1:0.16. Elemental composition of nanocomposites **10** and **15** was further verified from elemental mapping (Figure 4.41).
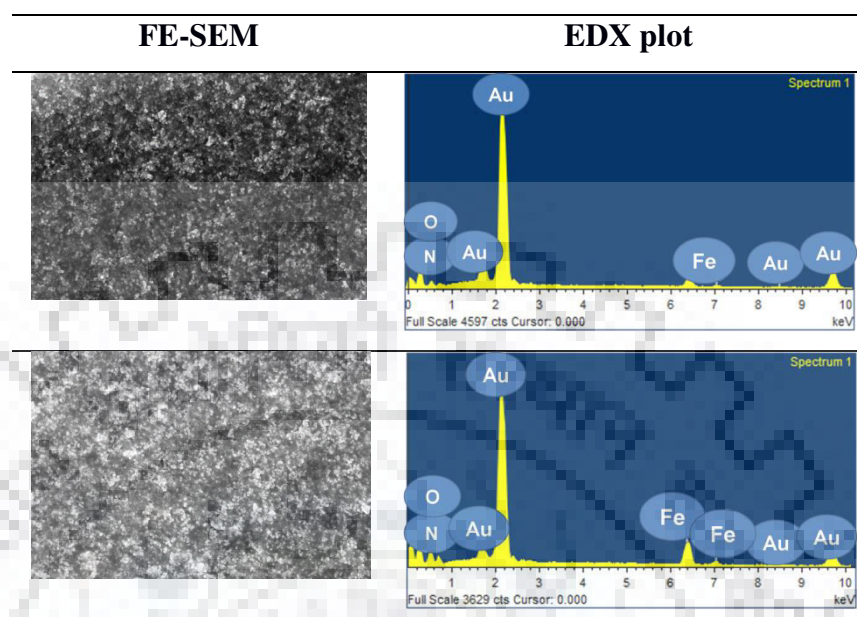
FE-SEM	EDX plot

Figure 4.40 FE-SEM images, EDX plot of nanocomposites **10** (top) and **15** (bottom).

Elemental mapping	Au-mapping	Fe-mapping	N-mapping	O-mapping
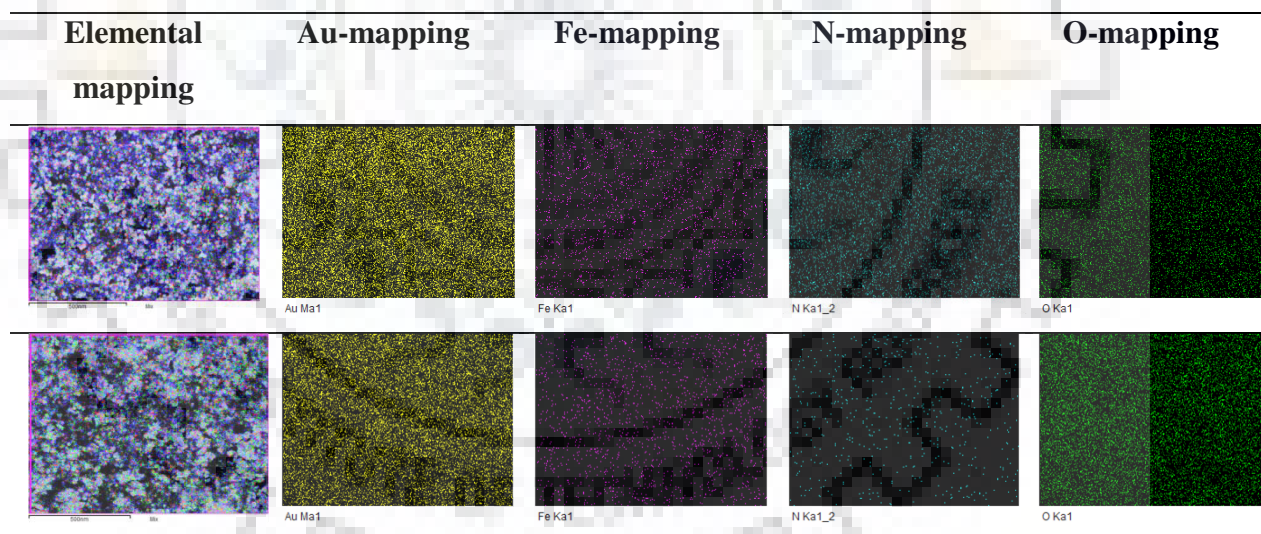
Figure 4.41 EDX elemental mapping of nanocomposite**10** (top) and **15** (bottom).

Further characterization with EDS line scanning also confirmed the formation of nanocomposites **10** and **15** and showed the peaks for gold , iron, nitrogen and oxygen (Figure 4.42 and 4.43).
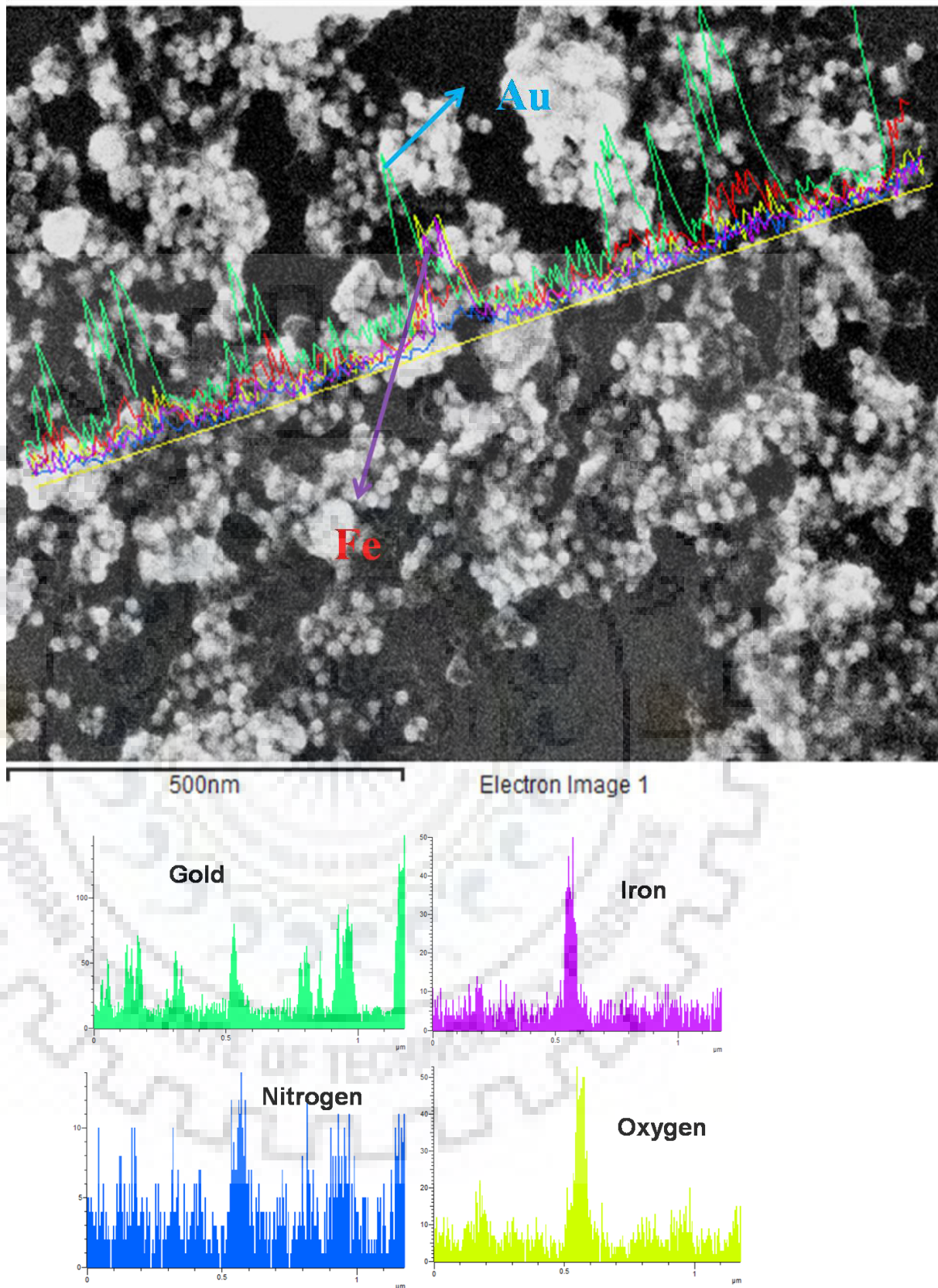
Figure 4.42 EDX line scanning of nanocomposite **10** showing peaks for gold, iron, nitrogen and oxygen.
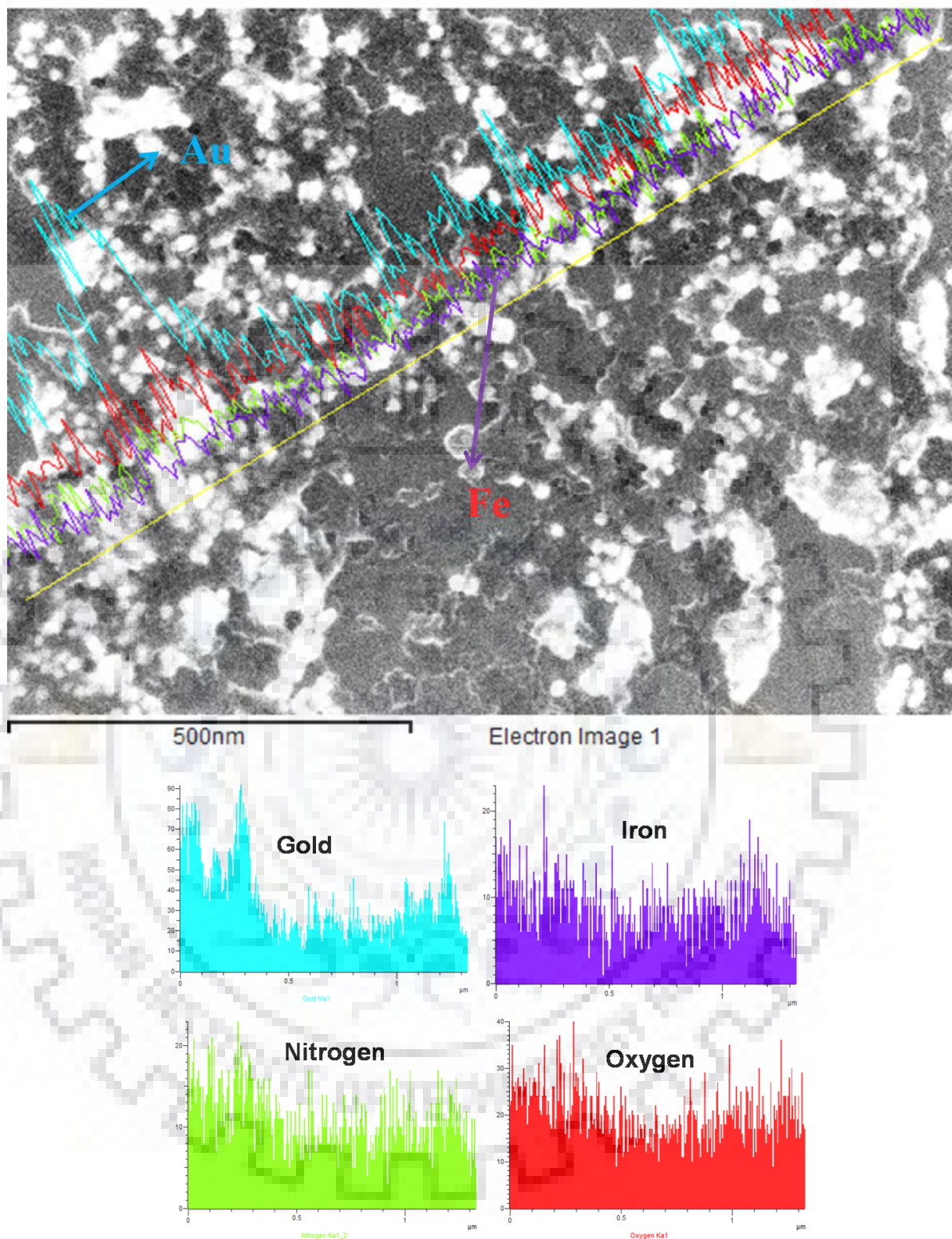
Figure 4.43 EDX line scanning of nanocomposite **15** showing peaks for gold, iron, nitrogen and oxygen.

Nanocomposites **21** and **25** were also characterized by EDX, Elemental mapping and EDX line scanning via FE-SEM. With increasing the iron amount, iron incorporation also increased with respect to gold. The iron amount was calculated from the EDX- analysis, (Figure 4.44) in case of nanocomposite **21** iron content increased 5.2 times compared to the nanocomposite **10** with

Au : Fe ratio 1: 0.26. This enhancement of iron content within these two nanocomposites in the presence of lower seed concentration can be correlated to the amount of iron used in the syntheses. However, the iron content with respect to gold showed slight enhancement in nanocomposite **25** (1.6 times) with Au : Fe ration 1: 0.20 compared to the nanocomposite **15** where the syntheses were performed with the higher seed amount. Elemental mapping was also verified from the elemental composition of **21** and **25** (Figure 4.45).
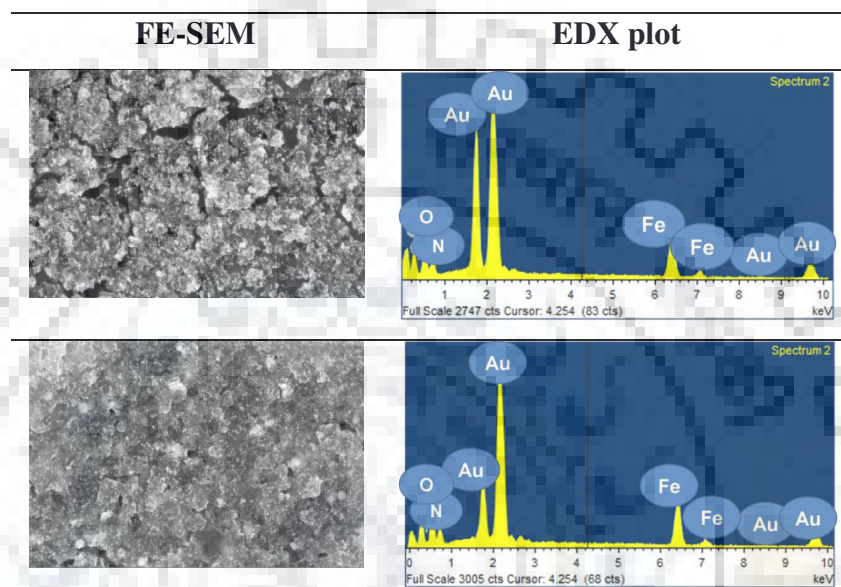
Figure 4.44 FE-SEM images, EDX plot of nanocomposites **21** (top) and **25** (bottom).
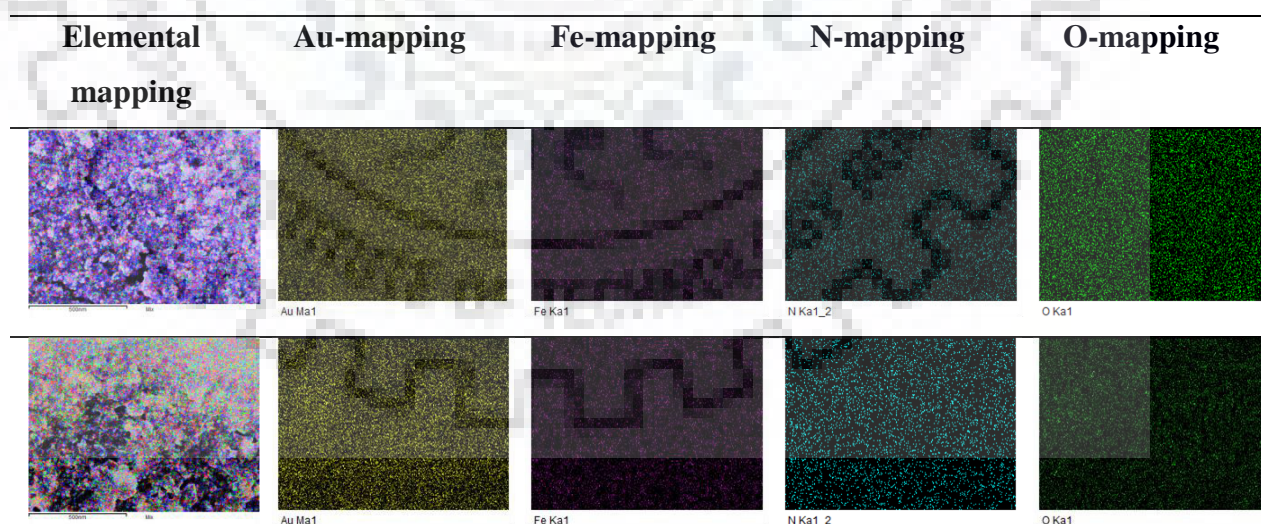
Figure 4.45 EDX elemental mapping of nanocomposite **21** (top) and **25** (bottom).

Further characterization with EDS line scanning also confirmed the formation of nanocomposites **21** and **25** and showed the peaks for gold , iron, nitrogen and oxygen (Figure 4.46 and 4.47).
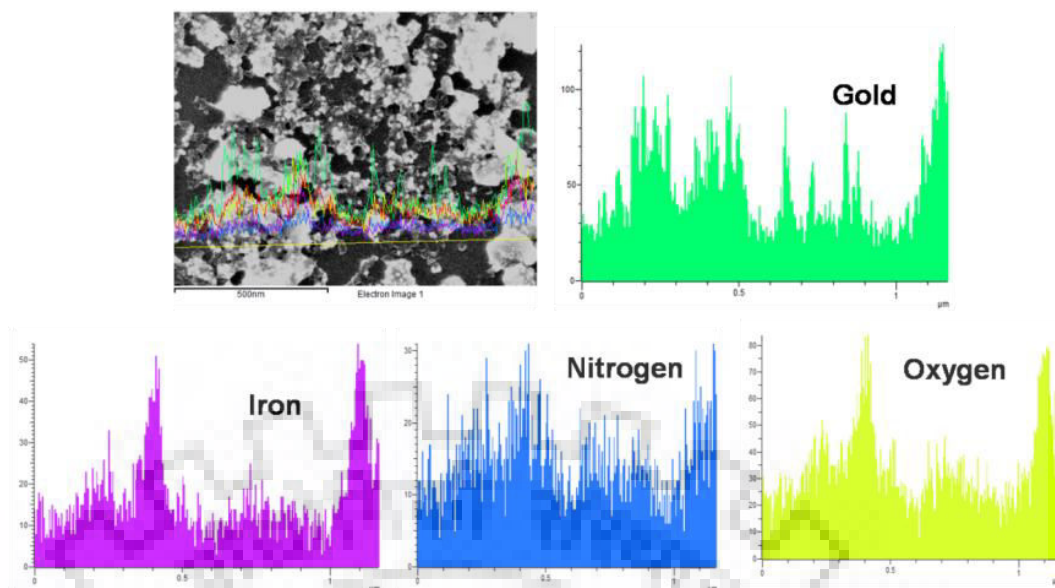
Figure 4.46 EDX line scanning of nanocomposite **21** showing peaks for gold, iron, nitrogen and oxygen.
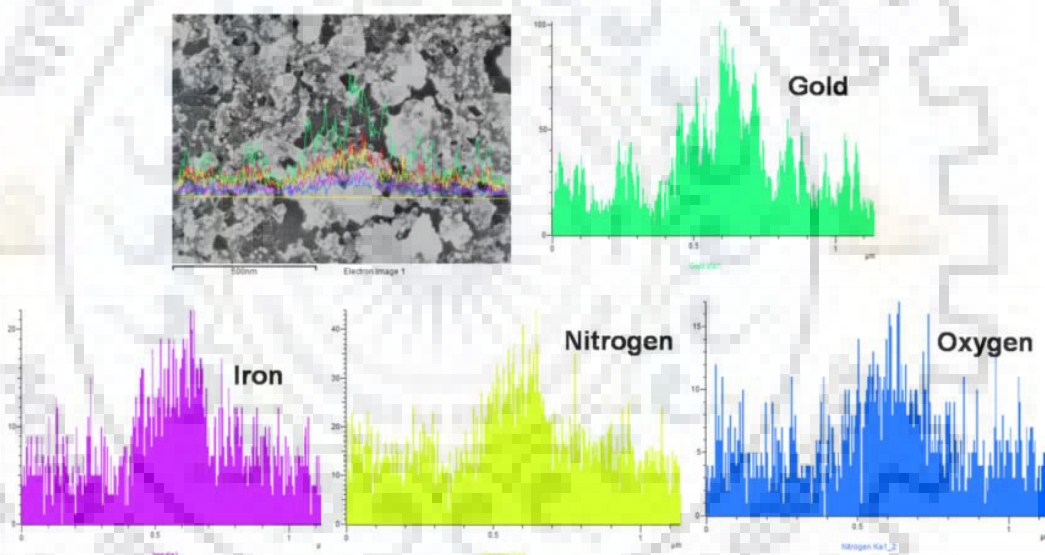
Figure 4.47 EDX line scanning of nanocomposite **25** showing peaks for gold, iron, nitrogen and oxygen.

4.8.8 XPS measurements

XPS measurements were carried out to further investigate the chemical compositions and elemental valence states for nanocomposites **10**, **15**, **21**, and **25**. The survey spectra confirmed the presence of gold, iron, carbon, nitrogen, and oxygen atoms in the nanocomposites (Figure 4.48). Binding energy studies confirmed the peaks for Au $4f_{7/2}$,[382] and O 1S [384] at 83.0eV, and 530 eV respectively. The detailed scans for N 1s (4.49A) for **21** showed two peaks around 398.3 and 401.0 eV after deconvolution due to the presence of the indole-based nitrogen atom and amine nitrogen of tryptophan. From high resolution scans for 2p of Fe, two distinct peaks

were identified at 709.88 eV and 723.3 eV, which can be assigned to the Fe $2p_{3/2}$ and Fe $2p_{1/2}$ electrons, respectively (Figure 4.49B).[383] The Fe $2p_{3/2}$ was associated with the satellite peak around 719 eV, indicating the predominance of Fe_2O_3 in these samples.
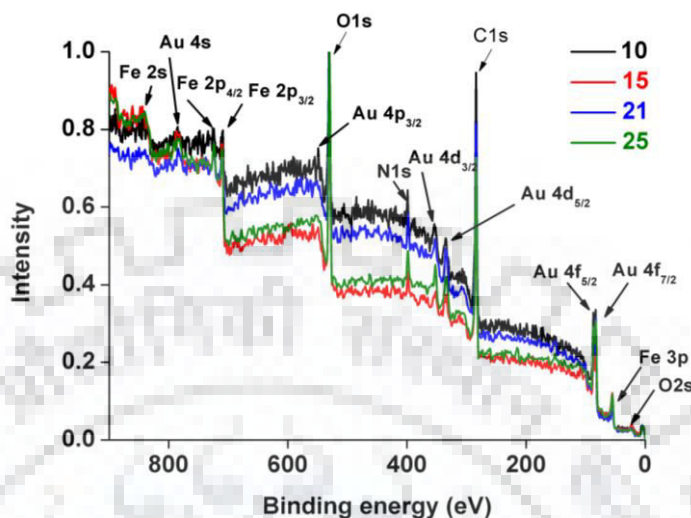
Figure 4.48 XPS survey spectra of nanocomposites **10**, **15**, **21** and **25**.
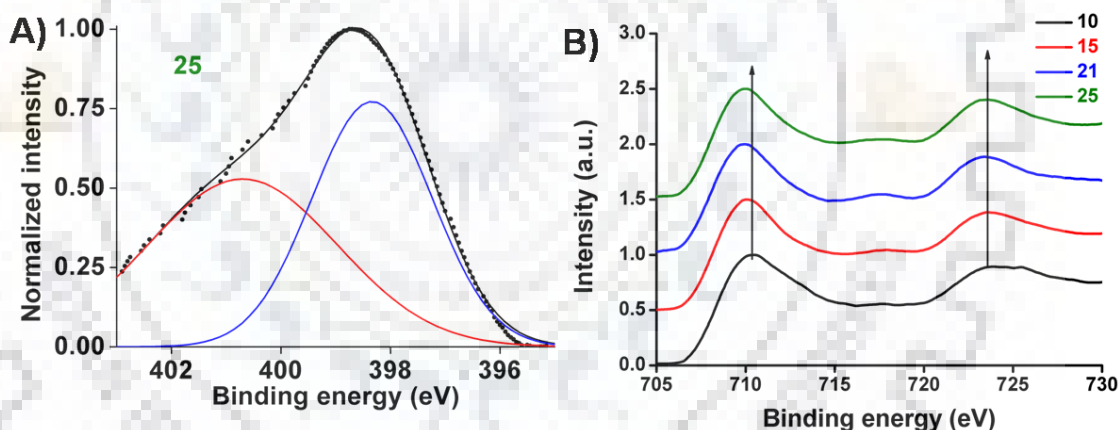
Figure 4.49 XPS survey spectra for nitrogen in **25** (A) after deconvolution and (B) iron in the nanocomposites **10**, **15**, **21** and **25**.

4.8.9 FTIR spectroscopy

The IR spectra, of the nanocomposites **10**, **15**, **21**, and **25** ranged between 450-500 cm^{-1}. The broad peak in IR spectra with maximum peak intensity at 3423 cm^{-1} was due to the stretching vibration of amine group from tryptophan. [98] The small peaks around 2925 cm^{-1} were due to methylene protons of tryptophan. The position of carbonyl frequency was shifted to 1615 cm^{-1} because of the interaction of carbonyl oxygen with the gold nanoparticle. [98] In addition to the XPS, the IR spectra within a part of the finger print region (400−1500 cm^{-1}) in samples **10** and

15 has absorption peak at 660 cm^{-1} suggested the formation of γ-Fe$_2$O$_3$ and in samples **21** and **25** has absorption peak at 550 cm^{-1} suggested formation of α-Fe$_2$O$_3$ (Figure 4.50) [387].
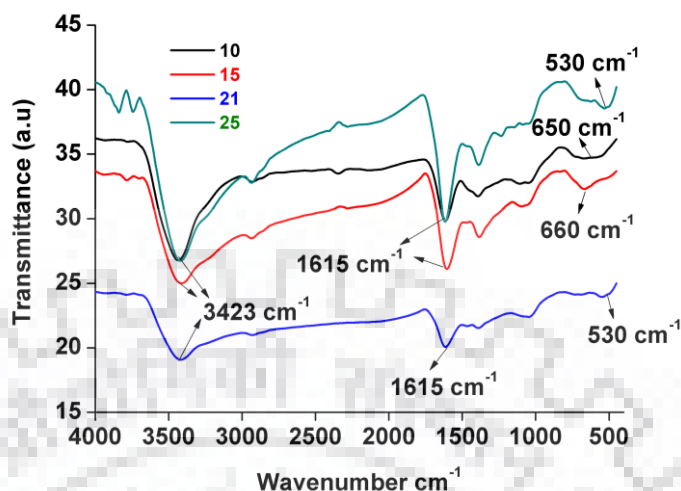
Figure 4.50 IR spectra of nanocomposites **10**, **15**, **21** and **25**.

4.8.10 PXRD

In PXRD, only the peaks due to Au(0) was observed. (Figure 4.51) The absence of diffraction pattern for iron oxide suggested the similar amorphous nature in the nanocomposites. The 2θ values at 38.3, 44.5, and 154.7 angles were due to (111), (200), and (220) planes, respectively, according to the JCPDS (Joint Committee on Powder Diffraction Standards) no. 04-0784, USA for Au nanoparticles. The crystallite size from XRD using the Scherrer equation for gold was found to be 15 nm, which was in good agreement to the size of gold nanoparticles obtained from TEM images.
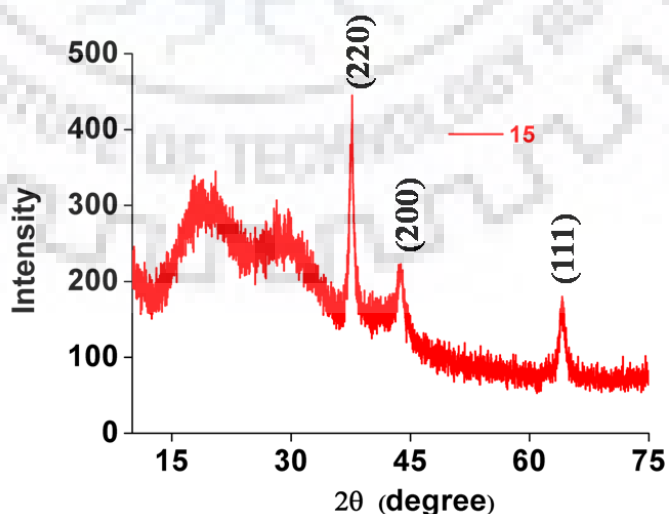
Figure 4.51 Representative PXRD of nanocomposites **15**.

4.8.11 Electrocatalytic behaviour

To investigate the electrocatalytic behaviour of the synthesized $Au-Fe_xO_y$ catalysts, cyclic voltametric scans for the nanocomposites (**10**, **15**, **21** and **25**) were executed in a 1.0 M KOH solution at 50 mVs^{-1} scan rate. The oxidation and reduction peaks in all the cases corresponded to a Fe^{3+}/Fe^{2+} redox couple. (Figure 4.52)
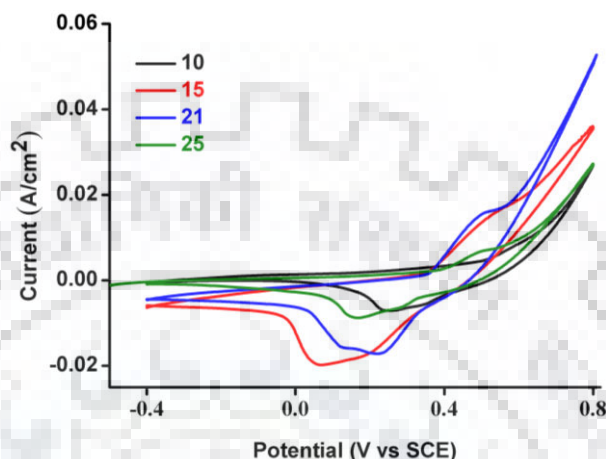
Figure 4.52 Cyclic voltammograms of the nanocomposites **10**, **15**, **21** and **25**.

The OER activities of the synthesized $Au-Fe_2O_3$ nanocomposites were investigated by LSV in an alkaline aqueous solution at pH 13.0 with the FTO glass plate coated with different nanomaterials as a working electrode. The polarization curves in (Figure 4.53A) demonstrated the comparative OER activity of the nanocomposites (**10**, **15**, **21** and **25**) and the mixture of seeds with commercially available Fe_2O_3 and Fe_3O_4 mixtures. In both these mixtures, 26% iron oxides were used with respect to gold amount. It was found that all the nanocomposites showed better OER activity with respect to control materials (Figure 4.53B).
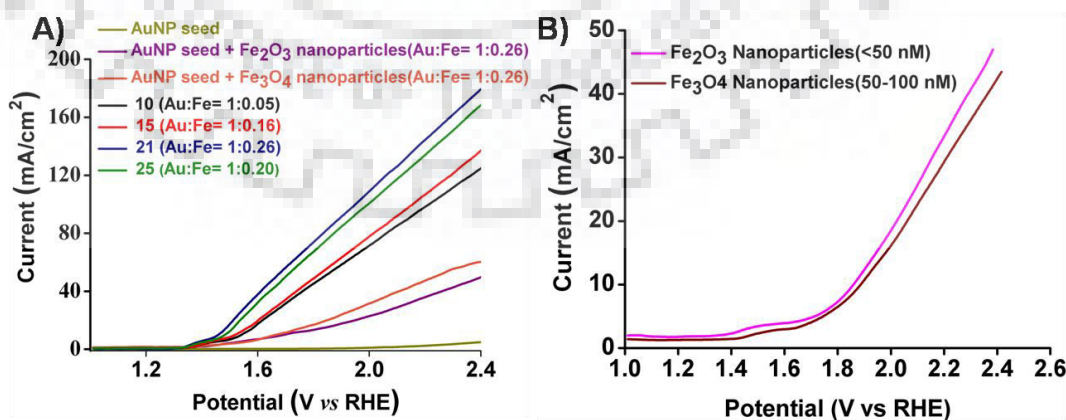
Figure 4.53 (a) LSV for the OER activity of nanocomposites **10**, **15**, **21**, **25** and the mixture of AuNP and commercially available Fe_xO_y nanoparticles at pH 13.0

The significant enhancement in the OER activity of the composites was probably due to strong localized interfacial interactions between Au and Fe_xO_y and the increase in the active surface area after composite formation, which was observed in the case of gold manganese oxides.[425]

For oxygen evolution reaction, the overpotential at a current density of 10 mA/cm^2 was commonly used as a figure of merit for the catalysts. The overpotential values were 0.53V, 0.52V, 0.45V, and 0.47 V for nanocomposites **10**, **15**, **21** and **25** respectively (Table 9). Therefore, nanocomposite **21** could be considered the best electrocatalyst among these four Au−Fe_xO_y nanocomposites for OER activity. Overpotentials of the controlled materials were greater than 0.155 V at 10 mA/cm^2 current density. The overpotential values in the presence of gold in the nanocomposites were similar to the reported observation.[304] The observed maximum enhancement in the OER activity of **21** was due to the presence of the highest Au:Fe ratio among the Au−Fe_xO_y nanocomposites. The better OER activity of nanocomposites in comparison to individual gold or iron oxide nanomaterial might be due to the local interaction of Au through its dissolution and deposition onto Fe_xO_y sites. This was similar to the reported case of Au/MnO_x OER activity.[425]

To analyze the comparative electrocatalytic behavior, tafel slope, which is an important parameter were calculated (Figures 4.54A). It is well-known that the smaller the tafel slope, the higher the charge transfer coefficient, resulting in lowering of energy barrier of the electrochemical reaction.[426] Tafel slopes obtained from the four nanocomposites,**10**, **15**, **21** and **25** from the plot of overpotential (η) versus the logarithm of current density were 210, 198, 132, and 159 mV/dec (Table 26), indicating the better electrocatalytic efficacy of **21** and **25** compared to **10** and **15**.
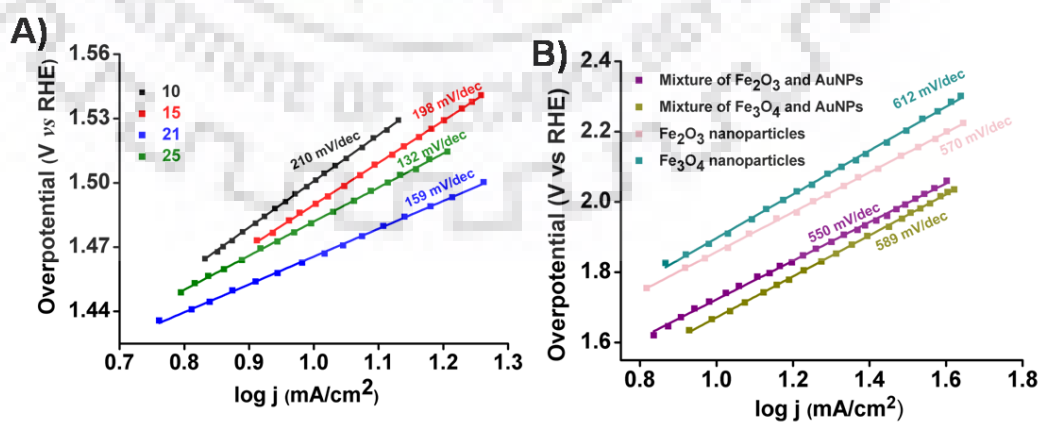
Figure 4.54 (A) Tafel plots obtained from the corresponding LSVs for **10**, **15**, **21** and **25**; (B) Tafel plot of commercially available iron−oxide nanoparticles and their mixures.

These tafel slopes were significantly smaller in comparison to the commercially available iron oxide nanomaterials (Figure 4.54B). However, the Tafel slopes for the nanocomposites **10**, **15**, **21** and **25** were higher in comparison to the core−shell Au−Fe_xO_y nanoparticles [304] of a much smaller size.

To investigate the electron transfer kinetics, electrochemical impedance spectroscopy (EIS) measurements were performed with the four nanocomposites. Figure 4.55 describes the Nyquist plots acquired for the nanocomposites at their overpotentials. The charge transfer resistances for **10**, **15**, **21** and **25** nanocomposites were 298 Ω, 250 Ω, 78 Ω, and 110 Ω (Table 4.6), which was again consistent with the OER activity of the catalysts. The electrocatalytic trend of the catalysts may be explained in terms of the iron content in the composites. The order of iron content in the catalysts is **21 > 25 > 15 > 10** which resembled the order of their catalytic activity, that is, the turn over frequency of the catalysts (Table 4.6). Increase in the iron content might result in the increment of the active sites in the catalysts, which caused enhancement in the OER activity.
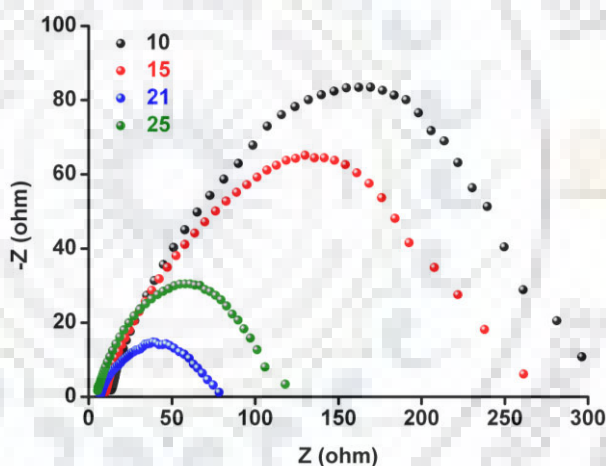
Figure 4.55 Impedance spectra of the nanocomposites **10**, **15**, **21** and **25**.

The nitrogen containing aromatic indole group in tryptophan showed a different one-electron oxidation potential at a different environment.[427] Tryptophan might be also effective in the catalytic activity as it can modulate the electrochemistry of nanocomposites at different concentrations.[428] The nitrogen of indole may contribute in the charge separation[429] because of the electronegativity differences between iron and the nitrogen. This charge separation may enhance the OH⁻ adsorption on the nanomaterial surface, which eventually resulted in the increase of the OER activity.

Table 4.6: Comparison of different parameters of four Au−Fe$_x$O$_y$ nanocomposites: **10**, **15**, **21** and **25**.

Nanocomposite	Au loading[a] (wt %)	Overpotential[b] (V)	R$_{ct}$[c] (Ω)	current[d] (mA/cm2)	TOF[e] (s^{-1})	Tafel slope (mV/dec)
10	70	0.53	298	123	0.17	210
15	59	0.52	250	136	0.21	198
21	52	0.45	78	178	0.31	132
25	48	0.47	110	166	0.29	159

[a]Actual gold loading has been confirmed by EDXS analysis of FE-SEM. [b]Overpotenials at a current density of 10 mA/cm^2. [c]R$_{ct}$ is the charge transfer resistance obtained by fitting the EIS data. [d]Current density was measured at 2.4 V (vs RHE). [e]Turnover frequency (TOF) at 1.44 V vs RHE has been calculated as per the available method. [414]

The Faradaic efficiencies (Figure 4.56) during OER were calculated at their corresponding onset potentials and the values were 84%, 86%, 93%, and 91% for the nanocomposites **10**, **15**, **21** and **25** respectively. Amounts of oxygen produced were 45.3, 47.4, 60.3, and 56.3 mmol for **10**, **15**, **21** and **25**, respectively (after blank subtraction), which was obtained from the calibration curve in. The total accumulated charge during 5 h of electrolysis was found to be 20.8, 25.3, 25.3, and 23.9 C (after blank subtraction) for **10**, **15**, **21**, and **25**, respectively (Figure 4.55B).
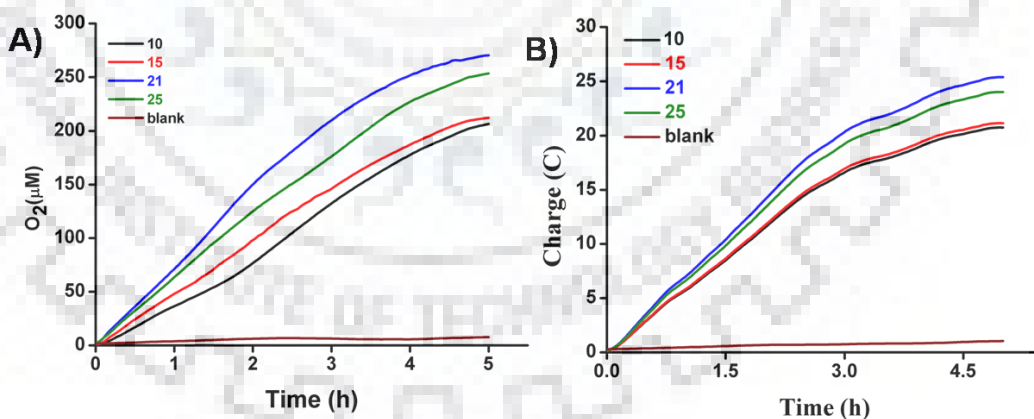
Figure 4.56 (A) Evolution of O$_2$ with time (B) total accumulated charge during bulk electrolysis with nanomaterials at pH 13.

To check the stability of the materials, a chronoamperometry test (Figure 4.57) were carried out for the nanocomposites at their corresponding overpotentials for 5 h, and the current densities were found to be extremely stable for nanocomposites **10** and **25** indicating a long-term viability of these materials. Ratios of gold and iron in the nanocomposites after electrochemistry were analyzed with the EDXS analysis of FE-SEM images (Figure 4.58 and

Table 4.7). Slight loss of iron (within 0.5−5%) with respect to the gold amount was observed in all the nanocomposites probably because of the formation of FeO_4^{2-} as reported.[208a] Because the loss of iron was less than 5%, these materials were sufficiently stable after their electrocatalytic performance.
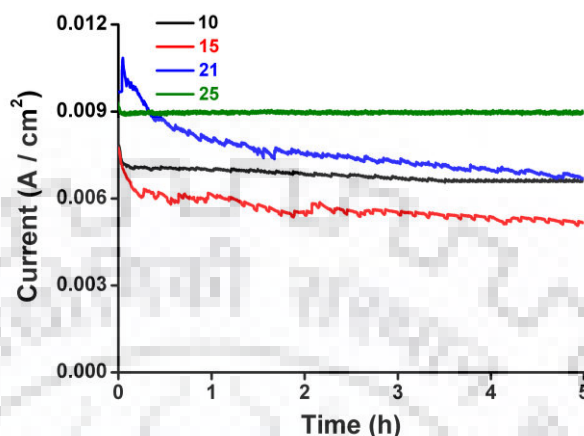
Figure 4.57 Chronoamperometric plot showing the stability of the nanocomposites **10**, **15**, **21** and **25**.
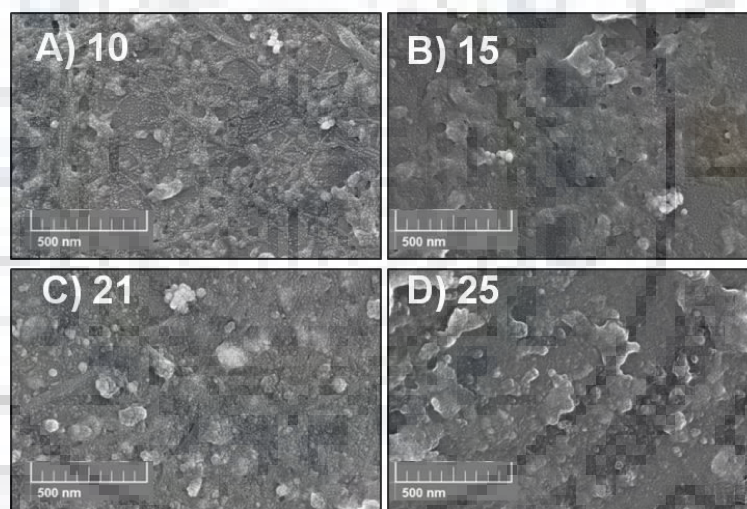
Figure 4.58 FE-SEM images of nanocomposites **10**, **15**, **21** and **25** (left to right) after electrocatalysis reactions. Scale bar in: 500 nm.

Table 4.7: The ratio of gold and iron in nanocomposites before and after electrocatalysis

Nanocomposite	Au:Fe	
	As synthesised	After Catalysis
10	1:0.05	1:0.05
15	1:0.16	1:0.13
21	1:0.26	1:0.21
25	1:0.20	1:0.25

4.9 CONCLUSION

In summary, a facile room temperature synthetic route for tryptophan-stabilized $Au-Fe_xO_y$ nanocomposites was developed. These nanocomposites were obtained in the presence of gold nanoparticle seed after the redox reaction between Au(III) and Fe(0). The variation of seed and ironamounts in the reaction mixture led to form $Au-Fe_xO_y$, with different Au : Fe ratio. These $Au-Fe_xO_y$ nanocomposites were explored for their role as electro catalysts during the OER from water in a basic condition. The OER activity of the catalysts was rationalized on the basis of their overpotentials, and it was seen that the catalytic performance directly depended upon the amount of the iron content in the nanocomposites. The stability of the materials was monitored by chronoamperometry test and the FE-SEM analysis of the nanocomposites after OER performance.

Overall Conclusion and Scope of the Future Work

The work presented in the thesis showed that gold nanoparticles as seed developed different architectures in a growth controlled manner using amino acids and amine modified DNA as capping agents. The seed mediated method was further used for the formation of bimetallic nanocomposites utilizing Fe powder as a reducing agent with different stabilizing agents like sodium citrate and tryptophan. The synthesized materials were applied for the biomolecule detection, drug release and catalytic applications

Different nanostructures from 16 nm AuNPseed were developed by controlling the amount of the seed and choice of the reducing agent. AuNP seed were incubated with 8-mer 5'-amine modified ssDNA for performing growth controlled reactions and resulted in the formation of nanoflowers and nanospheres. Seed variation methodology in presence of hydroxylamine developed nanoflowers at high concentration of seed. In contrast using hydroquinone as reducing agent developed nanoflowers with low seed amount and nanospheres with high seed amount. The nanoflowers formation resulted from the high affinity ACA terminal of amine modified DNA. The role of ACA terminal was verified from mutated sequences where cytosine in the ACA part has been replaced by thymine. The role of amine modification was verified fromno modification, modifications at both end and at 3' terminal of DNA. Decreasing the length of DNA sequence below 8-mer did not develop the nanoflowers. The different nanostructure like nanoflowers and nanospheres were used as colorimetric sensor for the detection of DNA sequence. Growth reactions with all natural amino acids using gold nanoparticles as seeds in presence of hydroxylamine developed precipitate or aggregate or non-aggregate or coral shaped nanostructures depending upon nature of the amino acids. The selective formation of coral shape resulted from the amino acid methionine. Control reactions with sulfur containing biomolecules, organic molecules and inorganic salts resulted in the formation of either aggregated or non aggregated nanoparticles..

Interactions between the amino acids and amine modified DNA were used to control the growth of the nanoparticles. The growth reactions in presence of all natural amino acids were further explored by incubating the nanoseeds with DNA prior to amino acid addition. Introduction of DNA developed selectivity among the amino acids based on hydrogen bonding interactions. The strongest hydrogen bonding between the arginine and DNA resulted in the nanoflowers formation. This observation were successfully transferred for the detection of single arginine modification closest to the carboxy terminus of 3_{10}-helical peptide Ac-$(AAAAK)_3A-NH_2$ for conformational change towards α-helix peptide in Ac-$(AAAAR)_3A$-

NH$_2$Time dependent growth reaction of AuNP seeds in presence of amino acids with polar uncharged side chains was observed. The growth reaction resulted in aggregation of nanoparticles immediately or gradually with time depending upon the nature of amino acids. Thegrowth reactions were again performed with two amine modified DNAs sequences, where in one case all the adenines of the DNA sequence were replaced by thymine. The aggregation process was inhibited in presence of DNA.The hydrogen bonding interactions, van der Waals interaction and water mediated bonds between amino acids and nucleic bases such as adenine and thymine were explored for controlling the aggregation process of gold nanoparticle with amine modified DNAs. The process was used for the differentiation of four amino acids containing polar uncharged side chains via time dependent aggregation process in presence of sub-nanomolar concentration of amine modified DNA and its mutated version.

Facile route for the syntheses of gold- iron oxide nanocomposites were introduce utilizing iron powder as a reducing agent, AuNPs as seed and sodium citrate or tryptophan as stabilizing agent. The ratio of Au and Fe in citrate stabilized nanocomposites was modulated by changing the three parameters seed, stabilizing agent and Fe amount. Increasing the Fe amount led to increase in Fe content and decreasing the citrate amount also led to increase in Fe content in the nanocomposites. The citrate stabilized nanocomposites showed the variable exchange bias and were applied for release of drug doxorubicin and catalytic nitroarene reduction. The tryptophan stabilized nanocomposites were developed from the selective stabilization by tryptophan among all natural amino acids. The syntheses resulted in the deposition of Au nanoparticles on the surface of iron oxide layer and nanocomposites showed variable Au to Fe ratio obtained by controlling the seed amount and reducing agent. These nanocomposites were used as electrocatalysts for thermodynamically unfavourable OER. The electro chemical performances of the nanocomposites depend on the Au to Fe ratio and highest active catalyst showed overpotential of 0.45 V at 10 mV/cm^2 Chronoamperometry test at corresponding overpotentials indicate long term stability of the nanocomposites. FE-SEM analysis after post electrocatalysis showed slight loss of Fe with respect to Au also indicating stability of the catalysts.

In future the growth reactions can be performed using AuNP seed of different sizes and shape and with silver nanoparticles for generation of different architectures. Nucleic acid template chemistry can be developed for the detection of nucleic acids utilizing oligonucleotides attached to gold nanoparticles as templates. The introduction of functional group modified organic molecule and the target molecule can develop particular structures which can be used for the selective detection of analytes. Controlling the aggregation and non-

aggregation of nanoparticles with different biomolecules can be used for the development of colorimetric sensors. Different DNA sequences can control the shape of metallic nanoparticles however controlling the shape of the bimetallic nanocomposites is challenging. DNA can be used for controlling the morphology of bimetallic nanocomposites and could find diverse applications especially in bio based systems. Nanocomposites can further be used for drug release and chemoselective conversions of nitroarenes. The OER acitivity of the nanocomposites can be enhanced so that the overpotential value less or equal to 0.3 V can be achieved.

References

1. Ghosh, S. K.; Pal, T. Interparticle coupling effect on the surface plasmon resonance of goldnanoparticles: From theory to applications. *Chem. Rev*. **2007,** *107*, 4797–4862.

2. Bain, C. D.; Evall, J.; Whitesides, G. M. Formation of monolayers by the coadsorption of thiols on gold: Variation in the head group, tail group, and solvent. *J. Am. Chem. Soc.* **1989**, *111*, 7155–7164.

3. Templeton, A. C.; Pietron, J. J.; Murray, R. W.; Mulvaney, P. Solvent refractive index and core charge influences on the surface plasmon absorbance of alkanethiolate monolayer protected gold clusters. *J. Phys. Chem. B* **2000**, *104*, 564–570.

4. Dreaden, E. C.; Alkilany, A. M.; Huang, X.; Murphy, C. J.; El-Sayed, M. A. The golden age: Gold nanoparticles for biomedicine. *Chem. Soc. Rev.* **2012,** *41*, 2740–2779.

5. Motl, N. E.; Smith, A. F.; DeSantis, C. J.; Skrabalak, S. E. Engineering plasmonic metal colloids through composition and structural design. *Chem. Soc. Rev.* **2014**, *43*, 3823–3834.

6. Reguera, J.; Langer, J.; de Aberasturi, D. J.; Liz-Marzán, L. M. Anisotropic metal nanoparticles for surface enhanced Raman scattering. *Chem. Soc. Rev*. **2017**, *46*, 3866–3885.

7. Hsu, S. W.; Rodarte, A. L.; Som, M.; Arya, G.; Tao, A. R. Colloidal plasmonic nanocomposites: From fabrication to optical function. *Chem. Rev*. **2018**, *118*, 3100–3120.

8. Yeh, Y. C.; Creran, B.; Rotello, V. M. Gold nanoparticles: preparation, properties, and applications in bionanotechnology. *Nanoscale* **2012**, *4,* 1871–1880.

9. Zhou, W.; Gao, X.; Liu, D.; Chen, X. Gold nanoparticles for in vitro diagnostics. *Chem. Rev*. **2015**, *115*, 10575−10636.

10. Niu, W.; Chua, Y. A.; Zhang, W.; Huang, H.; Lu, X. Highly symmetric gold nanostars: Crystallographic control and surface-enhanced Raman Scattering property. *J. Am. Chem. Soc.* **2015**, *137*, 10460–10463.

11. Lu, W.; Jiang, N.; Wang, J. Active electrochemical plasmonic switching on polyaniline coated gold nanocrystals. *Adv. Mater.* **2017**, *29*, 1604862.

12. Alvarez, M. M.; Khoury, J. T.; Schaaff, T. G.; Shafigullin, M. N.; Vezmar, I.; Whetten, R. L. Optical absorption spectra of nanocrystal gold molecules. *J. Phys. Chem. B* **1997**, *101*, 3706–3712.

13. Link, S.; El-Sayed, M. A. Size and temperature dependence of the plasmon absorption of colloidal gold nanoparticles. *J. Phys. Chem. B* **1999**, *103*, 4212–4217.

14. Rayleigh, L. On the dynamical theory of gratings. *Proc. R. Soc. London, Ser. A* **1907**, *79*, 399–416.

15. Jain, P. K.; Lee, K. S.; El-Sayed, I. H.; El-Sayed, M. A. Calculated absorption and scattering properties of gold nanoparticles of different size, shape, and composition: Applications in biological imaging and biomedicine. *J. Phys. Chem. B* **2006**, *110*, 7238–7248.

16. Eustis, S.; El-Sayed, M. A. Why gold nanoparticles are more precious than pretty gold: Noble metal surface plasmon resonance and its enhancement of the radiative and nonradiative properties of nanocrystals of different shapes. *Chem. Soc. Rev.* **2006**, *35*, 209–217.

17. Kreibig, U.; Vollmer, M. Optical Properties of Metal Clusters. *Springer*: Berlin, **1995**.

18. Burda, C.; Chen, X. B.; Narayanan, R.; El-Sayed, M. A. Chemistry and properties of nanocrystals of different shapes. *Chem. Rev*. **2005**, *105*, 1025–1102.

19. Lee, K.-S.; El-Sayed, M. A. Gold and silver nanoparticles in sensing and imaging: Sensitivity of plasmon response to size, shape and metal composition. *J. Phys. Chem. B* **2006**, *110*, 19220–19225.

20. Giri, A. K.; Spohr, E. Influence of chain length and branching on the structure of functionalized gold nanoparticles. *J. Phys. Chem. C* **2018,** *122*, 26739–26747.

21. Boisselier, E.; Astruc, D. Gold nanoparticles in nanomedicine: Preparations, imaging, diagnostics, therapies and toxicity. *Chem. Soc. Rev*. **2009**, *38*, 1759–1782.

22. Aldewachi, H.; Chalati, T.; Woodroofe, M. N.; Bricklebank, N.; Sharrackc, B.; Gardiner, P. Gold nanoparticle-based colorimetric biosensors. *Nanoscale* **2018**, *10*, 18–33.

23. Sperling, R. A.; Gil, P. R.; Zhang, F.; Zanella, M.; Parak, W. J. Biological applications of gold nanoparticles. *Chem. Soc. Rev.* **2008**, *37*, 1896–1908.

24. Ai, K.; Liu, Y.; Lu, L. Hydrogen-bonding recognition-induced color change of gold nanoparticles for visual detection of melamine in raw milk and infant formula. *J. Am. Chem. Soc*. **2009**, *131*, 9496–9497.

25. Saha, K.; Agasti, S. S.; Kim, C.; Li, X.; Rotello, V. M. Gold nanoparticles in chemical and biological sensing. *Chem. Rev*. **2012**, *112*, 2739–2779.

26. Chen, Y.; Xianyu, Y.; and Jiang, X. Surface modification of gold nanoparticles with small molecules for biochemical analysis. *Acc. Chem. Res*. **2017**, *50*, 310–319.

27. Sabela, M. I.; Balme, S.; Bechelany, M.; Janot, J. M.; Bisetty, K. A review of gold and silver nanoparticle-based colorimetric sensing assays. *Adv. Eng. Mater*. **2017**, *19*, 1700270.

28. Liu, P.; Yang, X.; Sun, S.; Wang, Q.; Wang, K.; Huang, J.; Liu, J.; He, L. Enzyme-free colorimetric detection of DNA by using gold nanoparticles and hybridization chain reaction amplification. *Anal. Chem*. **2013**, *85*, 7689–7695.

29. Prinz, J.; Heck, C.; Ellerik, L.; Merk, V.; Bald, I. DNA origami based Au-Ag-core-shell nanoparticle dimers with single-molecule SERS sensitivity. *Nanoscale* **2016,** *8*, 5612–5620.

30. Prinz, J.; Matkovic, A.; Pesic, J.; Gajic, R.; Bald, I. Hybridstructures for surface-enhanced raman scattering: DNA origami/gold nanoparticle dimer/grapheme. *Small* **2016**, *12*, 5458–5467.

31. Faraday, M. Experimental relations of gold (and other metals) to light. *Philos. Trans.* **1857**, *147*, 145–181.

32. Daniel, M, C.; Astruc, D. Gold nanoparticles: Assembly, supramolecular chemistry, quantum size-related properties, and applications toward biology, catalysis, and nanotechnology. *Chem. Rev*. **2004**, *104*, 293–346.

33. Grzelczak, M.; Perez-Juste, J.; Mulvaney, P.; Liz-Marzan, L. M. Shape control in gold nanoparticle synthesis. *Chem. Soc. Rev*. **2008**, *37*, 1783–1791.

34. Sardar, R.; Shumaker-Parry, J. S. Spectroscopic and microscopic investigation of gold nanoparticle formation: Ligand and temperature effects on rate and particle size. *J. Am. Chem. Soc*. **2011**, *133*, 8179–8190.

35. Turkevich, J.; Stevenson, P. C.; Hillier, J.A study of the nucleation and growth processes in the synthesis of colloidal gold. *Discuss. Faraday Soc*. **1951**, *11*, 55–75.

36. Frens, G. Controlled nucleation for the regulation of the particle size in monodisperse gold suspensions. *Nature: Phys. Sci*. **1973**, *241*, 20–22.

37. Chow, M. K.; Zukoski, C. F. Gold sol formation mechanisms: Role of colloidal stability. *J. Colloid Interface Sci*. **1994**, *165*, 97–109.

38. Yonezawa, T.; Kunitake, T. Practical preparation of anionic mercapto ligand-stabilized gold nanoparticles and their immobilization. *Colloids Surf. A: Physicochem. Eng. Asp*. **1999**, *149*, 193–199.

39. Martin, M. N.; Basham, J. I.; Chando, P Eah,; S. K., Charged gold nanoparticles in non-polar solvents: 10-min Synthesis and 2D Self-Assembly *Langmuir* **2010**, 26, 7410–7417.

40. Newman, J. D. S.; Blanchard, G. J. Formation of gold nanoparticles using amine reducing Agents. *Langmuir* **2006**, 22, 5882–5887.

41. Male, K. B.; Li, J.; Bun, C. C.; Ng, S-C, Luong, John H. T. Synthesis and Stability of Fluorescent Gold Nanoparticles by Sodium Borohydride in the Presence of Mono-6-deoxy-6-pyridinium-β-cyclodextrin Chloride *J. Phys. Chem. C* **2008**, 112, 443–451.

42. Wrigglesworth, E. G.; Johnston, J. H.; The use of dual reductants in gold nanoparticle syntheses. *RSC Adv*. **2017**, 7, 45757–45762.

43. Deraedt, C.; Salmon, L.; Gatard, S.; Ciganda, R,; Hernandez, R.; Ruiza, J.; Astruc, D.; Sodium borohydride stabilizes very active gold nanoparticle catalysts. *Chem. Commun*. **2014**, 50, 14194-14196.

44. Brown, K. R.; Natan, M. J. Hydroxylamine seeding of colloidal Au nanoparticles in solution and on surfaces. *Langmuir* **1998**, *14*, 726–728.

45. Jana, N. R.; Gearheart, L.; Murphy, C. J. Seeding growth for size control of 5−40 nm diameter gold nanoparticles. *Langmuir* **2001**, *17*, 6782–6786.

46. Rodriguez-Fernandez, J.; Perez-Juste, J.; Abajo, F. J. G. d.; Liz-Marzan, L. M. Seeded growth of submicron Au colloids with quadrupole plasmon resonance modes. *Langmuir* **2006,** *22*, 7007–7010.

47. Niu, J.; Zhu, T.; Liu, Z. One-step seed-mediated growth of 30-150 nm quasispherical gold nanoparticles with 2-mercaptosuccinic acid as a new reducing agent. *Nanotechnology* **2007,** *18*, 325607.

48. Perrault, S. D.; Chan, W. C.W. Synthesis and surface modification of highly monodispersed, spherical gold nanoparticles of 50−200 nm. *J. Am. Chem. Soc*. **2009,** *131*, 17042–17043.

49. Ziegler, C.; Eychmuller, A. Seeded growth synthesis of uniform gold nanoparticles with diameters of 15−300 nm. *J. Phys. Chem. C* **2011**, *115*, 4502–4506.

50. Bastús, N. G.; Comenge, J.; Puntes, V. Kinetically controlled seeded growth synthesis of citrate-stabilized gold nanoparticles of up to 200 nm: Size focusing versus Ostwald ripening. *Langmuir* **2011**, *27*, 11098–11105.

51. Meunier, M.; Rioux, D. Seeded growth synthesis of composition and size-controlled gold-silver alloy nanoparticles. *J. Phys. Chem. C* **2015**, *119*, 13160–13168.

52. Sun, X.; Li, D.; Guo, S.; Zhu, W.; Sun, S. Controlling core/shell Au/FePt nanoparticle electrocatalysis via changing the core size and shell thickness. *Nanoscale* **2016**, *8*, 2626–2631.

53. Piella, J.; Bastús, N. G.; Puntes, V. Size-controlled synthesis of sub-10-nanometer citrate-stabilized gold nanoparticles and related optical properties. *Chem. Mater.* **2016**, *28*, 1066–1075.

54. Wang, W.; Yan, Y.; Zhou, N.; Zhang, H.; Li, D.; Yang, D. Seed-mediated growth of Au nanorings with size control on Pd ultrathin nanosheets and their tunable surface plasmonic properties. *Nanoscale* **2016**, *8*, 3704–3710.

55. Park, J. E.; Lee, Y.; Nam, J. M. Precisely shaped, uniformly formed gold nanocubes with ultrahigh reproducibility in single-particle scattering and surface enhanced Raman scattering. *Nano Lett.* **2018**, *18*, 6475–6482.

56. .Cargnello, M.; Agarwal, R.; Klein, D. R.; Diroll, B. T.; Agarwal, R.; Murray, C. B. Uniform bimetallic nanocrystals by high-temperature seed-mediated colloidal synthesis and their catalytic properties for semiconducting nanowire growth. *Chem. Mater.* **2015**, *27*, 5833–5838.

57. Giersig, M.; Mulvaney, P. Preparation of ordered colloid monolayers by electrophoretic deposition. *Langmuir* **1993**, *9*, 3408–3413.

58. .Brust, M.; Walker, M.; Bethell, D.; Schiffrin, D. J.; Whyman, R. Synthesis of thiol-derivatised gold nanoparticles in a two-phase liquid–liquid system. *J. Chem. Soc., Chem. Commun*. **1994**, 801–802.

59. .Booth, S. G.; Uehara, A.; Chang, S.-Y.; La Fontaine, C.; Fujii, T.; Okamoto, Y.; Imai, T.; Schroeder, S. L. M.; Dryfe, R. A. W. The significance of bromide in the Brust-Schiffrin synthesis of thiol protected gold nanoparticles. *Chem. Sci*. **2017**, *8*, 7954–7962.

60. Templeton, A. C.; Hostetler, M. J.; Kraft, C. T.; Murray, R. W. Reactivity of monolayer-protected gold cluster molecules: Steric effects. *J. Am. Chem. Soc.* **1998**, *120*, 1906–1911.

61. Hostetler, M. J.; Templeton, A. C.; Murray, R. W. Dynamics of place-exchange reactions on monolayer-protected gold cluster molecules. *Langmuir* **1999**, *15*, 3782–3789.

62. Jadzinsky, P. D.; Calero, G.; Ackerson, C. J.; Bushnell, D. A.; Kornberg, R. D. Structure of a thiol monolayer-protected gold nanoparticle at 1.1 Å resolution. *Science* **2007**, *318*, 430–433.

63. Woehrle, G. H.; Brown, L. O.; Hutchison, J. E. Thiol-functionalized, 1.5-nm gold nanoparticles through ligand exchange reactions: Scope and mechanism of ligand exchange *J. Am. Chem. Soc.* **2005**, *127*, 2172–2183.

64. Leff, D. V.; Ohara, P. C.; Heath, J. R.; Gelbart, W. M. Thermodynamic control of gold nanocrystal size: Experiment and theory. *J. Phys. Chem.* **1995**, *99*, 7036–7041.

65. .Manzanares, J. A.; Peljo, P.; Girault, H. H. Understanding digestive ripening of ligand- stabilized, charged metal nanoparticles. *J. Phys. Chem. C* **2017**,*121,* 13405–13411.

66. Prasad, B. L. V.; Stoeva, S.; Sorensen, C. M.; Klabunde, K. J. Digestive ripening of thiolated gold nanoparticles: The effect of alkyl chain length. *Langmuir* **2002**, *18*, 7515–7520.

67. Shimpi, J. R.; Sidhaye, D. S.; Prasad, B. L. V. Digestive ripening: A fine chemical machining process on the nanoscale. *Langmuir* **2017**, *33*, 9491–9507.

68. Sahu, P.; Shimpi, J.; Lee, H. J.; Lee, T. R.; Prasad, B. L. V. Digestive ripening of Au nanoparticles using multidentate ligands. *Langmuir* **2017**, *33*, 1943–1950.

69. Luo, Y.; Geng, S.; Dube, L.; Jing, Z. Tuning the valency of heterogeneous Au–Silica nanostructure via controlled Ostwald ripening process. *J. Phys. Chem. C* **2018**, *122*, 18077–18085.

70. Sylvestre, J.-P.; Poulin, S.; Kabashin, A. V.; Sacher, E.; Meunier, M.; Luong, J. H. T. Surface chemistry of gold nanoparticles produced by laser ablation in aqueous media. *J. Phys. Chem. B* **2004**, *108*, 16864–16869.

71. Toit, H. d.; Macdonald, T. J.; Huang, H.; Parkinb, I. P.; Gavriilidis, A. Continuous flow synthesis of citrate capped gold nanoparticles using UV induced nucleation. *RSC Adv*. **2017**, *7*, 9632–9638.

72. González-Rubio, G.; Guerrero-Martínez, A.; Liz-Marzán, L. M. Reshaping, fragmentation, and assembly of gold nanoparticles assisted by pulse lasers. *Acc. Chem. Res*. **2016**, *49*, 678–686.

73. Xu, H.; Zeigera,B. W.; Suslick, K. S. Sonochemical synthesis of nanomaterials. *Chem. Soc. Rev*. **2013**, *42*, 2555–2567.

74. Li, C.; Liu, Z.; Yao, P. Gold nanoparticles coated with a polydopamine layer and dextran brush surface for diagnosis and highly efficient photothermal therapy of tumors. *RSC Adv*. **2016**, *6*, 33083–33091.

75. Liu, S.; Qileng, A.; Junying, H.; Gao, Q.; Liu, Y. Polydopamine as a bridge to decorate monodisperse gold nanoparticles on Fe_3O_4 nanoclusters for the catalytic reduction of 4-nitrophenol. *RSC Adv*. **2017**, *7*, 45545–45551.

76. Wang, J.-G.; Hua, X.; Li, M.; Long, Y.-T. Mussel-inspired polydopamine functionalized plasmonic nanocomposites for single-particle catalysis. *ACS Appl. Mater. Interfaces* **2017**, *9*, 3016–3023.

77. Koczkur, K. M.; Mourdikoudis, S.; Polavarapu, L.; Skrabalak, S. E. Polyvinyl-pyrrolidone (PVP) in nanoparticle synthesis. *Dalton Trans*. **2015**, *44*, 17883–17905.

78. Que, Y.; Feng, C.; Zhang, S.; Huang, X. Stability and catalytic activity of PEG-b-PS-capped gold nanoparticles: A matter of PS chain length. *J. Phys. Chem. C* **2015**, *119*, 1960–1970.

79. Zhang, Y.; Wen, S.; Zhao, L.; Li, D.; Liu, C.; Jiang, W.; Gao, X.; Gu, W.; Ma, N.; Zhao, J.; Shi, X.; Zhao, Q. Ultrastable polyethyleneimine stabilized gold nanoparticles modified with polyethylene glycol for blood pool, lymph node and tumor CT imaging. *Nanoscale* **2016**, *8*, 5567–5577.

80. Shi, Weili.; Sahoo, Y.; Swihart, M. T.; Prasad, P. N. Gold nanoshells on polystyrene cores for control of surface plasmon resonance. *Langmuir* **2005,** *21*, 1610–1617.

81. Li, Y.; Gao, Y.; Yang, C. A facile and efficient synthesis of polystyrene/gold–platinum composite particles and their application for aerobic oxidation of alcohols in water. *Chem. Commun.* **2015**, *51*, 7721–7724.

82. Shokri, E.; Hosseini, M.; Davari, M. D.; Ganjali, M. R.; Peppelenbosch, M. P.; Rezaee, F. Disulfide-induced self-assembled targets: A novel strategy for the label free colorimetric detection of DNAs/RNAs via unmodified gold nanoparticles. *Sci. Rep.* **2017,** *7*, 45837.

83. Hofmann, A.; Schmiel, P.; Stein, B.; Graf, C. Controlled formation of gold nanoparticle dimers using multivalent thiol ligands. *Langmuir* **2011**, *27*, 15165–15175.

84. Mourdikoudis, S.; Liz-Marzán, L. M. Oleylamine in nanoparticle synthesis. *Chem. Mater.* **2013**, *25*, 1465–1476.

85. Koposova, E.; Kisner, A.; Shumilova, G.; Ermolenko, Y.; Offenhäusser, A.; Mourzina, Y. Oleylamine-stabilized gold nanostructures for bioelectronic assembly. Direct electrochemistry of cytochrome C. *J. Phys. Chem. C* **2013**, *117*, 13944–13951.

86. Hermes, J. P.; Sander, F.; Peterle, T.; Urbani, R.; Pfohl, T.; Thompson, D.; Mayor, M. Gold nanoparticles stabilized by thioether dendrimers. *Chem. Eur. J*. **2011**, *17*, 13473–13481.

87. Tam, N. C. M.; McVeigh, P. Z.; MacDonald, T. D.; Farhadi, A.; Wilson, B. C.; Zheng, G. Porphyrin–Lipid stabilized gold nanoparticles for surface enhanced Raman scattering based imaging. *Bioconjugate Chem*. **2012**, *23*, 1726–1730.

88. Tran, T. T.; Lu, X. Synergistic effect of Ag and Pd ions on shape-selective growth of polyhedral Au nanocrystals with high-index facets. *J. Phys. Chem. C* **2011**, *115*, 3638–3645.

89. Sapsford, K. E.; Algar, W. R.; Berti, L.; Gemmill, K. B.; Casey B. J.; Oh, E.; Stewart, M. Functionalizing nanoparticles with biological molecules: Developing chemistries that facilitate nanotechnology. *Chem. Rev.* **2013**, *113*, 1904–2074.

90. Zhang, S.; Moustafa, Y.; Huo, Q. Different interaction modes of biomolecules with citrate-capped gold nanoparticles. *ACS Appl. Mater. Interfaces* **2014**, *6*, 21184–21192.

91. Berg, J. M.; Stryer, L.; Tymoczko, J. L.; Gatto, G. J. *Biochemistry Eight edition* W.H. Freeman & Company: New York, **1995**. ISBN-13: 978-1-4641-2610-9.

92. Creighton, T. E.; Freeman, W. H. *Proteins: structures and molecular properties* W.H. Freeman & Company: New York, **1993**.ISBN-13: 978-071677030.

93. Bhargava, S. K.; Booth, J. M.; Agrawal, S.; Coloe, P.; Kar, G. Gold nanoparticle formation during bromoaurate reduction by amino acids. *Langmuir*, **2005,** *21*, 5949–5956.

94. Selvakannan, P. R.; Mandal, S.; Phadtare, S.; Pasricha, R.; Sastry, M. Capping of gold nanoparticles by the amino acid lysine renders them water-dispersible. *Langmuir*, **2003**, *19*, 3545–3549.

95. Leontowich, A. F. G.; Calver, C. F.; Dasog, M.; Scott, R. W. J. Surface properties of water-soluble glycine-cysteamine protected gold clusters. *Langmuir* **2010**, *26*, 1285–1290.

96. Shao, Y.; Jin, Y.; Dong, S. Synthesis of gold nanoplates by aspartate reduction of gold chloride. *Chem. Commun*. **2004,** 1104–1105.

97. Maruyama, T.; Fujimoto, Y.; Maekawa, T. Synthesis of gold nanoparticles using various amino acids. *J. Colloid Interface Sci.* **2015**, *447*, 254–257.

98. Kim, D.-Y.; Kim, M.; Shinde, S.; Saratale, R. G.; Sung, J.-S.; Ghodake, G. Temperature dependent synthesis of tryptophan-functionalized gold nanoparticles and their application in imaging human neuronal cells. *ACS Sustainable Chem. Eng.* **2017**, *5*, 7678–7689.

99. Singh, A. V.; Bandgar, B. M.; Kasture, M.; Prasad, B. L. V.; Sastry, M. Synthesis of gold, silver and their alloy nanoparticles using bovine serum albumin as foaming and stabilizing agent. *J. Mater. Chem.* **2005**, *15*, 5115-5121.

100. Yarramala, D.S.; Doshi, S.; Rao. C. P. Green synthesis, characterization and anticancer activity of luminescent gold nanoparticles capped with apo-α-lactalbumin. *RSC Adv.* **2015**, *5*, 32761-32767.

101. Yarramala, D. S.; Baksi, A.; Pradeep, T.; Rao C. P. Green Synthesis of Protein-Protected Fluorescent Gold Nanoclusters (AuNCs): Reducing the Size of AuNCs by Partially Occupying the Ca2+ Site by La^{3+} in Apo-α-Lactalbumin. *ACS Sustainable Chem. Engg.* **2017**, *5*, 6064–6069.

102. Liu, B.; Liu, J. Methods for preparing DNA-functionalized gold nanoparticles, a key reagent of bioanalytical chemistry. *Anal. Methods* **2017**, 9, 2633.

103. Cutler, J. I.; Auyeung, E.; Mirkin, C. A. Spherical nucleic acids. *J. Am. Chem. Soc.* **2012**, *134*, 1376–1391.

104. Mirkin, C. A.; Letsinger, R. L.; Mucic, R. C.; Storhoff, J. J. DNA-based method for rationally assembling nanoparticles into macroscopic materials. *Nature* **1996**, *382*, 607–609.

105. Hurst, S. J.; Lytton-Jean, A. K. R.; Mirkin, C. A.; Maximizing DNA loading on a range of gold nanoparticle sizes. *Anal. Chem.* **2006**, *78*, 8313–8318.

106. Zhang, X.; Servos, M. R.; Liu, J. Instantaneous and quantitative functionalization of gold nanoparticles with thiolated DNA using a pH-assisted and surfactant-free route. *J. Am. Chem. Soc.* **2012**, *134*, 7266–7269.

107. Huang, Z.; Liu, B.; Liu, J. Parallel polyadenine duplex formation at low pH facilitates DNA conjugation onto gold nanoparticles. *Langmuir* **2016**, *32*, 11986–11992.

108. Gill, R.; Goeken, K.; Subramaniam, V. Fast, single-step, and surfactant-free oligonucleotide modification of gold nanoparticles using DNA with a positively charged tail. *Chem. Commun.* **2013**, *49*, 11400–11402.

109. Xu, Q., Lou, X.; Wang, L.; Ding, X.; Yu, H.; Xiao, Y. Rapid, surfactant-free, and quantitative functionalization of gold nanoparticles with thiolated DNA under physiological pH and its application in molecular beacon-based biosensor. *ACS Appl. Mater. Interfaces* **2016**, *8*, 27298–27304.

110. Jaworska, A.; Jablonska, A.; Wilanowski, T.; Palys, B.; Sek, S.; Kudelski, A. Influence of amine and thiol modifications at the 3′ ends of single stranded DNA molecules on their adsorption on gold surface and the efficiency of their hybridization. *Spectrochim. Acta A Mol Biomol Spectrosc.* **2018**, *203*, 31–39.

111. Zhou, W.; Wang, F.; Ding, J.; Liu, J.; Tandem phosphorothioate modifications for DNA adsorption strength and polarity control on gold nanoparticles. *ACS Appl. Mater. Interfaces* **2014**, *6*, 14795–14800.

112. Liu, B.; Wu, P; Huang, Z.; Ma, L.; Liu, L. Bromide as a robust backfiller on gold for precise control of DNA conformation and high stability of spherical nucleic acids. *J. Am. Chem. Soc.* **2018**, *140*, 4499–4502.

113. Liu, B.; Wu, T.; Huang, Z, Liu, Y.; Liu, L. Freezing-directed stretching and alignment of DNA oligonucleotides. *Angew. Chem. Int. Ed.* **2019**, *58*, 2109–2113.

114. Quinn, B. M.; Liljeroth, P.; Ruiz, V.; Laaksonen, T.; Kontturi, K. Electrochemical resolution of 15 oxidation states for monolayer protected gold nanoparticles. *J. Am. Chem. Soc.* **2003**, *125*, 6644–6645.

115. Antonello, S.; Holm, A. H.; Instuli, E.; Maran, F. Molecular electron-transfer properties of Au$_{38}$ clusters. *J. Am. Chem. Soc*. **2007**, *129*, 9836–9837.

116. Schmid, G.; Simon, U. Gold nanoparticles: Assembly and electrical properties in 1–3 dimensions. *Chem. Commun.* **2005**, 697–710.

117. Subramaniam, C.; Pradeep, T.; Chakrabarti, J. Flow-induced transverse electrical potential across an assembly of gold nanoparticles. *Phys. Rev. Lett*. **2005**, *95*, 164501–164504.

118. Templeton, A. C.; Pietron, J. J.; Murray, R. W.; Mulvaney, P. Solvent refractive index and core charge influences on the surface plasmon absorbance of alkanethiolate monolayer-protected gold clusters. *J. Phys. Chem. B* **2000**, *104*, 564–570.

119. Link, S.; El-Sayed, M. A. Size and temperature dependence of the plasmon absorption of colloidal gold nanoparticles. *J. Phys. Chem. B* **1999**, *103*, 4212–4217.

120. Itoh, T.; Asahi, T.; Masuhara, H. Femtosecond light scattering spectroscopy of single gold nanoparticles. *Appl. Phys. Lett.* **2001**, *79*, 1667–1669.

121. Su, K. H.; Wei, Q. H.; Zhang, X.; Mock, J. J.; Smith, D. R.; Schultz, S. Interparticle coupling effects on plasmon resonances of nanogold particles. *Nano Lett.* **2003**, *3*, 1087–1090.

122. Jain, P. K.; Lee, K. S.; El-Sayed, I. H.; El-Sayed, M. A. Calculated absorption and scattering properties of gold nanoparticles of different size, shape, and composition: Applications in biological imaging and biomedicine. *J. Phys. Chem. B* **2006**, *110*, 7238–7248.

123. Khlebtsov, N. G. Determination of size and concentration of gold nanoparticles from extinction spectra *Anal. Chem.* **2008**, *80*, 6620–6625.

124. Oh, E.; Hong, M. Y.; Lee, D.; Nam, S. H.; Yoon, H. C.; Kim,H. S.Inhibition assay of biomolecules based on fluorescence resonance energy transfer (FRET) between quantum dots and gold nanoparticles. *J. Am. Chem. Soc.* **2005**, *127*, 3270-3271.

125. Thomas, K. G.; Kamat, P. V. Chromophore functionalized gold nanoparticles. *Acc. Chem. Res*. **2003**, *36*, 888-898

126. Freese, C.; Anspach, L.; Deller, R.; Richards, S.-J.; Gibson, M. I.; Kirkpatrick, C. J.; Unger, R. Gold nanoparticle interactions with endothelial cells cultured under physiological conditions. *Biomater. Sci.* **2017**, *5*, 707–717.

127. Syed, A. M.; Sindhwani, S.; Wilhelm, S.; Kingston, B. R.; Lee, D. S. W.; Gommerman, J. L.; Chan, W. C. W. Three-dimensional imaging of transparent tissues via metal nanoparticle labelling. *J. Am. Chem. Soc.* **2017**, *139*, 9961–9971.

128. Lubin, A. A.; Plaxco, K. W. Folding-based electrochemical biosensors: The case for responsive nucleic acid architectures. *Acc. Chem. Res*. **2010**, *43*, 496–505.

129. Wang, F.; Elbaz, J.; Orbach, R.; Magen, N.; Willner, I. *J. Am. Chem. Soc.* **2011**, *133*, 17149–17151.

130. Wilhelm, S.; Tavares, A. J.; Dai, Q.; Ohta, S.; Audet, J.; Dvorak, H. F.; Chan, W. C.W. Analysis of nanoparticle delivery to tumours. *Nat Rev Mater.* **2016**, *1*, 16014.

131. Dai, Q.; Wilhelm, S.; Ding, D.; Syed, A. M.; Sindhwani, S.; Zhang, Y.; Chen, Y. Y.; MacMillan, P.; Chan, W. C. W. Quantifying the ligand-coated nanoparticle delivery to cancer cells in solid tumors. *ACS Nano* **2018**, *12*, 8423–8435.

132. Kolpashchikov, D. M. Binary probes for nucleic acid analysis. *Chem. Rev.* **2010**, *110*, 4709–4723.

133. Pisa, D. M.; Seitz, O. Nucleic acid templated reactions for chemical biology. *ChemMedChem* **2017**, *12*, 872 –882.

134. Sadhu, K. K.; Winssinger, N. Detection of miRNA in live cells by using templated Ru^{II}-catalyzed unmasking of a fluorophore. *Chem. Eur. J.* **2013**, *19*, 8182–8189.

135. Chang, D., Kim, K. T., Lindberg, E., Winssinger, N. Accelerating turnover frequency in nucleic acid templated reactions. *Bioconjugate Chem.* **2018**, *29*, 158–163.

136. Zavoiura, O.; Resch-Genger, U.; Oliver Seitz. Quantum dot-PNA Conjugates for target-catalyzed RNA detection. *Bioconjugate Chem.* **2018**, *29*, 1690–170.

137. Li, H.; Rothberg, L. Colorimetric detection of DNA sequences based on electrostatic interactions with unmodified gold nanoparticles. *Proc. Natl. Acad. Sci. U.S.A.* **2004**, *101*, 14036–14039.

138. Zhang, J.; Wang, L.; Pan, D.; Song, S.; Boey, F. Y. C.; Zhang, H.; Fan, C.Visual cocaine detection with gold nanoparticles and rationally engineered aptamer structures. *Small* **2008**, *4*, 1196–1200.

139. Kanjanawarut, R.; Su, X. Colorimetric detection of DNA using unmodified metallic nanoparticles and peptide Nucleic acid probes. *Anal. Chem.* **2009**, *81*, 6122–6129.

140. Storhoff, J. J., Elghanian, R.; Mucic, C. R.; Mirkin, C. A.; Letsinger, R. L. One-pot colorimetric differentiation of polynucleotides with single base imperfections using gold nanoparticle probes. *J. Am. Chem. Soc.* **1998**, *120,* 1959–1964.

141. Li, H. X.; Rothberg, L. Colorimetric detection of DNA sequences based on electrostatic interactions with unmodified gold nanoparticles. *Proc. Natl. Acad. Sci. U.S.A.* **2004**, *101*, 14036–14039.

142. Xu, W.; Xie, X.; Li, D.; Yang, Z.; Li, T.; Liu, X. Ultrasensitive colorimetric DNA detection using a combination of rolling circle amplification and nicking endonuclease-assisted nanoparticle amplification. *Small* **2012**, *8*, 1846–1850.

143. Lam, M. K.; Gadzikwa, T.; Nguyen, T.; Kausar, A.; Alladin-Mustan, B. S.; Sikder, M. D.; Gibbs-Davis, J. M. Tuning toehold length and temperature to achieve rapid, colorimetric detection of DNA from the disassembly of DNA–gold nanoparticle aggregates. *Langmuir* **2016**, *32*, 1585–1590.

144. Ma, C. P.; Wang, W. S.; Li, Z. X.; Cao, L. J.; Wang, Q. Y. Simple colorimetric DNA detection based on hairpin assembly reaction and target-catalytic circuits for signal amplification. *Anal. Biochem.* **2012**, *429*, 99–102.

145. Liu, P.; Yang, X.; Sun, S.; Wang, Q.; Wang, K.; Huang, J.; Liu, J.; He. Enzyme free colorimetric detection of DNA by using gold nanoparticles and hybridization chain reaction amplification. *Anal. Chem.* **2013**, *85*, 7689–7695.

146. Wang, Q.; Liu, R.; Yang, X.; Wang, K.; Zhu, J.; He, L.; Li, Q. Surface plasmon resonance biosensor for enzyme-free amplified micro RNA detection based on gold nanoparticles and DNA supersandwitch. *Sens. Actuators B Chem*. **2016,** *223*, 613–620.

147. Stefani, G.; Slack, F. J. Small non-coding RNAs in animal development. *Nat. Rev. Mol.Cell Biol*. **2008,** *9*, 219.

148. Hobert, O. Gene Regulation by transcription factors and microRNAs. *Science* **2008**, *319*, 1785.

149. Seferos, D. S.; Giljohann, D. A.; Hill, H. D.; Prigodich, A. E.; Mirkin, C. A. Nano-flares: Probes for transfection and mRNA detection in living cells. *J. Am. Chem. Soc*. **2007**, *129, 15477–15479*.

150. Yang, Y.; Huang, J.; Yang, X.; Quan, K.; Wang, H.; Ying, L.; Xie, N.; Ou, M.; Wang, K. FRET nanoflares for intracellular mRNA detection: Avoiding false positive signals and minimizing effects of system fluctuations. *J. Am. Chem. Soc.* **2015**, *137*, 8340–8343.

151. Wu, Z.; Liu, G.-Q.; Yang, X.-L.; Jiang, J.-H. Electrostatic nucleic acid nanoassembly enables hybridization chain reaction in living cells for ultrasensitive mRNA imaging. *J. Am. Chem. Soc.* **2015**, *137*, 6829–6836.

152. Ki, J.; Jang, E.; Han, S.; Shin, M.-K.; Kang, B.; Huh, Y.-M.; Haam, S. Instantaneous pH-boosted functionalization of stellate gold nanoparticles for intracellular imaging of miRNA. *ACS Appl. Mater. Interfaces* **2017**, *9*, 17702–17709.

153. Hakimian, H.; Ghourchian, H.; Hashemi, A.; S.; Arastoo, M. R.; Rad, M, B. Ultrasensitive optical biosensor for detection of miRNA-155 using positively charged Au nanoparticles. *Sci. Reports* **2018**, *8*, 2943.

154. Daniels, M. J.; Wang, Y; Lee, M. Y; Venkitaraman, A. R., Abnormal cytokinesis in cells deficient in the breast cancer susceptibility protein BRCA2. *Science* **2004**, *306*, 876–879.

155. Bai, V. U.; Kaseb, A.; Tejwani, S.; Divine, G. W.; Barrack, E. R.; Menon, M.; Pardee, A. B.; Reddy, G. P.-V. Identification of prostate cancer mRNA markers by averaged differential expression and their detection in biopsies, blood, and urine. *Proc. Natl. Acad. Sci. U. S. A*. **2007**, *104*, 2343–2348.

156. Chen, C.; Luo, M.; Ye, T.; Li, N.; Ji, X.; He, Z. Sensitive colorimetric detection of protein by gold nanoparticles and rolling circle amplification.*Analyst* **2015**, *140*, 4515–4520.

157. Wang, X.; Ramstrom, O.; Yan, M. D. Quantitative analysis of multivalent ligand presentation on gold glyconanoparticles and the impact on lectin binding. *Anal. Chem.* **2010**, *82*, 9082.

158. Schofield, C. L.; Haines, A. H.; Field, R. A.; Russell, D. A. Silver and gold Glyconanoparticles for Colorimetric Bioassays. *Langmuir* **2006**, *22*, 6707–6711.

159. Watanabe, S.; Yoshida, K.; Shinkawa, K.; Kumagawa, D.; Seguchi, H. Thioglucose-stabilized gold nanoparticles as a novel platform for colorimetric bioassay based on nanoparticle aggregation. *Colloids Surf. B* **2010**, *81*, 570–577.

160. Richards, S.-J.; Otten, L.; Gibson, M. I. Glycosylated gold nanoparticle libraries for label-free multiplexed lectin biosensing. *J. Mater. Chem. B* **2016**, *4*, 3046–3053.

161. Mitchell, D. E.; Congdon, T.; Rodger, A.; Gibson, M. I. Gold nanoparticle aggregation as a probe of antifreeze (glyco) protein-inspired ice recrystallization inhibition and identification of new IRI active macromolecule. *Sci. Rep.* **2015**, *5*, 15716.

162. Park, S.; Kim, G.-H.; Park, S.-H.; Pai, J.; Rathwell, D.; Park, J.-Y.; Kang, Y.-S.; Shin. I. Probing cell-surface carbohydrate binding proteins with dual-modal glycan-conjugated nanoparticles. *J. Am. Chem. Soc.* **2015**, *137,* 5961–5968.

163. Sakurai, K.; Hatai, Y. Okada Gold nanoparticle-based multivalent carbohydrate probes: Selective photoaffinity labeling of carbohydrate-binding protein. *Chem. Sci.* **2016**, *7*, 702–706.

164. Wei, H.; Li, B. L.; Li, J.; Wang, E. K.; Dong, S. J. Simple and sensitive aptamer-based colorimetric sensing of protein using unmodified gold nanoparticle probes. *Chem. Commun.* **2007**, 3735–3737.

165. Liao, Y.-J.; Shiang, Y.-C.; Huang, C.-C.; Chang, H.-T. Molecularly imprinted aptamers of gold nanoparticles for the enzymatic inhibition and detection of thrombin. *Langmuir* **2012**, *28*, 8944–8951.

166. You, C. C.; Arvizo, R. R.; Rotello, V. M. Regulation of α-chymotrypsin activity on the surface of substrate-functionalized gold nanoparticles. *Chem. Commun.* **2006**, 2905–2907.

167. Laromaine, A.; Koh, L.; Murugesan, M.; Ulijn, R. V.; Stevens, M. M. Protease-triggered dispersion of nanoparticle assemblies. *J. Am. Chem. Soc.* **2007**, *129*, 4156–4157.

168. Chen, G.; Xie, Y.; Zhang, H.; Wang, P.; Cheung, H.-Y.; Yang, M.; Sun, H. A general colorimetric method for detecting protease activity based on peptide-induced gold nanoparticle aggregation. *RSC Adv.* **2014**, *4*, 6560–6563.

169. Xu, X. Y.; Han, M. S.; Mirkin, C. A. A gold-nanoparticle-based real-time colorimetric screening method for endonuclease activity and inhibition. *Angew. Chem. Int. Ed.* **2007**, *46*, 3468–3470.

170. Huang, Y.; Zhao, S.; Chen, Z.-F.; Liu, Y.-C; Liang, H. Ultrasensitive endonuclease activity and inhibition detection using gold nanoparticle-enhanced fluorescence polarization. *Chem. Commun.* **2011**, *47*, 4763–4765.

171. Zong, J.; Cobb, S. L.; Cameron, N. R. Peptide-functionalized gold nanoparticles: Versatile biomaterials for diagnostic and therapeutic applications. *Biomater. Sci.* **2017**, *5*, 872–886.

172. Baines, I. C.; Colas, P. Peptide aptamers as guides for small-molecule drug discovery. *Drug Discov. Today* **2006,** *11*, 334–341.

173. Retout, M.; Valkenier, H.; Tríffaux, E.; Doneux, T.; Bartik, K.; Bruylants, G. Rapid and selective detection of proteins by dual trapping using gold nanoparticles functionalized with peptide aptamers. *ACS Sens.* **2016**, *1*, 929–933.

174. Lin, S. Y.; Liu, S. W.; Lin, C. M.; Chen, C. H. Recognition of potassium ion in water by 15-Crown-5 functionalized gold nanoparticles. *Anal. Chem.* **2002**, *74*, 330–335.

175. Lin, S. Y.; Chen, C. H.; Lin, M. C.; Hsu, H. F. Cooperative effect of bifunctionalized nanoparticles on recognition: Sensing alkali ions by crown and carboxylate moieties in aqueous media. *Anal. Chem.* **2005**, *77*, 4821–4828.

176. Zheng, W.; Li, H.; Chen, W.; Ji, J.; Jiang, X. Recyclable colorimetric detection of trivalent cations in aqueous media using zwitterionic gold nanoparticles. *Anal. Chem.* **2016**, *88*, 4140–4146.

177. Parnsubsakul, A.; Oaew, S.; Surareungchai, W. Zwitterionic peptide-capped gold nanoparticles for colorimetric detection of Ni^{2+}. *Nanoscale*, **2018**, *10*, 5466–5473.

178. Obare, S. O.; Hollowell, R. E.; Murphy, C. J. Sensing strategy for lithium ion based on gold nanoparticles. *Langmuir* **2002**, *18*, 10407–10410.

179. Li, S.; Wei, T.; Ren, G.; Chai, F.; Wu, H.; Qu, F. Gold nanoparticles based colorimetric probe for Cr(III) and Cr(VI) detection. *Colloids Surf. A* **2017**, *535*, 215–224.

180. Samanta, K.; Rao, C. P. A Bifunctional thioether linked coumarin appended Calix[4]arene acquires selectivity toward Cu^{2+} sensing on going from solution to SAM on Gold. ACS *Appl. Mater. Interfaces* **2016**. *8*, 3135–3142.

181. Lee, J. S.; Han, M. S.; Mirkin, C. A. Colorimetric detection of mercuric ion (Hg^{2+}) in aqueous media using DNA-functionalized gold nanoparticles. *Angew. Chem. Int. Ed.* **2007**, *46*, 4093–4096.

182. Liu, J.; Lu, Y. Stimuli-responsive disassembly of nanoparticle aggregates for light-up colorimetric sensing. *J. Am. Chem. Soc.* **2005**, *127*, 12677–12683.

183. Lee, Y.-F.; Nan, F.-H.; Chen, M.-J.; Wu, H.-Y.; Ho, C.-W.; Chen, Y-Y.; Huang, C.-C. Detection and removal of mercury and lead ions by using gold nanoparticle-based gel membrane. *Anal. Methods* **2012**, *4*, 1709–1717.

184. Kim, M. H.; Kim, S.; Jang, H. H.; Yi, S.; Seo, S. H.; Han, M. S. A gold nanoparticle based colorimetric sensing ensemble for the colorimetric detection of cyanide ions in aqueous solution. *Tetrahedron Lett.* **2010**, *51*, 4712–4716.

185. Wei, S.-C.; Hsu, P.-H.; Lee, Y.-F.; Lin, Y.-W.; Huang, C.-C. Selective detection of iodide and cyanide anions using gold nanoparticle based fluorescent probes. *ACS Appl. Mater. Interfaces* **2012**, *4*, 2652–2658.

186. Rajamanikandan, R.; Ilanchelian, M. β-Cyclodextrin protected gold nanoparticle based cotton swabs as an effective candidate for specific sensing of trace levels of cyanide. *Anal. Methods* **2019**, *11*, 97–104.

187. Aslan, K.; Lakowicz, J. R.; Geddes, C. D. Nanogold Plasmon Resonance-Based Glucose Sensing. 2. Wavelength-Ratiometric Resonance Light Scattering. *Anal. Chem.* **2005**, *77*, 2007–2014.

188. Uehara, N.; Ookubo, K.; Shimizu, T. Colorimetric Assay of Glutathione Based on the Spontaneous Disassembly of Aggregated Gold Nanocomposites Conjugated with Water-Soluble Polymer *Langmuir* **2010**, *26*, 6818–6825.

189. Liang, X. S.; Wei, H. P.; Cui, Z. Q.; Deng, J. Y.; Zhang, Z. P.; You, X. Y.; Zhang, X. E. Colorimetric detection of melamine in complex matrices based on cysteamine-modified gold nanoparticles. *Analyst* **2011**, *136*, 179-183.

190. Liu, J. W.; Lu, Y. Fast colorimetric sensing of adenosine and cocaine based on a general sensor design involving aptamers and nanoparticles. *Angew. Chem.,Int. Ed.* **2006**, *45*, 90-94.

191. Soh, J. H.; Lin, V.; Rana, S.; Ying, J. Y.; Stevens, M. M.; *Anal. Chem.* **2015**, *87*, 7644–7652.

192. Choi, K. W.; Kang, S. W.; Kim, D.-Y.; Im, S. Y.; Park, Y.; Han, S., W.; Park, O. O. Size controlled gold nano-tetradecapods with tunable optical and electromagnetic properties. *J. Mater. Chem. C.* **2016**, *4*, 3149–3156.

193. Tan, L. H.; Xing, H.; Lu, Y. DNA as a powerful tool for morphology control, spatial positioning, and dynamic assembly of nanoparticles. *Acc. Chem. Res*. **2014**, *47*, 1881–1890.

194. Sun, W.; Boulais, E.; Hakobyan, Y.; Wang, W. L.; Guan, A.; Bathe, M.; Yin, P. Casting inorganic structures with DNA molds. *Science* **2014**, *346*, 1258361.

195. Jana, N. R.; Gearheart, L.; Murphy, C. J.; Wet chemical synthesis of high aspect ratio cylindrical gold nanorods. *J. Phys. Chem. B* **2001,** *105***,** 4065–4067.

196. Murphy, C. J.; San, T. K.; Gole, A. M.; Orendorff, C. J.; Gao, J. X.; Gou, L.; Hunyadi, S. E.; Li, T. Anisotropic metal nanoparticles: Synthesis, assembly, and optical applications. *J. Phys. Chem. B* **2005,** *109***,** 13857–13870**.**

197. Wang, Z. D.; Zhang, J. Q.; Ekman, J. M.; Kenis, P. J. A.; Lu, Y. DNA-mediated control of metal nanoparticle shape: One-pot synthesis and cellular uptake of highly stable and functional gold nanoflowers. *Nano Lett*. **2010**, *10*, 1886–1891.

198. Wang, Z.; Tang, L.; Tan, L. H.; Li, J.; Lu, Y. Discovery of the DNA "genetic code" for abiological gold nanoparticle morphologies. *Angew. Chem. Int. Ed.* **2012**, *51*, 9078–9082.

199. Tan, L. H.; Yue, Y.; Satyavolu, N. S. R.; Ali, A. S.; Wang, Z. D.; Wu, Y. Q.; Lu, Y. Mechanistic insight into DNA-guided control of nanoparticle morphologies. *J. Am. Chem. Soc*. **2015**, *137*, 14456–14464.

200. Oh, J.-W.; Lim, D.-W.; Kim, G.-H.; Suh, D. Y.; Nam, J.-M. Thiolated DNA-based chemistry and control in the structure and optical properties of plasmonic nanoparticles with ultrasmall interior nanogap. *J. Am. Chem. Soc*. **2014**, *136*, 14052–14059.

201. Song, T.; Tang, L.; Tan, L. H.; Wang, X.; Satyavolu, N. S. R.; Xing, H.; Wang, Z.; Li, J.; Liang, H.; Lu. Y. DNA-encoded tuning of geometric and plasmonic properties of nanoparticles growing from gold nanorod seeds. *Angew. Chem. Int. Ed.* **2015**, *54*, 8114–8118.

202. Satyavolu, N. S. R.; Tan, L. H.; Lu, Y. DNA-mediated morphological control of Pd–Au bimetallic nanoparticles. *J. Am. Chem. Soc.* **2016**, *138*, 16542–16548.

203. Ma, X.; Huh, J.; Park, W.; Lee, K. P.; Kwon, J. Y.; Sim, J. S. Gold nanocrystals with DNA-directed morphologies. *Nat. Commun*. **2016**, *7*, 12873.

204. Miller, S. M.; Simon, R. J.; Ng, S.; Zuckermann, R. N.; Kerr, J. M.; Moos, W. H. Comparison of the proteolytic susceptibilities of homologous L-amino-acid, D-amino-acid, and N-substituted glycine peptide and peptoid oligomers. *Drug Dev. Res*. **1995**, *35*, 20–32.

205. Walsh, T. R.; Knecht, M. R. Biointerface structural effects on the properties and applications of bioinspired peptide-based nanomaterials. *Chem. Rev*. **2017**, *117*, 12641–12704.

206. Sethi, M.; Knecht, M. R. Experimental studies on the interactions between Au nanoparticles and amino acids: Bio-based formation of branched linear chains. *ACS Appl. Mater. Interfaces* **2009**, *1*, 1270–1278.

207. Wright, L. B.; Merrill, N. A.; Knecht, M. R.; Walsh, T. R. Structure of arginine overlayers at the aqueous gold interface: Implications for nanoparticle assembly. *ACS Appl. Mater. Interfaces* **2014**, *6*, 10524–10533.

208. Jin, H.; Ding, Y.–H.; Wang, M.; Song, Y.; Liao, Z.; Newcomb, C. J.; Wu, X.; Tang, X.-Q.; Li, Z.; Lin, Y.; Yan, F.; Jian, T.; Mu, P.; Chen, C.–L. Controlled synthesis of highly-branched plasmonic gold nanoparticles through peptoid engineering*Nat. Commun*. **2018**, *9*, 23270.

209. Lee, H. E.; Ahn, H. Y.; Mun, J.; Lee, Y. Y.; Kim, M.; Cho, N. H.; Chang, K.; Kim, W. S.; Rho, J.; Nam, K. T. Amino-acid- and peptide-directed synthesis of chiral plasmonic gold nanoparticles. *Nature* **2018**, *556*, 360–365.

210. Mocanu, A.; Cernica, I.; Tomoaia, G.; Bobos, L.-D.; Horovitz, O.; Tomoaia-Cotisel, M. Self-assembly characteristics of gold nanoparticles in the presence of cysteine. *Colloids Surf. A* **2009**, *338*, 93–101.

211. Jain, P. K.; Lee, K. S.; El-Sayed, I. H.; El-Sayed, M. A. Calculated absorption and scattering properties of gold nanoparticles of different size, shape, and composition: Applications in biological imaging and biomedicine. *J. Phys. Chem. B* **2006**, 110, 7238–7248.

212. Chegel, V.; Rachkov, O.; Lopatynskyi, A.; Ishihara, S.; Yanchuk, I.; Nemoto, Y.; Hill, J. P.; Ariga, K. Gold nanoparticles aggregation: Drastic effect of cooperative functionalities in a single molecular conjugate. *J. Phys. Chem. C* **2012**, *116*, 2683–2690.

213. Zakaria, H. M.; Shah, A.; Konieczny, M.; Hoffmann, J. A.; Nijdam, A. J.; Reeves, M. E. Small molecule and amino acid induced aggregation of gold nanoparticles. *Langmuir* **2013**, *29*, 7661–7673.

214. Rani, M.; Moudgil, L.; Singh, B.; Kaushal, A.; Mittal, A.; Saini, G. S. S.; Tripathi, S. K.; Singhe, G.; Kaura, A. Understanding the mechanism of replacement of citrate from the surface of gold nanoparticles by amino acids: A theoretical and experimental investigation and their biological application. *RSC Adv*. **2016**, *6*, 17373–17379.

215. Sato, K.; Hosokawa, K.; Maeda, M. Rapid aggregation of gold nanoparticles induced by non-cross-linking DNA hybridization. *J. Am. Chem. Soc*. **2003**, *125*, 8102–8103.

216. Wang, G.; Akiyama, Y.; Shiraishi, S.; Kanayama, N.; Takarada, T.; Maeda, M. Cross-linking versus non-cross-linking aggregation of gold nanoparticles induced by DNA hybridization: A comparison of the rapidity of solution color change. *Bioconjugate Chem.***2017**, *28*, 270–277.

217. Zhang, X.; Liu, B.; Dave, N.; Servos, M. R.; Liu, J. Instantaneous attachment of an ultrahigh density of nonthiolated DNA to gold nanoparticles and its applications. *Langmuir* **2012**, *28*, 17053–17060.

218. Li, Y.; Liu, Z.; Yu, G.; Jiang, W.; Mao, C. Self-assembly of molecule-like nanoparticle clusters directed by DNA nanocages. *J. Am. Chem. Soc*. **2015**, *137*, 4320–4323.

219. Esashika, K.; Saiki, T. DNA hybridization assay using gold nanoparticles and electrophoresis separation provides 1 pM sensitivity. *Bioconjugate Chem*. **2018**, *29*, 182–189.

220. nature.com/subjects/nanocomposites

221. Wang, H.; Chen, L. Y.; Feng, Y. H.; Chen,H. Y. Exploiting core–shell synergy for nanosynthesis and mechanistic investigation. *Acc. Chem. Res*. **2013**, *46*, 1636–1646.

222. Chaudhuri, R. G.; Paria, S. Core/Shell nanoparticles: Classes, properties, synthesis mechanisms, characterization, and applications. *Chem. Rev*. **2012**, *112*, 2373–2433.

223. Gawande, M. B.; Goswami, A.; Asefa, T.; Guo, H. Core–shell nanoparticles: Synthesis and applications in catalysis and electrocatalysis. *Chem. Soc. Rev*. **2015**, *44*, 7540–7590.

224. Tuo, Y.; Liu, G.; Dong, B.; Zhou, J.; Wang, A.; Wang, J.; Jin, R. Microbial synthesis of Pd/Fe_3O_4, Au/Fe_3O_4 and $PdAu/Fe_3O_4$ nanocomposites for catalytic reduction of nitroaromatic compounds. *Sci. Rep*. **2015**, *5*, 13515.

225. Chen, D.; Li, C.; Liu, H.; Ye, F.; Yang, J. Core-shell Au@Pd nanoparticles with enhanced catalytic activity for oxygen reduction reaction via core-shell Au@Ag/Pd constructions. *Sci. Rep*. **2015**, *5*, 11949**.**

226. Li, X. M.; Liu, H. L.; Liu, X.; Fang, N.; Wang, X. H.; Wu, J. H. Synthesis of bi-phase dispersible core-shell FeAu@ ZnO magneto-opto-fluorescent nanoparticles. *Sci. Rep*. **2015**, *5*, 16384.

227. Leung, K. C. F.; Xuan, S.; Zhu, X.; Wang, D. Gold and iron oxide hybrid nanocomposite materials. *Chem. Soc. Rev*. **2012***, 41*, 1911–1928.

228. Umut, E.; Pineider, F.; Arosio, P.; Sangregorio, C. Magnetic, optical and relaxometric properties of organically coated gold–magnetite ($Au–Fe_3O_4$) hybrid nanoparticles for potential use in biomedical. *J. Magn. Magn. Mater*. **2012**, *324*, 2373–2379.

229. Wen, T.; Krishnan, K. M. Magnetic properties of Au_{core}-Co_{shell} nanoparticles. *Appl. Phys*. **2011**, *109*, 07B515.

230. Mangeney, C.; Bousalem, S.; Connan, C.; Vaulay, M.–J.; Bernard. S.; Chehimi, M. M. Latex and hollow particles of reactive polypyrrole: Preparation, properties, and decoration by gold nanospheres. *Langmuir* **2006**, *22*, 10163–10169.

231. Li, P.; Wei, Z.; Wu, T.; Peng, Q.; Li, Y. D. Au−ZnO hybrid nanopyramids and their photocatalytic properties. *J. Am. Chem. Soc*. **2011**,*133***,** 5660–5663.

232. Lee, N.; Yoo, D.; Ling, D.; Cho, M. H.; Hyeon, T.; Cheon, J. Iron oxide based nanoparticles for multimodal imaging and magnetoresponsive therapy. *Chem. Rev*. **2015**, *115*, 10637–10689.

233. Wei, H.; Bruns, O. T.; Kaul, M. G.; Hansen, E. C.; Barch, M.; Wisniowska, A.; Chen, O.; Chen, Y.; Li, N.; Okada, S.; Cordero, J. M.; Heine, M.; Farrar, C. T.; Montana, D. M.; Adam, G.; Ittrich, H.; Jasanoff, A.; Nielsen, P.; Bawendi, M. G. Exceedingly small iron oxide nanoparticles as positive MRI contrast agents. *Proc. Natl. Acad. Sci*. U.S.A. **2017**, *28*, 2325–2330.

234. Hu, F.; Macrenaris, K. W.; Waters, E. A.; Schultz-Sikma, E. A.; Eckermann , A. L.; Meade, T. J. Highly dispersible, superparamagnetic magnetite nanoflowers for magnetic resonance imaging. *Chem. Commun*. **2010**, *46*, 73–75.

235. Xuan, S. H; Wang, Y. X. J.; Yu, J. C.; Leung, K. C.-F. Tuning the grain size and particle size of superparamagnetic Fe_3O_4 microparticles. *Chem. Mater*. **2009**, *21*, 5079–5087.

236. Xuan, S. H.; Wang, Y. X. J.; Yu, J. C.; Leung, K. C.-F. Facile synthesis of size-controllable monodispersed ferrite nanospheres. *J. Mater. Chem*. **2010**, *20*, 5086–5094.

237. Hirsch, L. R.; Stafford, R. J.; Bankson, J. A.; Sershen, S. R.; Rivera, B.; Price, R. E.; Hazle, J. D.; Halas, N. J.; West, J. L. Nanoshell-mediated near-infrared thermal therapy of tumors under magnetic resonance guidance. *Proc. Natl. Acad. Sci. U.S. A.* **2003**, *100*, 13549–13554.

238. Devarakonda, S. B.; Myers, M. R.; Lanier, M.; Dumoulin, C.; Banerjee, R. K. Assessment of gold nanoparticle-mediated-enhanced hyperthermia using MR-guided high-intensity focused ultrasound ablation procedure. *Nano Lett*. **2017**, *17*, 2532–2538.

239. Jeong, U. Y.; Teng, X. W.; Wang, Y.; Yang, H.; Xia, Y. N. Superparamagnetic colloids: Controlled synthesis and niche applications. *Adv. Mater.* **2007**, *19*, 33–60.

240. Xuan, S. H.; Wang, Y. X. J.; Yu, J. C.; Leung, K. C.-F. Preparation, characterization, and catalytic activity of core/shell Fe_3O_4@Polyaniline@Au nanocomposites. *Langmuir* **2009**, *25*, 11835–11843.

241. Zhang, J.; Liu, X.; Wang, L.; Yang, T.; Guo, X.; Wu. S.; Zhang, S. Au-functionalized hematite hybrid nanospindles: General synthesis, gas sensing and catalytic properties. *J. Phys. Chem. C* **2011**, *115*, 5352–5357.

242. Tian, J.; Zheng, F.; Zhao, F. Nanoparticles with Fe_3O_4-nanoparticle cores and gold-nanoparticle coronae prepared by self-assembly approach. *J. Phys. Chem. C* **2011**, *115*, 3304–3312.

243. Serpell, C. J.; Cookson, J.; Ozkaya, D.; Beer, P. D. Core@shell bimetallic nanoparticle synthesis via anion coordination. *Nat. Chem.* **2011**, *3*, 478–483.

244. Levin, C. S.; Hofmann, C.; Ali, T. A.; Kelly, A. T.; Morosan, E.; Nordlander, P.; Whitmire, K. H.; Halas, N. J. Magnetic plasmonic core shell nanoparticles. *ACS Nano* **2009**, *3*, 1379–1388.

245. Bell, C. S.; Yu, S. S.; Giorgio, T. D. The multistrata nanoparticle: An FeO_x/Au Core/Shell enveloped in a silica-Au shell. *Small* **2011**, *7*, 1158–1162.

246. Wang, H.; Brandl, D. W.; Le, F.; Nordlander, P.; Halas, N. J. Nanorice: A hybrid plasmonic nanostructure. *Nano Lett*. **2006**, *6*, 827–832.

247. Wang, L. Y.; Park, H. Y.; Lim, S. I. I.; Schadt, M. J.; Mott, D.; Luo, J.; Wang, X.; Zhong, C. J. Core@shell nanomaterials: Gold-coated magnetic oxide nanoparticles. *J. Mater. Chem.* **2008**, *18*, 2629–2635.

248. Huang, W.-C.; Tsai, P.-J.; Chen, Y.-C. Multifunctional Fe_3O_4@Au nanoeggs as photothermal agents for selective killing of nosocomial and antibiotic-resistant bacteria. *Small*, **2009**, *5*, 51–56.

249. Lee, J.; Yang, J.; Ko, H.; Oh, S. J.; Kang, J.; Son, J.-H.; Lee, K.; Lee, S.-W.; Yoon, H.-G.; Suh, J.-S.; Huh, Y.-M.; Haam, S. Multifunctional magnetic gold nanocomposites: Human epithelial cancer detection via magnetic resonance imaging and localized synchronous therapy. *Adv. Funct. Mater.* **2008**, *18*, 258–264.

250. Yeo, K. M.; Shin, J.; Lee, I. S. Reductive dissolution of Fe_3O_4 facilitated by the Au domain of a Fe_3O_4/Au hybrid nanocrystal: Formation of a nanorattle structure composed of a hollow porous silica nanoshell and entrapped Au nanocrystal. *Chem. Commun.* **2010**, *46*, 64–66.

251. Yu, H.; Chen, M.; Rice, P. M.; Wang, S. X.; White, R. L.; Sun, S. H. Dumbbell-like bifunctional Au−Fe_3O_4 nanoparticles. *Nano Lett*. **2005**, *5*, 379–382.

252. Leung, K. C. -F.; Xuan, S.; Zhu, X.; Wang, D.; Chak, C. -P.; Lee, S.-F.; Ho, W. K.-W.; Chung, B. C.-T. Gold and iron oxide hybrid nanocomposite materials. *Chem. Soc. Rev.* **2012**, *41*, 1911–1928.

253. Xie, J.; Zhang, F.; Aronova, M.; Zhu, L.; Lin, X.; Quan, Q.; Liu, G.; Zhang, G.; Choi, K.-Y.; Kim, K.; Sun, X.; Lee, S.; Sun, S.; Leapman, R.; Chen, X. Manipulating the power of an additional phase: A flower-like Au-Fe$_3$O$_4$ optical nanosensor for imaging protease expressions *in vivo*. *ACS Nano* **2011**, *5*, 3043–3051.

254. Wei, Y. H.; Klajn, R.; Pinchuk, A. O.; Grzybowski, B. A. Synthesis, shape control, and optical properties of hybrid Au/Fe$_3$O$_4$ "Nanoflowers". *Small* **2008**, *4*, 1635–1639.

255. Feldman, M. D.; Ma, L. L.; Tam, J. M.; Paranjape, A. S.; Cheruku, K. K.; Larson, T. A.; Tam, J. O.; Ingram, D. R.; Paramita, V.; Villard, J. W.; Jenkins, J. T.; Wang, T.; Clarke, G. D.; Asmis, R.; Sokolov, K.; Chandrasekar, B.; Milner, T. E.; Johnston, K. P. Small multifunctional nanoclusters (nanoroses) for targeted cellular imaging and therapy. *ACS Nano* **2009**, *3*, 2686–2696.

256. Kojima, H.; Mukai, Y.; Yoshikawa, M.; Kamei, K.; Yoshikawa, T.; Morita, M.; Inubushi, T.; Yamamoto, T. A.; Yoshioka, Y.; Okada, N.; Seino, S.; Nakagawa, S. Simple PEG conjugation of SPIO via an Au-S bond improves its tumor targeting potency as a novel MR tumor imaging agent. *Bioconjugate Chem.* **2010**, *21*, 1026–1031.

257. Nash, M. A.; Yager, P.; Hoffman, A. S.; Stayton, P. S. Mixed stimuli-responsive magnetic and gold nanoparticle system for rapid purification, enrichment, and detection of biomarkers. *Bioconjugate Chem.* **2010**, *21*, 2197–2204.

258. Kolhatkar A. G.; Jamison, A. C.; Litvinov, D.; Willson, R. C.; Lee, T. R. Tuning the magnetic properties of nanoparticles. *Int. J. Mol. Sci.* **2013**, *14*, 15977–16009.

259. Lee, G.; Kim, J.; Lee, J. H. Development of magnetically separable polyaniline nanofibers for enzyme immobilization and recovery. *Enzyme Microb. Technol.* **2008**, *45*, 466–472.

260. Ge, J. P.; Lee, H.; He, L.; Kim, J.; Lu, Z. D.; Kim, H.; Goebl, J.; Kwon, S.; Yin, Y. D. Magnetochromatic microspheres: Rotating photonic crystals. *J. Am. Chem. Soc.* **2009**, *131*, 15687–15694.

261. Ge, J. P.; He, L.; Hu, Y. X.; Yin, Y. D. Magnetically induced colloidal assembly into field-responsive photonic structures. *Nanoscale* **2011**, *3*, 177–183.

262. Jeong, U. Y.; Teng, X. W.; Wang, Y.; Yang, Y.; Xia, Y. N. Superparamagnetic colloids: Controlled synthesis and niche Applications. *Adv. Mater.* **2007**, *19*, 33–60.

263. Suzuki, M.; Kawamura, N.; Miyagawa, H.; Garitaonandia, J. S.; Yamamoto, Y.; Hori, H. Measurement of a pauli and orbital paramagnetic state in bulk gold using X-ray magnetic circular dichroism spectroscopy. *Phys. Rev. Lett.* **2012**, *108*, 047201.

264. Pineider, F.; Fernández, C-J. Spin-polarization transfer in colloidal magnetic-plasmonic Au/iron oxide hetero-nanocrystals. *ACS Nano* **2013**, *7*, 857–866.

265. Frey, N. A.; Phan, M. H.; Srikanth, H.; Srinath, S.; Wang, C.; Sun, S. Interparticle interactions in coupled Au–Fe$_3$O$_4$ nanoparticles. *J. Appl. Phys.* **2009**, *105*, 07B502.

266. Oh, Y.-W.; Baek, S. C.; Kim, Y. M.; Lee, H. Y.; Lee, K.-D.; Yang, C.-G.; Park, E.-S.; Lee, K.-S.; Kim, K.-W.; Go, G.; Jeong, J.-R.; Min, B.-C.; Lee, H.-W.; Lee, K.-J.; Park, B.-G. Field-free switching of perpendicular magnetization through spin-orbit torque in antiferromagnet/ferromagnet/oxide structures. *Nat. Nanotechnol.* **2016**, *11*, 878–884.

267. Unni M.; Uhl, A. M.; Savliwala, S.; Savitzky, B. H.; Dhavalikar, R.; Garraud, N.; Arnold, D. P.; Kourkoutis, L. F.; Andrew, J. S.; Rinaldi, C. Thermal decomposition synthesis of iron oxide nanoparticles with diminished magnetic dead layer by controlled addition of oxygen. *ACS Nano* **2017**, *11*, 2284–2303.

268. Feygenson, M.; Bauer, J. C.; Gai, Z.; Marques, C.; Aronson, M. C.; Teng, X.; Su, D.; Stanic, V.; Urban, V. S.; Beyer, K. A.; Dai, S. Exchange bias effect in Au-Fe_3O_4 dumbbell nanoparticles induced by the charge transfer from gold. *Phys. Rev. B* **2015**, *92*, 054416.

269. Janib, S. M.; Moses, A. S.; Kackay, J. A. Imaging and drug delivery using theranostic nanoparticles. *Adv. Drug Delivery Rev.* **2010**, *62*, 1052–1063.

270. Sun, C.; Lee, J. S. H.; Zhang, M. Magnetic nanoparticles in MR imaging and drug delivery. *Adv. Drug Delivery Rev*. **2008**, *60*, 1252–1265.

271. García, I.; Gallo, J.; Genicio, N.; Padro, D.; Penadés, S. Magnetic glyconanoparticles as a versatile platform for selective immunolabeling and imaging of cells. *Bioconjugate Chem*. **2011**, *22*, 264–273.

272. Wang, Y.; Liu, X.; Deng, G.; Wang, Q.; Zhang, L.; Wang, Q.; Lu, J. Multifunctional PS@CS@Au–Fe_3O_4–FA nanocomposites for CT, MR and fluorescence imaging guided targeted-photothermal therapy of cancer cells. *J. Mater. Chem. B* **2017**, *5*, 4221–4232.

273. Bardhan, R.; Chen, W.; Perez-Torres, C.; Bartels, M.; Huschka, R. M.; Zhao, L. L.; Morosan, E.; Pautler, R. G.; Joshi, A.; Halas, N. J. Nanoshells with targeted simultaneous enhancement of magnetic and optical imaging and photothermal therapeutic response. *Adv. Funct. Mater*. **2009**, *19*, 3901–3909.

274. Smolensky, E. D.; Neary, M. C.; Zhou, Y.; Berquo, T. S.; Pierre, V. C. Fe_3O_4@organic@Au:core–shell nanocomposites with high saturation magnetisation as magnetoplasmonic MRI contrast agents. *Chem. Commun.* **2011**, *47*, 2149–2151.

275. Wang, Y.; Xu, C.; Chang, Y.; Zhao, L.; Zhang, L.; Zhao, L.; Gao, F.; Gao, X. Ultrasmall superparamagnetic iron oxide nanoparticle for T_2-weighted magnetic resonance imaging. *ACS Appl. Mater. Interfaces* **2017**, *9*, 28959–28966.

276. Sherwood, J.; Rich, M.; Lovas, K.; Warram, J.; Bolding, M. S.; Bao, Y. T_1-enhanced MRI-visible nanoclusters for imaging-guided drug delivery. *Nanoscale* **2017**, *9*, 11785–11792.

277. Bao, Y.; Sherwood, J. A.; Sun, Z. Magnetic iron oxide nanoparticles as T_1 contrast agents for magnetic resonance imaging. *J. Mater. Chem. C* **2018**, *6*, 1280–1290.

278. Jamieson, E. R.; Lippard, S. J. Structure, recognition, and processing of cisplatin DNA adducts. *Chem. Rev.* **1999**, *99*, 2467–2498.

279. Xu, C.; Wang, B.; Sun, S. Dumbbell-like Au-Fe_3O_4 nanoparticles for target-specific platin delivery. *J. Am. Chem. Soc*. **2009**, *131*, 4216–4217.

280. Adams, G. P.; Weiner, L. M. Monoclonal antibody therapy of cancer. *Nat. Biotechnol*. **2005**, *23*, 1147–1157.

281. Bhana, S.; Lin, G.; Wang, L.; Starring, H.; Mishra, S. R.; Liu, G.; Huang, X. Near-infrared-absorbing gold nanopopcorns with iron oxide cluster core for magnetically amplified photothermal and photodynamic cancer therapy. *ACS Appl. Mater. Interfaces* **2015**, *7*, 11637–11647.

282. Ma, P.; Xiao, H.; Yu, C.; Liu, J.; Cheng, Z.; Song, H.; Zhang, X.; Li, C.; Wang, J.; Gu, Z.; Lin, J. Enhanced cisplatin chemotherapy by iron oxide nanocarrier-mediated generation of highly toxic reactive oxygen species. *Nano Lett*. **2017**, *17*, 928–937.

283. Ulbrich, K.; Hola, K.; Subr, V.; Bakandritsos, A.; Tuce, J.; Zboril, R. Targeted drug delivery with polymers and magnetic nanoparticles: Covalent and noncovalent approaches, release control, and clinical studies. *Chem. Rev*. **2016**,*116*, 5338–5431.

284. Bhamidipati, M.; Fabris, L. Multiparametric assessment of gold nanoparticle cytotoxicity in cancerous and healthy Cells: The role of size, shape, and surface chemistry. *Bioconjugate Chem*. **2017**, *28*, 449–460.

285. Du, Y.; Xia, L.; Jo, A.; Davis, R. M.; Bissel, P.; Ehrich, M. F.; Kingston. D. G. I. Synthesis and evaluation of doxorubicin loaded gold nanoparticles for tumor targeted drug delivery. *Bioconjugate Chem*. **2018**, *29*,420–430.

286. Hashmi, A. S. K.; Hutchings, G. J. Gold Catalysis. *Angew. Chem. Int. Ed.* **2006**, *45*, 7896–7936.

287. Arcadi, A. Alternative synthetic methods through new developments in catalysis by gold. *Chem. Rev.* **2008**, *108*, 3266–3325.

288. Corm, A.; Garcia, H. Supported gold nanoparticles as catalysts for organic reactions. *Chem. Soc. Rev*. **2008**, *37*, 2096–2126.

289. Lin, F. H.; Doong, R. A. Bifunctional Au-Fe_3O_4 heterostructures for magnetically recyclable catalysis of nitrophenol reduction. *J. Phys. Chem. C* **2011**, *115*, 6591–6598.

290. Yin, H.; Wang, C.; Zhu, H.; Overbury, S. H.; Sun, S.; Dai, S. Colloidal deposition synthesis of supported gold nanocatalysts based on Au–Fe_3O_4 dumbbell nanoparticles. *Chem. Commun*. **2008**, 4357–4359.

291. Hung, W. H.; Aykol, M.; Valley, D.; Hou, W.; Cronin, S. B. Plasmon resonant enhancement of carbon monoxide catalysis. *Nano Lett*. **2010**, *10*, 1314–1318.

292. Edwards, J. K.; Solsona, B.; Landon, P. ; Carley, A. F.; Herzing, A.; Watanabe, M.; Kiely, C. J.; Hutchings, G. J. Direct synthesis of hydrogen peroxide from H_2 and O_2 using Au–Pd/Fe_2O_3 catalysts. *J. Mater. Chem.* **2005**, *15*, 4595–4600.

293. Ge, J.; Huynh, T.; Hu, Y.; Yin, Y. Hierarchical magnetite/silica nanoassemblies as magnetically recoverable catalyst supports. *Nano Lett.* **2008**, *8*, 931–934.

294. Lin, F. H.; Doong, R. A. Bifunctional Au−Fe_3O_4 heterostructures for magnetically recyclable catalysis of nitrophenol reduction. *J. Phys. Chem. C* **2011**, *115*, 6591–6598.

295. Ojha, K.; Saha, S.; Dagara, P.; Ganguli, A. K. Nanocatalysts for hydrogen evolution reactions. Phys. Chem. Chem. Phys. 2018, 20, 6777-6799.

296. Saha, S.; Ganguli, A. K. FeCoNi alloy as noble metal-free electrocatalyst for oxygen evolution reaction (OER). *Chemistry Select* 2017, 2, 1630-1636.

297. Lee, Y.; Garcia, M. A.; Huls, N. A. F.; Sun, S. Synthetic tuning of the catalytic properties of Au-Fe_3O_4 nanoparticles. *Angew. Chem. Int. Ed.* **2010**, *49*, 1271–1274.

298. Yeo, B. S.; Bell, A. T. Enhanced activity of gold-supported cobalt oxide for the electrochemical evolution of oxygen. *J. Am. Chem. Soc.* **2011**, *133*, 5587–5593.

299. Yeo, B. S.; Bell, A. T. In situ Raman study of nickel oxide and gold-supported nickel oxide catalysts for the electrochemical evolution of oxygen. *J. Phys. Chem. C* **2012**, *116*, 8394–8400.

300. Seitz, L. C.; Hersbach, T. J. P.; Nordlund, D.; Jaramillo, T. F. Enhancement effect of noble metals on manganese oxide for the oxygen evolution reaction. *J. Phys. Chem. Lett.* **2015**, *6*, 4178–4183.

301. Frydendal, R.; Busch, M.; Halck, N. B.; Paoli, E. A.; Krtil, P.; Chorkendorff, I.; Rossmeisl, J. Enhancing activity for the oxygen evolution reaction: the beneficial interaction of gold with manganese and cobalt Oxides. *ChemCatChem* **2015**, *7*, 149–154.

302. Görlin, M.; Ferreira de Araújo, J.; Schmies, H.; Bernsmeier, D.; Dresp, S.; Gliech, M.; Jusys, Z.; Chernev, P.; Kraehnert, R.; Dau, H.; Strasser, P. Tracking catalyst redox states and reaction dynamics in Ni–Fe oxy hydroxide Oxygen evolution reaction electrocatalysts: The role of catalyst Support and electrolyte pH. *J. Am. Chem. Soc.* **2017**, *139*, 2070–2082.

303. Klaus, S.; Trotochaud, L.; Cheng, M.-J.; Head-Gordon, M.; Bell, A. T. Experimental and computational evidence of highly active Fe impurity sites on the surface of oxidized Au for the electrocatalytic oxidation of water in basic media. *ChemElectroChem.* **2016**, *3*, 66–73.

304. Strickler, A. L.; Escudero-Escribano, M.; Jaramillo, T. F. Core- shell Au@Metal-oxide nanoparticle electrocatalysts for enhanced oxygen evolution. *Nano Lett.* **2017**, *17*, 6040–6046.

305. Wang, X.; Maeda, N.; Baiker, A. Synergistic effects of Au and FeO_x nanocomposites in catalytic NO reduction with CO. *ACS Catal.* **2016,** *6*, 7898–7906.

306. Larsen, G. K.; Farr, W.; Murph, S. E. H. Multifunctional Fe_2O_3-Au nanoparticles with different shapes: Enhanced catalysis, photothermal effects, and magnetic recyclability. *J. Phys. Chem. C* **2016**, *120*, 15162–15172.

307. Lu, V.; Hu, Y.; Wan, S.; McCaffrey, R.; Jin, Y.; Gu, V. Synthesis of ultrafine and highly dispersed metal nanoparticles confined in a thioether-containing covalent organic framework and their catalytic applications. *J. Am. Chem. Soc.* **2017**, *139*, 17082–17088.

308. Lin, F.; Doong, V. Catalytic nanoreactors of Au@Fe_3O_4 yolk–shell nanostructures with various Au sizes for efficient nitroarene reduction. *J. Phys. Chem. C* **2017,** *121*, 7844–7853.

309. Tanaka, S.; Lin, J.; Kaneti, Y. V.; Yusa, S.-I.; Jikihara, Y.; Nakayama, T.; Zakaria, M. B.; Alshehri, A. A.; You, J.; Hossaina, M. S. A.; Yamauchi, Y. Gold nanoparticles supported on mesoporous iron oxide for enhanced CO oxidation reaction. *Nanoscale* **2018**, *10*, 4779–4785.

310. Lu, F.; Gang, O.; DNA Functionalization of Nanoparticles. *Methods Mol. Biol.* **2016**, *1500*, 99–107.

311. Rosi, N. L.; Giljohann, D. A.; Thaxton, C. S.; Lytton-Jean, K. R.; Han, M. S.; Mirkin, C. A. Oligonucleotide modified gold nanoparticles for intracellular gene regulation. *Science* **2006**, *312*, 1027–1030.

312. Wu, J.; Liang, D.; Jin, Q.; Liu,J.; Zheng, M.; Duan,X.; Tang,X. Bioorthogonal SERS nanoprobes for mulitplex spectroscopic detection, tumor cell targeting, and tissue imaging *Chem. Eur. J.* **2015**, *21*, 12914–12918.

313. Xiang, C. C.; Kozhich, O. A.; Chen, M.; Inman, J. M.; Phan,Q. N.; Chen,Y.; Brownstein, M. J. Amine-modified random primers to label probes for DNA microarrays. *Nat. Biotechnol.* **2002**, *20*, 738–742.

314. Sharma, J.; Chhabra, R.; Anderson, C. S.; Gothlef, K. V.; Yan, H.; Liu,Y. Toward reliable gold nanoparticle patterning on self-assembled DNA nanoscaffold.*J. Am. Chem. Soc.* **2008**, *130*, 7820–7821.

315. Konrny, T.; Walt, D. R. Intelligent medical diagnostics via molecular logic. *J. Am. Chem. Soc.* **2009**, *131*, 13232–13233.

316. Sakurai, K.; Snyder, T. M.; Liu, D. R. DNA templated functional group transformations enable sequence-programmed synthesis using small-molecule reagents. *J. Am. Chem. Soc.* **2005**, *127*, 1660–1661.

317. Cox,W. G.; Singer,V. L. Fluorescent DNA hybridization probe preparation using amine modification and reactive dye coupling. *Bio Techniques*. **2004**, *36*, 114–122.

318. Ouyang, X.; Stefano, M. D.; Krissanaprasit, A.; Kodal, A. L. B.; Rosen, C. B.; Liu, T.; Helmig, S.; Fan, C.; Gothelf, K. V. Docking of antibodies into the cavities of DNA origami Structures. *Angew. Chem. Int. Ed.* **2017**, *56*, 14423–14427.

319. Thomas, K. G.; Zajicek, J.; Kamat, P. V.; Surface binding properties of tetraoctylammonium bromide-capped gold nanoparticles. *Langmuir* **2002**, *18*, 3722–3727.

320. Haiss, W.; Thanh, N. T. K.; Aveyard, J.; Fernig, D. G. Determination of size and concentration of gold nanoparticles from UV−Vis spectra. *Anal. Chem.***2007**, *79*, 4215–422.

321. Storhoff, J. J.; Elghanian, R.; Mirkin, C. A.; Letsinger, R. L.; Sequence dependent stability of DNA modified gold nanoparticles. *Langmuir* **2002**, *18*, 6666–6670.

322. Chiu, C.-Y.; Ruan, L.; Huang, Y. Biomolecular specificity controlled nanomaterial synthesis. *Chem. Soc*. *Rev.***2013**, *42*, 2512–2527.

323. Scholl, J. A.; Koh, A. L.; Dionne, J. A. Quantum plasmon resonances of individual metallic nanoparticles. *Nature* **2012**, 483, 421–427.

324. Sun, W.; Boulais, E.; Hakobyan, Y.; Wang, W. L.; Guan, A.;Bathe, M.; Yin, P.Casting inorganic structures with DNA molds. *Science* **2014**, *346*, 1258361.

325. Lohse, S. E.; Murphy, C. J. The quest for shape control: A history of gold nanorod synthesis. *Chem. Mater*. **2013**, *25*, 1250−1261.

326. Mourdikoudis, S.; Liz-Marzán, L. M. Oleylamine in nanoparticle synthesis. *Chem. Mater*. **2013**, *25*, 1465−1476.

327. Bealing, C. R.; Baumgardner, W. J.; Choi, J. J.; Hanrath, T.; Hennig, R. G. Predicting nanocrystal shape through consideration of surface-ligand interactions. *ACS Nano* **2012**, *6*, 2118–2127.

328. Boles, M. A.; Engel, M.; Talapin,D. V.Self-assembly of colloidal nanocrystals: From intricate structures to functional materials.*Chem. Rev.***2016**, *116*, 11220–11289

329. Weidman, M. C.; Nguyen, Q.; Smilgies, D.-M.; Tisdale, W. A. Impact of size dispersity, ligand coverage, and ligand length on the structure of PbS nanocrystal Superlattices. *Chem. Mater.* **2018**, *30*, 807–816.

330. Brust, M.; Walker, M.; Bethell, D.; Schiffrin, D. J.; Whyman, R. Synthesis of Thiol-Derivatized Gold Nanoparticles in a 2-Phase Liquid-Liquid System. *J. Chem. Soc., Chem. Commun.* **1994**, 801– 802.

331. Park, S. Y.; Lytton-Jean, A. K. R.; Lee, B.; Weigand, S.; Schatz, G.C.; Mirkin, C. A. DNA-programmable nanoparticle crystallization. *Nature* **2008**, *451*, 553.

332. Jones, M. R.; Seeman, N. C.; Mirkin, C. A. Programmable materials and the nature of the DNA bond. *Science* **2015**, *347*, 1260901.

333. Surana, S.; Shenoy, A. R.; Krishnan, Y. Designing DNA nanodevices for compatibility with the immune system of higher organisms. *Nat. Nanotechnol.* **2015**, *10*, 741−747.

334. Edwardson, T. G. W.; Lau, K. L.; Bousmail, D.; Serpell, C. J.; Sleiman, H. F. Transfer of molecular recognition information from DNA nanostructures to gold nanoparticles. *Nat. Chem.* **2016**, *8*, 162−170.

335. Li, Y.; Liu, Z.; Yu, G.; Jiang, W.; Mao, C. Self-assembly of molecule-like nanoparticle clusters directed by DNA nanocages. *J. Am. Chem. Soc.* **2015**, *137*, 4320−4323.

336. Sen, S.; Dasgupta, S.; Dasgupta, S. Does surface chirality of gold nanoparticles affect fibrillation of HSA. *J. Phys. Chem. C* **2017**, *121*, 18935-18946.

337. Konar, M.; Mathew, A.; Dasgupta, S. Effect of silica nanoparticles on the amyloid fibrillation of lysozyme. *ACS Omega* **2019**, *4*, 1015–1026.

338. Hunter, R. J. Foundations of Colloid Science, 2nd ed.; *Oxford University Press: Oxford,* U.K., 2001.

339. Kim, T.; Lee, K.; Gong, M.; Joo, S. Control of Gold Nanoparticle Aggregates by Manipulation of Interparticle Interaction. *Langmuir* **2005**, *21*, 9524−9528.

340. Zhou, W.; Gao, X.; Liu, D.; Chen, X. Gold Nanoparticles for In Vitro diagnostics *Chem. Rev.* **2015**, *115*, 10575−10636

341. Wu, J., Liang, D., Jin, Q., Liu, J., Zhang, M., Duan, X., Tang, X. Bioorthogonal SERS nanoprobes for mulitplex spectroscopic detection, tumor cell targeting, and tissue imaging. *Chem. Eur. J. 2015*, 21, 12914.

342. Kariuki, V. M., Hoffmeier, J. C., Yazgan, I.; Sadik, O. A. Seedless synthesis and SERS characterization of multi-branched gold nanoflowers using water soluble polymers. *Nanoscale* **2017**, *9*, 8330–8340.

343. Schreiber, R., Santigo, I., Ardavan, A., Turberfield, A. J., Ordering gold nanoparticles with DNA origami nanoflowers *ACS Nano,* **2016** *10*, 7303–7306.

344. Wang, K., Jiang, L., Zhang, F., Wei, Y., Wang, K., Wang, H., Qi, Z., and Liu, S., Strategy for in situ imaging of cellular alkaline phosphatase activity using gold nanoflower probe and localized surface plasmon resonance technique *Anal. Chem.* **2018**, *90*, 14056−14062.

345. Rawat, K. A., and Kailasa, S. K. (2014) Visual detection of arginine, histidine and lysine using quercetin-functionalized gold nanoparticles. *Microchim. Acta* **2014**, 181, 1917.

346. Kasibabu, B. S. S., Bhamore, J. R., D'souza, S. L., and Kailasa, S. K. Dicoumarol assisted synthesis of water dispersible gold nanoparticles for colorimetric sensing of cysteine and lysozyme in biofluids. *RSC Adv.* **2015**, 5, 39182–39191.

347. Bhamore, J., Rawat, K. A., Basu, H., Singhal, R. K., and Kailasa, S. K. Influence of molecular assembly and NaCl concentration on gold nanoparticles for colorimetric detection of cysteine and glutathione. *Sens. Actuators, B* **2015**, 212, 526–535.

348. Lee, H.-E., Lee, J., Ju, M., Ahn, H.-Y., Lee, Y. Y., Jang, H.-S., and Nam, K. T. Identifying peptide sequences that can control the assemble of gold nanostructures. *Mol. Syst. Des. Eng.* **2018**, 3, 581–590.

349. Futaki, S., and Nakase, I. Cell-Surface Interactions on Arginine-Rich Cell-Penetrating Peptides Allow for Multiplex Modes of Internalization. *Acc. Chem. Res.* **2017**, 50, 2449–2456.

350. Meng, X., Li, T., Zhao, Y., and Wu, C. CXC-Mediated Cellular Uptake of Miniproteins: Forsaking ″Arginine Magic″. *ACS Chem. Biol.* **2018**, 13, 3078.

351. Najjar, K., Erazo-Oliveras, A., Mosior, J. W., Whitlock, M. J., Rostane, I., Cinclair, J. M., and Pellois, J.-P. Unlocking Endosomal Entrapment with Supercharged Arginine-Rich Peptides. *Bioconjugate Chem.* **2017**, 28, 2932–2941.

352. Cobb, K. A., and Novotny, M. V. Selective determination of arginine-containing and tyrosine-containing peptides using capillary electrophoresis and laser-induced fluorescence detection. *Anal. Biochem.* **1992**, 200, 149.

353. Francis, P. S., Adcock, J. L., Costin, J. W., and Agg, K. M. Chemiluminescence detection of arginine-containing peptides separated with monolithic high-performance liquid chromatography. *Anal. Biochem.* **2005**, 336, 141–143.

354. Piguet, F., Ouldali, H., Pastoriza-Gallego, M., Manivet, P., Pelta, J., and Oukhaled, A. Identification of single amino acid differences in uniformly charged homopolymeric peptides with aerolysin nanopore. *Nat. Commun.* **2018**, 9, 966.

355. Meng, X., Li, T., Zhao, Y., Wu, C., CXC-Mediated cellular uptake of miniproteins forsaking "Arginine Magic" *ACS Chem. Biol.* **2018** *13*, 3078–3086.

356. DeRouchey, J., Hoover, B., and DC, Rau. A comparison of DNA compaction by arginine and lysine peptides: a physical basis for arginine rich protamines. *Biochemistry* **2013**, *52*, 3000–3009.

357. Fiori, W. R., Lundberg, K. M., and Millhauser, G. L. A single carboxy-terminal arginine determines the amino-terminal helix conformation of an alanine based peptide *Nat. Struct. Biol.* **1994**, *1*, 374.

358. Luscombe, N. M.; Laskowski, R. A.; Thornton, J. M. Amino acid-base interactions: a three-dimensional analysis of protein-DNA interactions at an atomic level. *Nucleic Acids Res.* **2001**, *29*, 2860–2874.

359. Walsh, T. R.; Knecht, M. R. Biointerface structural effects on the properties and applications of bioinspired peptide-based nanomaterials. *Chem. Rev.* **2017**, *117*, 12641−12704.

360. González-Rubio, G.; Liz-Marzán, L. M. Peptides used to make light-twisting nanoparticles. *Nature* **2018**, *556*, 313–314.

361. Lan, X.; Liu, T.; Wang, Z.; Govorov, A. O.; Yan, H.; Liu, Y. DNA guided plasmonic helix with switchable chirality *J. Am. Chem. Soc.* **2018**, **140**, 11763–11770.

362. Tan,S. J.; Campolongo,M. J.;Luoand, D.;Cheng, W. Building plasmonic nanostructures with DNA. *Nat. Nanotechnol.* **2011**, *6*, 268−276.

363. Bai, X.; Talukder, P.; Daskalova, S. M.; Roy, B.; Chen, S.; Li, Z.; Dedkova, L. M.; Hecht, S. M. Enhanced Binding Affinity for an i-Motif DNA Substrate Exhibited by a Protein Containing Nucleobase Amino Acids. *J. Am. Chem. Soc.* **2017**, *139*, 4611–4614.

364. Smith, A. J.; Thomas, F.; Shoemark, D.; Woolfson, D. N.; Sarvery, N. J. Guiding biomolecular inteactions in cells using de novo protein-protein interfaces. *ACS Synth. Biol.* **2019**, 8, 1284–1293.

365. Chiu, T.-P.; Rao, S.; Mann, R. S.; Honig, B,; Rohs, R. Genome-wide prediction of minor-groove electrostatic potential enables biophysical modeling of protein-DNA binding. *Nucleic Acids Res.* **2017**, *45*, 12565–12576.

366. Öz, R.; K K, S.; Westerlund, F. A nanofluidic device for real-time visualization of DNA-protein interactions on the single DNA molecule level. *Nanoscale* **2019**, *11*, 2071−2078.

367. Yin, Y.; Sieradzan,A. K.; Liwo, A.; He, Y.; Scheraga, H. A.Physics-Based Potentials for Coarse-Grained Modeling of Protein–DNA Interactions. *J. Chem. Theory Comput.***2015**, *11*, 1792–1808.

368. Yin, Y.; Sieradzan, A. K..; Liwo, A.; He, Y.; Scheraga, H. A. Physics-Based Potentials for Coarse-Grained Modeling of Protein-DNA Interactions. *J. Chem. Theory Comput*. **2015**, 11, 1792–1808.

369. Xu, Z.; Wei, Q.; Zhao, W.; Cui, Q.; Sahai, N. Essence of Small Molecule-Mediated Control of Hydroxyapatite Growth: Free Energy Calculations of Amino Acid Side Chain Analogues. *J. Phys. Chem. C*. **2018**, 122, 4372–4380.

370. Fan, W.; Yung, B. P. Huang, X. Chen. Nanotechnology for multimodal synergistic cancer therapy *Chem. Rev*. **2017**, *117*, 13566–13638.

371. Liu, H.; Qu, J.; Chen, Y.; Li, J.; Ye, F.; Lee, J. Y.; Yang, J. Hollow and cage-bell structured nanomaterials of noble metals. *J. Am. Chem. Soc.,* 2012, *134*, 11602–11610.

372. Leung, K. C.-F.; Xuan, S.; Zhu, X.; Wang, D.; Chak, C.-P.; Lee, S.-F.; Ho, W. K.-W.; Chung, B. C.-T. Gold and iron oxide hybrid nanocomposite materials. *Chem. Soc. Rev.* **2012**, *41*, 1911–1928.

373. Rosa-Pardo, I.; Roig-Pons, M.; Heredia, A. A.; Usagre, J. V.; Ribera, A.; Galian, R. E.;Pérez-Prieto,J.$Fe_3O_4@Au@mSiO_2$ as an enhancing nanoplatform for Rose Bengal photodynamic activity. *Nanoscale* **2017**, *9*, 10388–10396.

374. Fantechi, E.; Roca, A. G.; Sepúlveda, B.; Torruella, P.; Estradé, S.; Peiró, F.; Coy, E.; Jurga, S.; Bastús, N. G.; Nogués, J.; Puntes, V. Seeded growth synthesis of Au–Fe_3O_4heterostructured nanocrystals: Rational design and mechanistic insights. *Chem. Mater*. **2017**, *29*, 4022–4035.

375. Nogues, J.; Sort, J.; Langlais, V.; Skumryev, V.; Surinach, S. ; Munoz, J. S.; Baro, M. D. *Phys. Rep.* **2005**, *422*, 65−117.

376. Irfan, M.; Wang, C. J.; Khan, U.; Li, W. J.; Zhang, X. M.; Kong, W. J.; Liu, P.; Wan, C. H.; Liu, Y. W.; Han, X. F.; *Nanoscale*, **2017**, *9,* 5694−5700.

377. Felix, L. L.; Coaquira, J. A. H.; Martinez, M. A. R.; Goya, G. F.; Mantilla, J.; Sousa, M. H.; Valladares, L. S.; Barnes, C. H. W.; Morais, P. C. *Sci. Rep.* **2017**, *7*, 41732.

378. Feygenson, M.; Bauer, J. C.; Gai, Z.; Marques, C.; Aronson, M. C.; Teng, X.; Su, D.; Stanic, V.; Urban, V. S.; Beyer, K. A.; Dai, S.; *Phys. Rev. B*, **2015**, *92*, 054416.

379. Pineider, F.; Fernandez, C. J.; Videtta, V.; Carlino, E.; Hourani, A.; Wilhelm, F.; Rogalev, A.; Cozzoli, P. D.; Ghigna, P.; Sangregorio, C. *ACS Nano*, **2013**, *7*, 857−866.

380. Lewis, D. J.; Day, T. M.; Macpherson, J. V.; Pikramenou, Z. Luminescent nanobeads: attachment of surface reactive Eu(III) complexes to gold nanoparticles *Chem. Commun*. **2006**, 1433−1435.

381. Machala, L.; Zboril, R.; Gedanken, A. Amorphous iron(III) oxide: A review.*J. Phys. Chem. B*, **2007**, *111*, 4003–4018.

382. Fuggle ,J. C.; Kallne, E.; Watson, L. M.; Fabian, D. J. Electronic structure of aluminum and aluminum-noble-metal alloys studied by soft-X-ray and X-ray photoelectron spectroscopies. *Phys. Rev. B* **1977**, *25*, 750–761.

383. McIntyre, N. S.; Zetaruk, D. G. X-ray Photoelectron Spectroscopic Studies of Iron Oxides. *Anal. Chem.***1977**, *49*, 1521−1529.

384. Tan, B. J.; Klabunde, K. J.; Sherwood, P. M. A.X-ray photoelectron spectroscopy studies of solvated metal atom dispersed catalysts. Monometallic iron and bimetallic iron-cobalt particles on alumina. *Chem. Mater*. **1990**, *2*, 186–191.

385. Yamashita, T.; Hayes, P. Analysis of XPS spectra of Fe^{2+} and Fe^{3+} ions in oxide materials. *Appl. Surf. Sci.* **2008**, *254*, 2441–2449.

386. Wu, H.; Wang, L. Phase transformation-induced crystal plane effect of iron oxide micropine dendrites on gaseous toluene photocatalytic oxidation. *Appl. Surf. Sci.***2104**, *288*, 398–404.

387. Zhang, X.; Niu, Y.; Meng, X.; Li, Y.; Zhao, J. Structura Evolution and characteristics of the Phase Transformations between α-Fe_2O_3, Fe_3O_4 and γ-Fe_2O_3nanoparticles under reducing and oxidizing atmospheres. *Cryst Eng Comm.* **2013**, 15, 8166−8172.

388. Feygenson, M.; Bauer, J. C.; Gai, Z.; Marques, C.; Aronson, M. C.; Teng, X.; Su, D.; Stanic, V.; Urban, V. S.; Beyer, K. A.; Dai, S. Exchange bias effect in Au-Fe3O4 dumbbell nanoparticles induced by the charge transfer from gold.*Phys. Rev. B***2015**, *92*, 054416.

389. Hwang, Y.; Angappane, S.; Park,J.; An,K.; Hyeon,T.; Park,J.-G.Exchange bias behavior of monodisperse Fe_3O_4/γ-Fe_2O_3 core/shell nanoparticles.*Curr. App. Phys.* **2012**, *12*, 808−811.

390. Zysler, R. D.; Fiorani, D.; Testa,A. M.; Suber, L.; Agostinelli, E.; Godinho, M. Size dependence of the spin-flop transition in hematite nanoparticles *Phys. Rev. B***2003**, *158*, 221408.

391. Ozdemir, O.; Dunlop, D. J.; Berquo, T. S. Morin transition in hematite: Size dependence and thermal hysteresis. *Geochem.Geophys. Geosyst*. **2008**, *9*, Q10Z010.

392. Andrews, D. L.; Scholes, G. D.; Wiederrecht, G. P. Comprehensive nanoscience and technology., *Elsevier*, Academic Press, **2010**.

393. Cortie, D. L.; Lin, K.-W.; Shueh,C.; Hsu,H.-F.; Wang,X. L.; James,M.; Fritzsche,H.; Bruck,S.; Klose,F. Exchange bias in a nanocrystalline hematite/permalloy thin film investigated with polarized neutron reflectometry. *Phys. Rev. B***2012**, *815*, 054408.

394. Pineider, F.; Fernandez, C. J.;Videtta,V.; Carlino, E.; Hourani,A.; Wilhelm,F.; Rogalev,A.; Cozzoli,P. D.; Ghigna,P.; Sangregorio,C.Spin-polarization transfer in colloidal magnetic-plasmonic Au/iron oxide hetero-nanocrystals. *ACS Nano* **2013**, *7*, 857−866.

395. Liu, X. H.; Cui, W. B.; Liu, W.; Zhao, X. G.; Li, D.; Zhang. Z. D. Exchange bias and phase transformation in α-Fe$_2$O$_3$/Fe$_3$O$_4$ nanocomposites *J. Alloys Compd.***2009**, *475*, 42–45.

396. Ge, J.; Huynh, T.; Hu, Y.; Yin, Y. *Nano Lett*. **2008**, *8*, 931–934.

397. Gao, G.; Xi, Q.; Zhang, Y.; Jin, M.; Zhao, X. Y. ; Wu, U.; Zhou, H.; Guo, P.; Xu, J.; *Nanoscale* **2019**, *11*, 1169–1176.

398. Bera, K.; Ghosh, T.; Basak, S. *J. Phys. Chem. C* **2015**, *119*, 1800−1808.

399. Park, S.; Lee, I. S.; Park, J. *Org. Biomol. Chem.* **2013**, *11*, 395–399.

400. Li, H.; Liao, J.; Xibin, Z. *J. Mater. Chem. A* **2014**, *2*, 17530–17535.

401. Song, J.-M. Zhang, S.-S.; Yu, S.-H.; *Small* **2014**, *10*, 717–724.

402. Doherty, S.; Knight, J. G.; Backhouse, T.; Summers, R. J. et al. *ACS Catal.* **2019**, *9*, 4777−4791.

403. Parandhaman, T.; Pentela, N.; Ramalingam, B.; Samanta, D.; Das, S. K. *ACS Sustainable Chem. Eng.* **2017**, *5*, 489−501.

404. Ghosh, S.; Jagirdar, B. R.; *Dalton Trans.* **2018**, *47*, 17401–17411.

405. Kelly, S. M.; Lipshutz, B. H. *Org. Lett*. **2014**, *16*, 98−101.

406. Pia, D.; Zhoua, H.; Zhoua, Y.; Liua, Q.; Hea, R.; Shena, G.; Uozumi, Y. *Tetrahedron* **2018**, *74*, 2121-2129.

407. Jagadeesh, R. V.; Fer, G. W.; Westerhaus, F. A.; Surkus, A.-E.; Pohl, M.-M.; Junge, H.; Junge, K.; Beller, M. *Chem. Commun*. **2011**, *47*, 10972–10974.

408. Moreno-Hernandez, I. A.; Brunschwig, B. S.; Lewis, N. S. Tin Oxide as a protective heterojunction with Silicon for efficient photoelectrochemical water oxidation in strongly acidic or alkaline electrolytes. *Adv. Energy Mater.***2018**, *8*, 1801155−1801164.

409. Zhang, P.; Li, L.; Nordlund, D.; Chen, H.; Fan, L.; Zhang, B.;Sheng, X.; Daniel, Q.; Sun, L. Dendritic. Core-shell nickel-iron-copper metal/metal oxide electrode for efficient electro catalytic water xidation. *Nat. Commun*. **2018**, *9*, 381.

410. Suen, N.-T.; Hung, S.-F.; Quan, Q.; Zhang, N.; Xu, Y.-J.; Chen, H. M. Electrocatalysis for the oxygen evolution reaction: recent Development and Future Perspectives. *Chem. Soc. Rev*. **2017**, *46*, 337−365.

411. McCrory, C. C. L.; Jung, S.; Peters, J. C.; Jaramillo, T. F. Benchmarking heterogeneous electrocatalysts for the oxygen evolution reaction. *J. Am. Chem. Soc*. **2013**, *135*, 16977−16987.

412. Yeo, B. S.; Bell, A. T. Enhanced activity of gold-supported cobalt oxide for the electrochemical evolution of oxygen. *J. Am. Chem. Soc*. **2011**, *133*, 5587−5593.

413. Zhou, Y.; Zeng, H. C. Metal-hydroxide and gold-nanocluster interfaces: Enhancing catalyst activity and stability for oxygen evolution reaction. *J. Phys. Chem. C* **2016**, *120*, 29348−29357.

414. Kuo, C.-H.; Li, W.; Pahalagedara, L.; El-Sawy, A. M.; Kriz, D.; Genz, N.; Guild, C.; Ressler, T.; Suib, S. L.; He, J. Understanding the role of gold nanoparticles in enhancing the catalytic activity of manganese oxides in water oxidation reactions. *Angew. Chem., Int. Ed.* **2015**, *54*, 2345−2350.

415. Kraeutler, B.; Bard, A. J. Heterogeneous photocatalytic synthesis of methane from acetic acid - new Kolbe reaction pathway *J. Am. Chem. Soc*. **1978**, *100*, 2239– 2240.

416. Kudo, A.; Miseki, Y. Heterogeneous Photocatalyst Materials for Water Splitting. *Chem. Soc. Rev*. **2009**, *38*, 253–278.

417. Wang, Z,; Li, C.; Domen, K. *Chem. Soc. Rev*. **2019**, 48, 2109–2125.

418. Chen, S.; Takata, T.; Domen, K.; *Nat. Rev. Mater*. **2017**, 2, 17050.

419. Zhang, G.; Lan, Z.; Wang, X. *Chem. Sci*. **2017**, *8*, 5261−5264.

420. Wang, L.; Zhang, Y.; Chen, L.; Xu, H.; Xiong, Y. *Adv. Mater*. **2018**, 1801955.

421. Domen, K.; Naito, S.; Soma, M., Onishi, T.; Tamaru, K.; J. *Chem. Soc. Chem.Commun*. **1980***, 543-544.*

422. Maeda, K.; Teramura, K.; Lu, D.; Saito, N.; Inoue, Y.; Domen, K. *Angew. Chem., Int. Ed*. **2006**, *45*, 7806−7809.

423. Maeda, K.; Teramura, K.; Lu, D.; Takata, T.; Saito, N.; Inoue, Y.; Domen, K. *Nature* **2006**, *440*, 295.

424. Joshi, P.; Shewale, V.; Pandey, R.; Shanker, V.; Hussain, S.; Karna, S. P. Tryptophan-gold nanoparticle interaction: A first- principles quantum mechanical study. J. *Phys. Chem. C* **2011***, 115, 22818−22826.*

425. Gorlin, Y.; Chung, C.-J.; Benck, J. D.; Nordlund, D.; Seitz, L.; Weng, T.-C.; Sokaras, D.; Clemens, B. M.; Jaramillo, T. F. Understanding interactions between manganese oxide and gold that lead to enhanced activity for electrocatalytic water oxidation. *J. Am. Chem. Soc*. **2014**, 136, 4920−4926.

426. Lu, J.; Zhou, W.; Wang, L.; Jia, J.; Ke, Y.; Yang, L.; Zhou, K.; Liu, X.; Tang, Z.; Li, L.; Chen, S. Core−Shell nanocomposites based on gold nanoparticle@Zinc−Iron embed-ded porous carbons derived from metal−organic frameworks as efficient dual catalysts for oxygen reduction and hydrogen evolution reactions. *ACS Catal*. **2016**, *6*, 1045−1053.

427. Hayashi, T.; Yamaguchi, A.; Hasimoto, K.; Nakamura, R. Stability of organic compounds on the oxygen-evolving center of photosystem II and manganes oxide water oxidation catalysis. *Chem. Commun*. **2016**, 52, 13760−13763.

428. Zhang, P.; Wang, Y,; Zhang, D.; Liu, C.; Wang, D.; He, S.; Hu, G.; Tang, X. Calixarene-functionalized graphene oxide composites fixed on glassy carbone for electrochemical detection. *RSC Adv*. **2016**, *6*, 91910−91920.

429. Prasannachandran, R.; Vineesh, T. V.; Anil, A.; Krishna, B. M.; Shaijumon, M. M. Functionalized phosphorene quantum dots as efficient electrocatalyst for oxygen evolution reaction. *ACS Nano* **2018**, 12, 11511−11519.

List of Publications (Published /Prepared)

1. **Lone, S. A.** and Sadhu, K. K. Differentiation of amino acids containing polar uncharged side chains by time dependent growth of gold nanoparticles in presence of amine modified DNAs. *J. Phys. Chem. C* **2019**, *DOI: 10.1021/acs.jpcc.9b04911*

2. **Lone, S. A.** and Sadhu, K. K. Gold nanoflower for selective detection of single arginine effect in α-helix conformational change over lysine in 3_{10}-helix peptide. *Bioconjugate Chem.* **2019**, *8,* 112–118.

3. **Lone, S. A.** and Sadhu, K. K. Formation of Growth-Mediated Gold Nanoflowers: Roles of the Reducing Agent and Amine-Modified, Single-Strand DNA Sequences. *ChemPlusChem* **2019**, *84*, 112–118.

4. **Lone, S. A.** Ghosh, S. and Sadhu, K. K. Tryptophan-Stabilized Au$-$Fe$_x$O$_y$ nanocomposites as Electrocatalysts for Oxygen Evolution Reaction. *ACS Omega* **2019**, *4*, 3385–3391.

5. **Lone, S. A.;** Sanyal, P.; Das, P.; and Sadhu, K. K. Citrate Stabilized Au$-$Fe$_x$O$_y$ Nanocomposites: Variable Exchange Bias, Catalytic Properties and Host-guest Chemistry with Doxorubicin. *ChemistrySelect* **2019**, *4,* 8237–8245.

6. **Lone, S. A.** and Sadhu, K. K. Growth mediated formation of different gold nanoarchitectures by treatment with natural amino acids. *Manuscript under preparation.*

Patent Filed

Sadhu, K. K. and **Lone, S. A.** A system method of syntheses of gold-iron oxide and gold-zinc oxide nanocomposites in aqueous medium at room temperature. *Patent No. IN 201711024170.*

Poster Presentation at National/International conferences

1. **Lone, S. A.** and Sadhu, K. K. 'Synthesis of Au-Fe x O y with variable iron content' poster presentation at Modern Trends in Inorganic Chemistry (MTIC-XVII) held at CSIR-NCL, Pune and IISER, Pune during December 11-14, 2017.

2. **Lone, S. A.** and Sadhu, K. K. Citrate Stabilized Au-Fe$_x$O$_y$ nanocomposites with variable exchange bias and catalytic properties poster presentation at 'ACS on Campus Symposium' held at IIT Roorkee on February 7, 2018.